Pore- and core-scale studies for development of the Kinetic Interface Sensitive tracer
–
A novel reactive tracer technique to measure the fluid-fluid interfacial area for dynamic two-phase flow in porous media

Dissertation

for the award of the degree

"Doctor rerum naturalium" (Dr.rer.nat.)

of the Georg-August-Universität Göttingen

within the doctoral program Geoscience

of the Georg-August University School of Science (GAUSS)

submitted by

Huhao Gao

From Zhejiang, China

Göttingen, 2022

Thesis Committee:

Prof. Dr. Martin Sauter

(Department of Applied Geology, University of Göttingen)

Dr. Alexandru Tatomir

(Department of Applied Geology, University of Göttingen)

Prof. Dr. Holger Steeb

(Institute of Applied Mechanics, University of Stuttgart)

Members of the Examination Board:

Reviewer: Prof. Dr. Martin Sauter

(Department of Applied Geology, University of Göttingen)

Reviewer: Prof. Dr. Holger Steeb

(Institute of Applied Mechanics, University of Stuttgart)

Further members of the Examination Board:

Prof. Dr. Volker Thiel

(Department of Geobiology, University of Göttingen)

Dr. Alexandru Tatomir

(Department of Applied Geology, University of Göttingen)

Dr. Nikolaus Karadimitriou

(Institute of Applied Mechanics, University of Stuttgart)

Dr. Iulia Ghergut

(Department of Applied Geology, University of Göttingen)

Date of the oral examination: 21.07.2022

Abstract

Fluid-Fluid Interfacial Area (FIFA) is an important parameter relevant in numerous geological applications where two phases of fluids exist and interphase reactive mass transfer can happen. For example, in geological storage of carbon dioxide, the FIFA can be monitored to evaluate the extent of capillary trapping and dissolution reaction rates. A new type of tracer, termed Kinetic Interface Sensitive (KIS) tracer is developed to measure the FIFA during dynamic two-phase flow in porous media. This thesis demonstrate a series of studies at both pore- and core-scale to investigate the reactive transport of the KIS tracer, and to validate the concept of the KIS tracer. At the pore-scale, direct numerical simulations of reactive transport of the KIS tracer are implemented with a novel Continuous Species Transfer formulation which is in consistent with the Phase-Field Method. The PFM-CST model is employed to investigate the retention of the reacted tracer solute mass due to capillary effects, during drainage in a 2D sandstone porous media, and a single 2D fracture with rough surfaces. The mobile and immobile zones are distinguished, and the corresponding FIFA, and reacted tracer solute mass in these two zones are quantified. It is showed that the KIS tracer method can be employed to selectively determine the mobile part of the FIFA. Additionally, the PFM-CST model is further employed to study the possibility of KIS tracer application in push-pull tests. The interpretation of the tracer breakthrough curves (BTCs) and how the different hydraulic parameters can affect the BTCs are investigated. Furthermore, at the core-scale, column drainage experiments employing the KIS tracer are implemented on numerous porous media comprised of glass beads and natural sands at different grain sizes, grain roundness and surface textures. The specific capillary-associated FIFA is found to be larger for sands with smaller grain sizes and for sands with rougher surfaces. Through these column experiments, the concept of KIS tracer method is validated, and the spectrum of porous media where the KIS tracer can be applied is extended. Besides, the macro-scale KIS tracer reactive transport model is employed to study the effects of heterogeneity in the 2D flume consist of two different porous materials. The deformation of the BTCs due to aquifer heterogeneity are demonstrated, and the linear relationship between the slopes of the BTCs and the averaged specific FIFA in the 2D flume are found. Finally, the pros and cons of the KIS tracer applications in dipole configurations and push-pull setups are summarized, and the further perspectives about the KIS tracer methods are discussed.

Acknowledgement

First and foremost, I would like to express my greatest appreciation to my supervisors, Prof. Dr. Martin Sauter and Dr. Alexandru Tatomir, for their constant support through the time of my doctoral studies, for their guidance, patience, encouragement and immense knowledge, and for the opportunity to become a member of this esteemed group with the interesting research topic. I would like to emphasize the extensive support for improving my writing skills and the freedom I was given to develop and process my ideas. I would also like to express my gratitude to my co-supervisors, Prof. Dr. Holger Steeb and Dr. Nikolaus Karadimitriou, for their creative ideas, interesting discussions, and valuable suggestions. I would like to thank all my supervisors for the corrections and improvements being made during reviewing of the manuscripts and the thesis. In addition, I would like to thank the rest of my thesis committee, Dr. Iulia Ghergut, Prof. Dr. Volker Thiel, for their thoughtful comments on my thesis and their valuable advice.

Furthermore, I would like to thank all my colleagues in the Department of Applied Geology. I would like to thank my officemates and friends Dejian Zhou, Quan Liu, Hiwa Abdullah, and former classmates and friends Xue Xu and Chujun Zang, for the friendship and enjoyable time we spent together. I would like to thank Reza Taherdangkoo and Pengxiang Qiu for the helpful advice. I would like to express my gratitude to Prof. Tobias Licha, Wiebke Warner, and Mechthild Rittmeier, for their help during my experimental work in the laboratory.

I would like to acknowledge the German Research Foundation (Deutsche Forschungsgemeinschaft, DFG, Project Number 428614366), for funding my doctoral study. I would like to acknowledge the master's program Hydrogeology and Environmental Geoscience, for giving me the comprehensive basic knowledge that I need in preparation for my doctoral study.

Last but not least, I would like to thank all my families for their care and support. This thesis is dedicated to my beloved parents, who always support and encourage me on this way. This thesis is dedicated to my beloved wife Yiyi Lu, for her constant support, patience, and love.

Contents

1. Introduction 1
1.1 Background and motivation 1
1.2 Objectives and Outline 3
1.3 Reference 4
2. A two-phase, pore-scale reactive transport model for the kinetic interface-sensitive tracer 8
Abstract: 9
2.1 Introduction 9
2.1.1 Kinetic Interfacial Sensitive tracer: theoretical background 9
2.1.2 Pore-scale numerical methods 12
2.2 Mathematical model 14
2.2.1 Phase-Field Method 14
2.2.2 Two phase flow dynamics 15
2.2.3 Reactive transport 16
2.2.4 Numerical implementation 18
2.3 Numerical Method and details 18
2.3.1 Model verification 18
2.3.2 Model test in a 2D slit 21
2.3.3 Model application for flow in porous media 22
2.4 Results and discussion 23
2.4.1 Model verification 23
2.4.2 Model test in a 2D slit 25
2.4.3 Application of KIS tracer transport in porous media 27
2.5 Summary and Conclusions 34
Nomenclature 35
2.6 Acknowledgement 37
2.7 Supporting information 37
2.8 Reference 47
3. Effects of surface roughness on the kinetic interface-sensitive tracer transport during drainage processes 53
Abstract: 54
3.1 Introduction 54
3.1.1 Kinetic Interfacial Sensitive tracer 55
3.1.2 Surface roughness-related effects 57
3.1.3 Pore-scale reactive transport modelling 57
3.1.4 Objectives 58
3.2 Mathematical model 58
3.2.1 Phase-Field Method 58
3.2.2 Two phase flow dynamics 59
3.2.3 Reactive transport 59
3.2.4 Numerical implementation 61
3.3 Numerical details 61
3.3.1 Model setups 61
3.3.2 Construction of the rough surface 62
3.3.3 Data treatment 64
3.4 Results and discussion 64
3.4.1 Identification of mobile and immobile zones 64

3.4.2 Mobile interfacial area 65
3.4.3 Immobile interfacial area and deposited water volume.....66
3.4.4 Retention of the mobile solute mass 68
3.4.5 Relation between the mobile interfacial area and mobile solute mass.....68
3.4.6 Determination of the film-associated mobile mass retention term 70
3.5 Summary and Conclusions.....71
3.6 Acknowledgement.....72
3.7 Reference.....72
4. Reservoir characterization by push-pull tests employing Kinetic Interface Sensitive tracers - a pore-scale study for understanding large-scale processes.....78
Abstract: 79
4.1 Introduction 79
4.1.1 Background of the KIS tracer.....79
4.1.2 A novel push-pull KIS tracer method 81
4.1.3 Pore-scale direct numerical simulation 83
4.1.4 Objectives.....83
4.2 Mathematic model.....84
4.2.1 Phase-Field Method.....84
4.2.2 Two phase flow dynamics.....84
4.2.3 Reactive transport.....85
4.3 Numerical model 86
4.3.1 Numerical implementation.....86
4.3.2 Pore-scale numerical experiment setups 86
4.3.3 Pore-scale data treatment 88
4.3.4 Continuum-scale numerical modeling 89
4.4 Column experiment.....90
4.4.1 Materials and setup.....90
4.4.2 Experimental procedure 91
4.5 Results and discussion.....92
4.5.1 Concentration distributions from the pore-scale simulation 92
4.5.2 Interpretation of the breakthrough curve.....96
4.5.3 Application to column experiments 98
4.6 Summary and Conclusions.....100
4.7 Acknowledgement.....101
4.8 Reference.....101
5. Kinetic Interface Sensitive Tracers – Experimental Validation in a Two-Phase Flow Column Experiment. A Proof of Concept.....105
Abstract: 106
5.1 Introduction 106
5.2 Theory 109
5.2.1 KIS tracers' principles.....109
5.2.2 Immiscible wetting phase displacement by the non-wetting phase 111
5.2.3 KIS tracer transport in multiphase system 112
5.2.4 Mass transfer processes across the fluid-fluid interface.....113
5.2.5 Fluid-fluid interfacial area considerations.....113
5.2.6 Estimating specific interfacial areas.....114
5.3 Material and Methods.....115

5.3.1 Laboratory setup 115
5.3.2 Experimental procedure 119
5.3.3 Hydrolysis at the interface 120
5.3.4 Modeling multiphase flow and transport of KIS-tracer reaction product breakthrough 121
5.4 Results and discussion 122
5.4.1 Two phase flow sensitivity analysis 122
5.4.2 Reactive Transport 123
5.4.3 Evaluation of the specific interfacial area 125
5.5 Summary and Conclusions 126
5.6 Acknowledgements 127
5.7 References 127
6. Estimation of NAPL-Water interfacial areas for unconsolidated porous media by kinetic interface sensitive (KIS) tracers 135
Abstract: 136
6.1 Introduction 136
6.1.1 Models for calculating the FIFA 137
6.1.2 Measurement techniques for fluid-fluid interfacial area 138
6.1.3 Studies comparing the experimental methods for FIFA measurement 138
6.1.4 Porous media characteristics influence on FIFA 139
6.1.5 Grain-size influence on fluid-fluid interfacial area 140
6.1.6 Porous-medium-texture influence on the fluid-fluid interfacial area 140
6.1.7 Objective 141
6.2 Materials and methods 141
6.2.1 Materials 141
6.2.2 Methods 147
6.2.3 NAPL-Water Experiments 149
6.2.4 Data analysis: Mathematical modelling and interpretation of the results 150
6.3 Results 151
6.3.1 Two-phase flow calibration 151
6.3.2 Interpretation of the hydrolyzed KIS tracer reaction product breakthrough curves 153
6.3.3 Capillary-associated specific interfacial area calculation 154
6.4 Discussion 156
6.4.1 Hydrolyzed KIS tracer breakthrough curves 157
6.4.2 Potential explanations of discrepancies in tracer BTC 158
6.4.3 Grain-diameter-size influence on IFA 158
6.4.4 Determination of maximum specific capillary-associated interfacial area with the KIS tracer method 159
6.4.5 Comparison of maximum capillary associated-specific interfacial area with literature 160
6.4.6 Comparison of total specific interfacial area with literature data 161
6.4.7 Texture influence on IFA 162
6.5 Conclusions 164
6.6 Acknowledgments 166
6.7 References 166
6.8 Appendix 171

7. Numerical investigations of front morphology and role of heterogeneity in two-phase flow in porous media using kinetic interface sensitive tracers 173
Abstract: 174
7.1 Introduction 174
7.1.1 Front instability during displacement 174
7.1.2 Experimental study on heterogeneity and front morphology 175
7.1.3 Darcy-scale modelling of front morphology 175
7.1.4 The kinetic interface sensitive (KIS) tracer 176
7.1.5 Objective 177
7.2 Mathematical model 178
7.2.1 Two-phase flow in porous media model 178
7.2.2 KIS tracer reactive transport model 179
7.2.3 Explicit interfacial area model 180
7.2.4 Numerical implementation 180
7.3 Numerical model setup and data processing 180
7.3.1 Model application to immiscible displacement in a flow cell 180
7.3.2 Data processing 183
7.4 Results and discussion 184
7.4.1 Comparison of concentration BTCs with porous media heterogeneity 184
7.4.2 Concentration BTCs with strong deformation of the front 187
7.5 Summary and Conclusions 191
7.6 Statements and declarations 192
7.7 References 192
8. Summary and perspectives 196
8.1 Summary and conclusions 196
8.2 Further perspectives 199

List of Figures

Figure 2.1 Schematic of the KIS tracer reactive transfer process (after Tatomir et al. 2018). A: Phenyl Naphthalene-2-Sulfonate. B: Naphthalene-2-Sulfonic Acid. C: Phenol……....11
Figure 2.2 Sketch of the numerical setups for verification of the reactive transport model in (a) a transient interfacial diffusion process (b) a simultaneous reaction-diffusion process at the interface and (c) an advection-diffusion process at equilibrium……..……..20
Figure 2.3 Plot of (a) geometry of the porous medium and boundary conditions (pore space in blue color) (b) mesh with triangle elements with side length h=1×10^{-6}m…….....22
Figure 2.4 Comparison of concentration profiles of 2-NSA concentration computed analytically and numerically: (a) (at ε=1×10^{-7}m) for the transient mass transfer at t=0.5s, for P_{ow}=1, P_{ow}=0.1, P_{ow}=0.01 and P_{ow}=0.001, (b) (at ε=1×10^{-6}m and ε=1×10^{-7}m) for mass transfer at t=0.5s near the interface region……...……24
Figure 2.5 Comparison between concentration profiles of analytical and numerical model simulations (ε=1×10^{-7}m) of the reaction-diffusion process at t=0.2s, t=1s and t=2s……..25
Figure 2.6 Comparison between concentration profiles of analytical and numerical model simulations of the transport process for Pe_g=10, Pe_g=10^3 and Pe_g=10^5 at t=1ms, t=2ms and t=3ms……..25
Figure 2.7 Model results of solute transport in octane/water displacement process in a capillary tube: (a) volume fraction of the water phase for with contact angles 45° at t=0.04s (b) Plot of the concentration profiles at the Péclet numbers of Pe_g=1, Pe_g=10 and Pe_g=100, as well as the corresponding streamline profile……27
Figure 2.8 Volume fraction of water phase (left) and solute concentration (right) just before breakthrough for each case. At three different inflow rates (in rows), simulations with two different diffusivities (in columns) are demonstrated……28
Figure 2.9 Plot of simulation results (a): 2-NSA concentration with n-octane phase in gray color, with the isoline of $\log_{10}(c_k)$=-4.5 for flowing zones plotted in magenta color; (b): distribution of the local Péclet number; (c): probability distribution of the local Péclet number, during the drainage process for Case 2 at t_c=0.15, t_c=0.3 and t_c=0.45……30
Figure 2.10 Plot of simulation results: the quantified 2-NSA mass in the mobile and immobile zones (M), the 2-NSA mass produced by mobile and immobile interface (M_{IFA}), and the 2-NSA mass calculated from interfacial areas with the mobile mass retention term (M_{RT}), versus the dimensionless time for all cases. The inset plot shows the corresponding specific interfacial area in the mobile and immobile zones. …….....32
Figure 2.11 Plot of simulation results of mobile mass retention process into the stagnant zones, in a zoom-in region from Case 2 at t_c=0.129, t_c=0.144 and t_c=0.159. The diagrams show the spatial distribution of solute concentrations with the non-wetting phase covered by gray color. The red arrows show the direction of velocity vector, and the length of the arrows is proportional to the natural logarithm of the norm of velocity vector…….33
Figure 2.S1 Model verification through the study of two-phase co-current flow through two parallel plates (a) Schematics of the viscous coupling in channel co-current flow. (b) Comparison of the velocity profiles along the channel width obtained by the model and the analytical solution at viscosity ratios (oil to water) β=10 and β=0.1……..38
Figure 2.S2 Model validation with the bubble retraction experiment from Guido and Villone (1999) (a) Plot of the simulated bubble at beginning of the simulations with deformations D_0=0.22 and D_0=0.42, and at the end when the bubble is at rest (b) Comparison of modelling results as ln(D/D_0) to the experimental and theoretical results…….…….39

Figure 2.S3 Benchmark of the simulated film thickness (during the quick displacement process of ethanol by air in a capillary tube): (a) Sketch of the model setup; (b) volume fraction of ethanol at t=1ms. The zoom-in frames show the deposited film thickness (solid black line is the center line of the diffuse interface V_f=0.5)……...……40
Figure 2.S4 Study of the mesh convergence: (a) Geometry of a sub-region of the porous media illustrated in the manuscript Gao et al. 2021 in Figure 2.3, and the boundary conditions (here, a mesh with h=1×10^{-6} m is demonstrated); (b) Results of the mesh convergence study based on the non-wetting phase volume fraction in the domain versus the time, at a fixed ratio of h=ε (left-hand side subfigure) and at a fixed element size h=1×10^{-6}m (right-hand side subfigure)……..42
Figure 2.S5 Analysis of mass balance for the fluid phases and the reacted solute: (a) Plot of the volumes of wetting phase, non-wetting phase and the total fluid volume of both phases, calculated from initial and boundary conditions in lines and that quantified from the modelled (sum of fluid volume that in the domain and leave the outlet) in markers; (b) Plot of solute mass calculated from the interfacial area in lines and that quantified from the model (the sum of solute mass in domain and that transport through the outlet) in markers……43
Figure 2.S6 Plot of the non-wetting phase saturation versus the dimensionless time during the drainage process, where the red dashed line shows the breakthrough times for each case. The shrinkage of the non-wetting phase volume due to the capillary end effect is observed shortly after the breakthrough, especially for the Case3 with the lowest inflow velocity…….…..44
Figure 2.S7 Sketch of local slight motion induced by local pressure change, in a zoom-in region from Case2. The volume fraction of water (top) and corresponding fluid pressures (bottom) are shown at three different times t_c=0.261 t_c=0.265 and t_c=0.269. The white arrows show the direction of the velocity vector, and the length of the arrows is proportional to the natural logarithm of the norm of the velocity vector. During t_c=0.261 to t_c=0.265, a rise of the local pressure triggers a very small movement of the trapped water (towards left). When the pressure drops again at t_c=0.269, the trapped water recedes……..…..44
Figure 2.S8 Sensitivity analysis for choosing the threshold local Péclet number for Case2, by quantification of (a) specific interfacial area and (b) solute mass, in the mobile zones of the domain. The threshold Pe_l is swapped at 0.8, 1.6, 2.4, 3.2, 4, 4.8. The quantified results start to converge when Pe_l=2.4……...……45
Figure 2.S9 Probability distribution of the local Péclet number for Case 1 and Case 3 at tc=0.0015 and tc=0.53. The difference of the probability distributions is shown for single phase of water flow in the domain at the beginning of drainage (tc=0.0015) and for two-phase flow at the end of drainage (tc=0.53). The red lines represent the threshold local Péclet number chosen for Case1: Pel=4.8 and for Case3: Pel=0.48.……...46
Figure 2.S10 Supplement for verification of section 2.3.1.1. Comparison of concentration profiles of 2-NSA concentration computed analytically and numerically: (at ε=1×10^{-7}m) for the transient mass transfer at t=0.5s, for P_{ow}=4×10^{-4}, P_{ow}=3×10^{-4}. When P_{ow}<4×10^{-4}, the model come to come unphysical results, which is not fitted to the analytical solution……46
Figure 3.1 Schematic of the KIS tracer reactive transfer process for smooth and rough surfaces (after Gao et al. 2021). A: Phenyl Naphthalene-2-Sulfonate. B: Naphthalene-2-Sulfonic Acid. C: Phenol…….…56
Figure 3.2 Geometry of the porous medium and boundary conditions (pore space in blue color) in subfigure (a). The mesh for a sub-region of the domain is shown in subfigure (b)……....62
Figure 3.3 Plot of the probability distribution of the local Péclet number for Surface10 after drainage (t=0.033 s) as an example. The inserted figure shows the profile of the local Péclet number for the slit.……...……65

Figure 3.4 Plot of (a) mobile interfacial area during the drainage process for the rough surface at R_{rms}=3 μm and (b) the averaged mobile interfacial area versus the root mean square roughness from all simulations. The inserted figures in subfigure (b) show the configurations of the moving menisci from three simulations at different R_{rms}. The inserted figures on top show the evolution of the moving menisci for the rough surface (R_{rms}=3 μm). The inserted figure at bottom left is for the smooth surface (R_{rms}=0), and the inserted figure at bottom right is for the roughest surface (R_{rms}=15.8 μm)……..……66
Figure 3.5 Plot of (a) immobile interfacial area per surface area and (b) deposited water volume per surface area, versus the root mean square roughness from all simulations. Examples of film configurations after drainage from Surface 4 (c) and Surface 10 (d)…….……67
Figure 3.6 Plot of the retention process of the solute mass in the flowing zone for a zoom-in region at t=0.014 s, t=0.015 s and t=0.016 s. The non-wetting phase is plotted in gray color. The red arrows show the direction of velocity vector, and the length of the arrows is proportional to the natural logarithm of the norm of velocity vector. ……..……68
Figure 3.7 Plot of the quantified solute mass in the mobile zone (M_m) in gray dots, the total solute mass produced by the moving meniscus ($M_{IFA,m}$) and mobile solute mass calculated with adding the retention term ($M_{RT,m}$), versus the time for four simulations as examples……...…….70
Figure 3.8 Plot of the film-associated mobile mass retention term versus the root mean square roughness from all simulations.…….…….……71
Figure 4.1 Conceptual illustration of the push-pull KIS tracer method: (top) field-scale application; (bottom) the molecular/FIFA-scale depicting the hydrolysis reaction of Eq.(4.1), modified from Tatomir et al. (2018)…….…..82
Figure 4.2 Plot of (a) geometry of the two-dimensional porous medium and boundary conditions, with the pore space in blue; (b) initial uniform distribution of the grains; (c) mesh built with triangular elements for a zoom-in section in the red frame (d) analysis of REV based on the porosity……..….88
Figure 4.3 Sketch of (a) column experiment setup (with arrows showing the flow direction during push-pull process, (b) scanning electron microscopy image of the glass beads (Tatomir et al. 2018), and (c) grain size distribution of the glass beads……91
Figure 4.4 Plot of the 2-NSA concentration during the push-pull process at t=0.07 s, t=0.15 s, t=0.18 s, t=0.21 s, t=0.24 s and t=0.32 s: (a) spatial distribution of 2-NSA concentration from pore-scale simulation, with NAPL plotted in gray; (b) comparison between averaged 2-NSA concentration in the REVs from pore-scale simulation (red dots) and NSA concentration predicted by the macro-scale reactive transport model (in blue dashed lines)…….……..94
Figure 4.5 S_w and a_{wn} obtained from the REVs of pore-scale simulations (in dots), and S_w and a_{wn} given by explicit expression for the macro-scale reactive transport model (in dashed lines), during the push-pull process……...…96
Figure 4.6 Plot of the 2-NSA concentration BTCs: (a) comparison of the concentration BTC monitored at the measurement line (control plane) of the pore-scale simulations (dots) and of the calibrated macro-scale model (line). Sensitivity analysis of (b) specific interfacial area during primary drainage (a_{wn}^{D}), (c) specific interfacial area during main imbibition (a_{wn}^{I}), and (d) dispersion coefficient for main imbibition (D_{dis}^{I})……..……..98
Figure 4.7 Results from the column experiment: (a) fitting of the BTCs from the macro-scale reactive transport model to the (triplicate) column experimental results; (b) comparing the measured specific FIFA from primary drainage (PD) and main imbibition (MI) to the results obtained from X-RCT by Culligan et al. (2004) and Porter et al. (2010)……100

Figure 5.1. Conceptual Model of KIS tracers at different scales of considerations: (top) field-scale application of the KIS tracer at a CO_2 storage pilot site; (left) pore-scale illustration of the types of IFAs (a_{wn}, capillary associated IFA, a_n, area of the non-wetting phase, a_w area of the wetting phase, a_s area of the solid phase; (right) the molecular/IFA-scale depicting the hydrolysis reaction, Eq. (5.4)……..……110
Figure 5.2. Experimental set up for the column experiment …….……117
Figure 5.3. Key experimental base data: **a**) Grain size distribution and the cumulative distribution function (line); **b**) comparison of n-octane breakthrough curves in two phase flow experiments for different flow directions. Note, that the horizontal mode has a higher sampling rate to resolve the n-octane front in greater detail; **c**) scaled MIP data (mercury-air scaled to octane-water) fitted using eq. (5.9); **d)** calculated $p_c - S_w - a_{wn}$ surface with eq. (5.24) **e**) microscopic photograph of the used glass beads and the contact angle (25x magnification) in n-octane/water fluid-system. The glass is wetted with ultra-pure water and surrounded by n-octane; **f)** scanning electron microscopy image of the glass beads with no-measurable surface roughness…….…..118
Figure 5.4. Determination of the hydrolysis kinetic rate using static batch test experiments: **a**) 2-NSA concentration evolution over time for different initial concentrations of the KIS tracer (i.e. 0.1, 0.3, 0.5, 0.7 µg/l); **b)** calculated hydrolysis reaction rate for different initial starting concentrations; **c**) 2-NSA concentration over time for an initial concentration of 0.5g/L using the *new* (commercially purchased) and *old* (self-synthesized) tracer; **d**) observed concentration of 2-NSA over time taken from Schaffer et al. (2013) using continuous measurements..……...…..120
Figure 5.5. Best fitting predicted BTC and the predicted saturation over the column length for each experiment (EXNT01 stands for experiment with new tracer 01; EXOT01 stands for experiment with old tracer 01)…….……123
Figure 5.6. Predicted results for experiment EXNT01. **a**) Non-wetting saturation along the column length **b**) non-wetting saturation over time and **c**) the non-wetting saturation for predicted values of specific IFA……...……124
Figure 5.7. Numerical simulations for each KIS tracer experiment. The highlighted area denotes the entire spectrum of results required to fit the most off-set data points, the dashed lines show the best fitting solution for the non-linear description of the hydrolysis reaction rate over time……..125
Figure 6.1: a) Illustration of the different types of interfacial areas b) KIS tracer (A) adsorption on the fluid-fluid interface, followed by hydrolysis to form two by-products (B+C) dissolved in water, an acid and alcohol……..…..137
Figure 6.2: Experimental setup of two-phase flow system. 1) Reservoir of n-octane with KIS tracer. 2) Peristaltic pump. 3) Sand column. 4) Cap embedded with frit. 5) 5ml measuring cylinder. 6) Fluorescence spectrophotometer. 7) High precision fluorescence cuvette……142
Figure 6.3: Characterization of the five porous media used in the KIS tracer experiments: three glass beads (GB55, GB170 and GB240) and two natural sands (NS210 and NS250). Digital illustration of the media (left column), grain-size (distribution) with the cumulative frequency curve (middle), capillary pressure-saturation, $p_c - S_w$ relationship determined with MIP, and the calculated $a_{wn} - S_w$relationship with the explicit interfacial area model of (Grant and Gerhard 2007)……144
Figure 6.4: a) Relationship between mean pore-throat diameter (measured with MIP), p_{50}, pore uniformity coefficient ($C_{pu} = p_{60}/p_{10}$) and the mean grain diameter (measured with DIA), d_{50}; **b)**The upper p_{50} values at GB55 and NS250 are corrected to remove the micro-porosity determined with MIP…….…..145
Figure 6.5: Pore-diameter distribution determined with mercury-intrusion porosimetry, based on Washburn model (Washburn 1921)……..146

Figure 6.6: Measured kinetic rates in static batch experiments. a) 2-NSA concentration reaction rates over time expressed in intensity units as a function of initial 2-NSAPh concentration in n-octane. b) calculated hydrolysis reaction rates as a function of initial 2-NSAPh concentration using the experiments in subfigure a). Here the unit of intensity $a.u = 86.293 \cdot c_{2NSA} + 62.6$…….149
Figure 6.7: Breakthrough of the volumetric fraction of non-wetting phase to total fluid volume at the column outlet, experimental data (black) and simulated breakthrough curves with sensitivity analysis (color). The variation ranges are provided in **Table SI 6.1**…….…….152
Figure 6.8: Breakthrough curve of 2-NSA concentration (hydrolyzed KIS tracer) at column outlet. The black curve shows the experimental-data, while the colored plots correspond to a range of fitting coefficient a_0, varied between $a_{0,min}$ and $a_{0,max}$ (yellow) given in **Table 6.3**. The initial KIS tracer concentration in n-octane is specified in each subfigure…….……..153
Figure 6.9: Ranges for the specific capillary associated IFA, $a_{wn} - S_w$ relationships, for the five porous media. The best fitting curves in each experiment (Exp.1 - yellow, Exp.2 - blue, Exp.3 - red), and the Gerhard and Grant model applied to MIP derived $p_c - S_w$ curves ……..……155
Figure 6.10: Relationship between n-octane/water maximum specific capillary associated interfacial area, a_{wn}^{max} and inverse median grain diameter. Values determined using the KIS tracers on the five porous media, GB55, GB170, GB240, NS210, NS250. The values for a_{nw}^{max} are reported in **Table SI 1**…….……159
Figure 6.11: Mobile a_{wn}^{max} determined by KIS tracer experiment in an n-octane-water fluid system and comparison with literature data for capillary associated interfacial area…….161
Figure 6.12: Compiled total specific IFA, a_n, and capillary-associated IFA, a_{wn}^{max} from the literature and this study. The total IFA for the five materials calculated as SSSA-MIP and GSSA, and the mobile capillary-associated IFAs determined with KIS tracer method…….162
Figure 6.13: Specific capillary-associated IFA variation depending on the texture related parameters…….……164
Figure 7.1 Development of a fingering front starting at initial conditions (left); smoothed, conserved, increased, branched front shapes (classification after Bakharev et al. 2020). On the right, the zoom-in pore-scale region showing a fluid-fluid interface where the hydrolysis reaction of the kinetic interface sensitive tracer happens (from Eq.7.1, KIS tracer is A: phenyl naphthalene-2-sulphonate, B: Naphthalene-2-sulphonate acid, and C: Phenol) ……..177
Figure 7.2. a) Simulation domain, the boundary conditions and the monitoring line located at y=0.05 m; b) the fourteen heterogeneity patterns investigated (Pattern 1 and Pattern 2 are the ones where the domain is filled by coarse sand and fine sand and are not illustrated)……..……182
Figure 7.3. Plot of (a) the heterogeneity factor (γ) for the 14 patterns for Case 1 and (b) concentration breakthrough curves at the monitoring line for all simulated heterogeneity patterns……..185
Figure 7.4. Plot of the distribution of (a) the non-wetting phase saturation, (b) acid concentration in water, and (c) specific interfacial area at the time of concentration breakthrough, for simulation of Pattern 11 and Pattern 14…….…186
Figure 7.5. Plot of (a) the slope of the concentration BTCs versus the fraction of total bulk volume occupied by the fine sand; (b) the averaged specific interfacial area at the end of the drainage process versus the slopes of the concentration BTCs, resulted from all simulations of Case 1…..187
Figure 7.6. Plot of (a) the heterogeneity factor (γ) for the 14 patterns for Case 2 and (b)the concentration breakthrough curves at the measurement line for all simulated heterogeneity patterns with the inclusion lens permeability of 10^{-13} m^2, when the deformation of the front is enhanced ……..…188

Figure 7.7. Plot of (a) the nonwetting phase saturation and concentration distribution at three different time steps at t=1900s, 2700s and 5100s, from simulations of Pattern 11 when the front deformation is enhanced; (b) zoom-in of the marked domain selection at t=2700 s showing the advective transport towards and into the conductive lenses (the grey arrows are the streamlines computed for the wetting-phase velocity); (c) comparison of concentration breakthrough at the monitoring line for simulation of Pattern 11 before and after the front deformation enhancement…….190

List of Tables

Table 3.1 Parameters of the smooth surface (Surface 1) and the rough surfaces (Surface 2 to Surface 24)……..……63
Table 5.1. Summary of porous media and fluid properties……..….117
Table 5.2. Summary table of hydrolysis reaction rates as shown in Figure 5.4……....121
Table 5.3. Summary of best fitting injection rate and permeability for each experiment……..…123
Table 5.4. Summary of calculated specific IFAs ……..126
Table 6.1. Summary of relevant properties of the porous media used in the KIS tracer two-phase flow experiments……...……146
Table 6.2: Fluid and soil-fluid properties……..147
Table 6.3: Parameters ranges, $a_{0,min}$ to $a_{0,max}$ used to identify the best fitting for the capillary-associated IFA, a_{wn} in Eq. (6.7). Here $a_{0,GG}$ and $a_{0,BF}$ are the a_0 parameter best fit to the Grant and Gerhard (2007) model, and to the experimental data …….……154
Table 7.1. Parameters of the porous medium (fine- and coarse-glass beads) and of the fluids used in the simulations……..183

1. Introduction

1.1 Background and motivation

Chemical tracers have been used extensively for studying the movement of gases and liquids in porous media systems. While hydraulic methods allow the rapid assessment of reservoir properties, the actual (reactive) transport relevant characteristics can only be determined by tracer experiments, providing information such as the effective porosity, solute dispersivity, saturation of a residual phase, and the specific interfacial areas between the rock-fluid or fluid-fluid for multiphase flow conditions, etc., in the porous reservoirs.

Quantification of the Fluid-Fluid Interfacial Area (FIFA) is essential for studying reactive multiphase flow and transport in porous materials (Tatomir et al., 2018). The FIFA is an important parameter significant in the quantification of the interphase (reactive) mass transfer (e.g. dissolution, hydrolysis, volatilization, adsorption, etc.) (Miller et al., 1990). The quantification of the FIFA is relevant in a wide range of scientific and engineering applications including the remediation of aquifers contaminated by non-aqueous phase liquids (NAPL) (Brusseau, 1992; Miller et al., 1990), geological storage of carbon dioxide (Tatomir et al., 2016; Schaffer et al., 2013), enhanced oil recovery (Graveleau et al., 2017), etc. For example, in geological storage of CO_2, both the rate of CO_2 dissolution in brine and the extent of the residual trapping are determined by the FIFA (Tatomir et al., 2018). The larger the FIFA, the larger the reacted or dissolved mass of CO_2, meaning greater storage effectiveness in terms of long-term trapping (Schaffer et al., 2013). In this sense, novel "smart tracers" are required to quantify and describe the migration and the fate of the stored supercritical CO_2 and the development of the interface between phases in space and time. This is essential for studying different reservoir-related problems, including the effect of pressure stimulation on mixing, plume spreading, identification of the fingering effects, estimation of the residual/trapped saturation, design of optimized operational strategies, and management of the wells (Tatomir et al., 2018).

Besides, thermodynamic theories were proposed during the last three decades for describing the macroscale flow and transport in porous media, including the conservation of mass, momentum, and energy (Hassanizadeh and Gray, 1993, 1990). The volume normalized FIFA (a_{wn}) is included as a macro-scale quantity of significance for these theories (Hassanizadeh and Gray, 1993, 1990). The classical capillary pressure saturation relation (P_c-S_w) is extended to a relation including the specific interfacial area (P_c-S_w-a_{wn}), and FIFA is considered a separate state variable in the macro-scale numerical models (Niessner and Hassanizadeh 2008). Using a pore-scale network model, Reeves and Celia (1996) demonstrated that the P_c-S_w-a_{wn} relation yields a convex shaped surface, suggesting that a_{wn} could be regarded as a function of P_c and S_w, which is proved experimentally by Cheng et al. (2004). Studies using pore-network models demonstrated that the FIFA is an important parameter in diminishing or removing the hysteresis in P_c-S_w and K_r-S_w relations (Held and Celia, 2001; Helland and Skjæveland, 2007; Joekar-Niasar et al., 2010, 2008).

Existing techniques for FIFA measurement mainly comprise tracer techniques, e.g., Interfacial Partitioning Tracer Tests (IPTT) (Brusseau et al., 2010, 2009; McDonald et al., 2016), imaging techniques e.g. X-Ray Computed Micro-Tomography (XRCT) (Culligan et al., 2004; Porter et al., 2010) and Photo-luminescent Volumetric Imaging (PVI) (Montemagno and Gray, 1995). Standard IPTT tracers are typically classified into water-phase tracers (frequently surfactants), and gas-phase

tracers, introduced into unsaturated or saturated systems (Kibbey and Chen, 2012). The subsequent effluent tracer concentration is then measured, and the retardation of the partitioning tracer breakthrough comparing to the non-partitioning tracer breakthrough is a measure of the interfacial area. IPTT measures the "total" FIFA, including the FIFA associated with water films and the capillary-associated IFA. However, it is challenging to differentiate between the two FIFAs from an IPTT. On the other hand, XRCT, providing a good measurement for the capillary-associated FIFA, is reported to derive interfaces that are smaller than those obtained with the IPTT, caused by pore-scale features (e.g., microscopic surface roughness) below the resolution of the XRCT scanner (Narter and Brusseau, 2010). Despite the above limitations, one major disadvantage of the existing approaches is that they can only be applied in static or quasi-static conditions, and little has yet been done in the delineation of the fluid-fluid interfaces for dynamic flow conditions (Tatomir et al., 2016). Numerous researches have reported a variation of the P_c-S_w-a_{wn} relation for porous media two-phase flow at different capillary numbers under dynamic conditions (Joekar-Niasar and Hassanizadeh, 2012; Karadimitriou et al., 2014). Besides, measuring the FIFA under dynamic conditions is important, because many engineering applications or infiltration events happen under transient/dynamic conditions.

To overcome the current limitations of the monitoring techniques and to provide a new method to measure the FIFA under dynamic conditions, a new type of tracer termed Kinetic Interface Sensitive (KIS) tracer, was developed in the Department of Applied Geology, at the University of Göttingen (Schaffer et al., 2013; Tatomir et al., 2018). KIS tracers represent a time-dependent in-situ monitoring technique for the evolution of the FIFA in the reservoirs.

After comparing the kinetic rates of interphase mass transfer for several tracer candidates, the KIS tracer compound was identified as phenyl naphthalene-2-sulfonate (2-NSAPh, CAS 62141-80-4) by Schaffer et al. (2013). The 2-NSAPh is a non-polar phenolic ester, soluble in NAPL, such as supercritical CO_2, or its analog liquid-phase n-octane (Schaffer et al. 2013). With the KIS tracer dissolved, the NAPL is injected into the initial water-saturated porous medium and the KIS tracer molecules are adsorbed onto the fluid-fluid interface. The adsorption process is assumed to follow Langmuir's isotherm (Schaffer et al. 2013). At the fluid-fluid interface, the adsorbed 2-NSAPh molecules undergo an irreversible hydrolysis reaction when in contact with the water molecules. Due to the excess supply of tracer in the non-wetting phase, its concentration at the interface can be assumed to remain constant at its maximum value. Thus, the originally first-order hydrolysis reaction can be simplified into a pseudo-zero-order reaction. The two reaction products are naphthalene-2-sulfonic acid (2-NSA) and phenol, both measurable in the water samples through the fluorescence spectrometer. It was reported that the 2-NSA is the compound better for measurement in the experiment because it has lower back partitioning into the NAPL. As the 2-NSA is characterized by high polarity, being highly hydrophilic and non-adsorptive on either the water-solid interface or the fluid-fluid interfaces, it can be expected to be dispersed rapidly into the bulk water (Schaffer et al. 2013). Thus, in a KIS tracer test, the 2-NSA concentration in water can be measured to determine the reacted acid mass, which can be used to back-calculate the interfacial area. Due to the constant zero-order reaction at the interface, the decay and the transport of the tracer (2-NSAPh) in the non-wetting phase becomes simpler. Therefore, the most relevant object component of the study is the reaction product acid (2-NSA), present only in the water. Tatomir et al. (2015) first developed a macro-scale, two-phase, four-component, flow and transport model with a kinetic mass transfer of the KIS tracer between the two fluids and taking the dissolution of CO2 in brine into account. Tatomir et al. (2016) applied the model to design a column experiment, where the KIS tracer was applied in a primary drainage process. The sensitivity of the KIS tracer

to a range of material and operational parameters was investigated. The KIS tracer method was designed for a dipole configuration, requiring one port/well for injection of the NAPL (dissolved with the tracer) and another port/well at a certain distance for monitoring the effluent water sample concentration.

Numerical and experimental works are required for the development of the KIS tracer technique. On the one hand, the designed KIS tracer method and the developed numerical models by Tatomir et al. (2016) and Tatomir et al. (2015) need to be validated through laboratory core/column scale experiments. Numerous macro-scale effects (e.g. heterogeneities of porous material) can only be studied through macro-scale experiments, such as the experiments in the two-dimensional or three-dimensional flow flumes (Heiß et al. 2011). On the other hand, the pore-scale studies play important role in the understanding the reactive transport of the KIS tracer in dynamic two-phase flow. The working mechanism of the KIS tracer is quite different from general conservative tracers or interfacial partitioning tracers. The KIS tracer dissolved in the invading phase depends on the hydrolysis reaction at the interface and the detection of the by-product in the receding phase. The reactive transport of the tracer and its reaction product becomes more complicated, as the tracer experiment is conducted in the dynamic two-phase flow and displacement processes. The success in the application of the KIS tracer is possible only when its reactive transport behavior during the dynamic two-phase flow is fully understood, taking into account the different pore-scale effects in natural aquifers, e.g. capillary trapping, rock surface roughness, grain size, and texture, etc. These effects on the reactive transport of the tracer can be studied through pore-scale experiments or direct numerical simulations. Due to the low reaction rate of the KIS tracer, as well as the short operation time in pore-scale experiments, such as the micro-model experiments (Karadimitriou et al., 2017, 2016, 2014), 2-NSA concentration in pore-scale experiments may be too low to be detected by the currently available measurement techniques (e.g. fluorescence spectrometer). In this sense, direct numerical simulation is a feasible way for pore-scale studies.

1.2 Objectives and Outline

The overall objective of this thesis is the development of an innovative, rapid, accurate tracer technique for measuring the FIFA for dynamic two-phase flow in porous media. The KIS tracer is designed to quantify the dynamic production and evolution of FIFA with time. Additionally, to provide a sound theoretical basis for the KIS tracer method, this thesis aims to gain a fundamental insight into the non-Fickian transport behavior of the interfacially-reactive, water-based tracer (reaction product 2-NSA) in the two-phase displacement processes, with consideration of multiple pore-scale hydrodynamic and capillary effects. The focus of the work is also put on bringing the KIS tracer technique closer to field applications, by considering large-scale effects present in natural aquifers (e.g. aquifer heterogeneity) and designing the economical and fast way for field implementation (e.g. push-pull tests). The KIS tracer method is studied in this thesis by pore-and core-scale numerical and experimental studies. The pore-scale studies are first presented in Chapters 2 to 4, and then the core-scale studies are demonstrated in Chapters 5 to 7.

Chapter 2 presents the pore-scale numerical study for (1) the establishment of a novel KIS tracer model using the approach of Computational Fluid Dynamics (CFD), as well as (2) the application of the model to study the effects of the capillary trapping and stagnant zones on the transport of the KIS tracer. The model is developed based on the phase field method (PFM), which is outstanding in treating the zero-order reaction of the tracer at the interface, and a new continuous mass transfer formulation consistent with the PFM. The numerical model is verified with the analytical solutions

of multiple flow and transport processes. The KIS tracer transport during drainage is then studied in a 2D sandstone porous media.

Chapter 3 presents a further pore-scale numerical study of the effects of thick water films induced by surface roughness on the KIS tracer method. This study applies the PFM-CST model developed in the work of Chapter 2. The study is implemented during primary drainage in a 2D slit/fracture with rough solid walls, with fractal geometries of the solid surfaces. The study aims to figure out how much reacted solute mass in the flowing water would be lost during drainage due to water films induced by the rock surface roughness, and how it will affect the measurement results from a KIS tracer experiment.

Chapter 4 presents and validates the employment of KIS tracer in a "push-pull" experimental set-up. The push-pull KIS tracer method is proposed to overcome the limitation that the volume of the usable water sample after breakthrough is often insufficient during drainage experiments. This study applies both a pore-scale numerical experiment and a column experiment to investigate the application of KIS tracer in push-pull processes. The advective-dispersive-reactive transport of 2-NSA during both primary drainage and main imbibition processes is discussed.

Chapter 5 presents the core-scale experimental study to provide a proof of concept for the KIS tracer method through a well-controlled dynamic column experiment. The experiment is simulated with the previously developed macroscale two-phase flow reactive transport model, implemented both using an academic code and commercial software. The tracer BTCs are interpreted by the macroscale model to obtain the specific FIFA, which is compared to the literature data.

Chapter 6 presents a further core-scale experimental study employing kinetic interface sensitive (KIS) tracers, and the experimental setup is the same as that demonstrated in Chapter 5. This study investigates the FIFA during drainage in five porous media comprised of three kinds of glass beads and two kinds of nature sand of different sizes. This study aim to extend the spectrum of porous media where the KIS tracer can be applied.

Chapter 7 presents a numerical study that employs a Darcy-scale two-phase flow reactive transport model to investigate the KIS tracers transport in heterogeneous porous media. The simulations are carried out for the primary drainage process in a 2D heterogeneous porous domain, with different geometrical distributions, numbers of lenses, and different effective permeabilities. The study focuses on how the front morphology, averaged specific FIFA and the tracer BTCs are affected by the aquifer heterogeneities.

Chapter 8 summarizes the conclusions with respect to the focus of the thesis and gives an outlook for future research.

1.3 Reference

Brusseau, M.L., 1992. Rate-limited mass transfer and transport of organic solutes in porous media that contain immobile immiscible organic liquid. Water Resources Research 28, 33–45. https://doi.org/10.1029/91WR02498

Brusseau, M.L., Narter, M., Janousek, H., 2010. Interfacial Partitioning Tracer Test Measurements of Organic-Liquid/Water Interfacial Areas: Application to Soils and the

Influence of Surface Roughness. Environ. Sci. Technol. 44, 7596–7600. https://doi.org/10.1021/es101312n

Brusseau, M.L., Narter, M., Schnaar, G., Marble, J., 2009. Measurement and Estimation of Organic-Liquid/Water Interfacial Areas for Several Natural Porous Media. Environ. Sci. Technol. 43, 3619–3625. https://doi.org/10.1021/es8020827

Cheng, J.-T., Pyrak-Nolte, L.J., Nolte, D.D., Giordano, N.J., 2004. Linking pressure and saturation through interfacial areas in porous media. Geophysical Research Letters 31. https://doi.org/10.1029/2003GL019282

Culligan, K.A., Wildenschild, D., Christensen, B.S.B., Gray, W.G., Rivers, M.L., Tompson, A.F.B., 2004. Interfacial area measurements for unsaturated flow through a porous medium. Water Resources Research 40. https://doi.org/10.1029/2004WR003278

Graveleau, M., Soulaine, C., Tchelepi, H.A., 2017. Pore-Scale Simulation of Interphase Multicomponent Mass Transfer for Subsurface Flow. Transp Porous Med 120, 287–308. https://doi.org/10.1007/s11242-017-0921-1

Hassanizadeh, S.M., Gray, W.G., 1993. Thermodynamic basis of capillary pressure in porous media. Water Resources Research 29, 3389–3405. https://doi.org/10.1029/93WR01495

Hassanizadeh, S.M., Gray, W.G., 1990. Mechanics and thermodynamics of multiphase flow in porous media including interphase boundaries. Advances in Water Resources 13, 169–186. https://doi.org/10.1016/0309-1708(90)90040-B

Held, R.J., Celia, M.A., 2001. Pore-scale modeling extension of constitutive relationships in the range of residual saturations. Water Resources Research 37, 165–170. https://doi.org/10.1029/2000WR900234

Helland, J.O., Skjæveland, S.M., 2007. Relationship between capillary pressure, saturation, and interfacial area from a model of mixed-wet triangular tubes. Water Resources Research 43. https://doi.org/10.1029/2006WR005698

Heiß VI, Neuweiler I, Ochs S, Färber A (2011) Experimental investigation on front morphology for two-phase flow in heterogeneous porous media: FRONT MORPHOLOGY. Water Resour Res 47:. https://doi.org/10.1029/2011WR010612

Joekar-Niasar, V., Hassanizadeh, S.M., 2012. Uniqueness of Specific Interfacial Area–Capillary Pressure–Saturation Relationship Under Non-Equilibrium Conditions in Two-Phase Porous Media Flow. Transp Porous Med 94, 465–486. https://doi.org/10.1007/s11242-012-9958-3

Joekar-Niasar, V., Hassanizadeh, S.M., Leijnse, A., 2008. Insights into the Relationships Among Capillary Pressure, Saturation, Interfacial Area and Relative Permeability Using Pore-Network Modeling. Transp Porous Med 74, 201–219. https://doi.org/10.1007/s11242-007-9191-7

Joekar-Niasar, V., Prodanović, M., Wildenschild, D., Hassanizadeh, S.M., 2010. Network model investigation of interfacial area, capillary pressure and saturation relationships in granular porous media. Water Resources Research 46. https://doi.org/10.1029/2009WR008585

Karadimitriou, N.K., Hassanizadeh, S.M., Joekar-Niasar, V., Kleingeld, P.J., 2014. Micromodel study of two-phase flow under transient conditions: Quantifying effects of specific

interfacial area. Water Resources Research 50, 8125–8140. https://doi.org/10.1002/2014WR015388

Karadimitriou, N.K., Joekar-Niasar, V., Babaei, M., Shore, C.A., 2016. Critical Role of the Immobile Zone in Non-Fickian Two-Phase Transport: A New Paradigm. Environ. Sci. Technol. 50, 4384–4392. https://doi.org/10.1021/acs.est.5b05947

Karadimitriou, N.K., Joekar-Niasar, V., Brizuela, O.G., 2017. Hydro-dynamic Solute Transport under Two-Phase Flow Conditions. Scientific Reports 7, 1–7. https://doi.org/10.1038/s41598-017-06748-1

Kibbey, T.C.G., Chen, L., 2012. A pore network model study of the fluid-fluid interfacial areas measured by dynamic-interface tracer depletion and miscible displacement water phase advective tracer methods. Water Resources Research 48. https://doi.org/10.1029/2012WR011862

McDonald, K., Carroll, K.C., Brusseau, M.L., 2016. Comparison of fluid-fluid interfacial areas measured with X-ray microtomography and interfacial partitioning tracer tests for the same samples. Water Resources Research 52, 5393–5399. https://doi.org/10.1002/2016WR018775

Miller, C.T., Poirier-McNeil, M.M., Mayer, A.S., 1990. Dissolution of Trapped Nonaqueous Phase Liquids: Mass Transfer Characteristics. Water Resources Research 26, 2783–2796. https://doi.org/10.1029/WR026i011p02783

Montemagno, C.D., Gray, W.G., 1995. Photoluminescent volumetric imaging: A technique for the exploration of multiphase flow and transport in porous media. Geophysical Research Letters 22, 425–428. https://doi.org/10.1029/94GL02697

Narter, M., Brusseau, M.L., 2010. Comparison of interfacial partitioning tracer test and high-resolution microtomography measurements of fluid-fluid interfacial areas for an ideal porous medium. Water Resources Research 46. https://doi.org/10.1029/2009WR008375

Niessner J, Hassanizadeh SM (2008) A model for two-phase flow in porous media including fluid-fluid interfacial area. Water Resour Res 44:10 PP. . doi: 200810.1029/2007WR006721

Porter, M.L., Wildenschild, D., Grant, G., Gerhard, J.I., 2010. Measurement and prediction of the relationship between capillary pressure, saturation, and interfacial area in a NAPL-water-glass bead system. Water Resources Research 46. https://doi.org/10.1029/2009WR007786

Reeves, P.C., Celia, M.A., 1996. A Functional Relationship Between Capillary Pressure, Saturation, and Interfacial Area as Revealed by a Pore-Scale Network Model. Water Resources Research 32, 2345–2358. https://doi.org/10.1029/96WR01105

Schaffer, M., Maier, F., Licha, T., Sauter, M., 2013. A new generation of tracers for the characterization of interfacial areas during supercritical carbon dioxide injections into deep saline aquifers: Kinetic interface-sensitive tracers (KIS tracer). International Journal of Greenhouse Gas Control 14, 200–208. https://doi.org/10.1016/j.ijggc.2013.01.020

Tatomir, A., Vriendt, K.D., Zhou, D., Gao, H., Duschl, F., Sun, F., Licha, T., Sauter, M., 2018. Kinetic Interface Sensitive Tracers: Experimental Validation in a Two-Phase Flow Column Experiment. A Proof of Concept. Water Resources Research 54, 10,223-10,241. https://doi.org/10.1029/2018WR022621

Tatomir, A.B., Schaffer, M., Kissinger, A., Hommel, J., Nuske, P., Licha, T., Helmig, R., Sauter, M., 2015. Novel approach for modeling kinetic interface-sensitive (KIS) tracers with respect to time-dependent interfacial area change for the optimization of supercritical carbon dioxide injection into deep saline aquifers. International Journal of Greenhouse Gas Control 33, 145–153. https://doi.org/10.1016/j.ijggc.2014.11.020

Tatomir, A., Halisch, M., Duschl, F., Peche, A., Wiegand, B., Schaffer, M., Licha, T., Niemi, A., Bensabat, J., Sauter, M., 2016. An integrated core-based analysis for the characterization of flow, transport and mineralogical parameters of the Heletz pilot CO2 storage site reservoir. International Journal of Greenhouse Gas Control, Characterization of formation properties for geological storage of CO2 - Experiences from the Heletz test injection site and other example sites from the EU project MUSTANG 48, 24–43. https://doi.org/10.1016/j.ijggc.2016.01.030

2. A two-phase, pore-scale reactive transport model for the kinetic interface-sensitive tracer

H. Gao[1], A. B. Tatomir[2,1], N. K. Karadimitriou[3], H. Steeb[3,4], and M. Sauter[1]

Citation:

Gao H, Tatomir AB, Karadimitriou NK, Steeb H, Sauter M (2021) A two-phase, pore scale reactive transport model for the kinetic interface-sensitive tracer. Water Resour Res 57(6). https://doi.org/10.1029/2020WR028572

[1]Department of Applied Geology, University of Göttingen, 37073, Göttingen, Germany.

[2]Department of Earth Sciences, Uppsala University, 752 36 Uppsala, Sweden.

[3]Institute of Applied Mechanics (CE), University of Stuttgart, 70569 Stuttgart, Germany.

[4]Stuttgart Center for Simulation Technology, Pfaffenwaldring 5a, 70569 Stuttgart, Germany

Corresponding author: Alexandru Tatomir (alexandru.tatomir@geo.uu.se)

Abstract:

Previous laboratory experiments with the Kinetic Interface Sensitive (KIS) tracers have shown promising results with respect to the quantification of the fluid-fluid interfacial area (IFA) under dynamic, two-phase flow conditions. However, pore-scale effects relevant to two-phase flow (e.g. the formation of hydrodynamically stagnant/ immobile zones) are not yet fully understood, and quantitative information about how far these effects influence the transport of the tracer reaction products is not yet available. Therefore, a pore-scale numerical model that includes two-phase, reactive flow and transport of the KIS tracer at the fluid-fluid interface is developed. We propose a new method to quantitatively analyze how the mass of the KIS-tracer reaction product in the flowing water is affected by the presence of the immobile zones. The model employs the phase field method (PFM) and a new continuous mass transfer formulation, consistent with the PFM. We verify the model with the analytical solutions of transport involving advection, reaction and diffusion processes. The model is tested for two-phase flow conditions in a conceptual 2D slit. The applicability of the model is demonstrated in NAPL/water drainage scenarios in a conceptual porous domain, comparing the results in terms of the spatial distribution of the phases and solute concentration. Furthermore, we distinguish the mobile and immobile zones based on the local Péclet number, and the corresponding IFA, and solute mass in these two zones is quantified. Finally, we show that the solute mass in flowing water can be employed to selectively determine the mobile part of the IFA.

2.1 Introduction

Understanding multi-phase, multi-component, reactive flow and transport in porous media is important for a wide range of scientific and engineering applications. Such applications comprise for example the geological storage of carbon dioxide, groundwater remediation, enhanced oil recovery, material manufacturing, etc. (Scheer et al. 2021). In this context, the quantification of the magnitude of the Fluid-Fluid Interfacial Area (FIFA) is essential for studying reactive multi-phase flow and transport in porous materials (Miller et al. 1990; Hassanizadeh and Gray 1990; Reeves and Celia 1996). For example, in geological storage of CO_2, both the rate of CO_2 dissolution in brine and the extent of the residual trapping are determined by the FIFA (Tatomir et al. 2018). Existing techniques for FIFA measurement mainly comprise tracer techniques, e.g., Interfacial Partitioning Tracer Tests (IPTT) (Brusseau et al. 2009, 2010; McDonald et al. 2016), imaging techniques e.g. X-Ray Computed Micro-Tomography (XMT) (Dalla et al. 2002; Culligan et al. 2004; Porter et al. 2010; Wildenschild and Sheppard 2013; McDonald et al. 2016) and Photo-luminescent Volumetric Imaging (PVI) (Montemagno and Gray 1995). However, one limitation of these methods is that they are mainly applied under steady state or quasi-static conditions (Tatomir et al. 2018). The Kinetic Interface Sensitive tracer test (KIS-TT) was developed for tracking the FIFA in dynamic processes (Tatomir et al. 2016b; Tatomir et al. 2018), as an alternative to IPTT and XMT methods for determining the FIFA under transient conditions (Tatomir et al. 2018; Tatomir et al. 2020).

2.1.1 Kinetic Interfacial Sensitive tracer: theoretical background

The KIS tracer concept and application are described in detail in Schaffer et al. (2013) and Tatomir et al. (2018). A chemically stable KIS tracer compound was identified to be the phenyl naphthalene-2-sulfonate (2-NSAPh) by Schaffer et al. (2013). 2-NSAPh is a non-polar hydrolysable phenolic ester which dissolves in nonpolar liquids, such as supercritical CO_2, or its analogue liquid-phase n-octane (see Schaffer et al. 2013). Thus, a KIS tracer is dissolved in a nonpolar liquid usually acting

as a non-wetting phase. With the KIS tracer dissolved, the nonpolar liquid is injected into the initially water saturated porous medium and the KIS tracers are adsorbed onto the fluid-fluid interface (**Figure 2.1**). The adsorption process is assumed to follow Langmuir's isotherm (Eq. 2.1):

$$\frac{c_i}{c_{i,max}} = \frac{K_L \cdot c_a}{1 + K_L \cdot c_a} \tag{2.1}$$

where K_L is the Langmuir adsorption coefficient of the (non-wetting phase) dissolved KIS tracer at the fluid-fluid interface, c_a the concentration of the KIS tracer in the (bulk) non-wetting phase, c_i the KIS concentration at the interface, usually assumed to be approximately equal to the maximum concentration of the saturated interface $c_{i,max}$. The adsorbed 2-NSAPh molecules at the fluid-fluid interface, when getting in contact with the water molecules, undergo an irreversible hydrolysis reaction.

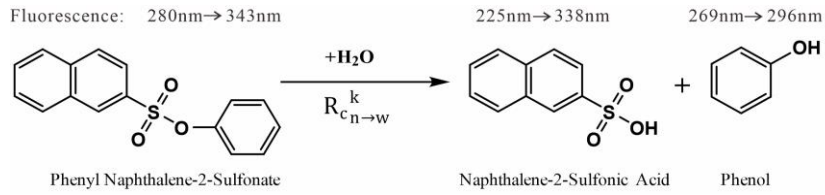

(2.2)

Due to the excessive supply of the tracer in the non-wetting phase (high c_a), its concentration at the interface c_i can be assumed to remain constant at $c_{i,max}$ (Schaffer et al. 2013; Tatomir et al. 2018). Thus, the originally first order hydrolysis reaction can be simplified into a pseudo zero-order reaction. The measured FIFA can be expressed with Eq.(2.3):

$$A_{wn} = \frac{M^k_{nw\to w}}{R_{c_{nw\to w}} \cdot \Delta t} \tag{2.3}$$

where $R_{c_{nw\to w}}$[mol·s^{-1}m^{-2}] is the reaction rate of the KIS tracer per unit interfacial area, $M^k_{nw\to w}$ [mol] is the mass of the reaction product k, Δt is the reaction time, and A_{wn} is the FIFA [m^2]. In a series of batch experiments $R_{c_{nw\to w}}$ was determined at 1.04×10^{-11} mol·s^{-1}m^{-2} (Tatomir et al. 2018). From Eq.(2.3) it is obvious that the mass transfer rate is only controlled by the magnitude of the FIFA. The two reaction products are naphthalene-2-sulfonic acid (2-NSA) and phenol, both measurable in the water phase samples. Tatomir et al. (2018) and Schaffer et al. (2013) showed in static batch experiments with the FIFA kept constant, that the 2-NSA is the compound more easily measured in a tracer experiment because of its enhanced fluorescence (2-NSA concentration in the order of μgL^{-1}). With 2-NSA characterized by high polarity i.e. highly hydrophilic, it will be distributed into the bulk water (here also the wetting phase) away from the interface. The octanol/water partition coefficient of 2-NSA is equal to $\log D_{ow}$=-2.87 at PH>5, as stated in the work of (Schaffer et al. 2013). The high water solubility explains a negligible back-partitioning. Static batch experiments showed a linear increase of the 2-NSA concentration in water (Tatomir et al. 2018). Furthermore, the adsorption of 2-NSA on water-solid interfaces has not been observed to have any visible effect on mass transport in previous laboratory studies, and thus it is not considered further (Schaffer et al. 2013; Tatomir et al. 2018). With a zero-order reaction at the interface, numerical modeling of 2-NSAPh decay and transport in the non-wetting phase becomes redundant, and the most relevant component of mass transport modeling is the reaction product 2-NSA, present only in the wetting phase. On the pore-scale, modeling of the hydrolysis reaction and the 2-NSA transport imply several main steps: 1) zero-order reaction, which is equivalent to a constant production of 2-NSA at the interface, 2) distribution of produced 2-NSA in the water phase controlled by molecular diffusion and high water solubility, and 3) transport of 2-NSA in the water phase controlled by advection and molecular diffusion.

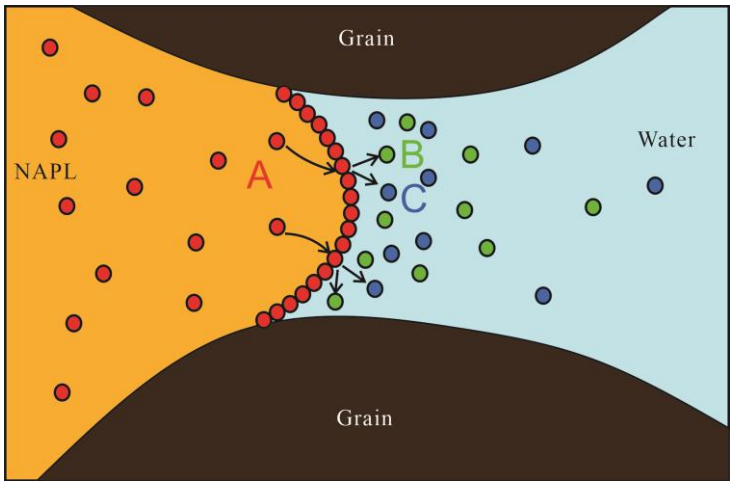

Figure 2.1 Schematic of the KIS tracer reactive transfer process (after Tatomir et al. 2018). A: Phenyl Naphthalene-2-Sulfonate. B: Naphthalene-2-Sulfonic Acid. C: Phenol.

The potential of applying KIS tracers in real porous media to determine the FIFA under dynamic conditions was first demonstrated by Tatomir et al. (2018). Tatomir et al. (2018) provided a proof-of-concept using controlled column experiments with well-characterized porous media composed of glass beads. The KIS tracers were dissolved in a NAPL (n-octane) to displace the water in, initially, fully saturated columns. At the column outlet measurements of fluid volume and 2-NSA concentration of the samples collected at defined time intervals provided breakthrough curves (BTCs) of fluid volumes and the 2-NSA concentration in the water phase. The analysis of the experimental data was conducted employing a macro-scale, reactive, two-phase flow and transport model (Tatomir et al. 2015; Tatomir et al. 2016b; Tatomir et al. 2018; Tatomir et al. 2019; Tatomir et al. 2020), with the interfacial reaction of the tracer being specified in the zones with both fluids co-existing, and the FIFA approximated explicitly as a function of saturation. The model predicted a nearly linear concentration BTC which could fit most of the experimental data points. The resulting specific FIFA (defined as the interfacial area per unit volume of porous medium) ranged between 500-750m^{-1} for glass beads with a mean diameter of 240μm. Despite the successful application of the KIS tracers in laboratory column experiments, new questions came up, such as: a) what do the FIFA tracers actually measure, i.e., capillarity- associated interfacial area (terminal menisci), film-associated interfacial area or total interfacial area, b) how much 2-NSA will end up in the water-film coating the grains and in the hydro-dynamically stagnant zones, and c) how do these stagnant zones influence the resulting solute mass in the flowing water?

The stagnant zones, also referred to as the immobile zones, for the porous media flow are defined as the region where flow velocity is very weak and mass transport becomes diffusive (van Genuchten and Wierenga 1976; Karadimitriou et al. 2016; Aziz et al. 2019). The experimental study at column scale found that the presence of immobile zones can affect the BTCs of the tracer in two-phase flow systems, i.e. larger longitudinal dispersion, early breakthrough and long tailings (Smedt and Wierenga 1984; Bond and Wierenga 1990; Khan and Jury 1990; Bromly and Hinz 2004). The pore-scale micro-model experiments studying the development, role and importance of immobile zones was first conducted by Karadimitriou et al. (2016), who found a nonlinear contribution of the immobile zone to the dispersion coefficient and a non-monotonic relation between immobile zone saturation and total saturation under transient transport conditions.

Karadimitriou et al. (2017) further studied the impact of the Péclet number (ratio of the advective to the diffusive transport rates) under several given saturation topologies, and they found that the ratio of immobile zone saturation to total saturation is not influenced by the different flow rates, if the tortuosity remains identical. By pore-scale direct simulation with the volume of fluid method, Aziz et al. (2018) found the hydrodynamic transport can be non-Fickian in a homogeneous porous medium, and they proposed that relative permeability is possibly a proxy for the stagnant saturation. Hasan et al. (2019) confirmed these findings with pore-network modeling, and they found a link between the immobile zone saturation and the relative permeability. The flaws of the existing macroscopic models to describe the non-Fickian transport in two-phase flow process were proposed in these recent studies (Karadimitriou et al. 2016; Karadimitriou et al. 2017; Aziz et al. 2018; Hasan et al. 2019). In contrast to these studies with a conservative tracer injected simultaneously with the invading phase, the KIS tracer dissolved in the invading phase depends on the hydrolysis reaction at the interface and the detection of the by-product in the receding phase. This means, in our case, the effect of the immobile zones is manifested in the solute transport in the receding phase.

The above questions, regarding the effect of the immobile zones on the distribution of the reacted solute in KIS-TT, can probably be answered by investigating KIS tracer transport mechanisms at the pore-scale. Experimentally, the pore-scale study of KIS tracer reactive transport in two- phase flow can be carried out in micro-models (Karadimitriou et al. 2016), considering its good fluorescent properties. The problem can also be studied by pore-scale modeling. Pore-scale modeling plays an important role in understanding the pore-scale phenomena and can provide fundamental insight to understand the macro-scale processes (Meakin and Tartakovsky 2009). With pore-scale modeling, the flow and transport properties of the soil/ rock matrix are not averaged but are directly resolved, and the pore-space geometry is explicitly represented either by using idealized geometries or by reconstructed geometries based on XMT images (e.g., Culligan et al. 2004; Tatomir et al. 2016a; Peche et al. 2016). In addition, running pore-scale simulations is a more flexible approach than the experiments since there is freedom to tune accordingly the fluids' physical and chemical properties, and the geometry of the porous medium for a variety of boundary conditions. Considering all the above, the main objective of this study is to develop a pore-scale model that can simulate the behavior of the reactive KIS tracer transport under two-phase flow conditions. The following sections review the relevant literature on pore-scale models including reactive transport.

2.1.2 Pore-scale numerical methods

Pore-scale modeling methods mainly include Pore-Network Modeling (PNM) and Direct Numerical Simulation (DNS) approaches. The DNS approaches include particle-based methods e.g. the Lattice Boltzmann Method (LBM), Smooth Particle Hydrodynamics (SPH), and grid based Computational Fluid Dynamics (CFD), such as the Level-Set Method (LSM), the Volume-Of-Fluid method (VOF), and the Phase-Field Method (PFM) (Meakin and Tartakovsky 2009; Alpak et al. 2016). Pore-Network Modeling (PNM) is a well-developed method for pore-scale studies (Blunt and King 1990; Joekar-Niasar et al. 2008; Raoof et al. 2013; Hasan et al. 2019). PNM simplifies porous media into networks of pores and throats, where flow is governed by Poiseuille's law (Joekar-Niasar et al. 2008). PNM is computationally more efficient than DNS, which provides the full coupling between capillary and viscous forces (Alpak et al. 2016). With PNM it is computationally cheaper to consider domains with a size large enough to be considered as Representative Elementary Volumes (REV), and thus the model can be applied for evaluation of

continuum-scale problems. Despite these advantages, PNM is limited by its basis on simplified physics and simplified representations of the rock (Meakin and Tartakovsky 2009; Alpak et al. 2016; Basirat et al. 2017; Yin et al. 2019). Thus, the DNS methods, based on first principles, are better in capturing transport phenomena and fluid dynamics on the micro-scale, in (natural) pore space with complex geometries (Meakin and Tartakovsky 2009; Alpak et al. 2016). The LBM is a popular method for pore-scale studies of multiphase reactive transport, because of its advantages in several aspects, such as being able to deal with complex boundaries, to incorporate microscopic fluid-fluid and fluid-solid interactions, and being able to implement a parallelization of the algorithm (Kang et al. 2006b; Liu et al. 2014; Liu et al. 2015). The LBM model solves the LB equations for fluid flow and solute transport. In LB simulations the chemical reaction of species is treated as a homogenous reaction in the bulk fluid and a heterogeneous reaction at the interface as a kinetic boundary condition. The LBM modelling approach has been used in applications such as geological storage of CO_2, which involves precipitation and dissolution at the fluid-solid surface (Kang et al. 2010) and CO_2 dissolution trapping (Chen et al. 2018). However, one of the disadvantages of the LBM models is that the relation between interaction forces and fluid dynamics requires complex calibration procedures, with many adjustment parameters, such as the adequate approximation of a specific physical system (Ferrari and Lunati 2013; Frank et al. 2018). With the CFD approach, the Navier-Stokes equations are directly solved in a discretized domain by finite volume or finite element techniques, and the interface between two fluids is represented by an indicator function, such as the volume fraction in VOF and the phase variable in PFM. One challenge for the simulation of multiphase reactive transport with the CFD method is the handling of the concentration jump at the interface when a solute solubility is different in the fluids on either side of the interface (Maes and Soulaine 2018). Haroun et al. (2010) managed to tackle this challenge with a new Continuous Species Transfer (CST) formulation developed in the VOF framework. In the CST formulation, a constant partition coefficient (or Henry's constant) is introduced to solve the thermodynamic equilibrium of the solute at the interface between two fluids (Haroun et al. 2010). The approach of Haroun et al. (2010) allows for the modeling of the discontinuous solute concentration across the interface, while respecting the continuity of the local diffusive solute mass flux. Graveleau et al. (2017) applied the VOF-CST model to simulate subsurface flow problems with moving contact lines. Maes and Soulaine (2018) identified that the CST generates large numerical diffusion in the phase concentration, which leads to inaccurate simulation of solute mass partitioning between two phases. Therefore, they proposed a new approach, termed compressive CST (C-CST), by adding a compressive term. The C-CST formula managed to significantly reduce numerical errors. However, one major disadvantage of the VOF method is that, since the volume fraction is a step function, accurate curvature and smooth physical quantities near the interface are hard to be obtained (Sun and Tao 2010; Alpak et al. 2016). Another limitation of the VOF method is that a solid wall boundary is implemented indirectly with an additional moving contact line model (Meakin and Tartakovsky 2009; Basirat et al. 2017).

In contrast to the VOF method, LSM and PFM with a smooth indicator function are better to treat the curvature and the physical quantities at the interface. LSM has been reported to generate more numerical errors when the interface experiences severe stretching or tearing, and the mass is not conserved (Sussman and Puckett 2000; Sun and Tao 2010). Major advantages of the PFM are both the mass conservation and the ability to compute accurately the curvature at the interface (Akhlaghi Amiri and Hamouda 2013). Furthermore, PFM treats the interface thermodynamically as a diffusive thin layer formed by the mixture of the two fluid phases, and the dynamics of the diffusive interface is governed by the free energy it contains (Yue et al. 2006). Thus, the PFM is physically more consistent than the VOF or the LSM models (Alpak et al. 2016). Another advantage is that

considering a diffusive interface rather than a sharp interface around the contact line results effectively in slip, through the diffusive fluxes between the bulk fluids (Ding and Spelt 2007). Besides, with a diffusive interface in PFM, the zero-order reaction of 2-NSA at fluid-fluid interface can be directly implemented as a homogenous reaction in the region of the diffusive interface, where the two fluids exhibit some limited mixing. The PFM, solving the coupled Cahn-Hilliard and Navier-Stokes equations, is already well developed and numerous simulation studies were performed addressing the two-phase flow system (Jacqmin 1999; Yue et al. 2004; Yue et al. 2006; Akhlaghi Amiri and Hamouda 2013; Alpak et al. 2016). In addition, numerous recent studies have applied PFM to study various subsurface flow problems related to fluid viscosity, capillarity, temperature, wettability, heterogeneity and fractures (Akhlaghi Amiri and Hamouda 2013, 2014; Basirat et al. 2017; Rokhforouz and Akhlaghi Amiri 2017, 2018). To our knowledge, PFM has not yet been applied to study reactive transport for two phase flow in porous media.

Here, we derive a new CST formulation in a PFM framework, and therefore the model is termed PFM-CST. At first, we verify the developed PFM-CST model, and, we consequently employ the code to study the KIS tracer reaction and transport processes in immiscible two-phase flow in porous media. We focus on the understanding of how the fluid immobile zones affect the magnitude of the total transported solute mass. The paper is organized as follows: Section 2.2 introduces the mathematical and numerical models. In Section 2.3 we present the details of numerical setup for model verifications and its application to a realistic pore space geometry to study the KIS tracer reaction and transport of its reaction by-product 2-NSA. The result of the model verifications and application are shown in Section 2.4. Section 2.5 lists the main conclusions.

2.2 Mathematical model

2.2.1 Phase-Field Method

The basics of the PFM can be found in e.g., Jacqmin (1999), Yue et al. (2004) and Alpak et al. (2016). In this section, we briefly review the basic underlying theory implemented in the model. Instead of a sharp interface between two fluids, the PFM treats the interface as a thin diffusive layer formed by the mixture of two fluids. The PFM introduces a smoothly changing phase variable ϕ to describe the composition of the fluid mixture at the interface, and ϕ remains constant in the bulk fluid phases. The PFM is based on the free energy density as a function of the phase variable and its gradient (Jacqmin 1999). The free energy density (f_{mix}) [J/m^3] for isothermal mixing of two fluids can be expressed in the Ginzburg-Landau form (Eq.(2.4)) (Yue et al. 2006):

$$f_{mix}(\phi, \nabla\phi) = \frac{1}{2}\lambda|\nabla\phi|^2 + \frac{\lambda}{4\varepsilon^2}(\phi^2 - 1)^2 \tag{2.4}$$

where λ [N] is the magnitude of the mixing energy and ε [m] is a capillary width representing the thickness of the diffusive interface. The free energy density is made up of two components (on the right side of the Eq. 2.4): the first term accounts for the surface energy and the second term is the bulk energy. The surface energy represents the interaction between two fluids and the preference of two fluids for complete mixing (Yue et al. 2004). The bulk energy describes the two-phase immiscibility and involves two minimal values, where ϕ=-1 and ϕ=1, representing the two bulk phases (wetting and non-wetting fluid), respectively (Jacqmin 1999). These two competing energies determine the ϕ profile across the interface (Jacqmin 1999; Yue et al. 2004). The chemical potential G [J/m^3] can be defined as the variation of the free energy with respect to the dimensionless phase variable (Eq. 2.5):

$$G = \frac{\delta \int_{\Omega} f_{mix}\, dx}{\delta \phi} = -\lambda \nabla^2 \phi + \frac{\lambda}{\varepsilon^2} \phi(\phi^2 - 1) \tag{2.5}$$

where Ω is the region of space occupied by the system. Considering the interface in one-dimension with boundary conditions: $\phi^2|_{x=\pm\infty} = 1, \frac{d\phi}{dx}|_{x=\pm\infty} = 0$ and $\phi(0) = 0$, the equilibrium profile of $\phi(x)$ at zero chemical potential (G=0) writes (Eq. 2.6):

$$\phi(x) = \tanh\left(\frac{x}{\sqrt{2}\varepsilon}\right) \tag{2.6}$$

The interfacial tension σ [N/m] is the total free energy at the interface per unit area of the interface, and the relationship between the interfacial tension, the capillary width, and the mixing energy density can be obtained at equilibrium from Eq.(2.7) (Yue et al. 2004):

$$\sigma = \frac{2\sqrt{2}\lambda}{3\varepsilon} \tag{2.7}$$

Fluid mass conservation is governed by the Cahn-Hilliard equation (Eq. 2.8), which assumes that the diffusive fluid flux is proportional to the gradient of the chemical potential (Cahn and Hilliard 1959):

$$\frac{\partial \phi}{\partial t} + \mathbf{u} \cdot \nabla \phi = \nabla \cdot (\gamma \nabla G) \tag{2.8}$$

where γ [m^{3}s/kg] is the mobility expressed as a function of the interface thickness and a tuning factor: $\gamma = \chi \cdot \varepsilon^2$. The tuning factor χ [m·s/kg] is called the characteristic mobility governing the relaxation time of the interface (Akhlaghi Amiri and Hamouda 2013). χ needs to be large enough to maintain a constant thickness of the interface, but small enough not to dampen the flow (Jacqmin 1999).

2.2.2 Two phase flow dynamics

Momentum conservation for an incompressible fluid is governed by the Navier-Stokes equation (Eq. 2.9):

$$\rho\left(\frac{\partial u}{\partial t} + \mathbf{u} \cdot \nabla \mathbf{u}\right) = \nabla \cdot [-p\mathbf{I} + \mu(\nabla \mathbf{u} + (\nabla \mathbf{u})^T)] + G\nabla\phi \tag{2.9}$$

$$\nabla \cdot \mathbf{u} = 0 \tag{2.10}$$

where **I** is the identical tensor, p is pressure, **u** is the fluid velocity vector, the surface tension is considered as a body force (Yue et al. 2006),

$$-\frac{\delta \int_{\Omega} f_{mix}\, dx}{\delta x} = G\nabla\phi \tag{2.11}$$

and ρ and μ are respectively the density and viscosity of the mixture (non-wetting fluid and wetting fluid) according to volume fraction of the fluids:

$$\rho = \rho_w V_{f,w} + \rho_{nw} V_{f,nw} \text{ and } \mu = \mu_w V_{f,w} + \mu_{nw} V_{f,nw} \tag{2.12}$$

where subscripts w and nw indicate the wetting and non-wetting phase, respectively. ρ and μ are independent of the concentration of KIS tracer and its reacted product, because the tracer and its reacted product have negligible mass fraction in the fluids. The volume fraction of the fluids can be obtained as:

$$V_{f,w} = (1 - \phi)/2 \text{ and } V_{f,nw} = (1 + \phi)/2 \tag{2.13}$$

At the grain surfaces, a no-slip boundary is applied, which implies that **u**=0 in Eq.(2.9) for solid wall boundaries. The wetting condition on the solid wall is expressed by Eq.(2.14):

$$n \cdot \nabla\phi = cos\theta_w |\nabla\phi| \tag{2.14}$$

where **n** is the (outward) normal vector to the wall and θ_w is the contact angle.

2.2.3 Reactive transport

2.2.3.1 Solute advection

To obtain the solute mass conservation equation, we first write the fluid mass conservation equation with the volume fraction of phases. For the wetting phase, by substituting $\phi = 1 - 2V_{f,w}$ (Eq. 2.13) into the Cahn-Hilliard equation (Eq. 2.8), one obtains:

$$\frac{\partial(1 - 2V_{f,w})}{\partial t} + \mathbf{u} \cdot \nabla(1 - 2V_{f,w}) - \nabla \cdot (\gamma\nabla G) = 0 \tag{2.15}$$

Due to $\nabla \cdot \mathbf{u} = 0$, by dividing the constant coefficient one obtains:

$$\frac{\partial V_{f,w}}{\partial t} + \nabla \cdot \left(\mathbf{u}V_{f,w} + 0.5\gamma\nabla G\right) = 0 \tag{2.16}$$

Similarly, by substituting $\phi = 2V_{f,\mathrm{nw}} - 1$ (Eq. 2.13) into the Cahn-Hilliard equation (Eq. 2.8), one obtains the volume fraction based mass conservation equation for the non-wetting phase. Thus, the total fluid volumetric flux for the wetting phase $\mathbf{F_w}$ and non-wetting phase $\mathbf{F_{nw}}$ can be expressed as:

$$\mathbf{F_w} = \mathbf{u}V_{f,w} + 0.5\gamma\nabla G \quad and \quad \mathbf{F_{nw}} = \mathbf{u}V_{f,nw} - 0.5\gamma\nabla G \tag{2.17}$$

Hence, for the solute *k* dissolving in fluid phase *α* (*α*=*w*, *nw*) with the concentration of $c_{a,k}$, the solute mass conservation equation writes:

$$\frac{\partial(V_{f,\alpha}c_{\alpha,k})}{\partial t} + \nabla \cdot (\mathbf{F}_{\boldsymbol{a}}c_{a,k}) = 0 \tag{2.18}$$

where only the solute advection is included here, and the other processes (reaction, diffusion, solubility) will be discussed and added in next sections. Solute advection is the transport process due to the bulk fluid motion. The bulk fluid motion consists of two parts: the advective flux and the diffusive flux at the interface due to the gradient of the chemical potential. In this case, the advection of the solute is ensured to be consistent with the fluid motion. The advection term applied here is similar to that in the C-CST model developed by Maes and Soulaine (2018), where the compressive term for VOF method is replaced by the interface diffusion term for PFM.

2.2.3.2 Reaction at the interface

A zero-order interfacial reaction of the KIS tracer is assumed in the model as a homogeneous reaction taking place at the diffusive interface, where the two fluids mix. The diffusive interface is located at the region with $\phi \in$(-1,1), and due to the smooth change in ϕ there is no clear boundary. Thus, we take the interface with 90% variation of the phase variable $\phi \in$[-0.9,0.9], corresponding to $V_{f,w} \in$[0.05,0.95], as the region of constant zero-order reaction. It is worth noting that the reaction source term applied here is discontinuous. With the constant interface thickness, the reaction rate per unit interfacial region (R_c^{dif} [mol·s^{-1}m^{-3}]) for the model can be calculated as:

$$R_c^{dif} = \frac{R_{c_{nw\to w}}}{b_{wn}} \tag{2.19}$$

where $R_{c_{nw\to w}}$ is the experimentally determined tracer reaction rate per unit interfacial area (Tatomir et al. 2018), and b_{wn} is the thickness of the interfacial reaction region with $V_{f,w} \in [0.05,0.95]$, obtained as 4.1641ε from Eq.(2.6).

2.2.3.3 Solute distribution across the interface

As mentioned in the introduction, the reaction product (2-NSA) has high water solubility and distributes homogeneously into the water phase. This selective distribution mechanism is not included in the classical advection-diffusion equation. In this case, we applied the method developed by (Haroun et al. 2010), where a partitioning coefficient is introduced in the formulation. The partitioning coefficient is expressed as the concentration ratio of the solute in the two-phase fluids system at equilibrium.

$$P_{ow,k} = \frac{c_{nw,k}}{c_{w,k}} \tag{2.20}$$

where $c_{nw,k}$ and $c_{w,k}$ are the concentration of the product (2-NSA) in the non-wetting phase and the wetting phase respectively, and $P_{ow,k}$ is the partition coefficient.

2.2.3.4 Continuous transport equation

To obtain the single-field formulation of the (2-NSA) concentration for both phases in the entire domain, we define the global concentration as:

$$c_k = V_{f,w} c_{w,k} + V_{f,nw} c_{nw,k} \tag{2.21}$$

The sum of the mass conservation Eq.(2.18) for solute k in both phases writes:

$$\frac{\partial (V_{f,w} c_{w,k} + V_{f,nw} c_{nw,k})}{\partial t} + \nabla \cdot (\mathbf{F_w} c_{w,k} + \mathbf{F_{nw}} c_{nw,k}) = 0 \tag{2.22}$$

By substituting Eq.(2.17) and Eq.(2.21) into the above equation, and adding the molecular diffusion term and the interfacial reaction term, one obtains the conservation of global concentration which writes as:

$$\frac{\partial c_k}{\partial t} + \nabla \cdot \left[\mathbf{u} c_k + 0.5\gamma \nabla G \left(c_{w,k} - c_{nw,k}\right)\right] - \nabla \cdot \mathbf{J_k} + R_c^{dif} = 0 \tag{2.23}$$

where the solute molecular diffusion flux for the mixture is defined as (Haroun et al. 2010):

$$\mathbf{J_k} = D_k \cdot (V_{f,w} \nabla c_{w,k} + V_{f,nw} \nabla c_{nw,k}) = D_k [\nabla c_k - \left(c_{w,k} - c_{nw,k}\right) \nabla V_{f,w}] \tag{2.24}$$

As $V_{f,w} + V_{f,nw} = 1$, here only $V_{f,w}$ is used in the expression, and the molecular diffusion coefficient is expressed as $D_k = V_{f,w} D_{w,k} + V_{f,nw} D_{nw,k}$. The diffusion term Eq.(2.24) indicates an additional flux term resulting from the solubility law. This solubility flux is in the direction normal to the interface, which governs the distribution of the species between the two phases. With the definition of Eq.(2.20) and Eq.(2.21), one obtains:

$$c_{w,k} - c_{nw,k} = \frac{c_k (1 - P_{ow,k})}{V_{f,w} + P_{ow,k}(1 - V_{f,w})} \tag{2.25}$$

Thus, the final governing equation for global concentration of solute k is reorganized:

$$\begin{aligned} &\frac{\partial c_k}{\partial t} + \nabla \cdot [\mathbf{u} c_k + 0.5\gamma \nabla G \frac{c_k \left(1 - P_{ow,k}\right)}{V_{f,w} + P_{ow.k}\left(1 - V_{f,w}\right)}] \\ &\qquad - \nabla \cdot [D_k (\nabla c_k - \nabla V_{f,w} \frac{c_k \left(1 - P_{ow,k}\right)}{V_{f,w} + P_{ow,k}\left(1 - V_{f,w}\right)})] + R_c^{dif} = 0 \end{aligned} \tag{2.26}$$

2.2.4 Numerical implementation

The model is implemented into COMSOL Multiphysics™. COMSOL is an interactive environment for simulating different scientific and engineering problems employing the finite element method for spatial discretization (Akhlaghi Amiri and Hamouda 2013; Tatomir et al. 2018). The governing system comprises four governing equations and four fundamental variables. The coupled governing equations of the Navier-Stokes equation (Eq.2.9 and Eq.2.10) and the Cahn-Hilliard equation (Eq.2.8) are solved for fluid velocity (**u**), pressure (p) and the phase variable (ϕ). And the governing reactive transport equation (Eq.2.26) is solved for the solute concentration (c_k). The partial differential equations are solved by the COMSOL linear solver PARDISO. Time stepping is solved with the backward Euler method known for its stability. The initial time step and maximum time steps are controlled to be small enough in order to avoid a singularity. The mesh elements consist of regular triangles with side length h. The mesh size is refined according to the complexity of the geometry and thickness of the interface. The computations were performed on a single CPU with 12 cores at 4.3 GHz, and 32 GB RAM.

2.3 Numerical Method and details

We first verify the reactive transport model by applying the newly implemented continuous transport algorithm (Eq.2.26) (section 2.3.1). Then, the model is tested for a drainage process in a 2D slit (section 2.3.2). Finally, the model is applied to study the KIS tracer reactive transport in a realistic 2D porous medium geometry proposed by Keller et al. (1997) (section 2.3.3).

2.3.1 Model verification

For the model verification, we provide first verifications of the two-phase flow simulation with the phase-field method. The two-phase flow model is verified in two different cases: a pressure-difference-driven, co-current two-phase flow through a thin channel (supporting material 2.S1) and a surface tension driven, deformed bubble retraction process in a quiescent domain (supporting material 2.S2). The important parameters for the phase-field method, such as characteristic mobility, capillary width and mesh size, are studied. Besides, since the model is to be employed to simulate two-phase flow and reactive transport in porous materials, the phase distribution in the regions close to the grain surface needs to be resolved by the model in detail. Thus, we set up a benchmark simulation of the deposited water films on the grain surface (supporting material 2.S3). Then, we provide a verification of the reactive transport simulation governed by the above Eq.(2.26). The verification is accomplished by comparing the results of the numerical model with those of an analytical solution for a transient interfacial diffusion process (section 2.3.1.1), a simultaneous reaction-diffusion process at the interface (section 2.3.1.2), and an advection-diffusion process (section 2.3.1.3). In these three one-dimensional model verifications, the mesh element size to capillary width ratio is fixed as $h/\varepsilon=1$.

2.3.1.1 Diffusion across the interface

When a solute dissolves in a two-phase fluid system with non-equal solubilities in each fluid phase, a concentration jump will be established at the interface at equilibrium, assuming this interface is a sharp one. In this section, we study how this concentration jump is dealt with for a diffusive interface by the model. We consider a simple two-phase system without any reaction, and only the wetting phase contains the chemical component 2-NSA initially. The model is setup in 1D as follows: in a 0.2mm long domain, the interface is located at x=0.1mm. Water is located at x>0.1mm and the non-wetting phase is located at x<0.1mm, as shown in **Figure 2.2**(a). The system is at rest

without any inflow or outflow. Water has an initial solute (2-NSA) concentration of $c_{w,0}$=1 mol/m^3, and the non-aqueous, or in this case the non-wetting, phase has an initial solute (2-NSA) concentration $c_{nw,0}$=0. The molecular diffusion coefficient is D_w=D_{nw}=1×10^{-9}m^2/s for both phases. With this modeling setup, solute diffusion across the interface is allowed to take place. This transient diffusion process can be described by the analytical solution from Eq.(2.27) for water and Eq.(2.28) for the non-wetting phase (Bird 2002):

$$\frac{c_w - c_{w,0}}{c_{nw,0} - P_{ow} \cdot c_{w,0}} = \frac{1 + \mathrm{erf}\left[\frac{x - 0.1}{\sqrt{4D_w t}}\right]}{P_{ow} + \sqrt{D_w/D_{nw}}} \tag{2.27}$$

$$\frac{c_{nw} - c_{nw,0}}{c_{w,0} - \left(\frac{1}{P_{ow}}\right) \cdot c_{nw,0}} = \frac{1 - \mathrm{erf}\left[\frac{x - 0.1}{\sqrt{4D_{nw} t}}\right]}{\left(\frac{1}{P_{ow}}\right) + \sqrt{D_{nw}/D_w}} \tag{2.28}$$

where erf( ) is the error function. The system with very small partition coefficient is the focus of our study, as the 2-NSA has P_{ow}<0.01, which means it has very small partition into the non-wetting phase.

Then, we provide a verification of how solute distribution is treated at the diffusive interface. With the very low partitioning coefficient (P_{ow}<0.01), the solute concentration in water is much larger than that in the non-wetting phase $c_{w,k}$>>$c_{nw,k}$. Additionally, the solute concentration in water almost remains at $c_{w,k}$=1 mol/m^3 because of the weak diffusion across the interface and the absence of the chemical reaction. In this case, Eq.(2.21) can be simplified to $c_k = V_{f,w} c_{w,k}$. This means that the solute concentration of the mixture (c_k) at the interface is approximately linearly proportional to the volume fraction of the water phase ($V_{f,w}$), with a ratio of $c_{w,k}$. By comparing the simulated concentration curve to the corresponding volume fraction of the fluid, we are able to check if the solute concentration distribution at the diffusive interface is accurately solved by the model.

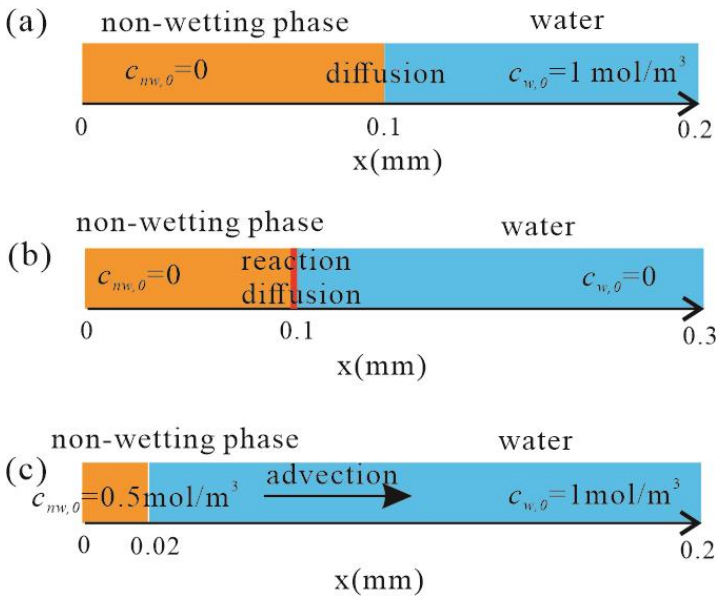

Figure 2.2 Sketch of the numerical setups for verification of the reactive transport model in (a) a transient interfacial diffusion process (b) a simultaneous reaction-diffusion process at the interface and (c) an advection-diffusion process at equilibrium.

2.3.1.2 Interfacial reaction and molecular diffusion

The model is verified for the condition that a zero-order reaction is active. We consider a one-dimensional quiescent channel with two phase fluids. The solute is assumed to react at the interface and diffuse into the water. The channel is 0.3mm in length, with the interface located at x=0.1mm. Water is located at x>0.1mm and the non-wetting phase (n-octane) is located at x<0.1mm, as shown in **Figure 2.2**(b). The initial 2-NSA concentration in the domain is c_0=0 mol/m^3. The molecular diffusion coefficient is equal to D=1×10^{-9}m^2/s for both phases. The zero-order reaction rate is R_c^{dif}=1 mol/m^{-3}s. The capillary width for the model is set at ε=1×10^{-7}m, thus the reaction region at the interface has a thickness of 4.16ε according to section 2.2.3.2.

The above process can be described by the reaction-diffusion equation:

$$\partial c/\partial t = \nabla \cdot (-D\nabla c) + W \tag{2.29}$$

which can be solved analytically. For the analytical solution, the interface between two phases is defined as a no flow boundary for the solute, and the zero-order reaction is active in a narrow region with 0.1mm<x<L. The analytical solution for Eq.(2.29) is shown below (Carslaw and Jaeger 1959):
At $0.1mm < x < L$

$$c = R_c \cdot t \cdot \left\{1 - 2i^2\mathrm{erfc}\frac{L - x + 0.1}{2\sqrt{D \cdot t}} - 2i^2\mathrm{erfc}\frac{L + x - 0.1}{2\sqrt{D \cdot t}}\right\} \tag{2.30}$$

At $x > L$

$$c = 2R_c \cdot t \cdot \left\{i^2\mathrm{erfc}\frac{L - x + 0.1}{2\sqrt{D \cdot t}} - i^2\mathrm{erfc}\frac{L + x - 0.1}{2\sqrt{D \cdot t}}\right\} \tag{2.31}$$

where $i^2\mathrm{erfc}\, x = 0.25[(1 + 2x^2)\mathrm{erfc}\, x - 2xe^{-x^2}/\sqrt{\pi}]$, erfc is the complementary error function, and L is the thickness of the reaction region for the analytical solution. To be consistent with the model, the thickness of reaction region is set as L=4.16ε.

2.3.1.3 Advection diffusion

Then, the model is verified under the condition of two-phase flow, where the solute advection is active. The inaccurate modelling of solute advection can cause the artificial (unphysical) mass transfer near the interface (Maes and Soulaine 2020, 2018). The artificial mass transfer is induced when the solute advection is not consistent with fluids motion. The artificial mass transfer is reported to be greater in the systems with larger Péclet numbers (Maes and Soulaine 2018; Yang et al. 2017). To verify that there is no artificial mass transfer, we consider an advection-diffusion process with the solute concentration in both phases at equilibrium. The model is setup in 1D with a 0.2mm long domain, where the non-aqueous phase locates at 0<x<0.02mm and water locates at 0.02<x<0.2mm initially, as shown in **Figure 2.2**(c). Water has initial solute concentration $c_{w,0}$=1 mol/m^3. The non-aqueous phase has initial solute concentration $c_{nw,0}$=0.5 mol/m^3. The non-aqueous phase ($c_{nw,0}$=0.5 mol/m^3) is injected continuously from the left boundary at U_{in}=0.05m/s beginning with time t=0. There is no reaction (R_c^{dif}=0) and the partitioning coefficient is P_{ow}=0.5, meaning that the solute concentration in both phases is at equilibrium. In this case, the solute concentration along x can be analytically expressed as: $c_k(x) = V_{f,w}(x)c_{w,0} + V_{f,nw}(x)c_{nw,0}$. The global Péclet number for the system is calculated as: $Pe_g = U_{in} * L_c/D_k$, where L_c is the characteristic length, in this case equal to the domain length L_c=0.2mm. The molecular diffusion coefficient D_k is swapped 1×10^{-6} m^2/s, 1×10^{-8} m^2/s and 1×10^{-10}m^2/s, to apply the verifications of the system at different Péclet numbers. The capillary width for the model is set at ε=5×10^{-7}m.

2.3.2 Model test in a 2D slit

The model is tested for the relevant processes (reaction, two-phase flow, advection and diffusion) in a single, two-dimensional slit setup. We focus on the effect of fluid flow (advection) and molecular diffusion on the transport of solute for a spectrum of Péclet numbers. The slit is 0.8mm long with a slit opening of 0.1mm, and in 2D the top and bottom boundaries are the solid walls accounting for the pore space surface. The slit (0.02mm<x<0.8mm) is initially filled with water and the inlet part (0<x<0.02mm) is initially filled with n-octane, as the initial interface is necessary for the simulation. n-octane is injected from the left side at a constant velocity of U_{in}=0.01m/s at t=0. The contact angle between the two fluids and the boundary wall is set to 45°. The interfacial tension for n-octane/water is equal to σ=0.0504 N/m (Tatomir et al. 2018), and R_c^{dif}=1mol/m^{-2}s. The initial concentration and boundary conditions are: $c_{k,t=0} = 0, c_k|_{inlet} = 0, \nabla c_k|_{outlet} = 0$. The characteristic length equals to the half of the slit opening L_c=0.05mm. As the L_c is fixed, the Péclet number of the systems is determined by the ratio between the inflow rate and diffusivity. To obtain the systems with different Péclet numbers, we maintain the inflow rate and swap the molecular diffusion coefficients with D=1×10^{-8}m^2/s, D=1×10^{-7}m^2/s and D=1×10^{-6}m^2/s in three simulations. The mesh element size and capillary width for the model are h=ε=2×10^{-6}m.

2.3.3 Model application for flow in porous media

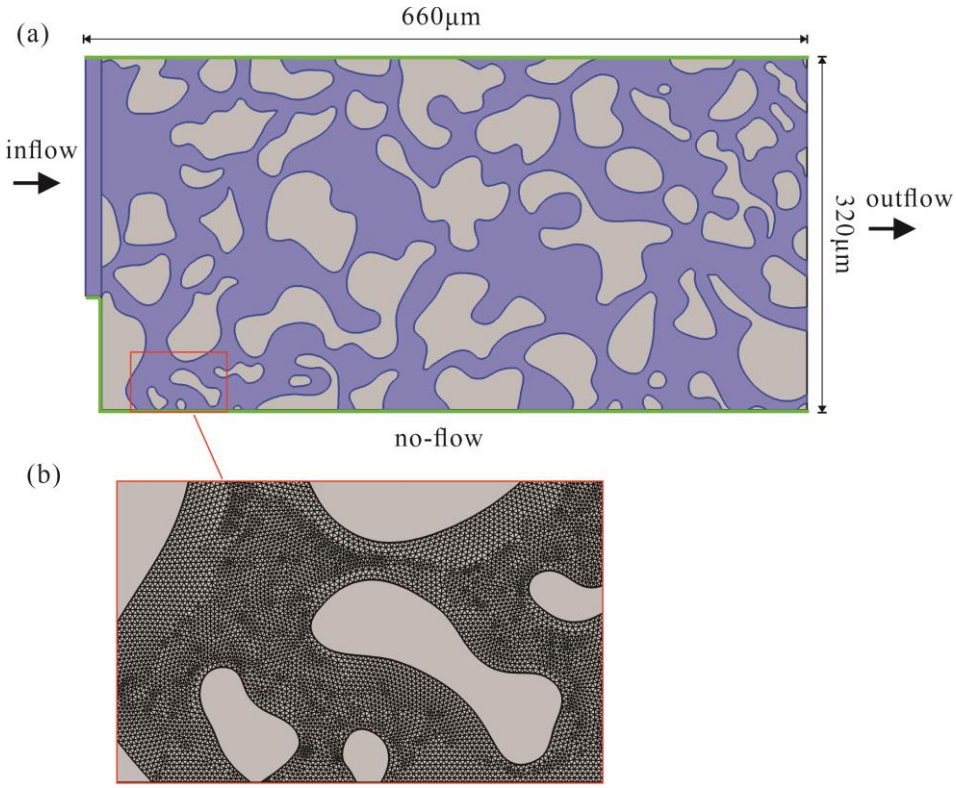

Figure 2.3 Plot of (a) geometry of the porous medium and boundary conditions (pore space in blue color) (b) mesh with triangle elements with side length h=1×10^{-6}m.

We applied the PFM-CST model to study KIS tracer reactive transport in a hydrophilic 2D porous medium. The focus of the study is to understand the effect of the induced immobile zones on transport of the reaction product (2-NSA). We assumed a 2D porous medium from a thin slice of Berea sandstone, first presented by Keller et al. (1997) for a micro-model experiment. The geometry has already been used as the computational domain in Basirat et al. (2017) and Rokhforouz and Akhlaghi Amiri (2019). The domain measures 660μm×320μm in size. The domain is divided into two parts: the main domain with the porous material and an extensive rectangular zone serving as an inlet for the non-wetting phase on the left side (**Figure 2.3**a). The domain is discretized with triangular elements with slide lengths h (**Figure 2.3**b). The mesh convergence study is implemented on a sub-section of the geometry, which shows the results convergences at h=ε=1×10^{-6}m (supporting material S4). The main domain is initially saturated with water and the inlet part is initially saturated with n-octane, as the initial interface is necessary for numerical stability (Basirat et al. 2017). At t=0, n-octane with dissolved KIS tracer is injected from the left boundary with a constant velocity U_{in}. The right-hand side of the domain is the outlet, and the upper and lower sides of the domain are no flow boundaries. The initial concentration of the reacted solute in the domain and the concentration at the inlet are both zero, and the solute is produced from the interfacial reaction during the drainage process, according to the KIS tracer theory. The relevant parameters of the non-wetting fluid are ρ_{octane}=703kg/m^3 and μ_{octane}=0.54×10^{3}Pa·s, the contact angle θ_w=45°, and interfacial tension for n-octane/water σ=0.0504 N/m. With the solution of the reaction-diffusion equation Eq.(2.30) and Eq.(2.31), we know that the zero-order reaction

rates can only influence the magnitude of the resulting solute concentration curves, but not its shape. This means that the reaction rate does not affect solute transport, and transport of the solute depends on its diffusivity and the bulk fluid motion. As the study focuses on providing an understanding of the transport and the distribution of the tracer reacted product, and the result is not compared to a real experiment where solute concentration needs to be calibrated, here we use a unit reaction rate of R_c^{dif}=1mol/m^{-3}s. Time is expressed in a dimensionless manner using a characteristic time. The characteristic time is defined as $t_c = L_c/U_{in}$, where L_c is the characteristic length. The length of the domain is chosen as the characteristic length L_c=0.66mm. Changes in Péclet number of the flow system can influence the transport process of the KIS tracer and its reaction products. The global Péclet number Pe_g is determined as the ratio of the inflow velocity and solute diffusivity, as the characteristic length is known. The inflow velocities are chosen to be large enough so that the non-wetting phase can enter the domain, meanwhile the flow is ensured to be laminar. Thus, a total of six simulations are conducted at three different inflow velocities of U_{in}=0.01m/s, U_{in}=0.05m/s, U_{in}=0.1m/s and the molecular diffusion coefficients of the solute D_k=1×10^{-7}m^2/s, D_k=1×10^{-8}m^2/s, resulting to global Péclet number from Pe_g=66 to Pe_g=6600. The Pe_g for the previous laboratory application of KIS tracer is covered (Tatomir et al. 2018). The inflow velocity chosen here conforms to the velocity spectrum for simulations done by Basirat et al. (2017) for drainage process with a less viscous non-wetting phase, on the same domain geometry.

2.4 Results and discussion

We first show the result of the model verification in section 2.4.1. Then, the results of simulating the 2D slit are shown in section 2.4.2. Finally, the results of model application to study the KIS tracer reactive transport in a realistic 2D porous medium geometry are shown in section 2.4.3.

2.4.1 Model verification

Simulation results are shown and compared with analytical solutions, for a transient interfacial diffusion process in section 2.4.1.1, for a simultaneous reaction-diffusion process at the interface in section 2.4.1.2 and for an advection-diffusion process in section 2.4.1.3.

2.4.1.1 Diffusion across the interface

The transient diffusion process depends on the partition coefficient of the solute. **Figure 2.4**(a) shows the comparison between breakthrough calculated by the analytical solution at t=0.5s for P_{ow}=1, P_{ow}=0.1, P_{ow}=0.01 and P_{ow}=0.001 and that of the numerical model. It is found that the model results match those of the analytical solution well. With a lower partition coefficient, solute partitioning into the non-wetting phase is reduced. When P_{ow}<0.01, the diffusion across the interface has already become very small. Thus, P_{ow}=0.01 is applied for 2-NSA in this study. When the partition coefficient is P_{ow}<4×10^{-4}, the model comes to some unphysical results (**Figure 2.S10**). The conditions with extremely small partition coefficient (P_{ow}<4×10^{-4}) can not be solved with this model, and this is one limitation of the model. **Figure 2.4**(b) shows the resulting concentration profiles near the interface at t=0.5s. The solid curve shows the analytical solution considering a sharp interface. The dashed curves show the modeling results at ε=1×10^{-6}m and ε=1×10^{-7}m. It shows that with a thicker interface, the deviation from the sharp interface solution becomes larger, as expected. Besides, the modeled concentration curves (in dashed lines) are smoothly changing across the diffusive interface, which is different from the analytical solution and its discontinuous concentration profile for the sharp interface. We plot the corresponding volume fraction of water in the second y-axis (with scale on the right side) in **Figure 2.4**, and it is found that the

concentration curve fits the corresponding volume fraction curves. This proves that the 2-NSA concentration is simulated accurately by the model for a mixture condition at the diffuse interface.

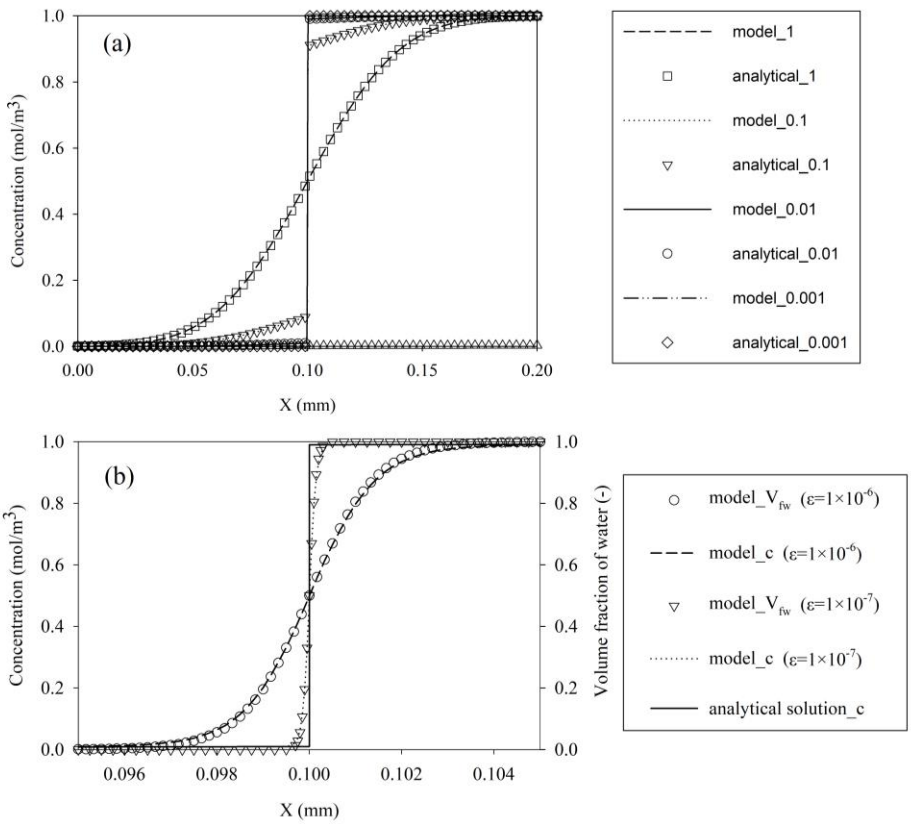

Figure 2.4 Comparison of concentration profiles of 2-NSA concentration computed analytically and numerically: (a) (at ε=1×10^{-7}m) for the transient mass transfer at t=0.5s, for P_{ow}=1, P_{ow}=0.1, P_{ow}=0.01 and P_{ow}=0.001, (b) (at ε=1×10^{-6}m and ε=1×10^{-7}m) for mass transfer at t=0.5s near the interface region.

2.4.1.2 Interfacial reaction and diffusion

Figure 2.5 shows the results of the reaction-diffusion process at t=0.2s, 1s and 2s. The integral of the concentration curves over x (area under the curves) indicates the produced 2-NSA mass in the domain, which is increasing with time. Meanwhile, the produced 2-NSA diffuses from the interface towards the bulk volume of water following the concentration gradient. The modelling results fit very well the analytical solution, demonstrating that the reaction-diffusion process can be successfully simulated by our modelling approach. **Figure 2.5** also shows that the mass transfer across the interface is negligible, which indicates that a partitioning coefficient of 0.01 is small enough to describe that the highly water-soluble product 2-NSA remains in the water phase (wetting phase).

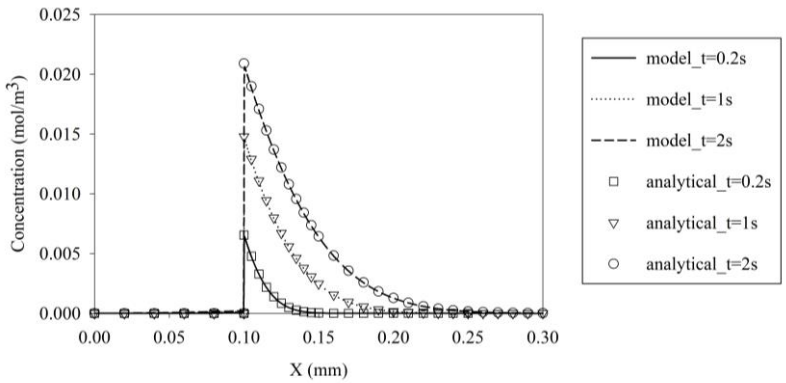

Figure 2.5 Comparison between concentration profiles of analytical and numerical model simulations (ε=1×10^{-7}m) of the reaction-diffusion process at t=0.2s, t=1s and t=2s.

2.4.1.3 Advection diffusion

Figure 2.6 shows the results of the transport process at t=1ms, 2ms and 3ms. The modelling results fit very well the analytical solution, demonstrating that the advection dominated transport process, with the system Péclet number up to Pe_g=10^5, is simulated successfully by the model. As the advection of solute is consistent with the fluid motion, no artificial mass transfer is observed near the interfacial region.

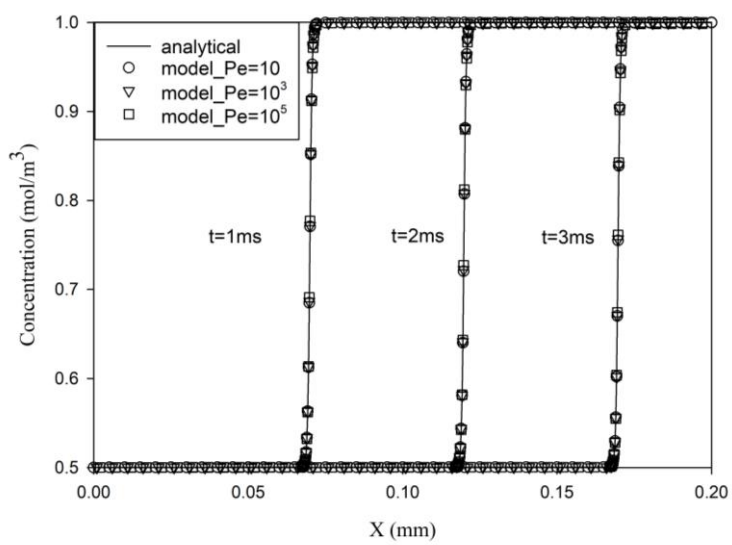

Figure 2.6 Comparison between concentration profiles of analytical and numerical model simulations of the transport process for Pe_g=10, Pe_g=10^3 and Pe_g=10^5 at t=1ms, t=2ms and t=3ms.

2.4.2 Model test in a 2D slit

The wettability of the solid wall of the pore space is characterized with the contact angle, which is expressed by Eq. (2.14) in the model. The contact angle on the solid wall is accurately simulated

by the two-phase flow model, as shown in **Figure 2.7**(a) for the setting of θ_w= 45°. Additionally, the characteristic mobility χ, which determines the time scale of Cahn-Hilliard diffusion (Eq. 2.8), needs to be chosen pragmatically (Yue et al. 2006). Straining flows can thin or thicken an interface, which must be resisted by large enough Cahn-Hilliard diffusion (Jacqmin 1999). The capillary number for the system is calculated as: $Ca = U_{in} \cdot \mu_{nw}/\sigma$. As the inflow velocity remains constant and the channel flow here is strongly affected by capillary forces (Ca =5e-4), there should be no changes in interface configuration during the flow process (Soares and Thompson 2009; Prokopev et al. 2019). It is found when χ is increased by two orders of magnitudes compared to the value of inflow velocity, the thickness and configuration of the interface is ensured to be invariant during the drainage process.

Figure 2.7(b) shows the concentration profiles for Pe_g=1, Pe_g=10 and Pe_g=100 at t=0.04s. The difference in the concentration profiles result from the competition between advection and diffusion. At Pe_g=1, the transfer process is dominated by molecular diffusion, which is verified by the model's results that the concentration contour lines are almost straight and vertical to the inflow direction. For the Péclet number being Pe_g=10, advection starts to have an obvious effect and concentration contour lines begin to blend. For Pe_g=100, the transfer process is dominated by advection, and the solute mass produced at the interface shows a trend to concentrate at the center of the slit. For a stable laminar flow condition in the slit, flow at the center of the slit is faster than the regions near the solid walls, where a no-slip boundary is considered, and all streamlines are parallel to each other. When a two-phase system is considered, near the fluid-fluid interface, the receding phase tends to flowing gathering at the center of the slit to restore the stable flow condition, as shown by streamline plot in **Figure 2.7**(b). Thus, as the effect of the advection, the water-based solute also shows a trend to concentrate at the center of the slit. A similar observation is found in the simulation results from the study for segmented channel two–phase flow by Yang et al. (2017). The same advection effect exists for all three conditions investigated, with different Péclet numbers. The effect becomes stronger when the diffusion is weak. This simulation provides a verification of the new two-phase reactive transport model.

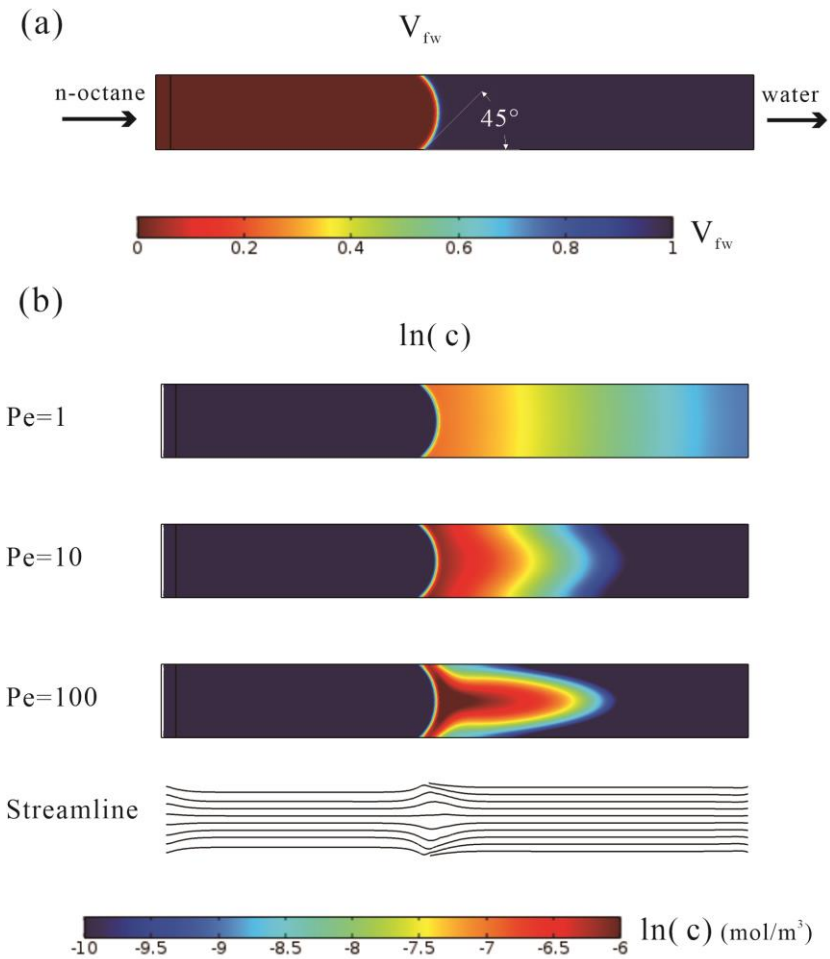

Figure 2.7 Model results of solute transport in octane/water displacement process in a capillary tube: (a) volume fraction of the water phase for with contact angles 45° at t=0.04s (b) Plot of the concentration profiles at the Péclet numbers of Pe_g=1, Pe_g=10 and Pe_g=100, as well as the corresponding streamline profile.

2.4.3 Application of KIS tracer transport in porous media

We first show the resulting displacement patterns and solute concentration distributions for the three cases in section 2.4.3.1. Then, we determine the threshold local Péclet number to distinguish the mobile and immobile zones of the pore space in section 2.4.3.2. Finally, we analyze the quantified interfacial area and the reacted solute mass separately in the mobile and immobile zones, in section 2.4.3.3.

2.4.3.1. Displacement patterns and solute concentration distribution

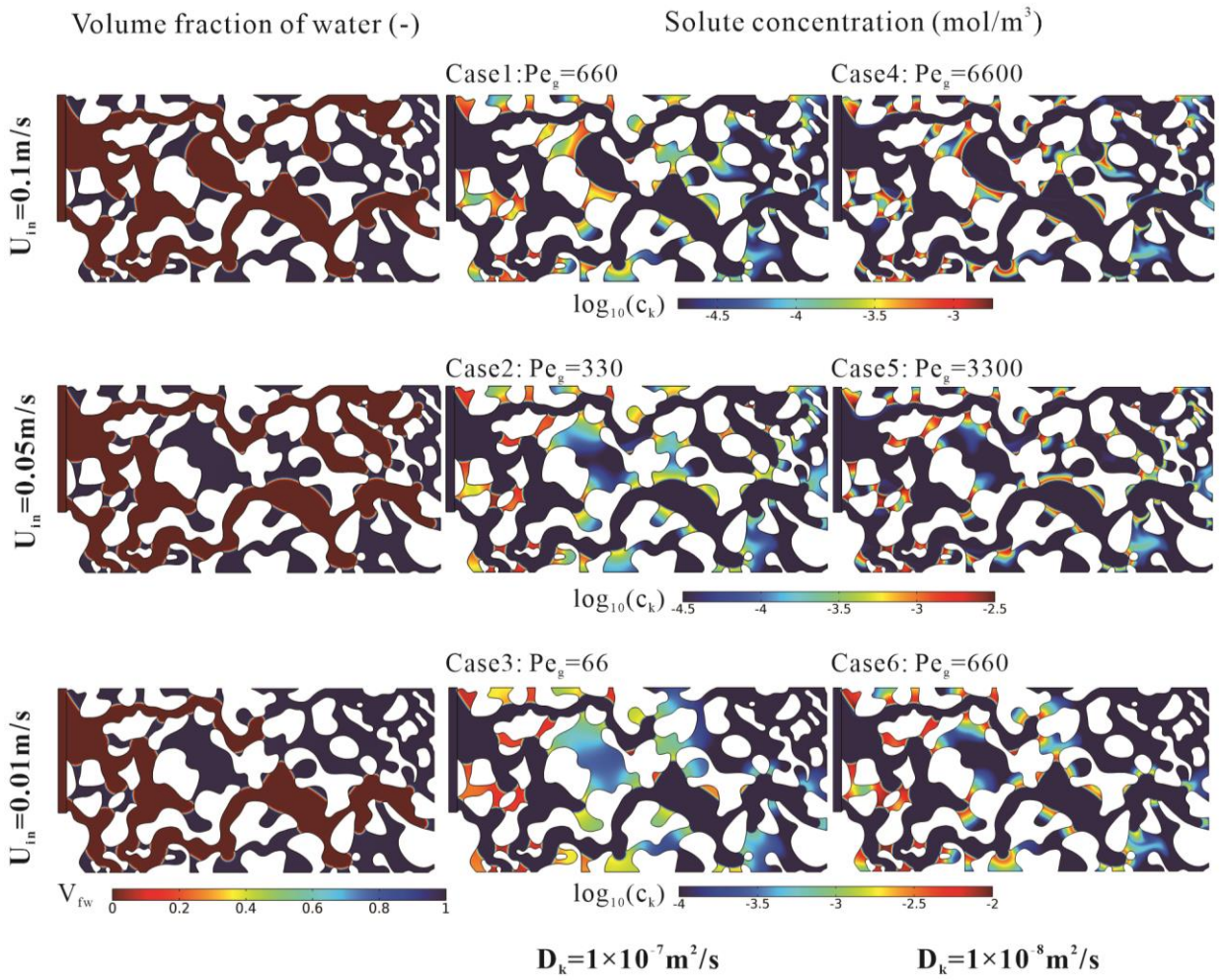

Figure 2.8 Volume fraction of water phase (left) and solute concentration (right) just before breakthrough for each case. At three different inflow rates (in rows), simulations with two different diffusivities (in columns) are demonstrated.

Figure 2.8 shows the distribution of the fluid phases and solute concentration before breakthrough for all cases. Since the 2-NSA concentration in the immobile water regions near the inlet where the reaction starts early is much larger than that at the moving front, we plot the concentration on a logarithmic scale to better illustrate the distribution of 2-NSA concentration. The fluid phase distribution is shown in **Figure 2.8**(left). At breakthrough, the non-wetting phase is more pore-filling when the inflow rate is larger. This means that a larger inflow rate is favorable for the drainage process. This result is in good agreement with Basirat et al. (2017). Besides, when the non-wetting phase reaches the outlet, the volume of the non-wetting phase in the domain shrinks, especially for Case3 with the lowest inflow rate (Figure S6). This is caused by the connected flow-paths of the non-wetting phase between inlet and outlet, formed until breakthrough. The non-wetting phase pressure is suddenly decreased leading to the expansion of the wetting phase. This refers to the capillary end effect, which was also observed in the simulations of Basirat et al. (2017).

The spatial distribution of concentration is shown in **Figure 2.8**(right). The solute concentration is changing about two orders of magnitude for each case. Trapped water clusters with smaller volumes and larger surrounding interfaces have higher concentration, as expected. Concentration at the front is generally smaller than that in trapped water clusters, mostly because the solute mass at the front is connected to the bulk water, and the solute concentration is diluted by advection and molecular diffusion towards the bulk water. It is observed that the spreading of 2-NSA in these trapped water clusters is much slower during drainage at larger Péclet numbers, as expected. The concentration distributions in Case 3 and Case 6 show the highest values. This is because, with lower inflow rate, the two fluid phases remain longer in contact with each other until the front reaches the outlet (breakthrough) which leads to a higher reaction by-product 2-NSA in the water phase. The mass balance analysis for both fluids and solute is conducted for the verification of the results (see supporting material S5).

2.4.3.2 Identification of the mobile and immobile zones

The local Péclet number can be calculated as $Pe_l = \|\mathbf{u}\| * L_c/D$, where **u** is the velocity, L_c is the characteristic length equal to the average throat width L_c=8μm (Rokhforouz and Akhlaghi Amiri 2019), and D is diffusivity. The mobile zones are generally defined as zones with Pe>>1 (Smedt and Wierenga 1984; Chhabra and Shankar 2018). The threshold local Péclet numbers to separate the flowing zones and stagnant zones can be chosen by analyzing its probability distribution (Aziz et al. 2018). The drainage process for Case2 at three different times is shown as an example in **Figure 2.9**. During the drainage process, the probability distribution (**Figure 2.9**c) turns from single-mode distribution to bimodal distribution, which is in agreement with Aziz et al. (2018) and Hansan et al. (2020). The first peak from the left-side indicting the formed capillary trapped regions is growing, and the second peak indicting the flowing regions is decaying. The reduction of flowing regions can be observed in **Figure 2.9**b. With the constant inflow boundary, the formed capillary trapped water is no longer to be drained. However, the capillary trapped water can still have slight local motion due to the surrounding pressure change during drainage (**Figure 2.S7**). This leads to the fact that the magnitude of the local Péclet number for capillary trapped region is smaller than the flowing regions, but larger than the regions of the dead-end pores. The magnitude of the local Péclet number for capillary trapped zones is more obviously displayed near the end of drainage (**Figure 2.9**c at t_c=0.45). To separate the majority of the capillary trapped regions from the flowing regions, we chose Pe_l=2.4 as the threshold for Case2 according to **Figure 2.9**c. Furthermore, we do a sensitivity analysis by applying a spectrum of local Péclet numbers near the threshold (Pe_l=0.8 to Pe_l=4.8) to quantify the specific interfacial area and solute mass in the mobile zones. The results converge at Pe_l=2.4 (**Figure 2.S8**), which proves that the chosen threshold Pe_l is appropriate. With the same method, we obtain a threshold Pe_l=4.8 for Case1 and a threshold Pe_l=0.48 for Case3 (**Figure 2.S9**). Since the flow parameters are the same, the identified mobile and immobile zones are the same for Case1, Case2, Case3 and Case4, Case5, Case6, respectively. However, even the lowest threshold Pe_l (Pe_l=0.48 in Case3) is larger than that reported in Aziz et al. (2018). The reasons could be the differences between the geometries used in the two studies, the parameters of the two systems (e.g. injection velocity, solute diffusivity), and in the study of Aziz et al. (2018) the calculation are done when the flow patterns reach steady state.

With the concentration map of the 2-NSA in the mobile zones (enclosed by isoline in magenta color) during the displacement (**Figure 2.9**a), it is clear that the 2-NSA carried by the flowing water is mainly produced and located at the menisci at the moving front in the main flow channels. And the flowing water at the front is not connected to the dispersed water clusters trapped in dead-end

pores or throats, which means there is no direct 2-NSA mass exchange between them. This part of 2-NSA mass in the flowing regions is measured for the KIS tracer test. With the model results and threshold local Péclet number, we can quantify the interfacial area and the reacted solute mass in the flowing regions to study the relationship between them.

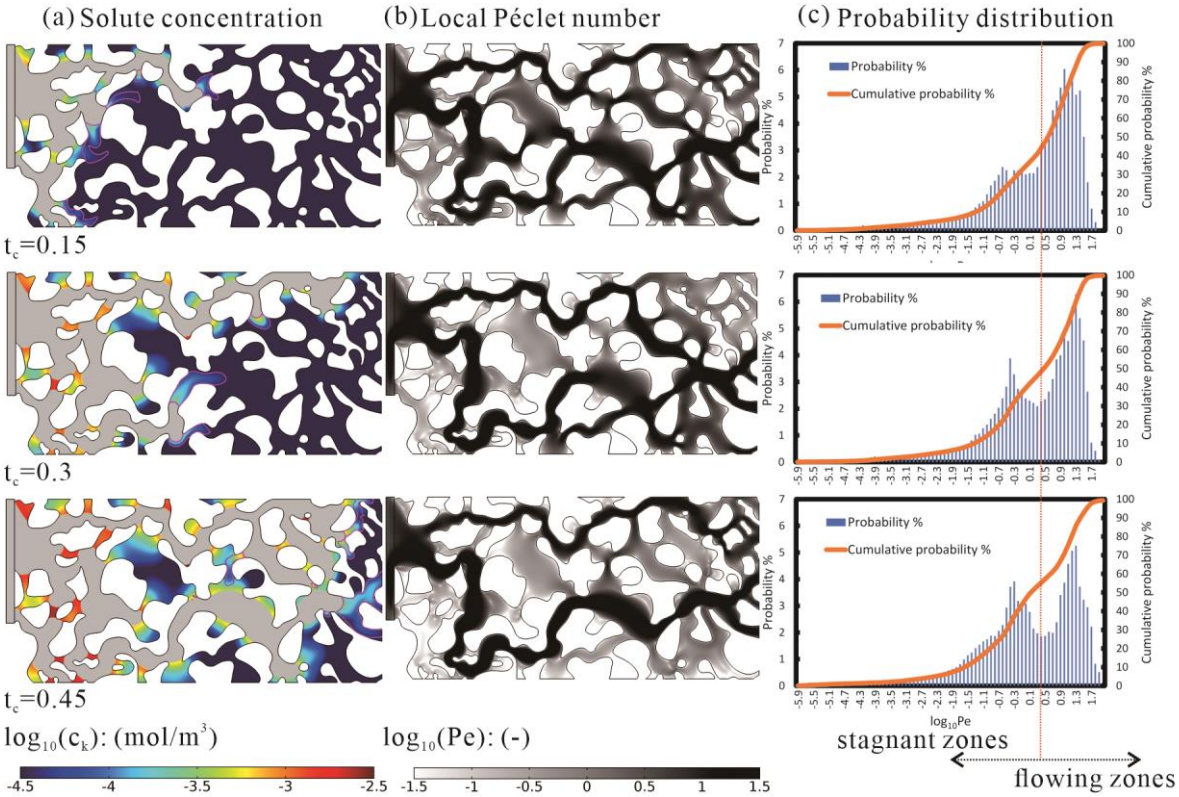

Figure 2.9 Plot of simulation results (a): 2-NSA concentration with n-octane phase in gray color, with the isoline of $\log_{10}(c_k)$=-4.5 for flowing zones plotted in magenta color; (b): distribution of the local Péclet number; (c): probability distribution of the local Péclet number, during the drainage process for Case 2 at t_c=0.15, t_c=0.3 and t_c=0.45.

2.4.3.3 Interpretation of the tracer reacted mass in flowing regions

The specific interfacial area (SIA) is calculated by Eq.(2.32):

$$a_{wn}^{m,im} = \frac{A_{wn}^{m,im}}{b_{wn}} \cdot \frac{1}{V_p} \tag{2.32}$$

where $A_{wn}^{m,im}$ is the interface region within $V_{fw} \in [0.05, 0.95]$ for flowing and stagnant regions, b_{wn}=4.16ε is the thickness of the reaction region obtained from Eq.(2.6), with the diffusive interface having a capillary width of ε=1e-6m, and V_p is the total volume of the porous media that is studied. Mobile and immobile SIA are plotted in **Figure 2.10** for changes in saturations during drainage. The mobile SIA values range between 200 – 1200 1/m (**Figure 2.10**) while the immobile SIA can reach an order of magnitude higher up to 5300 1/m (**Figure 2.10**). The mobile SIA has strong oscillations during drainage, which is mainly caused by switching of the mobile and immobile interfaces at the front. When one meniscus at the front meets narrow pore necks, the fluid will

become stagnant for several time steps, during which the meniscus that originally counted as the mobile interface will becomes temporarily immobile. Meanwhile, the nearby menisci, which are originally immobile, can also become mobile due to the equilibrium of the local pressure. As the menisci have different sizes, this switching of the mobile and immobile interfaces causes the oscillations of the curve of the accounted mobile interfacial area during the displacement. The overall change in mobile SIA is relatively small during drainage, and its values are similar for all cases. This can be attributed to the fact that the mobile interfacial area results from the menisci at the moving front, which depend on the width and geometry of the flow channels. On the other hand, the immobile SIA increases approximately linearly with saturation during the displacement process, due to the formation of trapped water clusters. Furthermore, the reacted solute mass can be directly quantified by:

$$M^m = \int_{V_v^m} c \cdot dV + \int_{t_0}^{t} \int_{L_{outlet}} u \cdot c \cdot dL\, dt$$
$$M^{im} = \int_{V_v^{im}} c \cdot dV \tag{2.33}$$

where $V_v^{m,im}$ is the volume of void space for flowing and stagnant regions. The temporal change in total 2-NSA mass in the mobile zones (M^m) and immobile zones (M^{im}) is shown in **Figure 2.10**, where the mobile 2-NSA mass is quantified as the sum of the 2-NSA mass in the mobile zone, and in the part exiting the domain through the outlet (Eq.2.33). It is found that the 2-NSA mass in the mobile zones is much smaller than that in the immobile zones. The curve oscillations for the quantified solute mass are also caused by the switching of the mobile and immobile zones during the Haines Jumps.

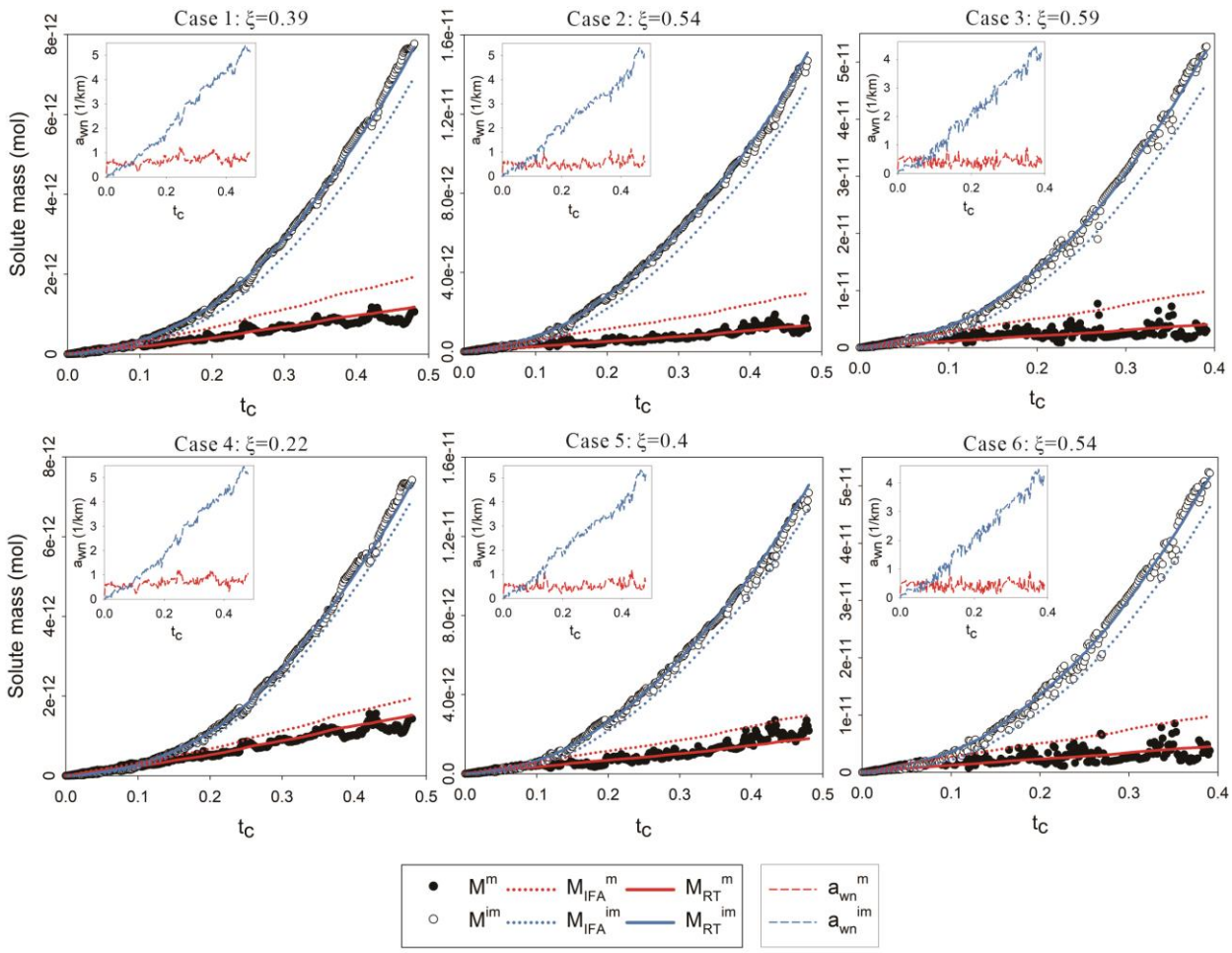

Figure 2.10 Plot of simulation results: the quantified 2-NSA mass in the mobile and immobile zones (M), the 2-NSA mass produced by mobile and immobile interface (M_{IFA}), and the 2-NSA mass calculated from interfacial areas with the mobile mass retention term (M_{RT}), versus the dimensionless time for all cases. The inset plot shows the corresponding specific interfacial area in the mobile and immobile zones.

We investigate if the 2-NSA mass transported by the mobile water phase can be related to the mobile interfacial area. Knowing the mobile and immobile interfacial areas, we can calculate the 2-NSA mass (M_{IFA}) produced by them respectively by Eq.(2.34).

$$M_{IFA}^{m,im}(t) = \int_{t_0}^{t} A_{wn}^{m,im}(t) \cdot R_c^{dif}\, dt \tag{2.34}$$

where superscripts m and im, indicate mobile and immobile, respectively. For the mobile zones, we found both curves of M^m and $M_{IFA}{}^m$ show (roughly) a linear increase with dimensionless time, but the curve of $M_{IFA}{}^m$ has a larger slope than M^m (**Figure 2.10**). This means a constant fraction of the 2-NSA produced by the mobile interface becomes residually trapped in the immobile zones. For the immobile zones, the curve of both M^{im} and $M_{IFA}{}^{im}$ show a parabolic increase, and the curves show that M^{im} is larger than $M_{IFA}{}^{im}$ (**Figure 2.10**). Because the total 2-NSA mass matches that

calculated from the total interfacial area (**Figure 2.S5**), the additional fraction of immobile 2-NSA mass is derived from the retention of part of the 2-NSA mass produced at the mobile interface. We introduced a mobile mass retention term ξ in Eq. (2.34) to formulate the relationship between mobile interface and 2-NSA in flowing water, as well as immobile interface with 2-NSA mass in immobile zones as Eq.(2.35) and Eq.(2.36):

$$M_{RT}^{m}(t) = \int_{t_0}^{t} [A_{wn}^{m}(t) \cdot (1-\xi)] \cdot R_c^{dif}\, dt \tag{2.35}$$

and

$$M_{RT}^{im}(t) = \int_{t_0}^{t} [A_{wn}^{im}(t) + \xi A_{wn}^{m}(t)] \cdot R_c^{dif}\, dt \tag{2.36}$$

where M_{RT} is the 2-NSA mass calculated by adding the mobile mass retention term (ξ). The curves are better fitted by adding ξ as shown in **Figure 2.10**. The deviation of the curves from M and M_{RT} is found near the end of the drainage process, because a large decrease in the mobile zones occurs shortly before breakthrough. The mobile mass retention terms determined for the six studied cases have values ranging from 0.22 to 0.59. At the same inflow rate, the system with larger molecular diffusion coefficients (smaller Pe_g) has larger ξ. With the same molecular diffusion coefficient, the system at larger inflow rate (larger Pe_g) has smaller ξ.

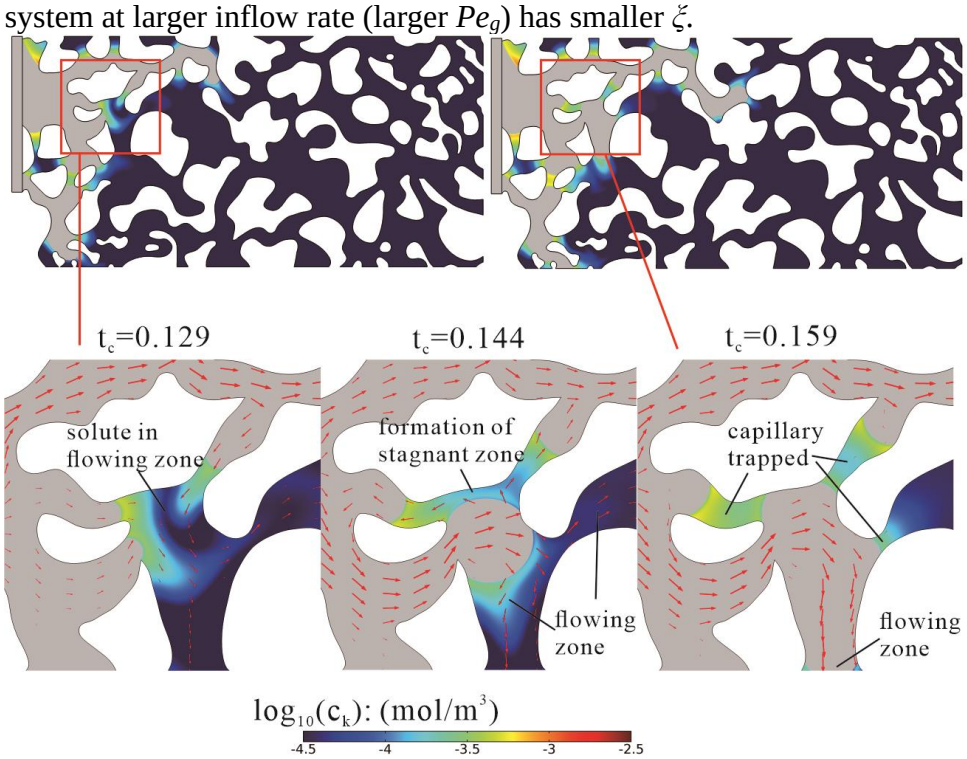

Figure 2.11 Plot of simulation results of mobile mass retention process into the stagnant zones, in a zoom-in region from Case 2 at t_c=0.129, t_c=0.144 and t_c=0.159. The diagrams show the spatial distribution of solute concentrations with the non-wetting phase covered by gray color. The red arrows show the direction of velocity vector, and the length of the arrows is proportional to the natural logarithm of the norm of velocity vector.

A zoom-in region for the retention process is shown in **Figure 2.11**. In the zoom-in region at t_c=0.129, the solute mass produced and pushed by three moving menisci (mobile interfaces) at the front are approaching an intersection, where the fluid velocities are slowed down due to the pore necks. At t_c=0.144, one meniscus first passes through the pore neck and the non-wetting fluid fills the pore, and the other two menisci are pushed back during pore filling. The reacted solute is separated into two parts: one part that keeps flowing and the other part that is trapped in stagnant zones, as demonstrated in the sub-figure at t_c=0.159. The retention of the reacted solute in the flowing water (at the front) occurs when flowing water is being capillary trapped. The retention process is also along with bursting and splitting of the moving menisci at the front (see **Figure 2.11** at t_c=0.144), and a part of the moving menisci is arrested and turns into immobile interfaces in the immobile zones, including dead-end pores and capillary trapped zones. The retention process happens frequently with the formation of the trapped water and the immobile interface during the displacement, leading to an approximate constant fraction of solute mass produced by mobile interface to be retained, in the relationships of Eq.(2.35) and Eq.(2.36).

Though the flowing water and trapped water are isolated as the receding phase, the solute mass exchange between mobile and immobile zones happens by means of mobile mass being capillary trapped and turning into immobile mass, during the dynamic process. This part of exchanged mass can be described by the mobile mass retention term. The results imply that when the mobile mass retention term is known, the reacted 2-NSA mass in the flowing water measured in KIS-TT can be used to determine the averaged mobile interfacial area during the drainage process (Eq.2.3).

2.5 Summary and Conclusions

We proposed and demonstrated a novel pore-scale model for simulating the KIS tracer reactive transport process for two-phase flow conditions in a porous medium. In the mathematical model, a continuous species transport formula consistent with PFM was derived. One major advantage of the model is that the fluid-fluid interface hydrolysis reaction of the KIS tracer, which is approximated by a zero-order reaction, can be directly implemented in the diffusive interface approach. We first provide three types of verification of the model. By comparing the solute concentration and water volume fraction across the interface in a simple diffusion process, we showed that the solute concentration at the diffusive interface can be accurately calculated by the model. We found that for low partitioning coefficients (P_{ow}=0.01), the model adequately describes the selective distribution of 2-NSA into water. The simultaneous process of 2-NSA interfacial reaction and diffusion was verified by comparing the numerical results and the analytical solution of the reaction-diffusion equation. Additionally, the advection of fluid and solute are proven to be consistent with no artificial interface mass transfer in an advection-diffusion process, when solute concentration of the two phases are at equilibrium. Next, the model was tested by simulating the drainage process (i.e., wetting phase displacement by the non-wetting phase) in a 2D silt. After testing the solute transport model for different Péclet numbers, we found that the concentration profile changes are diffusion-dominated at Pe_g=1 and advection-dominated at Pe_g=100.

Finally, the model was applied to a realistic 2D porous medium. Six cases with different global Péclet numbers were simulated. The mobile and immobile zones are separated using a threshold local Péclet number, which is obtained by analyzing the probability distribution of the local Péclet number during the drainage process. To understand how immobile zones affect the detectable solute mass in the outflow-based measurements, we quantified the interfacial area and the reacted 2-NSA mass separately in the mobile and immobile zones. It was observed that the fraction of 2-

NSA mass transported by the flowing water is related to the mobile interface. It was found that the mobile SIA is much lower than the total SIA (ca. 10%) and it varies little during the drainage process. We propose an interpolation relationship between the 2-NSA mass in the mobile zones and the mobile interfacial area. The relationship is formulated by adding a mobile mass retention term. This term relates to the part of 2-NSA produced by mobile interface that becomes residual in the immobile zones.

This study showed that the mobile interface, or the moving interface, plays an important role in the solute transport during the displacement process, especially when the solute is interfacial-reacted and dissolves in the receding phase. The KIS-TT, which is capable of measuring the mobile interface, can be a valuable technique in understanding the coupled flow and reactive transport processes in dynamic two-phase flow systems. Future work is required to study if the mobile mass retention term varies when applied to different pore geometries, or when using different fluid - porous media systems, such as changes in fluid viscosity ratio or medium wettability. Future work is also required to improve our macroscopic model of KIS tracer reactive transport (Tatomir et al. 2015, 2018), for further including the different transport patterns in the mobile and immobile zones observed at the pore-scale.

Nomenclature

Symbols	
A_{wn}	fluid-fluid interfacial area [m^2]
a_{wn}	specific interfacial area [m^{-1}]
b_{wn}	diffuse interface thickness [m]
c_i	interface tracer concentration [$mol \cdot s^{-1} m^{-2}$]
c_a	non-wetting phase tracer concentration [$mol \cdot s^{-1} m^{-3}$]
c	reacted solute (2-NSA) concentration [$mol \cdot s^{-1} m^{-3}$]
Ca	capillary number
D	molecular diffusion coefficient [m^2/s]
$\mathbf{F}$	fluid advection flux [m^2/s]
f_{mix}	free energy density [J/m^3]
G	chemical potential [J/m^3]
h	slide length of mesh triangle [m]
$\mathbf{J}$	solute diffusion flux [$mol \cdot s^{-1} m^{-2}$]]
K_L	Langmuir adsorption coefficient
L_c	characteristic length
M	reacted solute (2-NSA) mass [mol]
p	pressure [pa]
P_{ow}	partitioning coefficient
Pe_g	global Péclet number of the system
Pe_l	local Péclet number
R_c	macro-scale reaction rate [$mol \cdot s^{-1} m^{-2}$]
R_c^{dif}	reaction rate on diffuse interface [$mol \cdot s^{-1} m^{-3}$]
t	time [s]
t_c	characteristic time
$\mathbf{u}$	velocity [m/s]
U_{in}	inflow velocity [m/s]
V_v	volume of void space

V_p	volume of the porous media
V_f	volume fraction of fluid
ϕ	phase variable
λ	magnitude of the mixing energy [N]
ε	capillary width [m]
σ	surface tension [N/m]
γ	mobility [m^3s/kg]
χ	characteristic mobility [m·s/kg]
ρ	density [kg/m^3]
μ	viscosity [pa·s]
θ_w	contact angle
ξ	mobile mass retention term

Subscript	
a	phase
w	wetting phase
nw	non-wetting phase
wn	interface
k	solute
0	initial condition
m	mobile zones
im	immobile zones

Abbreviation	
BTC	Breakthrough curve
CFD	Computational Fluid Dynamics
CST	Continuous Species Transfer
C-CST	Compressive-Continuous Species Transfer
DNS	Direct Numerical Simulation
(F)IFA	Fluid-Fluid Interfacial Area
IPTT	Interfacial Partitioning Tracer Tests
KIS-TT	Kinetic Interface Sensitive tracer test
LBM	Lattice Boltzmann Method
LSM	Level set method
NAPL	Nonaqueous phase liquid
PVI	Photo-luminescent Volumetric Imaging
PFM	Phase-Field Method
PNM	Pore-Network Modeling
REV	Representative Elementary Volume
SPH	Smooth Particle Hydrodynamics
SIA	Specific interfacial area
VOF	Volume-Of-Fluid method
XMT	X-Ray Computed Micro-Tomography

2.6 Acknowledgement

We thank Tobias Licha for the constructive dialogue about the KIS tracer and overall support of the work. We thank Rainer Helmig and Holger Class (from the SFB1313 Collaborative Research Center) for the support in conducting and further extending this work.

We acknowledge DFG Project 428614366, European Community's 7th Framework Programme FP7 under grant number 309067 (trust-co2.org), and Horizon 2020 Research and Innovation Programme under grant number 636811.

HS and NKK acknowledge funding by the German Research Foundation (Deutsche Forschungsgemeinschaft, DFG) within the Collaborative Research Center 1313 (Project Number 327154368 – SFB 1313).

HS acknowledges funding by the Deutsche Forschungsgemeinschaft (DFG, German Research Foundation) under Germany's Excellence Strategy - EXC 2075 - 390740016. All data used to support this work are reported in the manuscript and the Appendix in the respective tables and figures.

2.7 Supporting information

Text 2.S1. Viscous coupling during co-current flow

The ability of this two-phase flow model to capture viscous coupling effects is verified by simulating the immiscible two-phase, co-current flow in a channel, where the wetting phase, i.e. water, flows along the channel walls and the non-wetting phase, i.e., oil, flows in the central area as shown in **Figure 2.S1**(a). The wetting phase is water with density of 1000 kg/m^3 and viscosity of μ_w=0.001 Pa·s. The non-wetting phase (density of 1000 kg/m^3) for two simulations has viscosities of μ_n=0.01 Pa·s and μ_n=0.0001 Pa·s, resulting in the viscosity ratios ($\beta=\mu_n/\mu_w$) of β=10 and β=0.1. The inlet the outlet boundaries are assigned as constant pressure (P_{in}=0.1pa and P_{out}=0) boundaries. At the channel wall no-slip boundary conditions are applied, and initially the flow velocity in the domain is zero. The lower boundary is the symmetry line (no flow boundary) passing through the middle of the two parallel plates. Both phases occupy half width of the half-channel 0.1mm. The interfacial tension is σ=0, so capillary force is not considered. This simulation tests if the viscous forces are well simulated by the model by comparing to the one dimensional analytical solution of Navier-Stokes equation in the channel of width l (Eq.(2.37), Eq.(2.38)) (Yiotis et al. 2007).

At $0.5l < x < l$

$$u(x) = \frac{\nabla p}{2\mu_w}(l^2 - x^2) \tag{2.37}$$

At $0 < x < 0.5l$

$$u(x) = \frac{3l^2 \cdot \nabla p}{8\mu_w} + \frac{\nabla p}{2\mu_n}\left(\frac{l^2}{4} - x^2\right) \tag{2.38}$$

The velocity profiles along the channel width are obtained at middle of the channel as the dashed line in **Figure 2.S1**(a). After a transient period at the beginning of the simulation, the model reaches a steady state which implies that the velocity is constant. **Figure 2.S1**(b) plots the velocity profile along the channel width for a viscosity ratio (oil to water) of β=10 and β=0.1. The channel width

(x axis) x=0 means the middle of the channel, and the channel wall at x=0.0002m. As the analytical solution is based on a sharp interface, modelling result with a thinner interface provides more accurate modeling results. The modeling results are in very good agreement with the analytical solution at $\varepsilon=1\times10^{-6}$m, h=0.5ε.

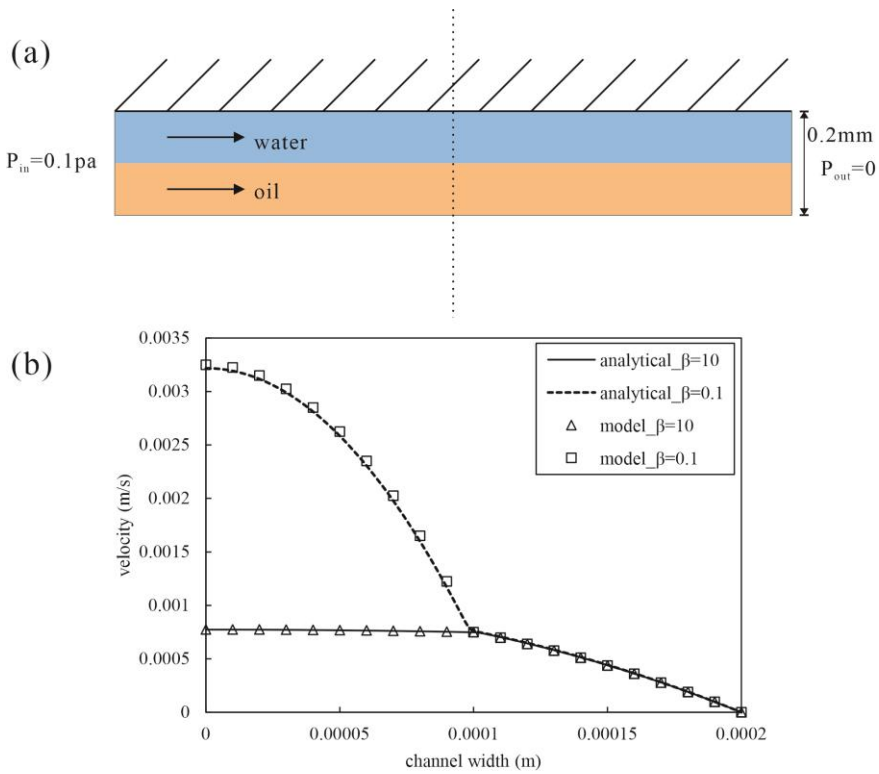

Figure 2.S1 Model verification through the study of two-phase co-current flow through two parallel plates (a) Schematics of the viscous coupling in channel co-current flow. (b) Comparison of the velocity profiles along the channel width obtained by the model and the analytical solution at viscosity ratios (oil to water) β=10 and β=0.1.

Text 2.S2. Bubble relaxation

Bubble relaxation is an experimentally well studied problem, which provides a good benchmark for the two-phase flow model. During the retraction of an initially elonged elliptic bubble towards the spherical shape in a quiescent matrix with no externally imposed velocity of the fluids. The major and minor axes (characterizing the elliptical shape of the blob) are measured for the back-calculation of the interfacial tension. The parameters used here are according to the experiment of Guido and Villone (1999). The dispersed phase has a density of 965 kg/m3 and a viscosity of μ_d=109 Pa·s and the continuous phase has a density of 920 kg/m^3 and a viscosity of μ_c=81 Pa·s. Fluids with high viscosities are used in these experiments to avoid the effect of inertia. The radius of the bubble at rest is R_0=55μm. The bubble is located at the center of a square domain with the side length of $4R_0$. The deformation parameter is defined as D=(a-b)/(a+b), where, a and b are the major axis and minor axis respectively. The characteristic time is expressed as $t_c=\mu_c R_0/\sigma$ according to Guido and Villone (1999). The known interfacial tension for the fluids σ=2.58 mN/m is set for

the model, and the verification is done by comparison between deformation parameters from the model and the experiment with respect to the characteristic time, during the bubble relaxation processes. Two bubble retraction experiments are simulated with initial bubble deformations of D_0=0.22 and D_0=0.42 (**Figure 2.S2**a). **Figure 2.S2**(b) plots the resulting data as ln(D/D_0) versus the characteristic time. For the sake of comparison, following Guido (1999), the original of the abscissa is taken corresponding to a value of D called D_0' (D_0'=0.13 for D_0=0.22 and D_0'=0.1 for D_0=0.42). The results are further compared to the theoretical approach by (Rallison 1984) at the limit of small deformations (Eq.(2.39)).

$$D = D_0 exp\,(-\frac{40(\beta+1)}{(2\beta+3)\cdot(19\beta+16)}\cdot t_c) \tag{2.39}$$

where β is the viscosity ratio $\beta=\mu_d/\mu_c$. **Figure 2.S2**(b) shows that the numerical results (with $\varepsilon=1.1\times10^{-6}$m, h=0.4ε, χ=1) fit the experimental results from Guido and Villone (1999), which all fall on the same master curve that is represented by Eq.(2.39). Deviations of the numerical and experimental results from the theoretical linear profile are only observed when the deformation of the bubble is large (ln(D/D_0)>1) (**Figure 2.S2**b), which is in agreement with Guido and Villone (1999).

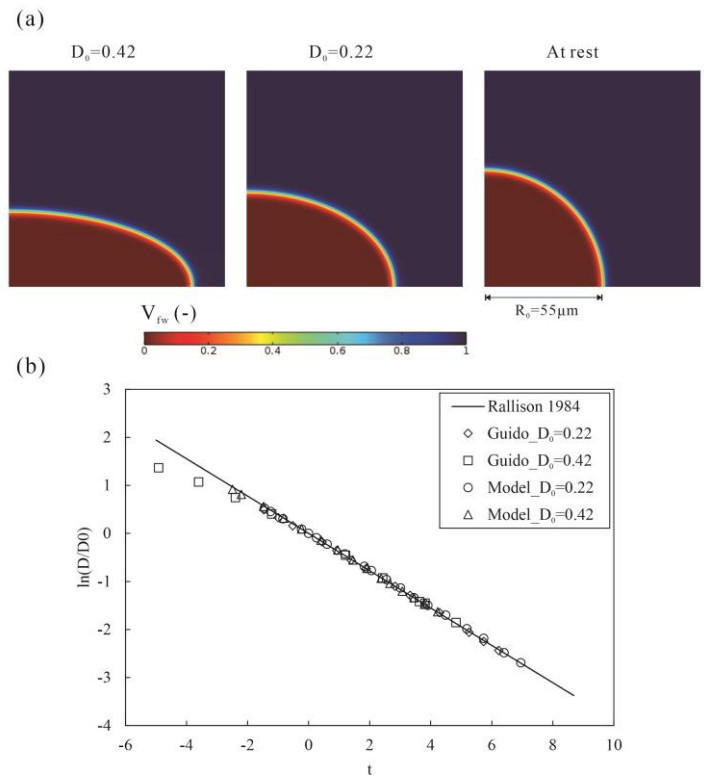

Figure 2.S2 Model validation with the bubble retraction experiment from Guido and Villone (1999) (a) Plot of the simulated bubble at beginning of the simulations with deformations D_0=0.22 and D_0=0.42, and at the end when the bubble is at rest (b) Comparison of modelling results as ln(D/D_0) to the experimental and theoretical results.

Text 2.S3. Deposited film thickness

During two-phase flow in porous media, such as the displacement of the wetting phase by an invading non-wetting phase, the wetting phase may form thin films on the grain surfaces (Brusseau et al. 2009; Brusseau et al. 2010; McDonald et al. 2016). To accurately capture these films, we consider a quick displacement process of ethanol ($\rho_{ethanol}$=789kg/m^3 ,$\mu_{ethanol}$=1.2mPas) by air (ρ_{air}=1kg/m^3 ,μ_{air}=18μPas) in a capillary tube according to the experiment demonstrated by Aussillous and Quéré (2000). The interfacial tension of ethanol/air is σ=0.02 N/m. The tube is 0.8mm long with a radius of R=0.05mm, and on both sides the boundaries are solid wall. The tube is initially filled with ethanol and air is injected from the left side with U_{in}=0.4m/s starting at t=0 s. A sketch of the model setup is shown in **Figure 2.S3**(a). Aussillous and Quéré (2000) proposed the thickness of the deposited film on the wall, which is given by the semi-empirical Taylor's law (Eq.(2.40)):

$$\frac{m}{R} = \frac{1.34Ca^{2/3}}{1 + 3.35Ca^{2/3}} \tag{2.40}$$

where m is the film thickness, Ca is the capillary number: $\mathrm{Ca} = \mathrm{u} \cdot \mu_l/\sigma$, and $m = 4.36\ \mu m$ is obtained from Eq.(2.40). In the model, the mesh size near the wall boundary is refined to h=1μm to better resolve the deposited film, while the mesh size in the middle of the tube is h=2μm. The results of the drained tube at t=1ms are shown in **Figure 2.S3**(b), and the film thickness is obtained as 4.42μm, which has a relative error of 1.3% compare to Taylor's law.

(a)

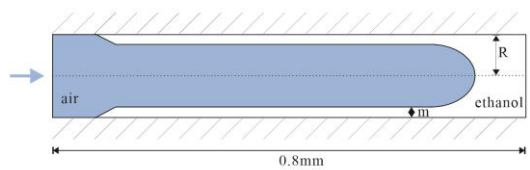

(b)

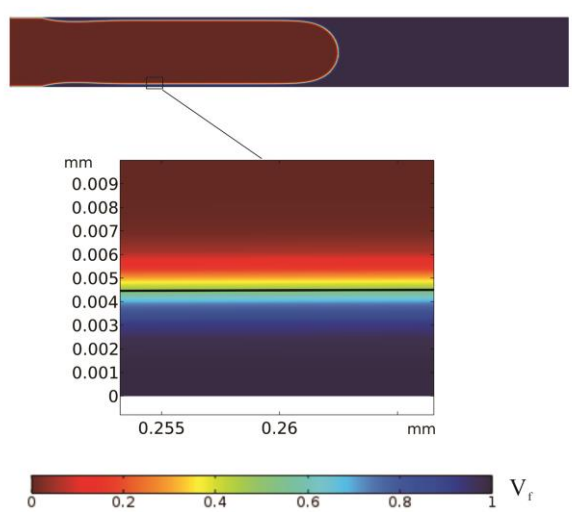

Figure 2.S3 Benchmark of the simulated film thickness (during the quick displacement process of ethanol by air in a capillary tube): (a) Sketch of the model setup; (b) volume fraction of ethanol at t=1ms. The zoom-in frames show the deposited film thickness (solid black line is the center line of the diffuse interface V_f=0.5).

Text 2.S4. Study of mesh convergence

Due to the complexity of two-phase flow in porous media systems, when the mesh grids are not fine enough, or the interfaces are not resolved by adequate mesh grid sizes, the results can become unreliable due to numerical distortions (Akhlaghi Amiri and Hamouda 2013). Using uniform equilateral triangular elements for generating the mesh, the element size can be represented by its side length (h). The element number on the diffusive interface can be indicated by the ratio of h to the capillary width (ε). Thus, the mesh convergence study focuses on these two factors (h and the ratio of h to ε). The mesh convergence study is implemented on a sub-region of the original geometry of porous media (**Figure 2.S4**a). The boundary conditions are: $u_{t=0} = 0, p_{t=0} = 0, u|_{inlet} = 0.05m/s, p|_{outlet} = 0$. The small section on left has $\phi_{t=0} = 1$, the main domain has $\phi_{t=0} = -1$, and $\phi|_{inlet}$ =1, meaning initially water filled domain is drained by the non-wetting phase. The channel wall boundary condition is no-slip.

The fraction of volume occupied by the non-wetting phase in the domain (Vn/V) as a function of time is studied. After breakthrough, Vn/V is stabilized, and a certain volume of water is trapped in the sub-channel at the bottom of the domain. The results are shown in **Figure 2.S4**b. At h=ε (**Figure 2.S4**b left), the result converges with mesh elements $h<1.5\times10^{-6}$m. Thus, we choose the $h=1\times10^{-6}$m to ensure the model convergence, and the mesh (at $h=1\times10^{-6}$m) for the sub-section geometry is shown in **Figure 2.S4**a. At $h=1\times10^{-6}$m (**Figure 2.S4**b right), the result converges with h>0.5ε. We choose h=ε to ensure the interface is adequately resolved.

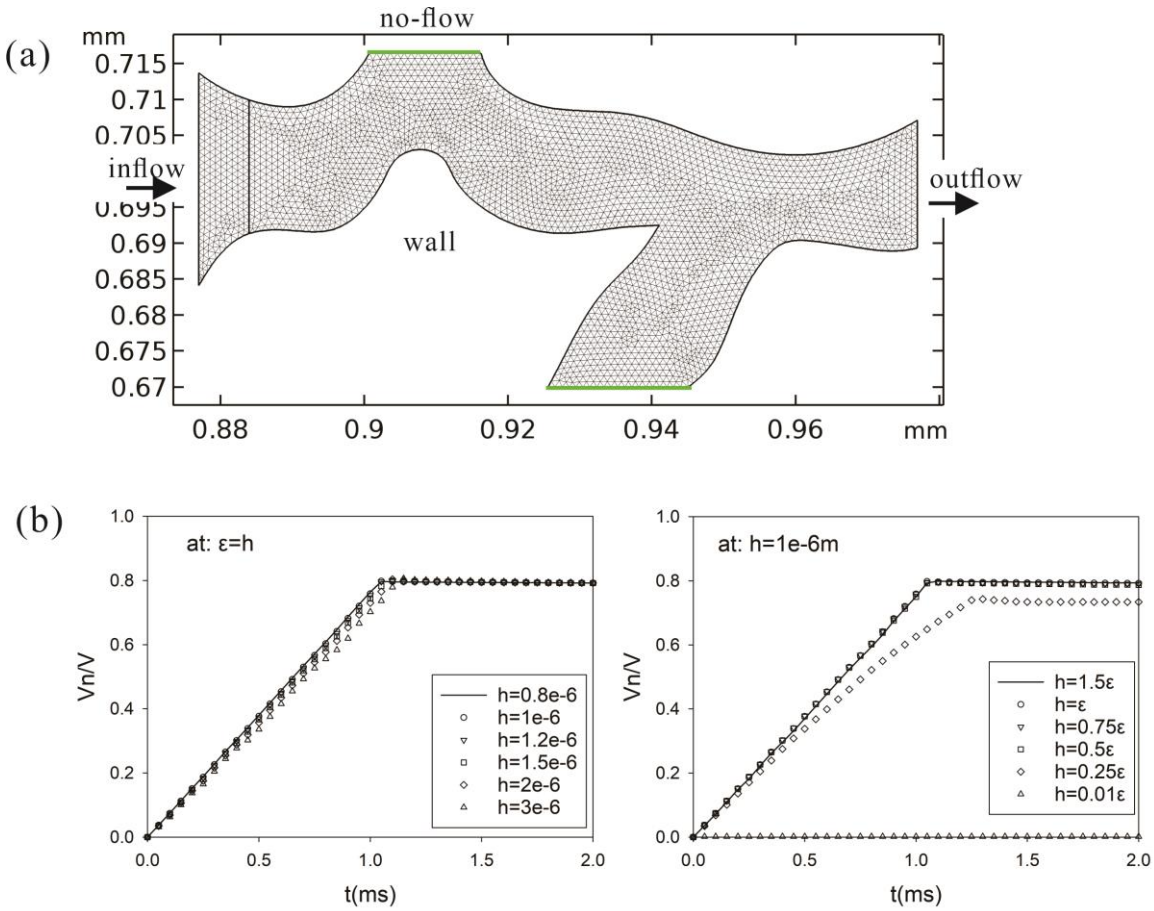

Figure 2.S4 Study of the mesh convergence: (a) Geometry of a sub-region of the porous media illustrated in the manuscript Gao et al. 2021 in Figure 2.3, and the boundary conditions (here, a mesh with $h=1\times10^{-6}$ m is demonstrated); (b) Results of the mesh convergence study based on the non-wetting phase volume fraction in the domain versus the time, at a fixed ratio of h=ε (left-hand side subfigure) and at a fixed element size $h=1\times10^{-6}$m (right-hand side subfigure).

Text 2.S5. Analysis of mass balance for fluids and solute

To analyze the mass conservation of the fluid phases, we consider the fluids of the whole systems, including fluids within the domain and the outflow. Mass conservation analysis is done by comparing between the total fluid volumes in the system that calculated based on the model setup and that quantified from the model results. The theoretical total fluid volumes of both phases in the system can be calculated from the initial conditions and boundary conditions (knowing the non-wetting phase inflow rate into the domain). The modelled total fluid volumes are obtained by summing the volumes quantified from the domain and the flow through the outlet. **Figure 2.S5**a shows that the total volume of water in the system is constant, which equals to the initial water volume in the domain, and the total volume of the non-wetting phase in the system is linearly increasing with a constant inflow boundary. The lines presenting the theoretical volume of fluids in the system fit the markers presenting the quantified volume of fluids from the model result, meaning the fluid mass of both phases is in balance (**Figure 2.S5**a). Concerning the mass

conservation of the solute (Fig. S5b), as the solute keeps being produced at the interface following a zero-order reaction, the solute mass conservation analysis is done by comparison between the total solute mass quantified from the model and the theoretical value that should be produced from the known interfacial area. The modelled total solute mass can be quantified as the sum of the solute mass in the domain and that transported through the outlet. We compare the quantified solute mass (in markers) with the theoretical solute mass that should be produced from the total fluid-fluid interfacial area (represented with lines). The good agreement between the markers and lines proves that the zero-order reaction at the fluid-fluid interface is accurately simulated by the model.

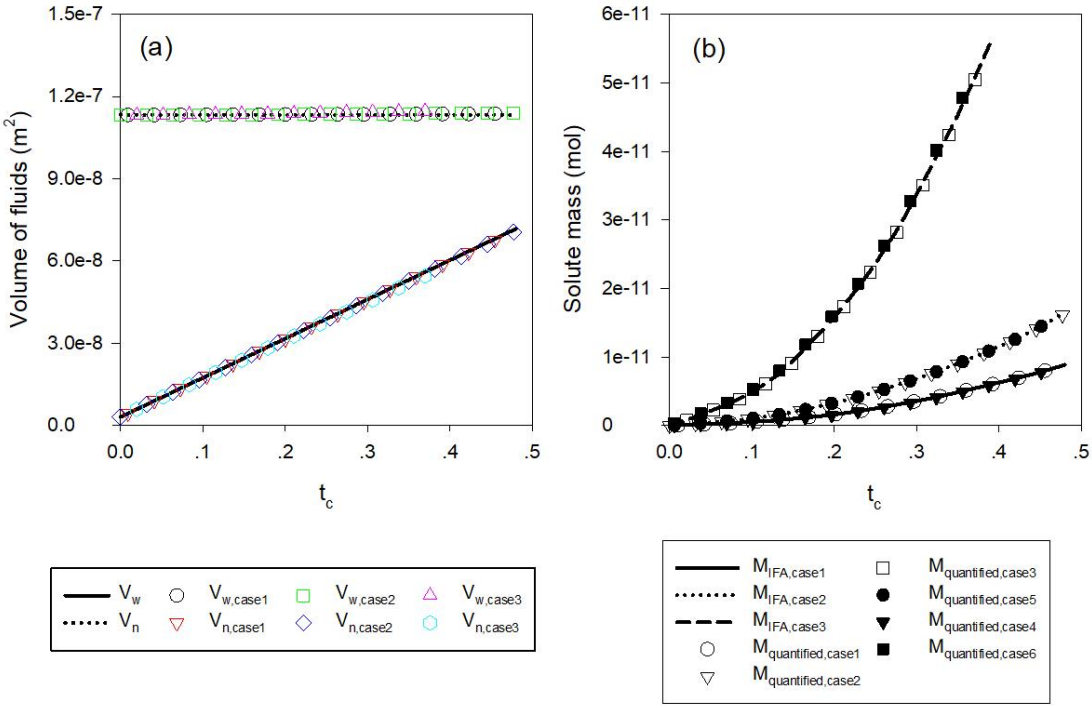

Figure 2.S5 Analysis of mass balance for the fluid phases and the reacted solute: (a) Plot of the volumes of wetting phase, non-wetting phase and the total fluid volume of both phases, calculated from initial and boundary conditions in lines and that quantified from the modelled (sum of fluid volume that in the domain and leave the outlet) in markers; (b) Plot of solute mass calculated from the interfacial area in lines and that quantified from the model (the sum of solute mass in domain and that transport through the outlet) in markers.

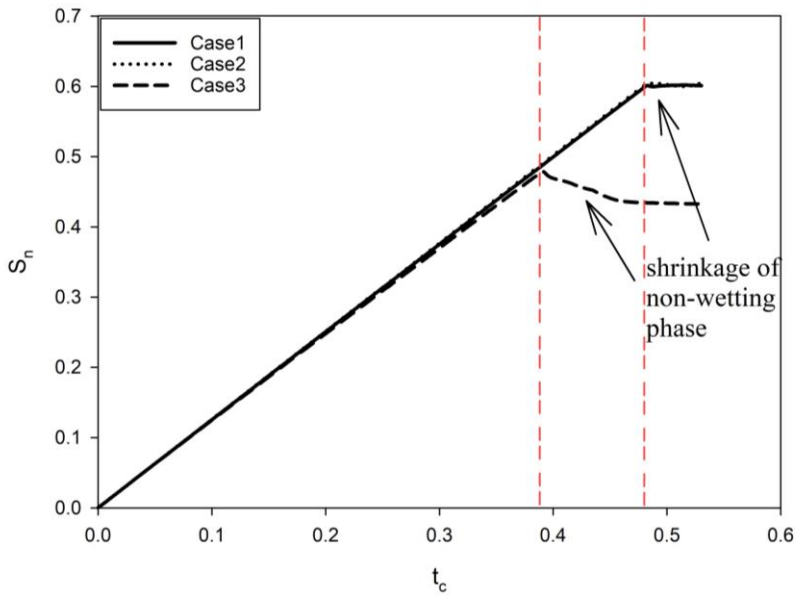

Figure 2.S6 Plot of the non-wetting phase saturation versus the dimensionless time during the drainage process, where the red dashed line shows the breakthrough times for each case. The shrinkage of the non-wetting phase volume due to the capillary end effect is observed shortly after the breakthrough, especially for the Case3 with the lowest inflow velocity.

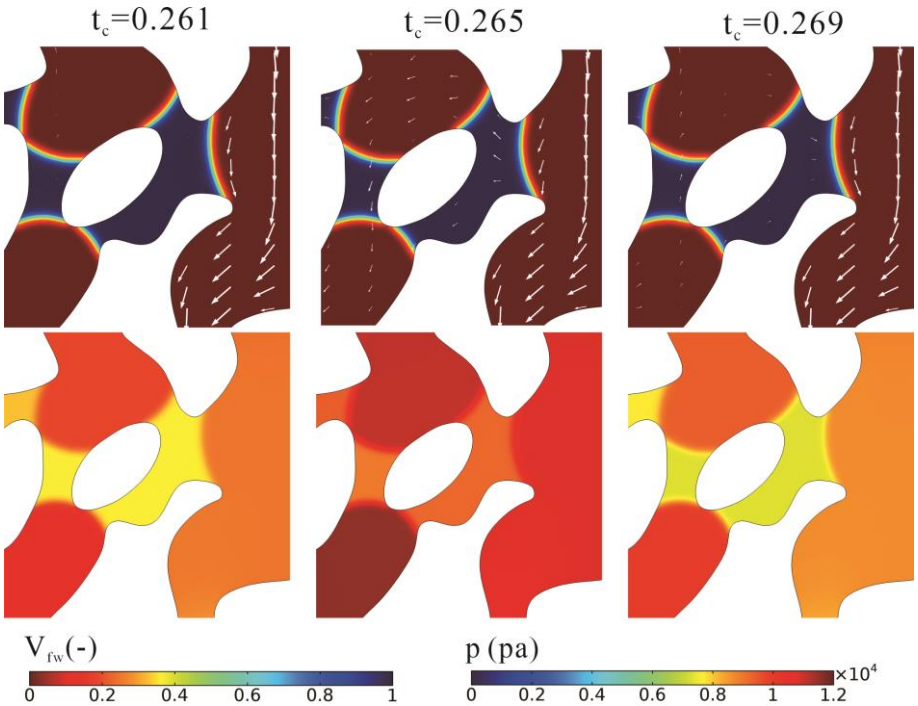

Figure 2.S7 Sketch of local slight motion induced by local pressure change, in a zoom-in region from Case2. The volume fraction of water (top) and corresponding fluid pressures (bottom) are shown at three different times t_c=0.261 t_c=0.265 and t_c=0.269. The white arrows show the direction of the velocity vector, and the length of the arrows is proportional to the natural logarithm of the norm of the velocity vector. During t_c=0.261 to t_c=0.265, a rise of the local pressure triggers a very small movement of the trapped water (towards left). When the pressure drops again at t_c=0.269, the trapped water recedes.

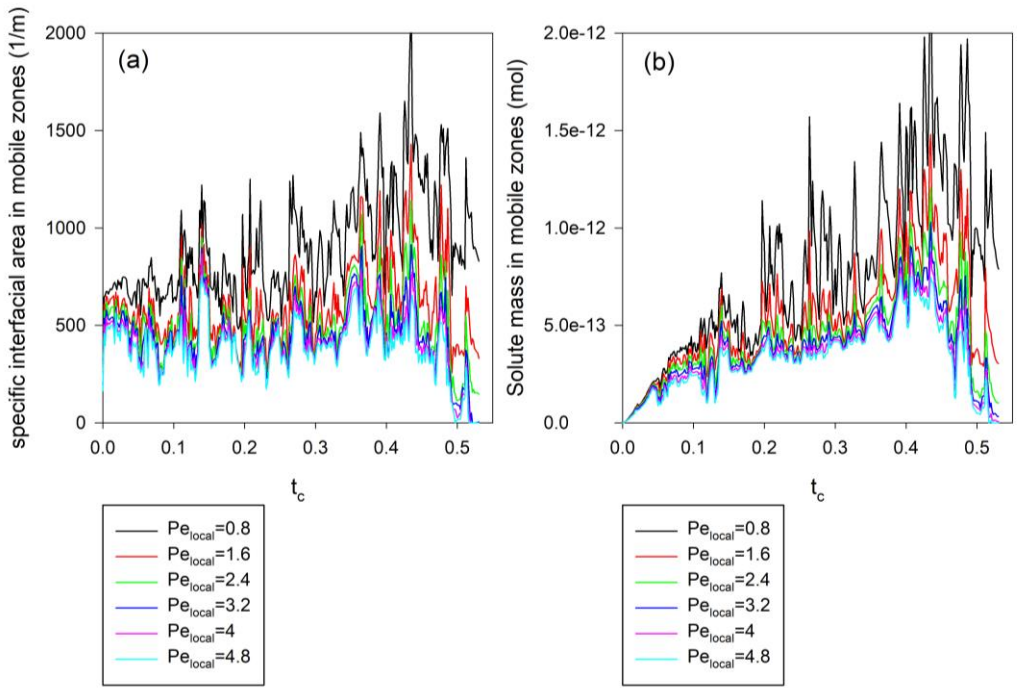

Figure 2.S8 Sensitivity analysis for choosing the threshold local Péclet number for Case2, by quantification of (a) specific interfacial area and (b) solute mass, in the mobile zones of the domain. The threshold Pe_l is swapped at 0.8, 1.6, 2.4, 3.2, 4, 4.8. The quantified results start to converge when Pe_l=2.4.

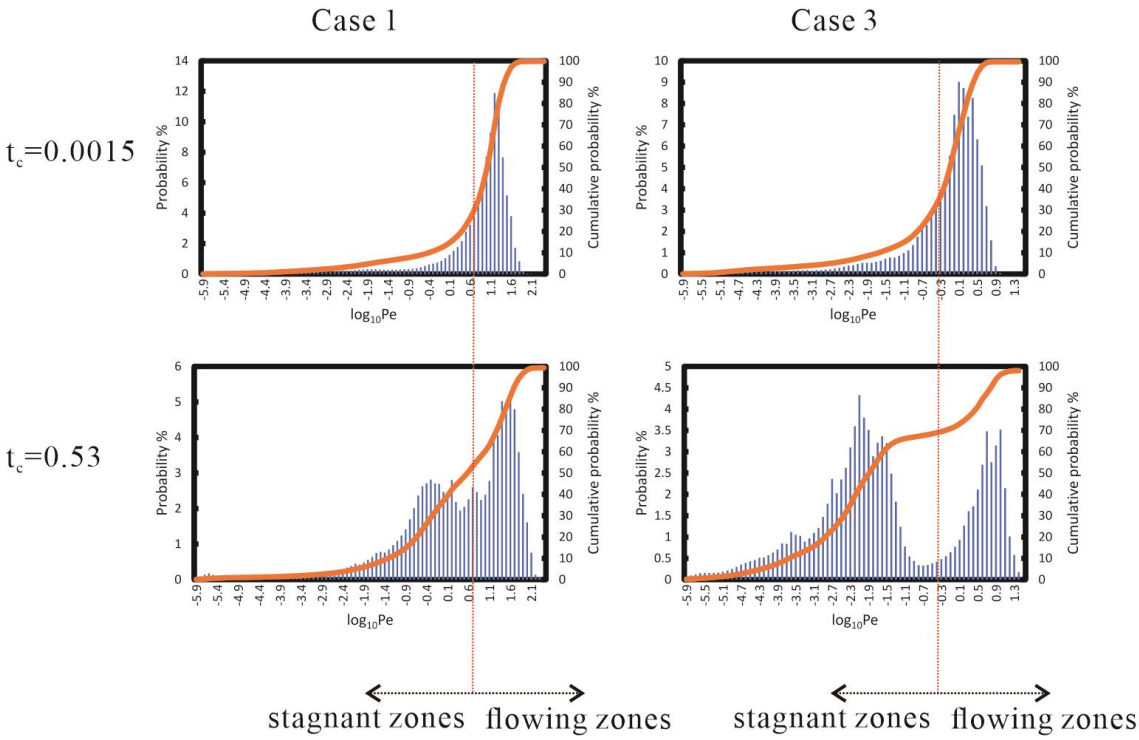

Figure 2.S9 Probability distribution of the local Péclet number for Case 1 and Case 3 at t_c=0.0015 and t_c=0.53. The difference of the probability distributions is shown for single phase of water flow in the domain at the beginning of drainage (t_c=0.0015) and for two-phase flow at the end of drainage (t_c=0.53). The red lines represent the threshold local Péclet number chosen for Case1: Pe_l=4.8 and for Case3: Pe_l=0.48.

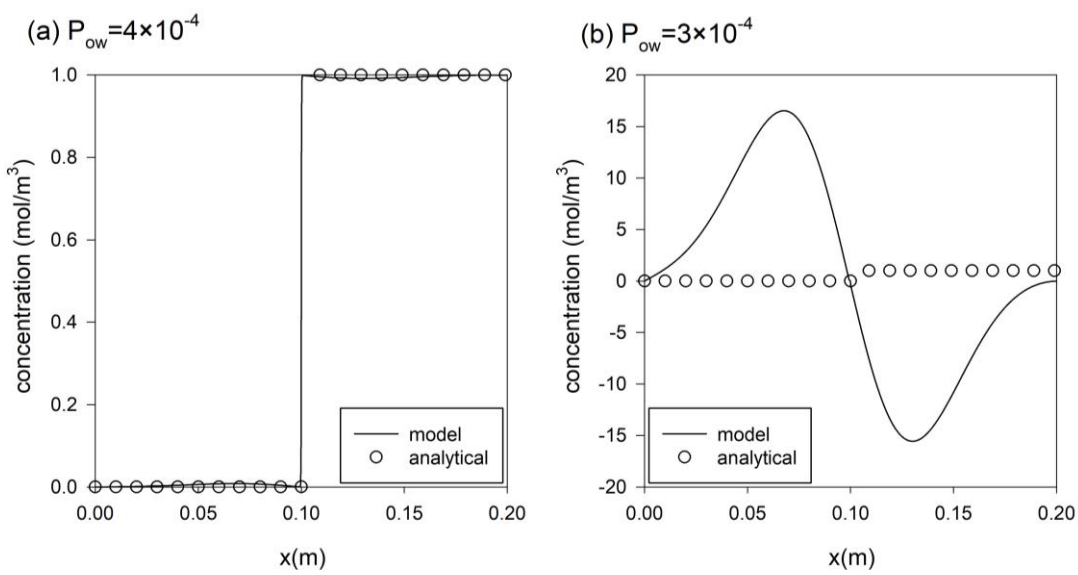

Figure 2.S10 Supplement for verification of section 2.3.1.1. Comparison of concentration profiles of 2-NSA concentration computed analytically and numerically: (at $\varepsilon=1\times10^{-7}$m) for the transient mass transfer at t=0.5s, for $P_{ow}=4\times10^{-4}$, $P_{ow}=3\times10^{-4}$. When $P_{ow}<4\times10^{-4}$, the model come to come unphysical results, which is not fitted to the analytical solution.

2.8 Reference

Akhlaghi Amiri HA, Hamouda AA (2013) Evaluation of level set and phase field methods in modeling two phase flow with viscosity contrast through dual-permeability porous medium. Int J Multiph Flow 52:22–34 . https://doi.org/10.1016/j.ijmultiphaseflow.2012.12.006

Akhlaghi Amiri HA, Hamouda AA (2014) Pore-scale modeling of non-isothermal two phase flow in 2D porous media: Influences of viscosity, capillarity, wettability and heterogeneity. Int J Multiph Flow 61:14–27 . https://doi.org/10.1016/j.ijmultiphaseflow.2014.01.001

Alpak FO, Riviere B, Frank F (2016) A phase-field method for the direct simulation of two-phase flows in pore-scale media using a non-equilibrium wetting boundary condition. Comput Geosci 20:881–908 . https://doi.org/10.1007/s10596-015-9551-2

Armstrong RT, Evseev N, Koroteev D, Berg S (2015) Modeling the velocity field during Haines jumps in porous media. Adv Water Resour 77:57–68 . https://doi.org/10.1016/j.advwatres.2015.01.008

Aussillous P, Quéré D (2000) Quick deposition of a fluid on the wall of a tube. Phys Fluids 12:2367–2371 . https://doi.org/10.1063/1.1289396

Aziz R, Joekar-Niasar V, Martinez-Ferrer P (2018) Pore-scale insights into transport and mixing in steady-state two-phase flow in porous media. International Journal of Multiphase Flow 109, 51–62. https://doi.org/10.1016/j.ijmultiphaseflow.2018.07.006

Aziz R, Joekar-Niasar V, Martínez-Ferrer PJ, Godinez-Brizuela OE, Theodoropoulos C, Mahani H (2019) Novel insights into pore-scale dynamics of wettability alteration during low salinity waterflooding. Scientific Reports 9, 9257. https://doi.org/10.1038/s41598-019-45434-2

Basirat F, Yang Z, Niemi A (2017) Pore-scale modeling of wettability effects on CO2–brine displacement during geological storage. Adv Water Resour 109:181–195 . https://doi.org/10.1016/j.advwatres.2017.09.004

Bird RB (2002) Transport phenomena. Appl Mech Rev 55:R1–R4 . https://doi.org/10.1115/1.1424298

Blunt M, King P (1990) Macroscopic parameters from simulations of pore scale flow. Phys Rev A 42:4780–4787 . https://doi.org/10.1103/PhysRevA.42.4780

Bond WJ, Wierenga PJ (1990) Immobile water during solute transport in unsaturated sand columns. Water Resour Res 26:2475–2481 . https://doi.org/10.1029/WR026i010p02475

Bromly M, Hinz C (2004) Non-Fickian transport in homogeneous unsaturated repacked sand. Water Resour Res 40: . https://doi.org/10.1029/2003WR002579

Brusseau ML, Narter M, Janousek H (2010) Interfacial Partitioning Tracer Test Measurements of Organic-Liquid/Water Interfacial Areas: Application to Soils and the Influence of Surface Roughness. Environ Sci Technol 44:7596–7600 . https://doi.org/10.1021/es101312n

Brusseau ML, Narter M, Schnaar G, Marble J (2009) Measurement and Estimation of Organic-Liquid/Water Interfacial Areas for Several Natural Porous Media. Environ Sci Technol 43:3619–3625 . https://doi.org/10.1021/es8020827

Cahn JW, Hilliard JE (1959) Free Energy of a Nonuniform System. III. Nucleation in a Two-Component Incompressible Fluid. J Chem Phys 31:688–699 . https://doi.org/10.1063/1.1730447

Carslaw HS, Jaeger JC (1959) Conduction of heat in solids

Chen L, Wang M, Kang Q, Tao W (2018) Pore scale study of multiphase multicomponent reactive transport during CO2 dissolution trapping. Adv Water Resour 116:208–218 . https://doi.org/10.1016/j.advwatres.2018.02.018

Chhabra R, Shankar V (eds) (2018) Chapter 6 - Transport Processes in Microfluidic Applications. In: Coulson and Richardson's Chemical Engineering (Seventh Edition). Butterworth-Heinemann, pp 529–546

Culligan KA, Wildenschild D, Christensen BSB, Gray WG, Rivers ML, Tompson AFB (2004) Interfacial area measurements for unsaturated flow through a porous medium. Water Resour Res 40:W12413 . https://doi.org/10.1029/2004WR003278

Dalla E, Hilpert M, Miller CT (2002) Computation of the interfacial area for two-fluid porous medium systems. J Contam Hydrol 56:25–48

Ding H, Spelt PDM (2007) Wetting condition in diffuse interface simulations of contact line motion. Phys Rev E 75:046708 . https://doi.org/10.1103/PhysRevE.75.046708

Ferrari A, Lunati I (2013) Direct numerical simulations of interface dynamics to link capillary pressure and total surface energy. Adv Water Resour 57:19–31 . https://doi.org/10.1016/j.advwatres.2013.03.005

Frank F, Liu C, Alpak FO, Berg S, Riviere B (2018) Direct Numerical Simulation of Flow on Pore-Scale Images Using the Phase-Field Method. SPE J 23:1,833-1,850 . https://doi.org/10.2118/182607-PA

Graveleau M, Soulaine C, Tchelepi HA (2017) Pore-Scale Simulation of Interphase Multicomponent Mass Transfer for Subsurface Flow. Transp Porous Media 120:287–308 . https://doi.org/10.1007/s11242-017-0921-1

Guido S, Villone M (1999) Measurement of Interfacial Tension by Drop Retraction Analysis. J Colloid Interface Sci 209:247–250 . https://doi.org/10.1006/jcis.1998.5818

Haroun Y, Legendre D, Raynal L (2010) Volume of fluid method for interfacial reactive mass transfer: Application to stable liquid film. Chem Eng Sci 65:2896–2909 . https://doi.org/10.1016/j.ces.2010.01.012

Hasan S, Joekar-Niasar V, Karadimitriou NK, Sahimi M (2019) Saturation Dependence of Non-Fickian Transport in Porous Media. Water Resour Res 55:1153–1166 . https://doi.org/10.1029/2018WR023554

Hasan S, Niasar V, Karadimitriou NK, Godinho JRA, Vo NT, An S, Rabbani A, Steeb H (2020) Direct characterization of solute transport in unsaturated porous media using fast X-ray synchrotron microtomography. PNAS 117, 23443–23449. https://doi.org/10.1073/pnas.2011716117

Hassanizadeh SM, Gray WG (1990) Mechanics and thermodynamics of multiphase flow in porous media including interphase boundaries. Adv Water Resour 13:169–186 . https://doi.org/10.1016/0309-1708(90)90040-B

Jacqmin D (1999) Calculation of Two-Phase Navier–Stokes Flows Using Phase-Field Modeling. J Comput Phys 155:96–127 . https://doi.org/10.1006/jcph.1999.6332

Joekar-Niasar V, Hassanizadeh SM, Leijnse A (2008) Insights into the Relationships Among Capillary Pressure, Saturation, Interfacial Area and Relative Permeability Using Pore-Network Modeling. Transp Porous Media 74:201–219 . https://doi.org/10.1007/s11242-007-9191-7

Kang Q, Lichtner PC, Viswanathan HS, Abdel-Fattah AI (2010) Pore Scale Modeling of Reactive Transport Involved in Geologic CO2 Sequestration. Transp Porous Media 82:197–213 . https://doi.org/10.1007/s11242-009-9443-9

Kang Q, Lichtner PC, Zhang D (2006a) Lattice Boltzmann pore-scale model for multicomponent reactive transport in porous media: MULTICOMPONENT REACTIVE TRANSPORT. J Geophys Res Solid Earth 111:n/a-n/a . https://doi.org/10.1029/2005JB003951

Kang Q, Lichtner PC, Zhang D (2006b) Lattice Boltzmann pore-scale model for multicomponent reactive transport in porous media. J Geophys Res Solid Earth 111: . https://doi.org/10.1029/2005JB003951

Karadimitriou NK, Joekar-Niasar V, Babaei M, Shore CA (2016) Critical Role of the Immobile Zone in Non-Fickian Two-Phase Transport: A New Paradigm. Environ Sci Technol 50:4384–4392 . https://doi.org/10.1021/acs.est.5b05947

Karadimitriou NK, Joekar-Niasar V, Brizuela OG (2017) Hydro-dynamic Solute Transport under Two-Phase Flow Conditions. Sci Rep 7:1–7 . https://doi.org/10.1038/s41598-017-06748-1

Keller AA, Blunt MJ, Roberts APV (1997) Micromodel Observation of the Role of Oil Layers in Three-Phase Flow. Transp Porous Media 26:277–297 . https://doi.org/10.1023/A:1006589611884

Khan AU-H, Jury WA (1990) A laboratory study of the dispersion scale effect in column outflow experiments. J Contam Hydrol 5:119–131 . https://doi.org/10.1016/0169-7722(90)90001-W

Liu H, Valocchi AJ, Werth C, Kang Q, Oostrom M (2014) Pore-scale simulation of liquid CO2 displacement of water using a two-phase lattice Boltzmann model. Adv Water Resour 73:144–158 . https://doi.org/10.1016/j.advwatres.2014.07.010

Liu H, Zhang Y, Valocchi AJ (2015) Lattice Boltzmann simulation of immiscible fluid displacement in porous media: Homogeneous versus heterogeneous pore network. Phys Fluids 27:052103 . https://doi.org/10.1063/1.4921611

Maes J, Soulaine C (2018) A new compressive scheme to simulate species transfer across fluid interfaces using the Volume-Of-Fluid method. Chem Eng Sci 190:405–418 . https://doi.org/10.1016/j.ces.2018.06.026

Maes J, Soulaine C, (2020). A unified single-field Volume-of-Fluid-based formulation for multi-component interfacial transfer with local volume changes. Journal of Computational Physics 402, 109024. https://doi.org/10.1016/j.jcp.2019.109024

McDonald K, Carroll KC, Brusseau ML (2016) Comparison of fluid-fluid interfacial areas measured with X-ray microtomography and interfacial partitioning tracer tests for the same samples. Water Resour Res 52:5393–5399 . https://doi.org/10.1002/2016WR018775

Meakin P, Tartakovsky AM (2009) Modeling and simulation of pore-scale multiphase fluid flow and reactive transport in fractured and porous media. Rev Geophys 47: . https://doi.org/10.1029/2008RG000263

Miller CT, Poirier-McNeil MM, Mayer AS (1990) Dissolution of Trapped Nonaqueous Phase Liquids: Mass Transfer Characteristics. Water Resour Res 26:2783–2796 . https://doi.org/10.1029/WR026i011p02783

Montemagno CD, Gray WG (1995) Photoluminescent volumetric imaging: A technique for the exploration of multiphase flow and transport in porous media. Geophys Res Lett 22:425–428 . https://doi.org/10.1029/94GL02697

Peche A, Halisch M, Bogdan Tatomir A, Sauter M (2016) Development of a numerical workflow based on μ-CT imaging for the determination of capillary pressure–saturation-specific interfacial area relationship in 2-phase flow pore-scale porous-media systems: a case study on Heletz sandstone. Solid Earth 7:727–739 . https://doi.org/10.5194/se-7-727-2016

Porter ML, Wildenschild D, Grant G, Gerhard JI (2010) Measurement and prediction of the relationship between capillary pressure, saturation, and interfacial area in a NAPL-water-glass bead system. Water Resour Res 46: . https://doi.org/10.1029/2009WR007786

Prokopev S, Vorobev A, Lyubimova T (2019) Phase-field modeling of an immiscible liquid-liquid displacement in a capillary. Phys. Rev. E 99, 033113. https://doi.org/10.1103/PhysRevE.99.033113

Rallison JM (1984) The Deformation of Small Viscous Drops and Bubbles in Shear Flows. Annu Rev Fluid Mech 16:45–66 . https://doi.org/10.1146/annurev.fl.16.010184.000401

Raoof A, Nick HM, Hassanizadeh SM, Spiers CJ (2013) PoreFlow: A complex pore-network model for simulation of reactive transport in variably saturated porous media. Comput Geosci 61:160–174 . https://doi.org/10.1016/j.cageo.2013.08.005

Reeves PC, Celia MA (1996) A Functional Relationship Between Capillary Pressure, Saturation, and Interfacial Area as Revealed by a Pore-Scale Network Model. Water Resour Res 32:2345 . https://doi.org/10.1029/96WR01105

Rokhforouz MR, Akhlaghi Amiri HA (2017) Phase-field simulation of counter-current spontaneous imbibition in a fractured heterogeneous porous medium. Phys Fluids 29:062104 . https://doi.org/10.1063/1.4985290

Rokhforouz MR, Akhlaghi Amiri HA (2018) Pore-level influence of micro-fracture parameters on visco-capillary behavior of two-phase displacements in porous media. Adv Water Resour 113:260–271 . https://doi.org/10.1016/j.advwatres.2018.01.030

Rokhforouz MR, Akhlaghi Amiri HA (2019) Effects of grain size and shape distribution on pore-scale numerical simulation of two-phase flow in a heterogeneous porous medium. Adv Water Resour 124:84–95 . https://doi.org/10.1016/j.advwatres.2018.12.008

Schaffer M, Maier F, Licha T, Sauter M (2013) A new generation of tracers for the characterization of interfacial areas during supercritical carbon dioxide injections into deep saline aquifers: Kinetic interface-sensitive tracers (KIS tracer). Int J Greenh Gas Control 14:200–208 . https://doi.org/10.1016/j.ijggc.2013.01.020

Scheer D, Class H, Flemisch B (2021) Introduction, in: Scheer, D., Class, H., Flemisch, B. (Eds.), Subsurface Environmental Modelling Between Science and Policy, Advances in Geophysical and Environmental Mechanics and Mathematics. Springer International Publishing, Cham, pp. 1–12. https://doi.org/10.1007/978-3-030-51178-4_1

Smedt FD, Wierenga PJ (1984) Solute Transfer Through Columns of Glass Beads. Water Resour Res 20:225–232. https://doi.org/10.1029/WR020i002p00225

Soares EJ, Thompson RL (2009) Flow regimes for the immiscible liquid–liquid displacement in capillary tubes with complete wetting of the displaced liquid. J. Fluid Mech. 641, 63–84. https://doi.org/10.1017/S0022112009991546

Sun DL, Tao WQ (2010) A coupled volume-of-fluid and level set (VOSET) method for computing incompressible two-phase flows. Int J Heat Mass Transf 53:645–655 . https://doi.org/10.1016/j.ijheatmasstransfer.2009.10.030

Sussman M, Puckett EG (2000) A Coupled Level Set and Volume-of-Fluid Method for Computing 3D and Axisymmetric Incompressible Two-Phase Flows. J Comput Phys 162:301–337 . https://doi.org/10.1006/jcph.2000.6537

Tatomir A, Gao H, Pötzl C, Karadimitriou NK, Licha T, Class H, Helmig R, Sauter M (2020) Estimation of NAPL-Water interfacial areas for unconsolidated porous media by kinetic interface sensitive (KIS) tracers (submitted). Water Resour Res

Tatomir A, Vriendt KD, Zhou D, Gao H, Duschl F, Sun F, Licha T, Sauter M (2018) Kinetic Interface Sensitive Tracers: Experimental Validation in a Two-Phase Flow Column Experiment. A Proof of Concept. Water Resour Res 54:10,223-10,241 . https://doi.org/10.1029/2018WR022621

Tatomir A, Zhou D, Gao H, Dimache A-N, Iancu I, Sauter M (2019) Modelling of kinetic interface sensitive tracers reactive transport in 2D two-phase flow heterogeneous porous media. E3S Web Conf 85:07003 . https://doi.org/10.1051/e3sconf/20198507003

Tatomir AB, Halisch M, Duschl F, Peche A, Wiegand B, Schaffer M, Licha T, Niemi A, Bensabat J, Sauter M (2016a) An integrated core-based analysis for the characterization of flow, transport and mineralogical parameters of the Heletz pilot CO2 storage site reservoir. Int J Greenh Gas Control 48, Part 1:24–43 . https://doi.org/10.1016/j.ijggc.2016.01.030

Tatomir AB, Jyoti A, Sauter M (2016b) Monitoring of CO2 Plume Migration in Deep Saline Formations with Kinetic Interface Sensitive Tracers (A Numerical Modelling Study for the Laboratory). In: Vishal V, Singh TN (eds) Geologic Carbon Sequestration: Understanding Reservoir Behavior. Springer International Publishing, Cham, pp 59–80

Tatomir AB, Schaffer M, Kissinger A, Hommel J, Nuske P, Licha T, Helmig R, Sauter M (2015) Novel approach for modeling kinetic interface-sensitive (KIS) tracers with respect to time-dependent interfacial area change for the optimization of supercritical carbon dioxide injection into deep saline aquifers. Int J Greenh Gas Control 33:145–153 . https://doi.org/10.1016/j.ijggc.2014.11.020

van Genuchten MT, Wierenga PJ (1976) Mass Transfer Studies in Sorbing Porous Media I. Analytical Solutions 1. Soil Sci Soc Am J 40:473–480 . https://doi.org/10.2136/sssaj1976.03615995004000040011x

Wildenschild D, Sheppard AP (2013) X-ray imaging and analysis techniques for quantifying pore-scale structure and processes in subsurface porous medium systems. Adv Water Resour 51:217–246 . https://doi.org/10.1016/j.advwatres.2012.07.018

Yang L, Nieves-Remacha MJ, Jensen KF (2017) Simulations and analysis of multiphase transport and reaction in segmented flow microreactors. Chem Eng Sci 169:106–116 . https://doi.org/10.1016/j.ces.2016.12.003

Yin X, Zarikos I, Karadimitriou NK, Raoof A, Hassanizadeh SM (2019) Direct simulations of two-phase flow experiments of different geometry complexities using Volume-of-Fluid (VOF) method. Chem Eng Sci 195:820–827 . https://doi.org/10.1016/j.ces.2018.10.029

Yiotis AG, Psihogios J, Kainourgiakis ME, Papaioannou A, Stubos AK (2007) A lattice Boltzmann study of viscous coupling effects in immiscible two-phase flow in porous media. Colloids Surf Physicochem Eng Asp 300:35–49 . https://doi.org/10.1016/j.colsurfa.2006.12.045

Yue P, Feng JJ, Liu C, Shen J (2004) A diffuse-interface method for simulating two-phase flows of complex fluids. J Fluid Mech 515:293–317 . https://doi.org/10.1017/S0022112004000370

Yue P, Zhou C, Feng JJ, Ollivier-Gooch CF, Hu HH (2006) Phase-field simulations of interfacial dynamics in viscoelastic fluids using finite elements with adaptive meshing. J Comput Phys 219:47–67 . https://doi.org/10.1016/j.jcp.2006.03.016

3. Effects of surface roughness on the kinetic interface-sensitive tracer transport during drainage processes

H. Gao[1], A. B. Tatomir[1,2], N. K. Karadimitriou[3], H. Steeb[3,4], and M. Sauter[1]

Citation:

Gao H, Tatomir AB, Karadimitriou NK, Steeb H, Sauter M (2021) Effects of surface roughness on the kinetic interface-sensitive tracer transport during drainage processes. Adv Water Resour 157:104044. https://doi.org/10.1016/j.advwatres.2021.104044

[1]Department of Applied Geology, University of Göttingen, 37073, Göttingen, Germany.

[2]Department of Earth Sciences, Uppsala University, 752 36 Uppsala, Sweden.

[3]Institute of Applied Mechanics (CE), University of Stuttgart, 70569 Stuttgart, Germany.

[4]Stuttgart Center for Simulation Technology, Pfaffenwaldring 5a, 70569 Stuttgart, Germany.

Corresponding author: Alexandru Tatomir (alexandru.tatomir@geo.uni-goettingen.de)

Abstract:

Porous media surface roughness strongly influences the transport of solutes during drainage due to the formation of thick water films (capillary condensation) on the surface of the porous medium. For interfacially-reacted, water-based solutes, these water films increase both the solute production at the fluid-fluid interface, due to the increased number of fluid-fluid interfaces, and the loss of the solute due to retention in the water films. This study applied a pore-scale, direct numerical simulation with the phase-field method-based continuous solute transport model to simulate the reactive transport of the kinetic interfacial sensitive tracer. The study is implemented during primary drainage in a 2D slit with rough solid walls, where the fractal geometries of the solid surfaces were generated numerically. The moving interfacial area is found to be changing non-monotonically with the root mean square of surface roughness. With increasing root mean square roughness, the average film thickness increases linearly, whereas the film-associated interfacial area per smooth surface area converges to a value slightly larger than one. The retention of the solute mass produced by the moving meniscus in the water film is observed, and this is described by a film-associated mobile mass retention term. An implicit relation between the mobile interfacial area and the solute mass in flowing zones is found. Finally, it is found that the film-associated mobile mass retention term is linearly related to the root mean square roughness.

Key words: reactive transport, surface roughness, two phase flow, phase field method, fluid-fluid interfacial area, kinetic interface sensitive tracer

3.1 Introduction

The quantification of the magnitude of the Fluid-Fluid Interfacial Area (FIFA) is essential for studying reactive two-phase flow and transport in porous materials (Miller et al. 1990; Hassanizadeh and Gray 1990; Reeves and Celia 1996). The FIFA plays an important role in the interphase mass and energy transfer. This is relevant for many fields of application, such as remediation of nonaqueous phase liquid contaminated sites, geological storage of carbon dioxide, assessment of potential nuclear waste repositories, etc. (Tatomir et al. 2018). For instance, in geological storage of CO_2, the rate of CO_2 dissolution in brine, and the extent of residual trapping are influenced by the magnitude of the FIFA.

FIFA measurement techniques mainly comprise interfacial partitioning tracer tests (IPTT) (Brusseau et al. 2010; McDonald et al. 2016), X-Ray computed micro-tomography (X-RCT) (Culligan et al. 2004; Porter et al. 2010; McDonald et al. 2016) and photo-luminescent volumetric imaging (PVI) (Montemagno and Gray 1995). One limitation of these methods is that they are mainly applied under steady state, or quasi-static conditions (Tatomir et al. 2018). The moving or mobile FIFA is a characteristic feature of transient flow regimes (Gao et al. 2006). The mobile FIFA is of significance in dynamic two-phase flow studies, e.g. colloid transport (El-Farhan et al. 2000; Saiers et al. 2003; Shang et al. 2009), FIFA accumulated contaminant (such as per- and poly-fluoroalkyl substances) migration (Brusseau 2018; Brusseau and Van Glubt 2019), etc. A Kinetic Interface Sensitive tracer test (KIS-TT) was recently developed for tracking the mobile FIFA in dynamic, two-phase, displacement processes (Tatomir et al. 2016; Tatomir et al. 2018; Gao et al. 2021).

3.1.1 Kinetic Interfacial Sensitive tracer

The concept of KIS tracer can be found in detail in Schaffer et al. (2013) and Tatomir et al. (2018). The KIS tracer compound was identified as phenyl naphthalene-2-sulfonate (2-NSAPh) by Schaffer et al. (2013). The 2-NSAPh is a non-polar, hydrolysable, phenolic ester, which dissolves in non-polar liquids, such as supercritical CO_2, or its analogue liquid-phase n-octane (Schaffer et al. 2013), usually acting as the non-wetting phase in natural porous media. With the KIS tracer dissolved, the non-polar liquid is injected into the initially water saturated porous medium and the KIS tracer molecules are adsorbed onto the fluid-fluid interface. In our laboratory experiments by (Tatomir et al. 2018) we used an n-octane-water fluid system (**Figure 3.1**). The adsorption process is assumed to follow Langmuir's isotherm (Schaffer et al. 2013). At the fluid-fluid interface (i.e., n-octane-water) the adsorbed 2-NSAPh molecules undergo an irreversible hydrolysis reaction when in contact with the water molecules.

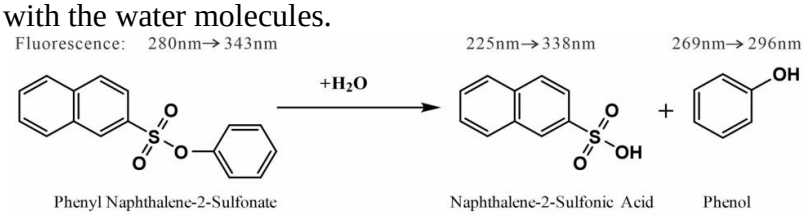

(3.1)

Due to the excess supply of tracer in the non-wetting phase, its concentration at the interface can be assumed to remain constant at its maximum value (Schaffer et al. 2013; Tatomir et al. 2018). Thus, the originally first order hydrolysis reaction can be simplified into a pseudo zero-order reaction, expressed by Eq.(3.2):

$$A_{wn} = \frac{M^k}{R_c \Delta t} \tag{3.2}$$

where R_c (kg·s^{-1}m^{-2}) is the constant reaction rate of the KIS tracer per unit interfacial area, M^k (kg) is the mass of the reaction product k, Δt is the reaction time, and A_{wn} is the FIFA (m^2). The two reaction products are naphthalene-2-sulfonic acid (2-NSA) and phenol, both measurable in the water samples. It has been shown that the 2-NSA is the compound more easily measured in a tracer experiment, because of its enhanced fluorescence (Schaffer et al. 2013; Tatomir et al. 2018). With the 2-NSA characterized by high polarity, being highly hydrophilic and non-adsorptive on either the water-solid interface or the fluid-fluid interfaces, it can be expected to be dispersed rapidly into the bulk water (the wetting phase) away from the fluid-fluid interface (Schaffer et al. 2013; Tatomir et al. 2018). Thus, in a KIS tracer test, we measure the 2-NSA concentration in water, and the obtained reacted 2-NSA mass (M^k) can be used to calculate the interfacial area according to Eq.(3.2). With a constant zero-order reaction at the interface, the study of the 2-NSAPh decay and transport in the non-wetting phase becomes redundant, and the most relevant component of study is the reaction product 2-NSA, present only in the wetting phase (water).

Tatomir et al. (2018) applied the KIS tracer in controlled column experiments with well-characterized porous media composed of glass beads. The KIS tracer was dissolved in n-octane to drain the initially water saturated columns. At the column outlet, samples were collected and measured at defined time intervals to provide the breakthrough curves (BTCs) of fluid volumes, and the 2-NSA concentration in the wetting phase. The experimental data was analyzed by employing a macro-scale, two-phase, reactive transport model with the interfacial reaction of the tracer being specified in the unsaturated zones, where both fluids co-exist (Tatomir et al. 2015; Tatomir et al. 2019). The resulting specific FIFA (defined as the interfacial area per unit bulk

volume of the porous medium) was measured between 500-750m^{-1} for glass beads with a mean diameter of 240μm.

Gao et al. (2021) developed a pore-scale, two-phase, reactive transport model for the KIS tracer. The model was applied to study the effect of stagnant zones on the reacted KIS tracer solute mass, during (n-octane/water) primary drainage in a conceptual two-dimensional porous medium (Gao et al. 2021). The stagnant zones, where solute transport can be assumed to be diffusion-dominated (Karadimitriou et al. 2016; Karadimitriou et al. 2017), and the flowing zones were distinguished by a threshold local Péclet number (Gao et al. 2021). After analyzing the quantified interfacial area and reacted solute mass in the flowing and stagnant zones, Gao et al. (2021) proposed that the 2-NSA mass in the flowing water is mainly produced by the reaction taking place at the moving menisci, and a fraction of solute mass produced by the moving menisci can be retained in the newly formed stagnant zones, due to the capillary entrapment of water during displacement. Since only the reacted solute mass in flowing water is measurable in a KIS tracer test, Gao et al. (2021) concluded that the KIS tracer method selectively measures the mobile part of the interfacial area.

The porous medium employed in the previous numerical study (Gao et al. 2021), and the glass beads used in the previous column experiment (Tatomir et al. 2018), both had smooth surfaces. However, surface roughness is an important property of natural soils and rocks, strongly affecting the fluid-solid interactions in porous media (Jiang et al. 2020). To apply the KIS tracer method on natural porous media systems, the effect of surface roughness on transport of the reacted 2-NSA needs to be understood to be able to assess its influence on the experimental findings.

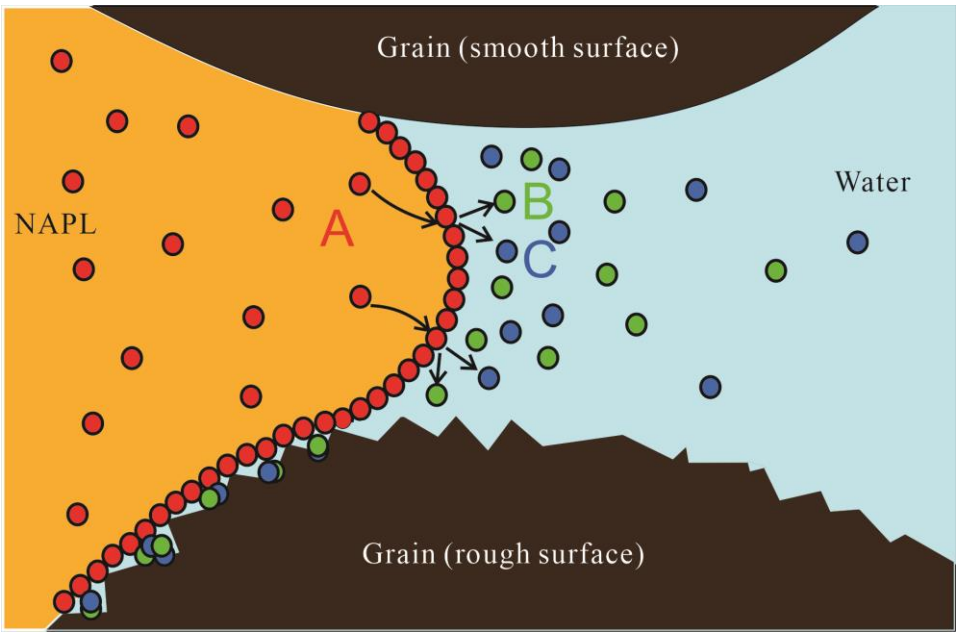

Figure 3.1 Schematic of the KIS tracer reactive transfer process for smooth and rough surfaces (after Gao et al. 2021). A: Phenyl Naphthalene-2-Sulfonate. B: Naphthalene-2-Sulfonic Acid. C: Phenol.

3.1.2 Surface roughness-related effects

Surface roughness can affect two-phase flow in porous media by changing the hydraulic conductivity (Zheng et al. 2015; Ghanbarian et al. 2016; Wang et al. 2016; Yi et al. 2019), the media wettability (AlRatrout et al. 2018; Sari et al. 2020), capillary trapping (Geistlinger et al. 2015; Mehmani et al. 2019; Geistlinger and Zulfiqar 2020; Zulfiqar et al. 2020), the capillary pressure-saturation curve (Tokunaga 2011) and the FIFA (Brusseau et al. 2010; McDonald et al. 2016; Jiang et al. 2020). Based on the above, the advective transport of a solute along with the bulk fluid motion can be assumed to be influenced by the degree of surface roughness. Additionally, the KIS tracer test can get affected by a rough surface via the retention of the reacted solute mass in the water films, as shown in **Figure 3.1**. The water films can form on a rough surface due to both adsorption and capillarity effects (Philip 1978; Kibbey 2013). The adsorbed water film is generally very thin (thickness of a few molecules), with the amount of the solute molecules dissolved being negligible thus it contributing very little to solute diffusion and transport (Tokunaga 2011). In this study we emphasize on the capillary condensed water films (or named surface-associated water by Kibbey (2013)) which can be several orders of magnitude thicker than the adsorbed water films. This study aims at answering the following questions: (1) how is the mobile and immobile interface influenced by the surface roughness; (2) how much solute mass will be retained in the water film coating on a rough solid surface; (3) what is the functional relation between the retained solute mass and surface roughness? The questions above, regarding the effect of the surface roughness on the KIS tracer test, are answered by investigating the KIS tracer transport mechanisms at the pore-scale numerically.

3.1.3 Pore-scale reactive transport modelling

Two phase flow can be simulated with the computational fluid dynamics (CFD) approach, where the Navier-Stokes equations are directly solved in a discretized domain by finite volume, or finite element methods. The interface between two fluids is represented by an indicator function, such as the volume fraction in volume of fluid method (VOF), and the phase variable in the phase-field method (PFM). The simulation of two-phase reactive transport with the CFD method is handled by a continuous species transfer (CST) formulation, first developed in the VOF framework by (Haroun et al. 2010). The CST formulation solves the concentration jump at the interface when a solute solubility is different in the fluids on either side of the interface, by introducing a constant partitioning coefficient (or Henry's constant). Maes and Soulaine (2018) showed that the CST method generates large numerical diffusion in the phase concentration, which leads to the inaccurate simulation of the interphase mass transfer. Therefore, they proposed a new C-CST formulation by adding a compressive term, and this modification managed to significantly reduce the numerical errors (Maes and Soulaine 2018). However, one major disadvantage of the VOF method is that, since the volume fraction is a step function, an accurate curvature and smooth physical quantities near the interface are hard to be obtained (Sun and Tao 2010; Alpak et al. 2016; Basirat et al. 2017). In contrast to the VOF method, PFM with a smooth indicator function can better simulate the curvature and physical quantities at the interface (Akhlaghi Amiri and Hamouda 2013). Besides, PFM is more physically consistent than VOF, because PFM employs thermodynamic principles for the description of the interface (Alpak et al. 2016). Gao et al. (2021) derive the CST formulations based on the PFM, and the new model is labelled as PFM-CST. The tracer's zero-order reaction at the fluid-fluid interface can be directly implemented as a homogenous reaction in the region of the diffusive interface, where the two fluid phases mix (Gao et al. 2021). The PFM-CST model successfully simulates the interfacial reaction and transport of the produced 2-NSA in the KIS tracer test at pore scale (Gao et al. 2021).

3.1.4 Objectives

In this paper, we employ the PFM-CST model to study the effect of grain surface roughness on KIS tracer reaction and transport processes in immiscible two-phase flow in porous media. The fluid system is NAPL-water, specifically liquid n-octane and liquid water. The study domain for the two-phase flow is a simple two-dimensional (2D) slit, within a rectangular domain. The solid surfaces of the slits are formed by rough profiles exhibiting different extents of roughness. With this simplified simulation setup, any hydrodynamic effect caused by the geometrical complexity or tortuosity of the pore structures is avoided, and the solute transport and two-phase flow can be studied in relation to the influence of the surface roughness. We focus on the understanding of how surface roughness can affect the magnitude of the interfacial area and the transported solute mass. The paper is organized as follows: Section 3.2 presents the mathematical and the numerical models employed. In Section 3.3 we outline the details of the model setup, rough surface generation and data processing. The results and discussions are demonstrated in Section 3.4. Finally, Section 3.5 lists the main conclusions and findings.

3.2 Mathematical model

3.2.1 Phase-Field Method

The theory for the PFM is described in detail in e.g., (Jacqmin 1999; Badalassi et al. 2003; Yue et al. 2004; Alpak et al. 2016). In this section, we briefly review the equations that are implemented in the model according to Yue et al. (2004). The interface is treated as a thin diffusive layer formed by the mixture of two fluids, and a smoothly changing phase variable ϕ is introduced to describe the composition of the fluid mixture at the interface, while ϕ remains constant in the bulk fluid phases. A fundamental concept of the PFM is that the free energy density can be expressed as a function of the phase variable, and its gradient (Jacqmin 1999). The free energy density (f_{mix}) (J/m^3) for isothermal mixing of two fluids can be expressed in the Ginzburg-Landau form (Eq.(3.4)) (Yue et al. 2006):

$$f_{mix}(\phi, \nabla\phi) = \frac{1}{2}\lambda|\nabla\phi|^2 + \frac{\lambda}{4\varepsilon^2}(\phi^2 - 1)^2 \tag{3.3}$$

where λ (N) is the magnitude of the mixing energy and ε (m) is the capillary width. The free energy density is made up of two components: the first component accounts for the surface energy, and the second component is the bulk energy (Basirat et al. 2017). The bulk energy describes the two-phase immiscibility, and it involves two minima corresponding to the two stable phases of the (wetting and non-wetting) fluids (Badalassi et al. 2003). The chemical potential G (J/m^3) can be defined as the variation of the free energy with respect to the dimensionless phase variable (Eq.3.4):

$$G = \frac{\delta \int_{\Omega} f_{mix}\, dx}{\delta\phi} = -\lambda\nabla^2\phi + \frac{\lambda}{\varepsilon^2}\phi(\phi^2 - 1) \tag{3.4}$$

where Ω is the region of space occupied by the two fluid phases. The interfacial tension σ (N/m) is the total free energy at the interface per unit area of the interface. With the diffuse interface at equilibrium, the interfacial tension is related to the capillary width and the mixing energy density, through Eq.(3.5) (Yue et al. 2004):

$$\sigma = \frac{2\sqrt{2}\lambda}{3\varepsilon} \tag{3.5}$$

Fluid mass conservation is governed by the Cahn-Hilliard equation (Eq.(3.6), which assumes that the diffusive fluid flux is proportional to the gradient of the chemical potential (Cahn and Hilliard 1959):

$$\frac{\partial \phi}{\partial t} + \mathbf{u} \cdot \nabla \phi = \nabla \cdot (\gamma \nabla G) \tag{3.6}$$

where **u** is the fluid velocity vector, and γ (m^3s/kg) is the mobility which is a function of the capillary width and a tuning factor: $\gamma = \chi \varepsilon^2$. The tuning factor χ (m·s/kg) is called the characteristic mobility, which governs the relaxation time of the interface (Akhlaghi Amiri and Hamouda 2013). The characteristic mobility χ needs to be large enough to maintain a constant thickness of the interface, but small enough not to dampen the flow (Jacqmin 1999).

3.2.2 Two phase flow dynamics

Momentum conservation for an incompressible fluid is governed by the Navier-Stokes equation (Eq.3.7), where the surface tension is considered as a body force (Yue et al. 2006):

$$\rho \left(\frac{\partial \mathbf{u}}{\partial t} + \mathbf{u} \cdot \nabla \mathbf{u} \right) = \nabla \cdot [-p\mathbf{I} + \mu(\nabla \mathbf{u} + (\nabla \mathbf{u})^{\mathrm{T}})] + G \nabla \phi \tag{3.7}$$

$$\nabla \cdot \mathbf{u} = 0 \tag{3.8}$$

where **I** is the second order identity tensor, p is pressure, and ρ and μ are respectively the density and viscosity of the mixture (non-wetting and wetting fluid) according to the volume fraction of the fluids $V_{f,\alpha}$ (α=w, nw):

$$\rho = \rho_w V_{f,w} + \rho_{nw} V_{f,nw} \text{ and } \mu = \mu_w V_{f,w} + \mu_{nw} V_{f,nw} \tag{3.9}$$

where subscripts w and nw indicate the wetting and non-wetting phase, respectively. It is worth noting that for simplicity we apply an incompressible formalism of the Navier-Stokes equation which is slightly different than the quasi-compressible model of Lowengrub and Truskinovsky (1998). This can be applied as long as the interface thickness is small enough, so that the results remain unaffected (Lowengrub and Truskinovsky, 1998; Zhou et al. 2010). The volume fraction of the fluids can be obtained as:

$$V_{f,w} = (1 - \phi)/2 \text{ and } V_{f,nw} = (1 + \phi)/2 \tag{3.10}$$

At the grain surfaces, a no-slip boundary is applied, which implies that **u**=**0** in Eq.(3.7) for solid wall boundaries. The wetting condition on the solid wall is expressed by:

$$\mathbf{n} \cdot \nabla \phi = \cos\theta_w |\nabla \phi| \tag{3.11}$$

where **n** is the (outward) normal vector to the wall and θ_w is the contact angle.

3.2.3 Reactive transport

The reactive transport model, based on the phase-field method, is developed in Gao et al. (2021). The major mechanisms to be considered regarding the KIS tracer transport are advection, molecular diffusion, partitioning (result from its solubility) and interfacial reaction. Here, we briefly review the derivation and major equations implemented in the model. The fluid mass conservation equation is first rewritten with the volume fraction of phases. By incorporating Eq.(3.10) into Eq.(3.6), as $\nabla \cdot \mathbf{u} = 0$, one obtains:

$$\begin{aligned} \frac{\partial V_{f,w}}{\partial t} + \nabla \cdot \left(\mathbf{u} V_{f,w} + 0.5\gamma \nabla G \right) = 0 \\ \frac{\partial V_{f,nw}}{\partial t} + \nabla \cdot \left(\mathbf{u} V_{f,nw} - 0.5\gamma \nabla G \right) = 0 \end{aligned} \tag{3.12}$$

For the solute k dissolving in fluid phase $\alpha$with the mass concentration of $c_{a,k}$, the solute mass conservation equation writes:

$$\frac{\partial(V_{f,w}c_{w,k})}{\partial t} + \nabla\cdot(\mathbf{u}V_{f,w}c_{w,k} + 0.5\gamma\nabla G c_{w,k}) = 0$$
$$\frac{\partial(V_{f,nw}c_{nw,k})}{\partial t} + \nabla\cdot(\mathbf{u}V_{f,nw}c_{nw,k} - 0.5\gamma\nabla G c_{nw,k}) = 0 \tag{3.13}$$

where only solute advection is included in this step, which is the dominant transport process due to the bulk fluid motion. The bulk fluid motion consists of two parts: the advective flux and the diffusive flux at the interface, due to the gradient of the chemical potential. To obtain the single-field formulation of the 2-NSA concentration for both phases in the entire domain, we define the global concentration as:

$$c_k = V_{f,w}c_{w,k} + V_{f,nw}c_{nw,k} \tag{3.14}$$

Thus, the sum of the mass conservation Eq.(3.13) for solute *k* in both phases writes:

$$\frac{\partial c_k}{\partial t} + \nabla\cdot\left[\mathbf{u}c_k + 0.5\gamma\nabla G\left(c_{w,k} - c_{nw,k}\right)\right] = 0 \tag{3.15}$$

Then, the mechanisms of molecular diffusion and interfacial reaction are considered by adding a diffusion term and a source term into the equation:

$$\frac{\partial c_k}{\partial t} + \nabla\cdot\left[\mathbf{u}c_k + 0.5\gamma\nabla G\left(c_{w,k} - c_{nw,k}\right)\right] - \nabla\cdot\mathbf{J}_k + R_c^{dif} = 0 \tag{3.16}$$

where the solute molecular diffusion flux for the mixture is defined as (Haroun et al. 2010):

$$\mathbf{J}_k = D_k(V_{f,w}\nabla c_{w,k} + V_{f,nw}\nabla c_{nw,k}) = D_k[\nabla c_k - \left(c_{w,k} - c_{nw,k}\right)\nabla V_{f,w}] \tag{3.17}$$

As $V_{f,w} + V_{f,nw} = 1$, here only $V_{f,w}$ is used in the expression, and the molecular diffusion coefficient is expressed as $D_k = V_{f,w}D_{w,k} + V_{f,nw}D_{nw,k}$. The diffusion term Eq.(3.17) indicates two fluxes: a diffusive flux driven by concentration gradient and an additional solubility flux resulting from the solubility law. This solubility flux is in the direction normal to the interface, which governs the distribution of the species between the two phases. The magnitude of the solubility flux is determined by the partitioning coefficient of the solute in two phase fluids. The partitioning coefficient is expressed as the concentration ratio of the solute in the two-phase fluids system at equilibrium.

$$P_{ow,k} = \frac{c_{nw,k}}{c_{w,k}} \tag{3.18}$$

where $c_{nw,k}$ and $c_{w,k}$ are the concentration of the product (2-NSA) in the non-wetting phase and the wetting phase respectively, and $P_{ow,k}$ is the partition coefficient. With the definition of Eq.(3.18) and Eq.(3.14), one obtains:

$$c_{w,k} - c_{nw,k} = \frac{c_k(1 - P_{ow,k})}{V_{f,w} + P_{ow,k}(1 - V_{f,w})} \tag{3.19}$$

Thus, by incorporating Eq.(3.19) into Eq.(3.16), the final governing equation for global concentration of solute *k* is reorganized:

$$\frac{\partial c_k}{\partial t} + \nabla\cdot[\mathbf{u}c_k + 0.5\gamma\nabla G\frac{c_k\left(1 - P_{ow,k}\right)}{V_{f,w} + P_{ow.k}\left(1 - V_{f,w}\right)}]$$
$$-\nabla\cdot[D_k(\nabla c_k - \nabla V_{f,w}\frac{c_k\left(1 - P_{ow,k}\right)}{V_{f,w} + P_{ow,k}\left(1 - V_{f,w}\right)})] + R_c^{dif} = 0 \tag{3.20}$$

where R_c^{dif} (mol·s^{-1}m^{-3}) is the zero-order interfacial reaction of the KIS tracer, which is assumed in the model as a homogeneous reaction taking place at the diffusive interface. The interfacial reaction region is taken with $V_{f,w} \in [0.05,0.95]$, whose thickness is b_{wn}=4.1641ε (Yue et al. 2004).

With the constant interface thickness, the reaction rate per unit interfacial region for the model can be calculated as:

$$R_c^{dif} = \frac{R_c}{b_{wn}} \quad \text{for } V_{f,w} \in [0.05, 0.95]$$
$$R_c^{dif} = 0 \quad \text{for } V_{f,w} \in [0, 0.05) \cup (0.95, 1] \tag{3.21}$$

where R_c is the experimentally determined tracer reaction rate per unit interfacial area (Tatomir et al. 2018).

3.2.4 Numerical implementation

The governing system comprises four fundamental variables and four governing equations. The coupled governing equations of the Navier-Stokes equation (Eq.3.7 and Eq.3.8) and the Cahn-Hilliard equation (Eq.3.6) are solved for fluid velocity (**u**), pressure (p) and the phase variable (ϕ). The governing reactive transport equation (Eq.3.20) is solved for the solute concentration (c_k). The model is implemented into COMSOL Multiphysics™, a software for solving of partial differential equations, employing the Finite Element method for spatial discretization (Akhlaghi Amiri and Hamouda 2013; Tatomir et al. 2018). The partial differential equations are solved by the linear solver PARDISO. The Backward Euler method is used to solve the time stepping. The initial time step and maximum time steps are controlled to be small enough in order to avoid a singularity. The mesh is generated in COMSOL with triangular elements, applying the advancing front algorithm for the tessellation. The computations were performed on a single CPU with 8 cores, operating at 4.3 GHz, and 128 GB RAM.

3.3 Numerical details

The details of the model setup are shown in section 3.3.1. The method to generate the rough surface is demonstrated in section 3.3.2. The data treatment to obtain the interfacial area and solute mass are shown in section 3.3.3.

3.3.1 Model setups

We assume a 2D rectangular domain, which can be considered as a slit or straight throat in porous media. The whole domain measures 400 μm×50 μm in size, representing half of the slit. The domain consists of a laterally extensive small rectangle (x<5μm) with the left side for the injection of the non-wetting fluid and the flow channel, shown in **Figure 3.2**(a). The upper side of the domain is considered as a symmetry (free slip) boundary, representing the center line of the channel, and the lower boundary is the rough solid surface. The right-hand side of the domain is the outlet. The non-wetting fluid applied here is n-octane according to the KIS tracer experiments by Tatomir et al. (2018). The channel is initially fully saturated with water, and the small rectangle on the left side is initially saturated with n-octane. Thus, the initial position of the interface is determined, which is necessary for numerical stability. At t=0, n-octane with dissolved KIS tracer is injected from the left boundary at a constant velocity of u_{in}=0.01 m/s. To avoid boundary effects at the outlet, we take the line x=300 μm as the fictive outlet, and thus the study domain is within the region of 5 μm<x<300 μm. The relevant properties of the non-wetting fluid (n-octane) are ρ_{octane}=703 kg/m^3 and μ_{octane}=0.54×10^{-3} Pa·s, and the interfacial tension for n-octane/water is σ=0.0504 N/m. The contact angle between the interface and the solid surface is assumed to be θ_w=45°. The initial solute concentration at the inlet is zero, and the solute is only produced from the interfacial reaction according to the theory of the KIS tracer. The zero-order reaction rate is assumed to be R_c^{dif}=1 mol/m^{-3}s. The partition coefficient of the solute is P_{ow}=0.01. The molecular

diffusion coefficient is assumed to be D_k=5×10^{-8} m^2/s. The domain is discretized with triangular elements with a side length of h=5×10^{-7} m. Two layers of mesh on the solid wall are further refined with the thickness of 1.25×10^{-7} m, as shown in **Figure 3.2**(b). The capillary width is $\varepsilon=h$, and the characteristic mobility is χ=10 m·s/kg.

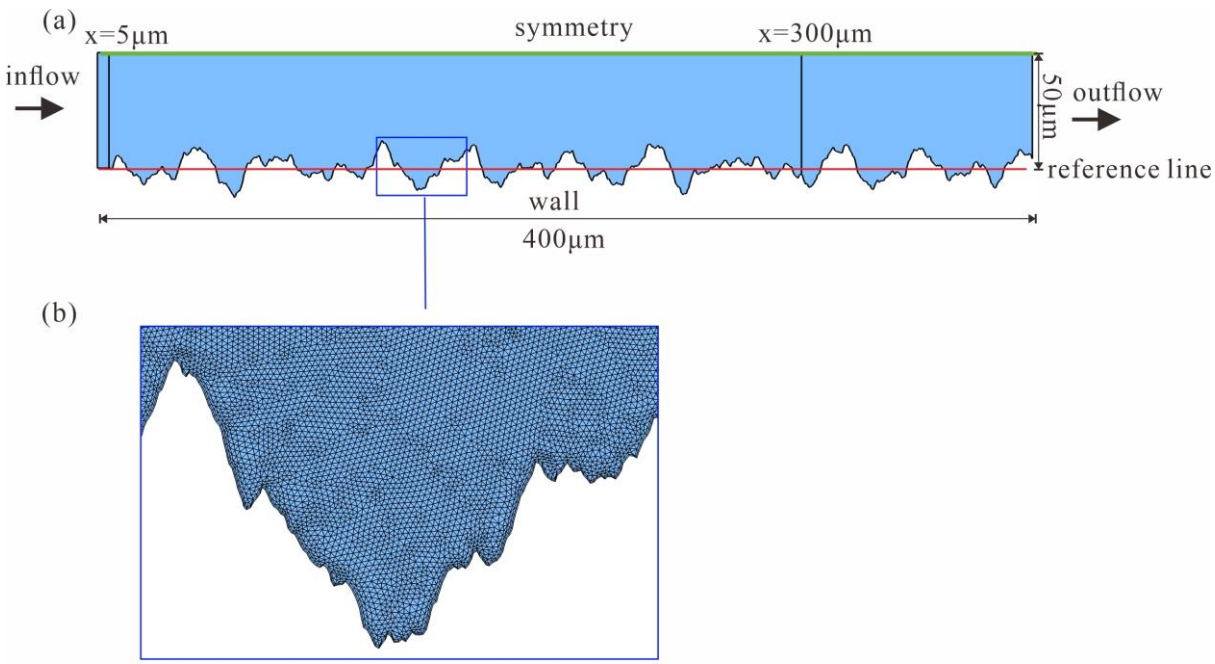

Figure 3.2 Geometry of the porous medium and boundary conditions (pore space in blue color) in subfigure (a). The mesh for a sub-region of the domain is shown in subfigure (b).

3.3.2 Construction of the rough surface

Numerous researches show that many rough surfaces from natural geological materials follow fractal geometries (Brown and Scholz 1985; Power and Tullis 1991; Schmittbuhl et al. 1993; Renard et al. 2013). This means that the subsections of the surface are statistically identical to the entire profile when magnified by a scaling factor for each direction (Deng et al. 2018). The surface is considered self-similar if the scaling factors for each direction are the same, and the fractal dimension for self-similar surface is close to one (Power and Tullis 1991). If the scaling factors for each direction are different, the surface is considered self-affine, and changing of the roughness with respect to the scale is described by a Hurst exponent (Renard et al. 2004). In this study, the 2D fractal rough surfaces are generated numerically using the method proposed in (Power and Tullis 1991; Deng et al. 2018). Following (Deng et al. 2018), we generated self-similar roughness profiles by overlapping a series of sinusoidal waves of random phases, with the same amplitude-to-wavelength ratio and discrete frequencies that occurred in geometric progression.

$$y = \sum_i a_i \sin\left[f_i(x - x_{i,0})\right] \tag{3.22}$$

and

$$f_i = \frac{2\pi}{W_{max} r_f^{i-1}} \tag{3.23}$$

where a_i is the amplitude, f_i is the wavenumber, $x_{i,0}$ is the phase, W_{max} is the maximum wavelength, and r_f^{i-1} is the ratio of the geometric progression. One example of the generated surface is shown in **Figure 3.2**(a). The maximum wavelength is fixed as 40μm, and each rough surface is the sum of 20 sinusoidal waves. Then, the rough surface profile is determined with the use of several parameters, including the amplitude-to-wavelength ratio (a/W), the ratio (r_f) of the geometric sequence of frequencies, and the random phases of the sinusoidal waves. In total, 24 surfaces are generated with different parameters as shown in **Table 3.1**.

The roughness of the surface can be quantified by numerous statistical factors, which are comprehensively listed in Wang et al. (2016). In this study, the roughness is mainly characterized with the root mean square roughness, which well represents the changes in elevation of the surfaces (Kibbey 2013; Renard et al. 2013). The root-mean-square roughness (R_{rms}) can be calculated as:

$$R_{rms} = \sqrt{\frac{1}{n}\sum_{j=1}^{n}(y_j - y_r)^2} \tag{3.24}$$

where y_j is the height of the points j on the rough surface, and y_r is height of the reference smooth surface. Besides, the roughness is also quantified as an area factor, as the ratio of the actual surface area to the geometric smooth area (Zheng et al. 2015; Jiang et al. 2020). The area factor (R_a) can be calculated as:

$$R_a = \frac{A_t}{A_s} \tag{3.25}$$

where A_t is the rough surface area and A_s the geometrical smooth surface area.

Table 3.1 Parameters of the smooth surface (Surface 1) and the rough surfaces (Surface 2 to Surface 24).

	a/W	r_f	R_{rms} (μm)	R_a
Surface 1	/	/	0	1
Surface 2	0.025	0.7	0.968	1.082
Surface 3	0.025	0.9	1.736	1.116
Surface 4	0.05	0.7	2.01	1.276
Surface 5	0.05	0.9	3.392	1.373
Surface 6	0.075	0.7	3.001	1.528
Surface 7	0.075	0.9	5.069	1.66
Surface 8	0.1	0.7	3.992	1.794
Surface 9	0.1	0.9	6.627	2.044
Surface 10	0.125	0.7	4.926	2.101
Surface 11	0.125	0.9	7.795	2.291
Surface 12	0.15	0.7	6.044	2.39
Surface 13	0.15	0.9	9.915	2.82
Surface 14	0.175	0.7	8.947	3.338
Surface 15	0.175	0.9	10.986	3.028
Surface 16	0.2	0.7	8.184	3.042
Surface 17	0.225	0.7	9.065	3.337
Surface 18	0.25	0.7	9.789	3.695
Surface 19	0.275	0.7	10.614	3.975

Surface 20	0.3	0.7	11.648	4.298
Surface 21	0.325	0.7	11.677	4.353
Surface 22	0.35	0.7	14.266	4.999
Surface 23	0.375	0.7	14.669	5.325
Surface 24	0.4	0.7	15.806	5.608

3.3.3 Data treatment

The data for the interfacial area and solute mass are obtained from the simulation results. The diffusive interfacial area is converted into a sharp interfacial area (in length for 2D system). The diffuse interfacial area (A_{wn}^{dif}) and the sharp interfacial area (A_{wn}) can be calculated with Eq.(3.27).

$$A_{wn}^{dif} = \int_{V_v} \delta \, dV \quad \text{and} \quad A_{wn} = \frac{A_{wn}^{dif}}{b_{wn}} \tag{3.26}$$

where V_v is the void space of the study domain at 5 μm<x<300 μm, b_{wn} is the thickness of the diffusive interface b_{wn}=4.1641ε according to section 2.3, and δ is the function indicating the diffusive interfacial region.

$$\begin{aligned} \delta &= 1 \quad for\ V_{f,w} \in [0.05, 0.95] \\ \delta &= 0 \quad for\ V_{f,w} \in [0,0.05) \cup (0.95,1] \end{aligned} \tag{3.27}$$

The solute mass in the domain can be quantified with Eq.(3.28).

$$M_{domain} = \int_{V_v} c_k dV \tag{3.28}$$

The accumulated solute mass pass through the outlet can be quantified with Eq.(3.29).

$$M_{outlet} = \int_{t_0}^{t} \int_{L_{outlet}} u_n c_k dL \, dt \tag{3.29}$$

where u_n is magnitude of the velocity normal to the outlet. The mobile and immobile interfaces and the solute mass are separately calculated for the mobile and immobile zones. The mobile and immobile zones are distinguished by the threshold local Péclet number, which is demonstrated in Section 3.4.1.

3.4 Results and discussion

In section 3.4.1, we distinguish between mobile and immobile zones. As the source of solute production, the interfacial area is studied first. The average mobile interfacial area during drainage is shown in section 3.4.2, and the results for the film-related interfaces and the water film volume per surface area in section 4.3. Then, the reactive transport of the solute is studied. The retention of the reacted solute mass in the water films is presented in section 3.4.4. The relation between the mobile interfacial area and the solute mass is explicitly formulated by data fitting with the addition of a film-associated mobile mass retention term, in section 3.4.5. Finally, the relation between the film-associated mobile mass retention term and the surface roughness is shown in section 3.4.6.

3.4.1 Identification of mobile and immobile zones

The water films are characterized with very low velocities and belong to the stagnant zones, where solute transport is dominated by diffusion (small Péclet number). Thus, a threshold local Péclet number is chosen to differentiate the film associated interface and the solute mass from those in the flowing regions (Aziz et al. 2018). The local Péclet number can be calculated as $Pe = \|\mathbf{u}\| * L_c/D_k$, where $\mathbf{u}$ is the velocity, L_c is the characteristic length, equal to the length of the domain

L_c=0.4 mm, and D_k is the diffusion coefficient. The probability distribution of the local Péclet number after drainage for a sample surface (Surface10 from **Table 1**) is shown in **Figure 3.3** as an example. The probability of the local Péclet number shows a bimodal distribution after drainage. The first peak on the left-hand side indicates the stagnant regions, and the second peak indicates the flowing regions. The profile of the local Péclet number for the slit is shown in the inserted figure, with the local Péclet number plotted in grey scale. The troughs and grooves (in black) on the rough surface belong to the stagnant regions and are mainly occupied by water films. We choose the threshold local Péclet number ($\log_{10}Pe$=1.2) between two peaks, so that the flowing regions and stagnant regions are identified.

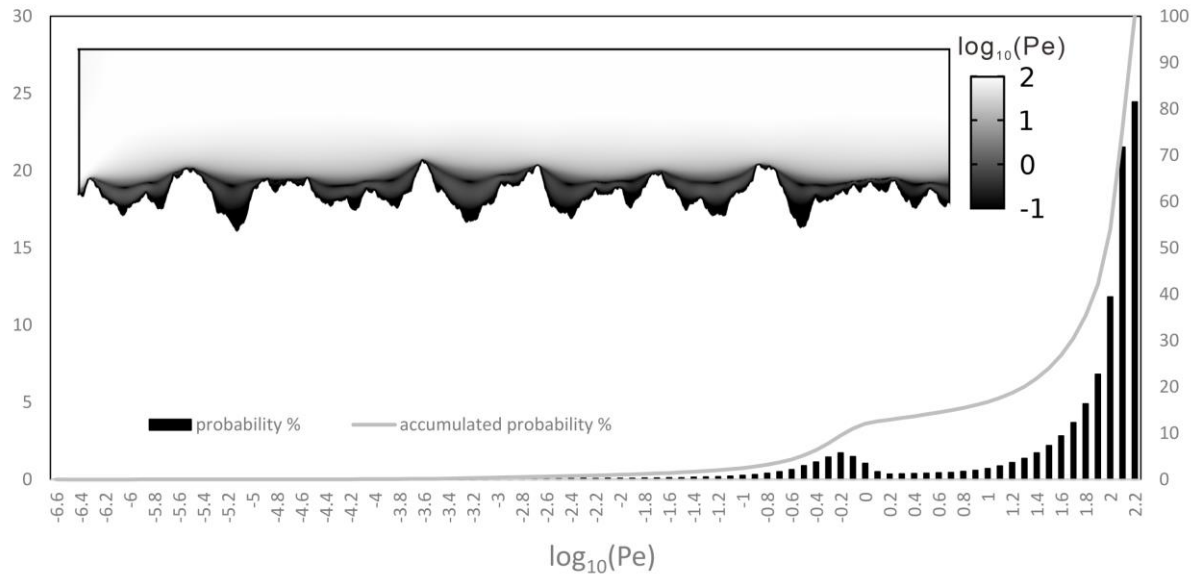

Figure 3.3 Plot of the probability distribution of the local Péclet number for Surface10 after drainage (t=0.033 s) as an example. The inserted figure shows the profile of the local Péclet number for the slit.

3.4.2 Mobile interfacial area

The mobile interfacial area is affected by surface roughness. For the smooth surface, the contact point is moving continuously during drainage, and the mobile interfacial area remains constant. The evolution of the moving menisci on a rough surface is shown in the inserted figure on top of **Figure 3.4**(b). When the contact point meets one peak of the rough surface, it can almost settle for several time steps, during which the moving meniscus keeps bursting. Until the meniscus touches the next peak, it splits into two parts. One part keeps moving forward to the next peak and the other part becomes the immobile interface. Thus, the mobile interfacial area for the case of a rough surface fluctuates during drainage, as shown in **Figure 3.4**(a). The process can be considered as Haines jump, where the fluid pressure fluctuates (Haines 1930). The non-wetting phase pressure increases when the moving meniscus touches a peak, and decreases during bursting of the meniscus. The time-averaged mobile interfacial area from all simulations is plotted in **Figure 3.4**(b). The mobile interfacial area for rough surfaces is larger than that from a smooth surface, because of the bursting process explained above. Additionally, rougher surfaces with higher R_{rms} show a decrease in mobile interfacial area. This can be explained by the flowing region being decreased and the

effective flow channel becoming narrower. Overall, the roughness has a non-monotonic effect on the mobile interfacial area, as shown in **Figure 3.4**(b).

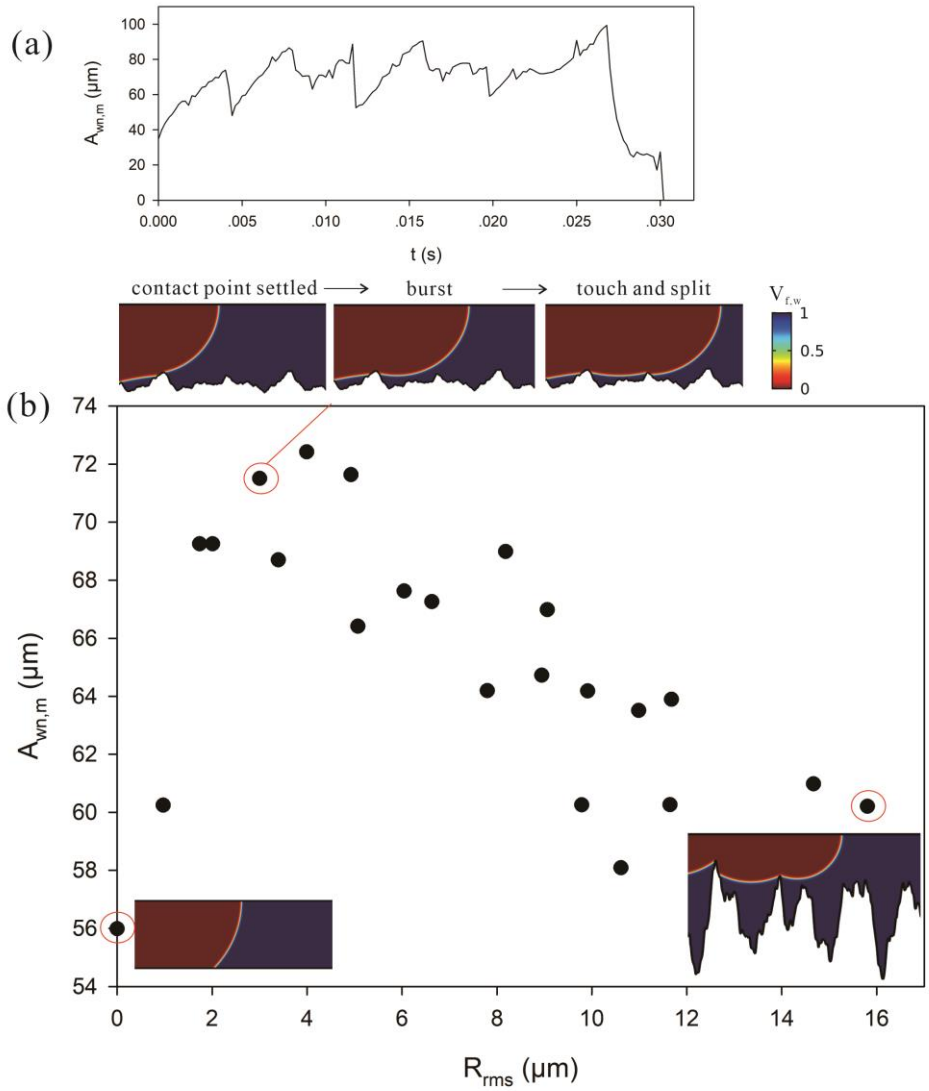

Figure 3.4 Plot of (a) mobile interfacial area during the drainage process for the rough surface at R_{rms}=3 μm and (b) the averaged mobile interfacial area versus the root mean square roughness from all simulations. The inserted figures in subfigure (b) show the configurations of the moving menisci from three simulations at different R_{rms}. The inserted figures on top show the evolution of the moving menisci for the rough surface (R_{rms}=3 μm). The inserted figure at bottom left is for the smooth surface (R_{rms}=0), and the inserted figure at bottom right is for the roughest surface (R_{rms}=15.8 μm).

3.4.3 Immobile interfacial area and deposited water volume

After drainage, the film-induced interfacial area and the deposited water volume can be calculated from the profile of the domain. The film-associated interfacial area and deposited water volume per smooth surface area from all simulations is plotted in **Figure 3.5**. When R_{rms}<3 μm (R_a<1.3),

the capillary condensed water film partially covers the solid surface (one example surface shown in **Figure 3.5**(c) and the immobile interfacial area increases fast with increasing roughness, as shown in **Figure 3.5**(a). When R_{rms}>3 μm (R_a>1.3), the immobile interfacial area can hardly increase, because the capillary condensed water films cover most of the solid (one example surface shown in **Figure 3.5**(d), and any further increase of roughness does not affect the fluid-fluid interfacial area. The immobile interfacial area per smooth surface area converges to a value slightly larger than 1. This means that the real film-associated interfacial can be better approximated by the smooth surface area rather than the true solid surface area, because the fluid-fluid interface is prevented from conforming to the rough solid surface by the thick water film, with its configurations governed by the capillary forces. This is in good agreement with (Kibbey 2013). Besides, the deposited water volume per smooth surface area, or called averaged film thickness, increases linearly with higher R_{rms}, as shown in **Figure 3.5**(b). This is because the troughs and grooves are generally deeper for higher R_{rms}, with more space holding more water due to the capillary forces. This is also in good agreement with Kibbey (2013), where the water film on rough surface for primary drainage is studied with stereoscopic scanning electron microscopy.

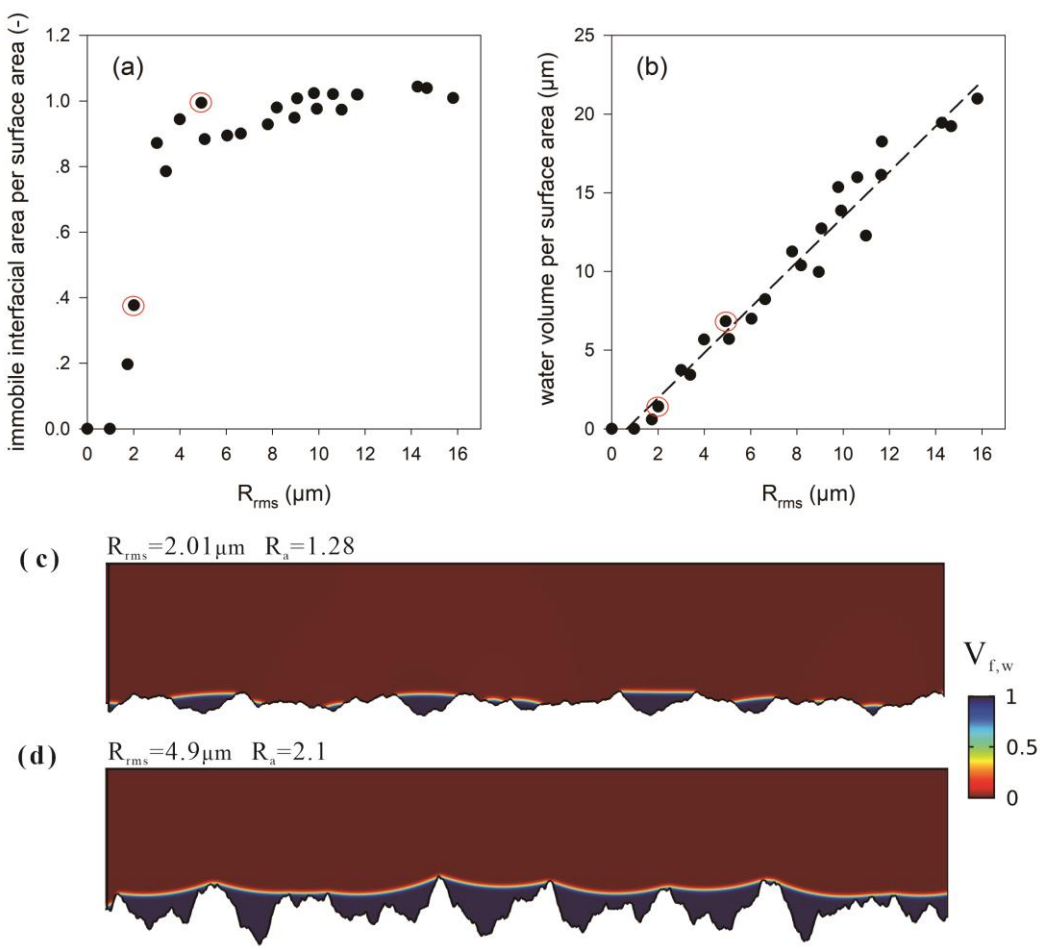

Figure 3.5 Plot of (a) immobile interfacial area per surface area and (b) deposited water volume per surface area, versus the root mean square roughness from all simulations. Examples of film configurations after drainage from Surface 4 (c) and Surface 10 (d).

3.4.4 Retention of the mobile solute mass

The measurable solute mass in the flowing zones (mobile solute mass) is produced by the moving meniscus at the front, as shown in the subfigure on the top in **Figure 3.6**. During the bursting of the moving meniscus, mobile solute mass can enter the stagnant zones in the troughs and grooves by advection and molecular diffusion, as shown in **Figure 3.6** (*t*=0.014 s). When the moving meniscus touches the next peak (**Figure 3.6** *t*=0.015 s), the water in the trough is being isolated from the flowing water body, and a recirculation zone is formed in the trough due to the inertial effects for a very short period of time. Finally, the mobile solute mass retained in the trough becomes stagnant (**Figure 3.6** *t*=0.016 s). From the aforementioned process, it is clear that a part of the mobile solute mass is being retained in water locked in the troughs.

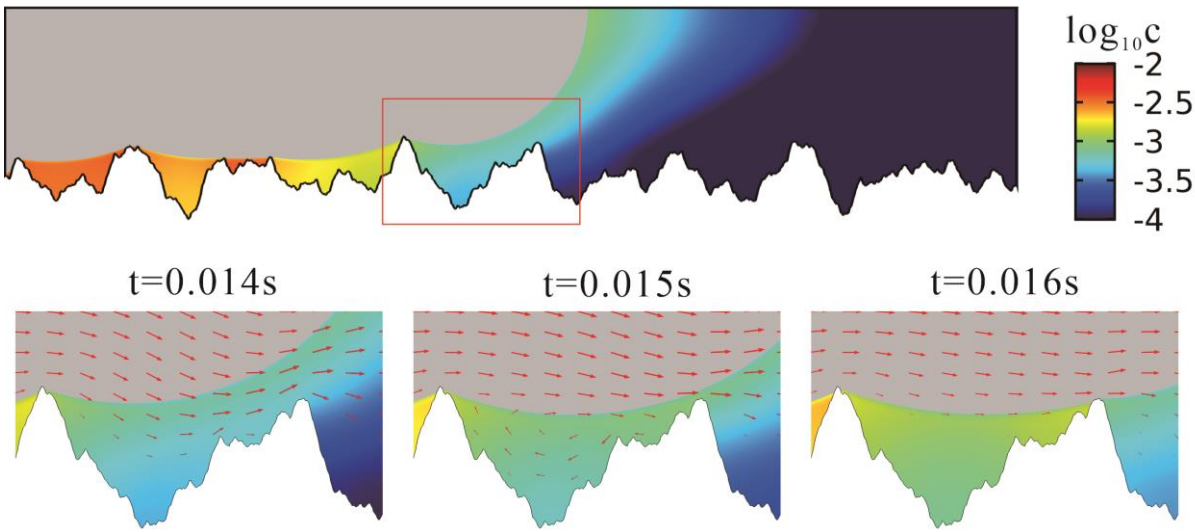

Figure 3.6 Plot of the retention process of the solute mass in the flowing zone for a zoom-in region at *t*=0.014 s, *t*=0.015 s and *t*=0.016 s. The non-wetting phase is plotted in gray color. The red arrows show the direction of velocity vector, and the length of the arrows is proportional to the natural logarithm of the norm of velocity vector.

3.4.5 Relation between the mobile interfacial area and mobile solute mass

The quantified solute mass in the mobile zone from four example simulations is plotted with gray dots in **Figure 3.7**. The results of simulations for the other twenty surfaces are given in the supporting information. As the mobile interfacial area is known, we can calculate the total solute mass produced by the mobile interface with Eq.(3.30).

$$M_{IFA,m} = R_c^{dif} \int_{t_0}^{t} A_{wn,m}^{dif}(t)dt \tag{3.30}$$

The total solute mass produced by the mobile interface is plotted with a solid line in **Figure 3.7**. For a smooth surface, all solute mass gets produced by the moving meniscus in the flowing region, so there is no difference for M_m and $M_{IFA,m}$. The difference between M_m and $M_{IFA,m}$ becomes significant for increasing surface roughness. Both curves show linear increase trends. We formulate

the relation between the mobile solute mass and mobile interfacial area by introducing of a film-associated mobile mass retention term ξ_f, as Eq.(3.31).

$$M_{RT,m} = (1 - \xi_f) M_{IFA,m} \tag{3.31}$$

The calculated $M_{RT,m}$ is plotted with dashed line in **Figure 3.7**. It is found that $M_{RT,m}$ and M_m can fit well, which can be expressed as:

$$M_{RT,m} = M_m \tag{3.32}$$

This indicates that rough surfaces can cause a constant fraction of the mobile solute mass produced by the moving meniscus to be retained in the isolated water films. It is reasonable that ξ_f is constant for a surface with homogeneous roughness, and the retention process discussed in section 3.4.4 is repeated continuously at the front. The value of ξ_f is different for each simulation depending on the surface roughness. With the definition of Eq.(3.21) and Eq.(3.26), the diffuse interfacial area can be converted into sharp interfacial area.

$$R_c^{dif} \int_{t_0}^{t} A_{wn,m}^{dif}(t)dt = R_c \int_{t_0}^{t} A_{wn,m}(t)dt \tag{3.33}$$

The integration of the fluctuating mobile interfacial area over the total reaction time can be expressed by a time-averaged mobile interfacial area multiplying the total reaction time:

$$\int_{t_0}^{t} A_{wn,m}(t)dt = \overline{A_{wn,m}}\Delta t \tag{3.34}$$

where Δt indicates the total reaction time. By incorporating of Eq.(3.30) to Eq.(3.34), one obtains:

$$\overline{A_{wn,m}} = \frac{M_m}{(1 - \xi_f) R_c \ \Delta t} \tag{3.35}$$

The relation between the measurable solute mass in flowing water and the time-averaged mobile interfacial area is formulated as Eq.(3.35). When reacted mass in flowing water is measured, and the reaction time and the reaction rate are known, one still needs to determine the film-associated mobile mass retention term, for measuring the average mobile interfacial area. Besides, we found that the absolute value of the mobile solute mass (plotted in gray dots in **Figure 3.7**) is generally lower with rougher surfaces. This is mainly because, with increasing surface roughness, the loss in the mobile solute mass (by the retention process) exceeds the increased production of the mobile solute mass (by the increment in the mobile interfacial area).

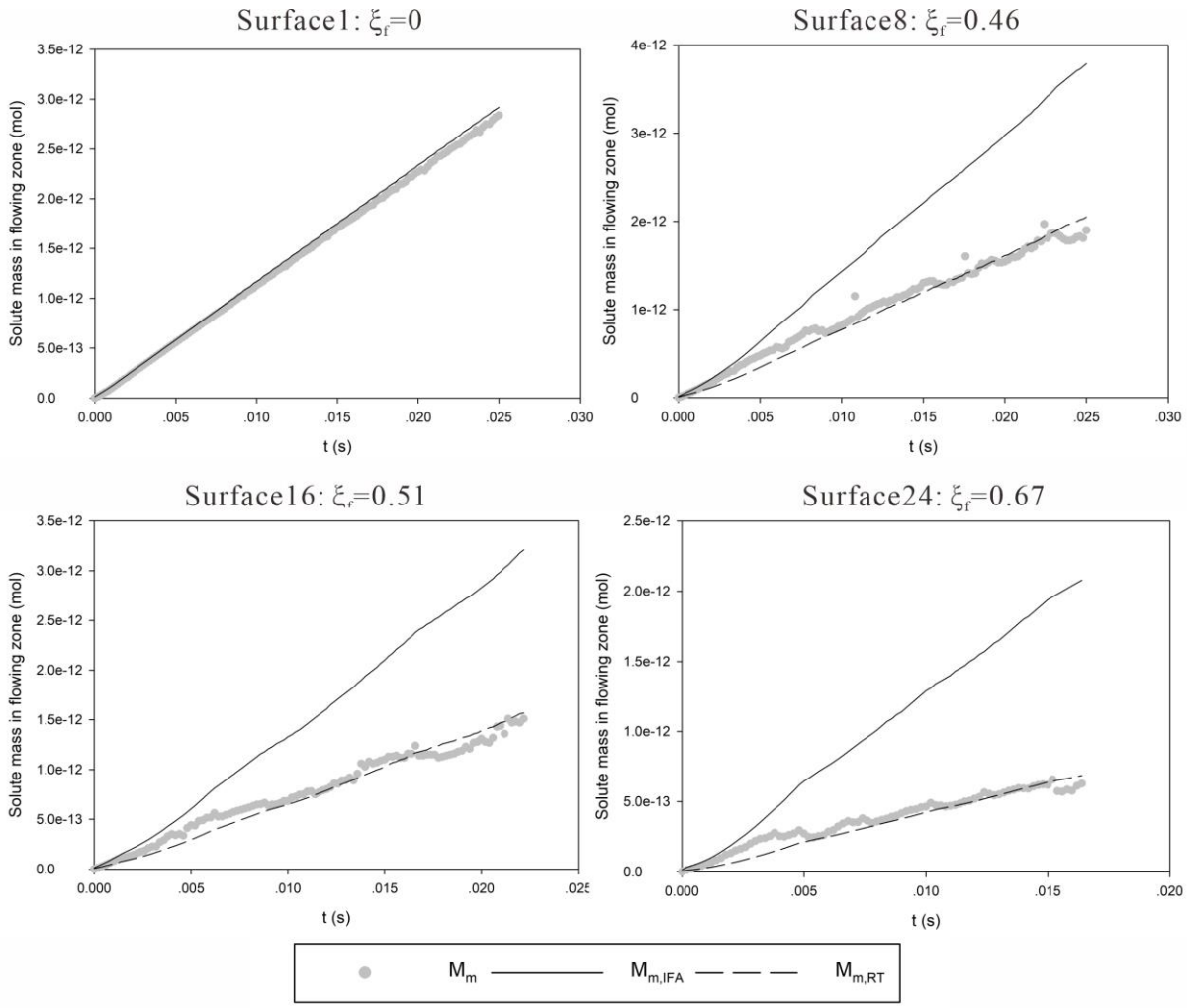

Figure 3.7 Plot of the quantified solute mass in the mobile zone (M_m) in gray dots, the total solute mass produced by the moving meniscus ($M_{IFA,m}$) and mobile solute mass calculated with adding the retention term ($M_{RT,m}$), versus the time for four simulations as examples.

3.4.6 Determination of the film-associated mobile mass retention term

The film-associated mobile mass retention term for all simulations is plotted with respect to the root mean square roughness in **Figure 3.8**. The mobile mass retention term is very small for R_{rms}<3 μm (R_a<1.3). This can be attributed mostly to the retention process happening rarely, with small water volume being deposited. When R_{rms}>3 μm (R_a>1.3), the film-associated mobile mass retention term increases linearly with the root mean square roughness. This can mostly be attributed to the increase of the deposited water volume, and the deposited water volume is also increasing linearly with respect to R_{rms}. The results imply that the film-associated mobile mass retention term can be directly determined from the root mean square roughness when R_{rms}>3 μm (R_a>1.3).

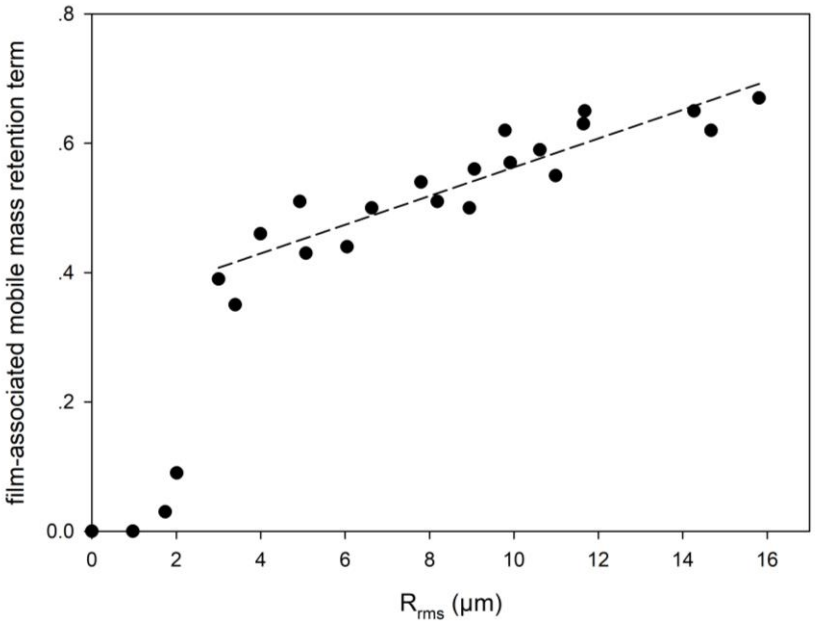

Figure 3.8 Plot of the film-associated mobile mass retention term versus the root mean square roughness from all simulations.

3.5 Summary and Conclusions

By applying the pore-scale PFM-CST model, we studied the KIS tracer reactive transport process for primary drainage in a 2D slit with rough surfaces. In total, 24 fractal surfaces were generated, with the root-mean-square roughness ranging from 0 (R_a=1) to 15.8 μm (R_a=5.6). The flowing and stagnant (film) water were distinguished by applying a threshold local Péclet number. The quantified mobile interfacial area, film-associated interfacial area, water film volume, and reacted solute mass in flowing water during drainage were quantified. The major results and findings of the study are listed below:

- The mobile FIFA for a rough surface is larger than the one for a smooth surface, due to Haines jumps. Rougher surfaces with higher R_{rms} show a decrease of the mobile FIFA, due to the effective narrowing of the flow channel.
- When R_{rms}>3 μm (R_a>1.3) the surface roughness has no effect on the (immobile) film-associated interfacial area. The deposited water volume per surface area (or the average film thickness) increases linearly with R_{rms}.
- A part of the solute mass produced by the mobile FIFA can enter the stagnant zones in the troughs and grooves by advection and molecular diffusion. This causes a decrease in measurable tracer reacted solute mass in the flowing water.
- For a rough surface, the relation between the mobile interfacial area and solute mass in flowing zones can be formulated with the addition of a film-associated mobile mass retention term, ξ_f (Eq.3.35), and ξ_f remains constant for a surface with homogeneous roughness.
- The film-associated mobile mass retention term (ξ_f) is found to be linearly dependent on R_{rms}, when R_{rms}>3 μm (R_a>1.3).

This study showed that the KIS tracer test can be used to measure the average mobile interfacial area for dynamic two-phase flow systems in porous media with rough solid surfaces. The fraction of the mobile mass retained in the deposited water film can be described by the film-associated mobile mass term (ξ_f), and the retention term can be directly determined from the root mean square roughness. Future work is required to improve our macroscopic model of KIS tracer reactive transport, for further inclusion of the effects of the surface roughness observed at the pore-scale.

3.6 Acknowledgement

We thank Farzad Basirat, Auli Niemi and Chin-Fu Tsang for the constructive dialogue about the KIS tracer and overall support of the work. We thank Rainer Helmig and Holger Class (from the SFB1313 Collaborative Research Center) for the support in conducting and further extending this work.

We acknowledge DFG Project 428614366, European Community's 7th Framework Programme FP7 under grant number 309067 (trust-co2.org), and Horizon 2020 Research and Innovation Programme (www.fracrisk.eu) under grant number 636811.

N.K. and H.S. would like to thank the Deutsche Forschungsgemeinschaft (DFG, German Research Foundation) for supporting this work by funding SFB 1313, Project Number 327154368. H.S. would like to thank the Deutsche Forschungsgemeinschaft (DFG, German Research Foundation) under German Excellence Strategy EXC 2075 390740016.

All data used to support this work are reported in the manuscript and the supporting information in the respective tables and figures.

The authors declare that they have no known competing financial interests or personal relationships that could have appeared to influence the work reported in this paper.

3.7 Reference

Akhlaghi Amiri HA, Hamouda AA (2013) Evaluation of level set and phase field methods in modeling two phase flow with viscosity contrast through dual-permeability porous medium. Int J Multiph Flow 52:22–34. https://doi.org/10.1016/j.ijmultiphaseflow.2012.12.006

Alpak FO, Riviere B, Frank F (2016) A phase-field method for the direct simulation of two-phase flows in pore-scale media using a non-equilibrium wetting boundary condition. Comput Geosci 20:881–908. https://doi.org/10.1007/s10596-015-9551-2

AlRatrout A, Blunt MJ, Bijeljic B (2018) Wettability in complex porous materials, the mixed-wet state, and its relationship to surface roughness. Proc Natl Acad Sci 115:8901–8906. https://doi.org/10.1073/pnas.1803734115

Aziz R, Joekar-Niasar V, Martinez-Ferrer P (2018) Pore-scale insights into transport and mixing in steady-state two-phase flow in porous media. Int J Multiph Flow 109:51–62. https://doi.org/10.1016/j.ijmultiphaseflow.2018.07.006

Badalassi VE, Ceniceros HD, Banerjee S (2003) Computation of multiphase systems with phase field models. J Comput Phys 190:371–397. https://doi.org/10.1016/S0021-9991(03)00280-8

Basirat F, Yang Z, Niemi A (2017) Pore-scale modeling of wettability effects on CO2–brine displacement during geological storage. Adv Water Resour 109:181–195. https://doi.org/10.1016/j.advwatres.2017.09.004

Brown SR, Scholz CH (1985) Broad bandwidth study of the topography of natural rock surfaces. J Geophys Res Solid Earth 90:12575–12582. https://doi.org/10.1029/JB090iB14p12575

Brusseau ML (2018) Assessing the potential contributions of additional retention processes to PFAS retardation in the subsurface. Sci Total Environ 613–614:176–185. https://doi.org/10.1016/j.scitotenv.2017.09.065

Brusseau ML, Narter M, Janousek H (2010) Interfacial Partitioning Tracer Test Measurements of Organic-Liquid/Water Interfacial Areas: Application to Soils and the Influence of Surface Roughness. Environ Sci Technol 44:7596–7600. https://doi.org/10.1021/es101312n

Brusseau ML, Van Glubt S (2019) The influence of surfactant and solution composition on PFAS adsorption at fluid-fluid interfaces. Water Res 161:17–26. https://doi.org/10.1016/j.watres.2019.05.095

Cahn JW, Hilliard JE (1959) Free Energy of a Nonuniform System. III. Nucleation in a Two-Component Incompressible Fluid. J Chem Phys 31:688–699. https://doi.org/10.1063/1.1730447

Culligan KA, Wildenschild D, Christensen BSB, Gray WG, Rivers ML, Tompson AFB (2004) Interfacial area measurements for unsaturated flow through a porous medium. Water Resour Res 40:W12413. https://doi.org/10.1029/2004WR003278

Deng H, Molins S, Trebotich D, Steefel C, DePaolo D (2018) Pore-scale numerical investigation of the impacts of surface roughness: Upscaling of reaction rates in rough fractures. Geochim Cosmochim Acta 239:374–389. https://doi.org/10.1016/j.gca.2018.08.005

El-Farhan YH, DeNovio NM, Herman JS, Hornberger GM (2000) Mobilization and Transport of Soil Particles during Infiltration Experiments in an Agricultural Field, Shenandoah Valley, Virginia. Environ Sci Technol 34:3555–3559. https://doi.org/10.1021/es991099g

Gao B, Saiers JE, Ryan J (2006) Pore-scale mechanisms of colloid deposition and mobilization during steady and transient flow through unsaturated granular media. Water Resour Res 42(1). https://doi.org/10.1029/2005WR004233

Gao H, Tatomir AB, Karadimitriou NK, Steeb H, Sauter M (2021) A two-phase, pore-scale reactive transport model for the kinetic interface-sensitive tracer. Water Resour Res 57(6). https://doi.org/10.1029/2020WR028572

Geistlinger H, Ataei-Dadavi I, Mohammadian S, Vogel H-J (2015) The impact of pore structure and surface roughness on capillary trapping for 2-D and 3-D porous media: Comparison with percolation theory. Water Resour Res 51:9094–9111. https://doi.org/10.1002/2015WR017852

Geistlinger H, Zulfiqar B (2020) The Impact of Wettability and Surface Roughness on Fluid Displacement and Capillary Trapping in 2-D and 3-D Porous Media: 1. Wettability-

Controlled Phase Transition of Trapping Efficiency in Glass Beads Packs. Water Resour Res 56:e2019WR026826. https://doi.org/10.1029/2019WR026826

Ghanbarian B, Hunt AG, Daigle H (2016) Fluid flow in porous media with rough pore-solid interface. Water Resour Res 52:2045–2058. https://doi.org/10.1002/2015WR017857

Haines WB (1930) Studies in the physical properties of soil. V. The hysteresis effect in capillary properties, and the modes of moisture distribution associated therewith. J Agric Sci 20:97–116. https://doi.org/10.1017/S002185960008864X

Haroun Y, Legendre D, Raynal L (2010) Volume of fluid method for interfacial reactive mass transfer: Application to stable liquid film. Chem Eng Sci 65:2896–2909. https://doi.org/10.1016/j.ces.2010.01.012

Hassanizadeh SM, Gray WG (1990) Mechanics and thermodynamics of multiphase flow in porous media including interphase boundaries. Adv Water Resour 13:169–186. https://doi.org/10.1016/0309-1708(90)90040-B

Jacqmin D (1999) Calculation of Two-Phase Navier–Stokes Flows Using Phase-Field Modeling. J Comput Phys 155:96–127. https://doi.org/10.1006/jcph.1999.6332

Jiang H, Guo B, Brusseau ML (2020) Pore-Scale Modeling of Fluid-Fluid Interfacial Area in Variably Saturated Porous Media Containing Microscale Surface Roughness. Water Resour Res 56:e2019WR025876. https://doi.org/10.1029/2019WR025876

Kang Q, Lichtner PC, Zhang D (2006) Lattice Boltzmann pore-scale model for multicomponent reactive transport in porous media. J Geophys Res Solid Earth 111(B5). https://doi.org/10.1029/2005JB003951

Karadimitriou NK, Joekar-Niasar V, Babaei M, Shore CA (2016) Critical Role of the Immobile Zone in Non-Fickian Two-Phase Transport: A New Paradigm. Environ Sci Technol 50:4384–4392. https://doi.org/10.1021/acs.est.5b05947

Karadimitriou NK, Joekar-Niasar V, Brizuela OG (2017) Hydro-dynamic Solute Transport under Two-Phase Flow Conditions. Sci Rep 7:1–7. https://doi.org/10.1038/s41598-017-06748-1

Kibbey TCG (2013) The configuration of water on rough natural surfaces: Implications for understanding air-water interfacial area, film thickness, and imaging resolution. Water Resour Res 49:4765–4774. https://doi.org/10.1002/wrcr.20383

Lowengrub, J., Truskinovsky, L. (1998) Quasi–incompressible Cahn–Hilliard fluids and topological transitions. Proceedings of the Royal Society of London. Series A: Mathematical, Physical and Engineering Sciences 454, 2617–2654. https://doi.org/10.1098/rspa.1998.0273

Maes J, Soulaine C (2018) A new compressive scheme to simulate species transfer across fluid interfaces using the Volume-Of-Fluid method. Chem Eng Sci 190:405–418. https://doi.org/10.1016/j.ces.2018.06.026

McDonald K, Carroll KC, Brusseau ML (2016) Comparison of Fluid-Fluid Interfacial Areas Measured with X-ray Microtomography and Interfacial Partitioning Tracer Tests for the same Samples. Water Resour Res 52:5393–5399. https://doi.org/10.1002/2016WR018775

Mehmani A, Kelly S, Torres-Verdín C, Balhoff M (2019) Capillary Trapping Following Imbibition in Porous Media: Microfluidic Quantification of the Impact of Pore-Scale

Surface Roughness. Water Resour Res 55:9905–9925. https://doi.org/10.1029/2019WR025170

Miller CT, Poirier-McNeil MM, Mayer AS (1990) Dissolution of Trapped Nonaqueous Phase Liquids: Mass Transfer Characteristics. Water Resour Res 26:2783–2796. https://doi.org/10.1029/WR026i011p02783

Montemagno CD, Gray WG (1995) Photoluminescent volumetric imaging: A technique for the exploration of multiphase flow and transport in porous media. Geophys Res Lett 22:425–428. https://doi.org/10.1029/94GL02697

Philip JR (1978) Adsorption and capillary condensation on rough surfaces. J Phys Chem 82:1379–1385. https://doi.org/10.1021/j100501a012

Porter ML, Wildenschild D, Grant G, Gerhard JI (2010) Measurement and prediction of the relationship between capillary pressure, saturation, and interfacial area in a NAPL-water-glass bead system. Water Resour Res 46(8). https://doi.org/10.1029/2009WR007786

Power WL, Tullis TE (1991) Euclidean and fractal models for the description of rock surface roughness. J Geophys Res Solid Earth 96:415–424. https://doi.org/10.1029/90JB02107

Reeves PC, Celia MA (1996) A Functional Relationship Between Capillary Pressure, Saturation, and Interfacial Area as Revealed by a Pore-Scale Network Model. Water Resour Res 32:2345. https://doi.org/10.1029/96WR01105

Renard F, Candela T, Bouchaud E (2013) Constant dimensionality of fault roughness from the scale of micro-fractures to the scale of continents. Geophys Res Lett 40:83–87. https://doi.org/10.1029/2012GL054143

Renard F, Schmittbuhl J, Gratier J-P, Meakin P, Merino E (2004) Three-dimensional roughness of stylolites in limestones. J Geophys Res Solid Earth 109(B3). https://doi.org/10.1029/2003JB002555

Saiers JE, Hornberger GM, Gower DB, Herman JS (2003) The role of moving air-water interfaces in colloid mobilization within the vadose zone. Geophys Res Lett 30(21). https://doi.org/10.1029/2003GL018418

Sari A, Al Maskari NS, Saeedi A, Xie Q (2020) Impact of surface roughness on wettability of oil-brine-calcite system at sub-pore scale. J Mol Liq 299:112107. https://doi.org/10.1016/j.molliq.2019.112107

Schaffer M, Maier F, Licha T, Sauter M (2013) A new generation of tracers for the characterization of interfacial areas during supercritical carbon dioxide injections into deep saline aquifers: Kinetic interface-sensitive tracers (KIS tracer). Int J Greenh Gas Control 14:200–208. https://doi.org/10.1016/j.ijggc.2013.01.020

Schmittbuhl J, Gentier S, Roux S (1993) Field measurements of the roughness of fault surfaces. Geophys Res Lett 20:639–641. https://doi.org/10.1029/93GL00170

Shang J, Flury M, Deng Y (2009) Force measurements between particles and the air-water interface: Implications for particle mobilization in unsaturated porous media. Water Resour Res 45(6). https://doi.org/10.1029/2008WR007384

Sun DL, Tao WQ (2010) A coupled volume-of-fluid and level set (VOSET) method for computing incompressible two-phase flows. Int J Heat Mass Transf 53:645–655. https://doi.org/10.1016/j.ijheatmasstransfer.2009.10.030

Tatomir A, Vriendt KD, Zhou D, Gao H, Duschl F, Sun F, Licha T, Sauter M (2018) Kinetic Interface Sensitive Tracers: Experimental Validation in a Two-Phase Flow Column Experiment. A Proof of Concept. Water Resour Res 54:10,223-10,241. https://doi.org/10.1029/2018WR022621

Tatomir A, Zhou D, Gao H, Dimache A-N, Iancu I, Sauter M (2019) Modelling of kinetic interface sensitive tracers reactive transport in 2D two-phase flow heterogeneous porous media. E3S Web Conf 85:07003. https://doi.org/10.1051/e3sconf/20198507003

Tatomir AB, Gao H, Pötzl C, Karadimitriou NK, Licha T, Class H, Helmig RH, Sauter M (2020) Estimation of NAPL-Water interfacial areas for unconsolidated porous media by kinetic interface sensitive (KIS) tracers. In: Earth Space Sci. Open Arch. http://www.essoar.org/doi/10.1002/essoar.10503948.1. Accessed 25 Apr 2021

Tatomir AB, Jyoti A, Sauter M (2016) Monitoring of CO2 Plume Migration in Deep Saline Formations with Kinetic Interface Sensitive Tracers (A Numerical Modelling Study for the Laboratory). In: Vishal V, Singh TN (eds) Geologic Carbon Sequestration: Understanding Reservoir Behavior. Springer International Publishing, Cham, pp 59–80

Tatomir AB, Schaffer M, Kissinger A, Hommel J, Nuske P, Licha T, Helmig R, Sauter M (2015) Novel approach for modeling kinetic interface-sensitive (KIS) tracers with respect to time-dependent interfacial area change for the optimization of supercritical carbon dioxide injection into deep saline aquifers. Int J Greenh Gas Control 33:145–153. https://doi.org/10.1016/j.ijggc.2014.11.020

Tokunaga TK (2011) Physicochemical controls on adsorbed water film thickness in unsaturated geological media. Water Resour Res 47(8). https://doi.org/10.1029/2011WR010676

Wang M, Chen Y-F, Ma G-W, Zhou J-Q, Zhou C-B (2016) Influence of surface roughness on nonlinear flow behaviors in 3D self-affine rough fractures: Lattice Boltzmann simulations. Adv Water Resour 96:373–388. https://doi.org/10.1016/j.advwatres.2016.08.006

Yi J, Xing H, Wang J, Xia Z, Jing Y (2019) Pore-scale study of the effects of surface roughness on relative permeability of rock fractures using lattice Boltzmann method. Chem Eng Sci 209:115178. https://doi.org/10.1016/j.ces.2019.115178

Yue P, Feng JJ, Liu C, Shen J (2004) A diffuse-interface method for simulating two-phase flows of complex fluids. J Fluid Mech 515:293–317. https://doi.org/10.1017/S0022112004000370

Yue P, Zhou C, Feng JJ, Ollivier-Gooch CF, Hu HH (2006) Phase-field simulations of interfacial dynamics in viscoelastic fluids using finite elements with adaptive meshing. J Comput Phys 219:47–67. https://doi.org/10.1016/j.jcp.2006.03.016

Zheng W, Yu X, Jin Y (2015) Considering Surface Roughness Effects in a Triangular Pore Space Model for Unsaturated Hydraulic Conductivity. Vadose Zone J 14:vzj2014.09.0121. https://doi.org/10.2136/vzj2014.09.0121

Zulfiqar B, Vogel H, Ding Y, Golmohammadi S, Küchler M, Reuter D, Geistlinger H (2020) The Impact of Wettability and Surface Roughness on Fluid Displacement and Capillary Trapping in 2-D and 3-D Porous Media: 2. Combined Effect of Wettability, Surface Roughness, and Pore Space Structure on Trapping Efficiency in Sand Packs and

Micromodels. Water Resour Res 56:e2020WR027965. https://doi.org/10.1029/2020WR027965

Zhou, C., Yue, P., Feng, J.J., Ollivier-Gooch, C.F., Hu, H.H., 2010. 3D phase-field simulations of interfacial dynamics in Newtonian and viscoelastic fluids. Journal of Computational Physics 229, 498–511. https://doi.org/10.1016/j.jcp.2009.09.039

4. Reservoir characterization by push-pull tests employing Kinetic Interface Sensitive tracers - a pore-scale study for understanding large-scale processes

H. Gao[1], A. B. Tatomir[1], N. K. Karadimitriou[2], H. Steeb[2,3], and M. Sauter[1]

Citation:

Gao H, Tatomir AB, Karadimitriou NK, Steeb H, Sauter M (2022) Reservoir characterization by push-pull tests employing Kinetic Interface Sensitive tracers - a pore-scale study for understanding large-scale processes. Submitted to Advances in Water Resources (under review).

[1]Department of Applied Geology, University of Göttingen, 37073, Göttingen, Germany.

[2]Institute of Applied Mechanics (CE), University of Stuttgart, 70569 Stuttgart, Germany.

[3]Stuttgart Center for Simulation Science (SC SimTech), Pfaffenwaldring 5a, 70569 Stuttgart, Germany

Corresponding author: Huhao Gao (huhao.gao@uni-goettingen.de)

Abstract:

The kinetic interface-sensitive (KIS) tracer experiment is a newly developed method to quantify the fluid-fluid interfacial area (FIFA) during drainage processes. The concentration breakthrough curves, obtained by measuring reaction product concentration in brine/water samples after breakthrough, are interpreted with a specialized numerical model to determine the FIFA. However, this method has its own limitations since the volume of the usable water sample (after breakthrough), based on which the analysis takes place, is often insufficient. This happens because this volume strongly depends on the aquifer material, i.e. sand type and system parameters. An alternative is to employ KIS tracers in a "push-pull" experimental set-up, i.e. primary drainage is followed by a consequent main imbibition process, with the flow direction being reversed. This study applies a pore-scale numerical model to study the KIS tracer reactive transport during a push-pull experiment in a 2D porous medium. The advective-dispersive-reactive transport during both primary drainage and main imbibition processes is discussed. The concentration breakthrough curves show a non-linear descending trend with time, until reaching a constant concentration at the steady state. By analyzing the spatial concentration distribution and the concentration breakthrough curve, the macro-scale KIS tracer reactive transport model can be interpreted for the push-pull process. Finally, the new method is applied in the column experiment, where the determined specific interfacial area is find to be close to literature data.

Key words: reactive transport, push-pull test, two-phase flow, phase field method, fluid-fluid interfacial area, kinetic interface sensitive tracer

4.1 Introduction

Measurement of the Fluid-Fluid Interfacial Area (FIFA) is essential for studying two-phase flow, and interphase mass transfer in porous media (Miller et al. 1990; Hassanizadeh and Gray 1990). The existing techniques to measure the FIFA mainly include interfacial partitioning tracer tests (IPTT) (Brusseau et al. 2010; McDonald et al. 2016), X-Ray computed micro-tomography (X-RCT) (Culligan et al. 2004; Porter et al. 2010) and photo-luminescent volumetric imaging (PVI) (Montemagno and Gray 1995). One common limitation of these methods is that they are only feasible for steady state/quasi-static conditions (Tatomir et al. 2018). A Kinetic Interface Sensitive tracer test method (KIS-TT) was recently developed for quantifying the FIFA in dynamic two-phase (Tatomir et al. 2016; Tatomir et al. 2018).

4.1.1 Background of the KIS tracer

The KIS tracer compound was first synthesized as phenyl naphthalene-2-sulfonate (2-NSAPh) by Schaffer et al. (2013). The 2-NSAPh is a non-polar, hydrolysable, phenolic ester, which dissolves in non-polar liquids, or non-aqueous phase liquids (NAPLs). When the NAPL (with dissolved KIS tracer) interacts with the resident water phase, the tracer molecules are being adsorbed onto the fluid-fluid interface, following Langmuir's isotherm (Schaffer et al. 2013). At the fluid-fluid interface, the adsorbed 2-NSAPh molecules undergo an irreversible hydrolysis reaction.

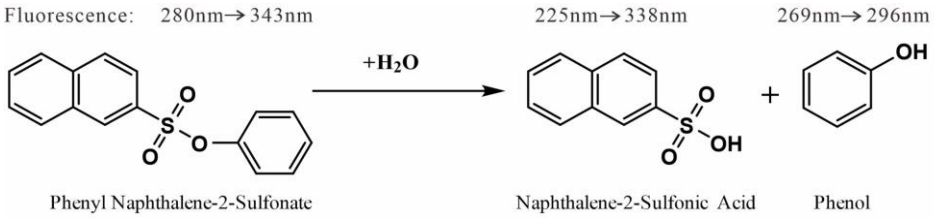

(4.1)

Due to the excess supply of tracer, i.e. its concentration at the interface stays constant at its maximum value, the original first order hydrolysis reaction can be simplified to a pseudo zero-order reaction (Schaffer et al. 2013), expressed by:

$$A_{wn} = \frac{M_k}{R_c \Delta t} \tag{4.2}$$

where R_c (kg·s^{-1}m^{-2}) is the reaction rate of the KIS tracer per unit interfacial area, M_k (kg) is the mass of the reaction product k, Δt is the reaction time, and A_{wn} is the FIFA (m^2). Among the two reaction products (naphthalene-2-sulfonic acid, i.e.,2-NSA and phenol), the 2-NSA is the compound more easily measured in a tracer experiment, because of its intrinsic fluorescent properties (Schaffer et al. 2013; Tatomir et al. 2018). With the 2-NSA characterized by high polarity, being highly hydrophilic and non-adsorptive on either the water-solid interface, or the fluid-fluid interfaces, it can be expected to disperse rapidly into the bulk water, at distance from the fluid-fluid interface (Schaffer et al. 2013; Tatomir et al. 2018). Thus, in a KIS tracer experiment, we measure the 2-NSA concentration in water, and the obtained reacted 2-NSA mass (M_k) can be used to calculate the interfacial area according to Eq.(4.2). With a constant zero-order reaction at the interface, the study of the 2-NSAPh decay and transport in the NAPL becomes redundant, and the most relevant component of study is the reaction product 2-NSA, which is present only in the aqueous phase.

The FIFA can be classified into film-associated FIFA, capillary-associated FIFA which can be further subdivided into a mobile part, and an immobile part. Tatomir et al. (2018) first applied the KIS tracer in drainage experiments in a column to measure the capillary-associated FIFA, and thus the method is here termed “drainage KIS tracer method for dynamic conditions”. In the work of Tatomir et al. (2018), the KIS tracer was dissolved in n-octane (NAPL) to drain the initially water saturated column. The porous media was a well-characterized in terms of grains size, porosity and permeability glass beads packing. At the column outlet, samples were collected and measured at defined time intervals and plotted as BTCs of 2-NSA concentration and cumulative pore volumes of the fluids. The experimental data was analyzed by employing a macro-scale, two-phase flow, reactive transport model with the interfacial reaction of the tracer being specified in the zones where two fluids coexist (Tatomir et al. 2015; Tatomir et al. 2019). The resulting maximum specific FIFA was determined at between 500 and 540 m^{-1} for glass beads with a mean diameter of 248 μm. Furthermore, applying the pore-scale direct numerical simulation method, Gao et al. (2021a) studied the effect of hydrodynamically stagnant zones on the “drainage KIS tracer method”, in a conceptual 2D porous medium. By analyzing the quantified interfacial area and reacted solute mass in the flowing and stagnant zones, Gao et al. (2021a) proposed that the 2-NSA mass in the flowing water is mainly produced by the reaction taking place at the moving menisci, and a fraction of solute mass produced by the moving menisci can be retained in the newly formed stagnant zones during displacement. This realization made it clear that there is a portion of the interfacial area related to the stagnant zones, which cannot be accounted for. They concluded that the “drainage KIS tracer method” measures that fraction of FIFA with a common boundary to the mobile water. Gao et al. (2021b) further consider the condition of variable surface roughness of the mineral grains,

in order to determine any potential losses related to surface roughness. They found that a mobile mass retention term needs only to be considered when the "root mean square roughness" is larger than 3 μm, concluding that the "drainage KIS tracer method" is also feasible for the determination of the mobile FIFA when the grain surface is reasonably rough (e.g., natural soils).

4.1.2 A novel push-pull KIS tracer method

Despite the promising results in the previous studies, the "drainage KIS tracer method" has two major limitations. First, the volume of usable effluent water sample (containing the reacted tracer) is often insufficient. In the column experiments, the 2-NSA concentration measured at the outlet is zero at early times before breakthrough (arrival of n-octane front at the outlet) and starts to increase only after first arrival of the tracer, which implies that usable data can only be obtained from a water sample retrieved after first arrival of the tracer (Tatomir et al. 2018). When in the effluent the volume fraction of water at the outlet sharply changes from one to zero, hardly any water samples with the reacted tracer can be retrieved because of insufficient water volume being discharged. The discharged water volume after first arrival of the tracer is dependent on the grain sizes and sand types. By conducting column experiments with unconsolidated porous media composed either of glass beads or natural soils of variable grain size, it was found that the "drainage KIS tracer method" is only applicable for fine sands (mostly of mean diameter smaller than 250 μm), and the water sample volumes collected during the experiments using natural soils generally are smaller than those composed of glass beads (Tatomir et al. 2020). The volume of the available water sample after breakthrough also depends on system parameters (capillary number, fluid viscosity, etc.), a stable displacement (without fingering front pattern) may lead to only small volumes of water discharged after breakthrough. This is also relevant when field-scale applications of the "drainage KIS tracer method" in natural aquifers are being planned, since natural aquifers generally exhibit a wide spectrum of sedimentary architectural elements (clay lenses, gravel lenses) of different geometric and hydraulic properties, including variable grain size, grain textures and system parameters.

The second limitation of the "drainage KIS tracer method" is that the reacted 2-NSA mass observable in the effluent is only relevant to the mobile FIFA at the front (Gao et al. 2021a), and the magnitude of the total specific FIFA cannot be measured. The information about the FIFA associated with capillary trapping in the hydrodynamically stagnant zones is missing.

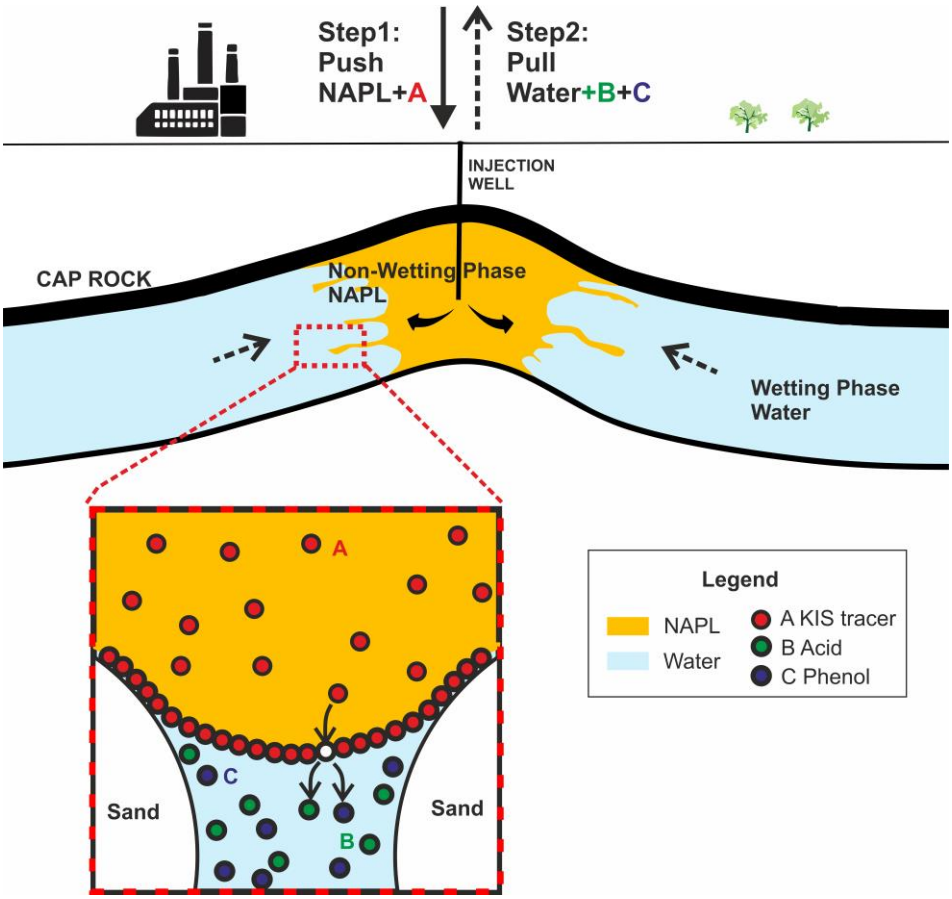

Figure 4.1 Conceptual illustration of the push-pull KIS tracer method: (top) field-scale application; (bottom) the molecular/FIFA-scale depicting the hydrolysis reaction of Eq.(4.1), modified from Tatomir et al. (2018).

To overcome the above limitations, we propose a novel "push-pull KIS tracer method" (**Figure 4.1**). The KIS tracer is dissolved in a finite volume of NAPL and injected into the water-saturated aquifer (push phase). Then, instead of monitoring the effluent concentration at another port/well, fluids are abstracted at the inlet (after start of the pull phase) immediately after the primary drainage process, and the porous material undergoes an imbibition process with reversed flow direction. The effluent mainly composed of mobile NAPL at beginning, followed by the discharged water which can be sampled to measure the 2-NSA concentration (BTCs). In this case, the volume of water available for the measurement of the reaction product acid 2-NSA concentration is no longer limited by the type of sand, or an unstable displacement. In the imbibition process, as water becomes the continuous flowing phase, both 2-NSA mass reacted at the water/NAPL front as well as in the capillary trapped water, can both expected to be transported and measured, and thus the total (mobile and immobile) FIFA can be measured. Besides, the "push-pull KIS tracer method" requires only one single well for experimental operations, and thus it is more economical for field application, especially for deep aquifers. The push-pull tests do not require such extended operation times compared to those of a NAPL plume travelling between injection and to a monitoring well, and thus the "push-pull KIS tracer method" can be conducted much faster. Furthermore, the push-pull tests have widely been used along with various types of tracers in the study of e.g. residual

NAPL saturation (Tomich et al. 1973; Davis et al. 2002; Istok et al. 2002), microbial activities (Istok et al. 1997; Urmann et al. 2005), methane oxidation (Gómez et al. 2008), solute sorption to aquifer sediments (Istok et al. 1999; Schroth et al. 2000), assessment of the effective heat exchange surface area in geothermal applications (Ghergut et al. 2013) etc. To the authors' knowledge, a tracer push-pull experiment has not yet been applied for the determination of the FIFA (for dynamic conditions).

4.1.3 Pore-scale direct numerical simulation

Pore-scale study approaches, i.e. experiments using microfluidic devices or direction numerical simulations, play important roles in understanding the pore-scale phenomena and can provide fundamental insights to understand the macro-scale processes (Meakin and Tartakovsky 2009). For example, the transient two-phase flow and the dynamics of the interfacial area are directly resolved at the pore-scale in experiments by Karadimitriou et al. (2014) and Godinez-Brizuela et al. (2017) using the micro-models with the network representing two-dimensional porous media. With the development of computers and numerical tools, direct numerical simulation of two-phase flow and reactive transport at the pore-scale, by applying Computational Fluid Dynamics (CFD) methods has become available. In a previous work, a pore-scale numerical model for the KIS tracer was built with the Phase Field Method (PFM) by Gao et al. (2021a). The PFM is outstanding for simulation of the KIS tracer reactive transport, compared to other widely applied two-phase flow reactive transport models (e.g., Lattice Boltzmann method, Volume Of Fluid method, Level Set method, etc.), because the interface is resolved as a thin diffusive layer, formed by the mixture of two fluids, according to thermodynamic principles. Thus, the zero-order reaction of the KIS tracer at fluid-fluid interface can be directly implemented as a homogenous reaction in the region of the diffusive interface. At the pore-scale, the transport of reacted 2-NSA involves several important mechanisms, including advection, molecular diffusion, partitioning/distribution between the two fluid phase, as well as the zero-order reaction at the interface. All these mechanisms are simulated with a continuous solute transport (CST) formulation derived in the PFM framework by (Gao et al. 2021a), and the PFM-CST model is verified with analytical solutions of advective-diffusion, reactive-diffusion and interphase mass transfer processes.

4.1.4 Objectives

Here, we employ the PFM-CST model to simulate a push-pull KIS tracer experiment in a conceptual 2D porous medium. This study aims at (1) providing a pore-scale insight into reactive transport of the (interfacially-reactive and water dissolved) tracer during primary drainage and main imbibition, at (2) validating the macro-scale numerical model used to interpret the BTCs obtained from push-pull KIS tracer experiments, and at (3) proving the concept of push-pull KIS tracer method through a column experiment. The paper is organized as follows: Section 4.2 presents the theory of the mathematical and the numerical models employed. The details of the model setup for the pore-scale numerical experiment, as well as the macro-scale reactive transport numerical model, are outlined in Section 4.3. The application of the new method to column experiments is elaborated in Section 4.4. The results and discussions are demonstrated in Section 4.5. Finally, Section 4.6 lists the main conclusions and findings.

4.2 Mathematic model

4.2.1 Phase-Field Method

The theory of the PFM is described in detail in e.g., (Jacqmin 1999; Badalassi et al. 2003; Yue et al. 2004; Alpak et al. 2016). In this chapter we briefly review the equations implemented in the two-phase flow model. The PFM treats the interface as a thin diffusive layer formed by a mixture of two fluids, and a smoothly changing phase variable ϕ (varying between -1 and 1) is introduced to describe the composition of the fluid mixture. A fundamental concept of the PFM is that free energy density can be expressed as a function of the phase variable, and its gradient (Jacqmin 1999). The free energy density (f_{mix}) (J/m^3) for an isothermal mixing of two fluids can be expressed in the Ginzburg-Landau form (Yue et al. 2006):

$$f_{mix}(\phi, \nabla\phi) = \frac{1}{2}\lambda|\nabla\phi|^2 + \frac{\lambda}{4\varepsilon^2}(\phi^2 - 1)^2 \tag{4.3}$$

where λ (N) is the magnitude of the mixing energy and ε (m) is the capillary thickness, which determines the thickness of the diffusive interface at equilibrium (Yue et al. 2004). The first term on the right side of the above equation accounts for the surface energy, and the second term accounts for the bulk energy which has two minima corresponding to the two stable phases of fluids (Basirat et al. 2017). The chemical potential G (J/m^3) can be defined as the variation of free energy with respect to the dimensionless phase variable:

$$G = \frac{\delta \int_{\Omega} f_{mix}\, dx}{\delta\phi} = -\lambda\nabla^2\phi + \frac{\lambda}{\varepsilon^2}\phi(\phi^2 - 1) \tag{4.4}$$

where Ω is the region of space occupied by the fluids. The interfacial tension σ (N/m) is the total free energy at the interface per unit interfacial area, which is related to the capillary thickness and the mixing energy density, through Eq.(4.5) (Yue et al. 2004):

$$\sigma = \frac{2\sqrt{2}\lambda}{3\varepsilon} \tag{4.5}$$

Fluid mass conservation is governed by the Cahn-Hilliard equation (Eq.4.6), which assumes that the diffusive fluid flux is proportional to the gradient of the chemical potential (Cahn and Hilliard 1959):

$$\frac{\partial\phi}{\partial t} + \mathbf{u}\cdot\nabla\phi = \nabla\cdot(\gamma\nabla G) \tag{4.6}$$

where $\mathbf{u}$ is the fluid velocity vector, and γ (m^{3}s/kg) is the mobility, which governs the intensity of the diffusive fluid flux and the relaxation time of the interface (Akhlaghi Amiri and Hamouda 2013). The mobility γ needs to be large enough to maintain a constant thickness of the interface, but small enough not to suppress the flow (Jacqmin 1999). The mobility γ is generally expressed as a function of the capillary thickness and a tuning factor: $\gamma = \chi\varepsilon^2$. The tuning factor χ (m·s/kg) is called the characteristic mobility.

4.2.2 Two phase flow dynamics

Momentum conservation is governed by the Navier-Stokes equation for the incompressible fluids (Eq.(4.7), where interfacial tension is considered as a body force:

$$\rho\left(\frac{\partial\mathbf{u}}{\partial t} + \mathbf{u}\cdot\nabla\mathbf{u}\right) = \nabla\cdot[-p\mathbf{I} + \mu(\nabla\mathbf{u} + (\nabla\mathbf{u})^{\mathrm{T}})] + G\nabla\phi \tag{4.7}$$

$$\nabla\cdot\mathbf{u} = 0 \tag{4.8}$$

where **I** is the second order identity tensor, p is pressure, and ρ and μ are respectively the density and viscosity of the mixture (non-wetting and wetting fluid) according to the volume fraction of the fluids $V_{f,\alpha}$ (α=w, nw):

$$V_{f,w} = (1-\phi)/2 \text{ and } V_{f,nw} = (1+\phi)/2 \tag{4.9}$$

and

$$\rho = \rho_w V_{f,w} + \rho_{nw} V_{f,nw} \text{ and } \mu = \mu_w V_{f,w} + \mu_{nw} V_{f,nw} \tag{4.10}$$

where subscripts w and nw indicate wetting and non-wetting phase, respectively. The incompressible formalism of the Navier-Stokes equation can be applied for the mixture condition at the interface as long as the interface thickness is small enough, so that the results remain unaffected (Lowengrub and Truskinovsky 1998; Zhou et al. 2010). At the grain surfaces, a no-slip boundary condition is applied with **u**=0 in Eq.(4.7) for solid wall boundaries. The wetting condition on the solid wall is expressed by:

$$\mathbf{n} \cdot \nabla\phi = \cos\theta_w |\nabla\phi| \tag{4.11}$$

where **n** is the (outward) normal vector to the wall and θ_w is the contact angle.

4.2.3 Reactive transport

The reactive transport model, based on the phase-field method, was developed in Gao et al. (2021a). The model considers KIS tracer transport mechanisms including advection, molecular diffusion, partitioning between two immiscible fluids, and reaction at the interface. Here, we briefly review the major components of the reactive transport model. For a solute k dissolved in a fluid phase α of mass concentration $c_{a,k}$, the solute mass conservation equation writes as (Gao et al. 2021a):

$$\begin{cases} \dfrac{\partial(V_{f,w}c_{w,k})}{\partial t} + \nabla\cdot(\mathbf{u}V_{f,w}c_{w,k} + 0.5\gamma\nabla G c_{w,k}) = 0 \\ \dfrac{\partial(V_{f,nw}c_{nw,k})}{\partial t} + \nabla\cdot(\mathbf{u}V_{f,nw}c_{nw,k} - 0.5\gamma\nabla G c_{nw,k}) = 0 \end{cases} \tag{4.12}$$

where only solute advection due to the bulk fluid motion is included. The local thermodynamic equilibrium of the solute in a two-phase system is described by a partitioning coefficient ($P_{ow,k}$), defined as the concentration ratio of the solute in each phase at equilibrium condition.

$$P_{ow,k} = \frac{c_{nw,k}}{c_{w,k}} \tag{4.13}$$

where $c_{nw,k}$ and $c_{w,k}$ are the concentration of the product (2-NSA) in the non-wetting phase and the wetting phase respectively, and $P_{ow,k}$ is the partition coefficient. To obtain the single-field formulation of the 2-NSA concentration for both phases in the entire domain, the global concentration is defined as:

$$c_k = V_{f,w}c_{w,k} + V_{f,nw}c_{nw,k} \tag{4.14}$$

where the solute molecular diffusion flux for the mixture is defined as (Haroun et al. 2010):

$$\mathbf{J_k} = D_k(V_{f,w}\nabla c_{w,k} + V_{f,nw}\nabla c_{nw,k}) = D_k[\nabla c_k - (c_{w,k} - c_{nw,k})\nabla V_{f,w}] \tag{4.15}$$

As $V_{f,w} + V_{f,nw} = 1$, here only $V_{f,w}$ is used in the expression, and the molecular diffusion coefficient is expressed as $D_k = V_{f,w}D_{w,k} + V_{f,nw}D_{nw,k}$. The diffusion term Eq.(4.15) indicates an additional flux term derived from the solubility law. This solubility flux is in the direction normal to the interface, which governs the distribution of the species between the two phases. Thus, by incorporating the equations from Eq.(4.12) to Eq.(4.15) and adding the source term for the chemical reaction, the final governing equation for the global concentration of solute k is reorganized:

$$\frac{\partial c_k}{\partial t} + \nabla \cdot \left[\mathbf{u} c_k + 0.5\gamma \nabla G \frac{c_k(1 - P_{ow,k})}{V_{f,w} + P_{ow.k}(1 - V_{f,w})} \right] - \nabla \cdot \left[D_k \left(\nabla c_k - \nabla V_{f,w} \frac{c_k(1 - P_{ow,k})}{V_{f,w} + P_{ow,k}(1 - V_{f,w})} \right) \right] + R_c^{dif} = 0 \quad (4.16)$$

where R_c^{dif} (kg·s^{-1}m^{-3}) is the zero-order interfacial reaction of the KIS tracer, which is assumed in the model as a homogeneous reaction taking place at the diffusive interface. The interfacial reaction region is taken with $V_{f,w} \in [0.05,0.95]$, whose thickness is b_{wn}=4.1641ε (Yue et al. 2004). With the constant interface thickness, the reaction rate per unit interfacial region for the model can be calculated as:

$$R_c^{dif} = \begin{cases} \frac{R_c}{b_{wn}}, & V_{f,w} \in [0.05, 0.95] \\ 0, & V_{f,w} \in [0, 0.05) \cup (0.95, 1] \end{cases} \quad (4.17)$$

where R_c (kg·s^{-1}m^{-2}) is the tracer reaction rate per unit sharp interfacial area.

4.3 Numerical model

The numerical implementation is explained in section 4.3.1. The details of the pore-scale numerical simulation setup are shown in section 4.3.2. The data treatment to obtain the concentration breakthrough curve and volume averaged parameters inside the domain are shown in section 4.3.3.

4.3.1 Numerical implementation

The model is implemented in COMSOL Multiphysics^{TM}, a software for solving of partial differential equations, employing the Finite Element method for spatial discretization (Tatomir et al. 2018; Gao et al. 2021a). The linear solver PARDISO is used to solve the partial differential equations. The Backward Euler method is used to solve the time stepping. The initial time step and maximum time steps are controlled to be small enough in order to avoid a singularity (Gao et al. 2021b). The mesh elements consist of regular triangles with a side length of *h*. The computations were performed on a single CPU with 8 cores, operating at 4.3 GHz, and 128 GB RAM.

4.3.2 Pore-scale numerical experiment setups

The study domain is assumed as a two-dimensional rectangle, measuring in total 14.72 mm × 3.53 mm (length × width), including two rectangles as inlets for the fluids on both sides of a porous domain in between (measuring 14.53 mm × 3.53 mm in size), as shown in **Figure 4.2**(a). The pore space is shaped by circular grains, which have been widely used in micro-model experiments and pore-scale numerical studies (Ferrari and Lunati 2013; Liu et al. 2014; Godinez-Brizuela et al. 2017). Each grain bears a size randomly chosen from three potential choices with diameters of 225μm, 250μm or 275μm, which are similar to the size of the glass beads used for column experiment in Section 4.4. The grains are first uniformly distributed to fill the domain, explained in **Figure 4.2**(b). Then, each grain is moved from its original place in both x- and y-directions. The distances of the movement in both directions are randomly determined but controlled to be shorter than 20μm, and the grains do not overlap. The porous medium is built at a porosity of 47.56%. The domain is discretized with triangular elements with a side length of h=8×10^{-6} m, and two layers of mesh on the solid wall are further refined with a thickness of h=2×10^{-6} m to better resolve the flow condition near the solid wall, as shown in **Figure 4.2**(c). The capillary thickness for the model is set at ε=1×10^{-5} m, so that the interface is resolved with adequate meshes (Gao et al. 2021a).

The simulation is carried out for a drainage process, followed by an imbibition process. During drainage, the porous domain is initially filled with water, and the inlet on the left-hand side is initially filled with n-octane (with the tracer dissolved). The initial location of the interface is determined (red dashed line in **Figure 4.2**), necessary to ascertain numerical stability. At t=0, the n-octane with the tracer dissolved in it is injected at the left boundary to displace the water at a constant specific flux of u_{in}=0.025 m/s, and the right-hand side of the domain is the outlet. The Reynolds number associated with the displacement can be calculated as $Re= u_{in}\cdot\rho\cdot L_c/\mu$. The averaged width of the throat in the porous media L_c=0.062 mm (estimated from distances between centers of the circular grains), and thus the Reynolds number is $Re\approx 2$, which indicates the flow regime is laminar. Drainage period lasts for 0.15 s, and this duration time is chosen such that the front does not arrive the outlet. Then, imbibition begins at t=0.15 s. As initial conditions for the simulation of the imbibition process simulated state variables of the last time step of the drainage period are specified. During imbibition water is injected at the right boundary to displace the n-octane, at a constant specific flux of u_{in}=0.05 m/s. The imbibition lasts until an equilibrium acid (2-NSA) concentration in the domain is obtained. In the whole simulation, the upper and lower sides of the domain are symmetry (free-slip and no-flow) boundaries. The characteristic mobility is χ=25 m·s/kg for the drainage and χ=50 m·s/kg for the imbibition, large enough to maintain the constant thickness of the interface during the simulation (Gao et al. 2021a). The relevant physical properties of the non-wetting fluid (n-octane) are its density ρ_{octane}=703 kg/m^3 and viscosity μ_{octane}=0.54×10^{-3} Pa·s, and the interfacial tension between n-octane and water is σ=0.0504 N/m (Tatomir et al. 2018). The porous medium is water-wet, with a contact angle between the two phases being θ_w=45°. The initial 2-NSA concentration in the domain is zero, and the 2-NSA is only produced by the interfacial reaction following the theory of the KIS tracer. The zero-order reaction rate is assumed to be R_c^{dif}=1 kg·m^{-3}·s^{-1}. The partitioning coefficient is set at P_{ow}=100, therefore the partitioning of the 2-NSA into the n-octane is negligible (Gao et al. 2021a). The distribution of 2-NSA is highly dependent on the rate of advective to diffusive transport rates, described by the Péclet number ($Pe=u_{in}\cdot L_c/D_k$). The molecular diffusion coefficient of the solute is assumed to be D_k=1×10^{-6} m^2/s, resulting in the Péclet numbers of Pe=15.5 and Pe=31 for drainage and imbibition, respectively. The parameters setup ensures that the Péclet number is close to the previously implemented KIS tracer experiments by (Tatomir et al. 2018) and the column experiment in Section 4.4. The 2-NSA concentration breakthrough curve is obtained at the measurement line on the left-hand side of the domain, at the same location as the initial interface was initially positioned (plotted with red dashed line in **Figure 4.2**). The 2-NSA concentration distribution in the domain is monitored in seven representative element volume (REV) domains along the longitudinal direction, labelled as REV 1-7 in **Figure 4.2**(a). Each REV measures 3.6325 mm × 3.53 mm in size. The porosity within randomly distributed frames (with sizes range from 0.2 to 12.8 mm^2) inside the porous medium are analyzed, as shown in **Figure 4.2**(d). The results show that the calculated porosity becomes stable at approximately 47.56% with regard to the domain size close to 12.8 mm^2, and this indicates the chosen REV is reasonable.

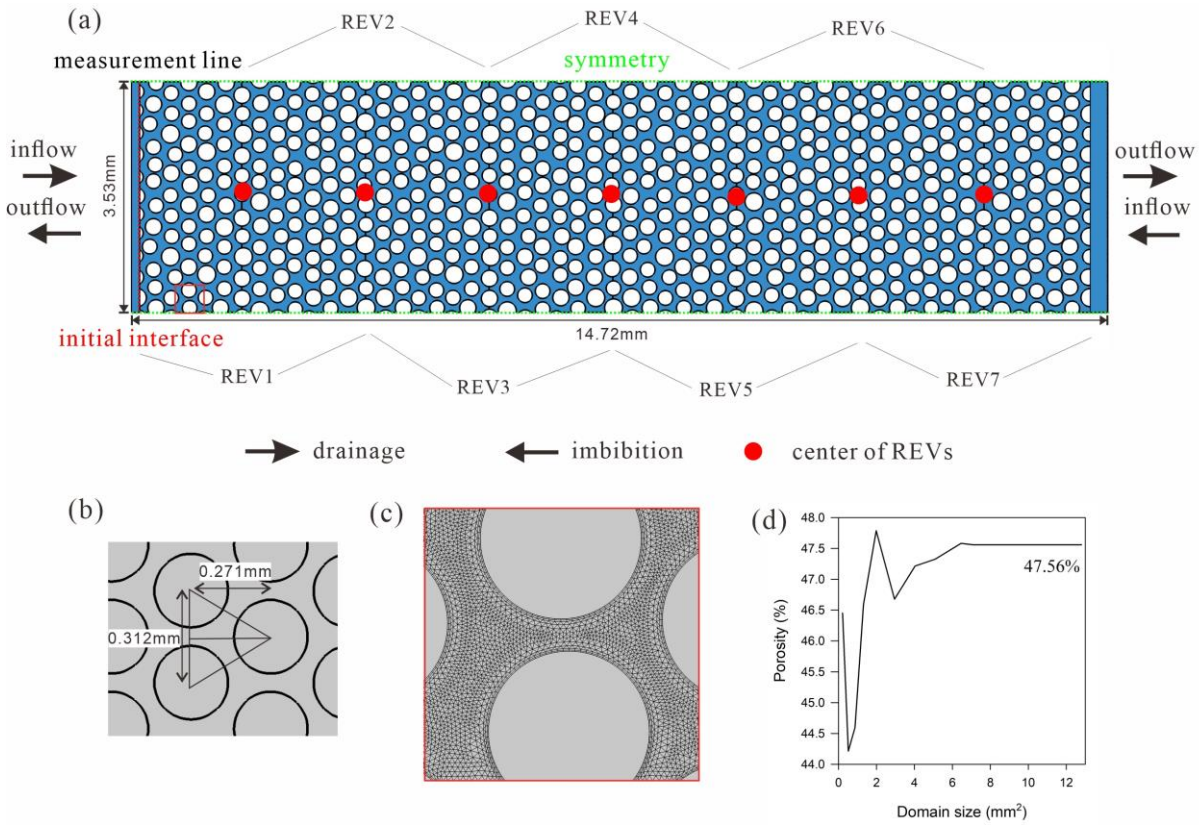

Figure 4.2 Plot of (a) geometry of the two-dimensional porous medium and boundary conditions, with the pore space in blue; (b) initial uniform distribution of the grains; (c) mesh built with triangular elements for a zoom-in section in the red frame (d) analysis of REV based on the porosity.

4.3.3 Pore-scale data treatment

The 2-NSA concentration (c^{BTC}) passing through the measurement line (control plane) can be obtained by dividing the 2-NSA mass flowrate (m^{BTC}) with the water volume flowrate (v_w^{BTC}) that is passing through the measurement line.

$$C^{BTC} = \frac{m^{BTC}}{v_w^{BTC}} \tag{4.18}$$

The 2-NSA mass flux that passing through the measurement line can be obtained with:

$$m^{BTC} = \int_{L_M} u_n c_k dL \tag{4.19}$$

where u_n is the magnitude of the velocity normal to the outlet, and L_M is the measurement line. The volume of water flow that is passing through the measurement line can be obtained with:

$$v_w^{BTC} = \int_{L_M} u_n \delta_w dL \tag{4.20}$$

where δ_w is the function indicating the aqueous phase.

$$\begin{cases} \delta_w = 1 & for\ V_{f,w} \in [0.5, 1] \\ \delta_w = 0 & for\ V_{f,w} \in [0, 0.5) \end{cases} \tag{4.21}$$

Besides, the macro-scale parameters in the domain (e.g. water saturation, specific interfacial area, macro-scale 2-NSA concentration) over the REVs can be obtained from the pore-scale simulation results. The diffusive interfacial area (A_{wn}^{dif}) in the domain and the corresponding sharp interfacial area (A_{wn}) can be calculated with:

$$A_{wn}^{dif} = \int_{V_v} \delta_{IFA}\, dV \quad \text{and} \quad A_{wn} = \frac{A_{wn}^{dif}}{b_{wn}} \tag{4.22}$$

where V_v is the void space in the porous domain, δ_{IFA} is the function indicating the diffusive interfacial region, and b_{wn} is the thickness of the diffusive interface b_{wn}=4.1641ε according to (Gao et al. 2021a).

$$\begin{cases} \delta_{IFA} = 1 \quad for\ V_{f,w} \in [0.05, 0.95] \\ \delta_{IFA} = 0 \quad for\ V_{f,w} \in [0,0.05) \cup (0.95,1] \end{cases} \tag{4.23}$$

Then, the specific interfacial area in the REV domains can be obtained as:

$$a_{wn} = \frac{A_{wn}}{V_p} \tag{4.24}$$

where V_p is the bulk volume of the porous medium. The water saturation in the REV domain can be obtained as:

$$S_w = \frac{\int_{V_v} \delta_w\, dV}{V_v} \tag{4.25}$$

The averaged 2-NSA concentration in the REV domain can be calculated as:

$$C_w = \frac{\int_{V_v} c_k\, dV}{\int_{V_v} \delta_w\, dV} \tag{4.26}$$

4.3.4 Continuum-scale numerical modeling

The breakthrough curve obtained from a push-pull KIS tracer experiment needs to be interpreted using a macro-scale, reactive transport model, to obtain the measured FIFA. In this research, the macro-scale reactive transport model is validated for the push-pull process by applying it to a single one-dimensional simulation (in the longitudinal direction) with the same setup as the pore-scale study. The model (section 4.3.2) is set up at the pore-scale in two dimensions and in one dimension at the macro-scale. The reactive transport model of the KIS tracer transport in the immiscible drainage process was demonstrated in (Tatomir et al. 2018), where transport of the acid is described by an advection-dispersion-reaction equation:

$$\frac{\partial(\Phi S_w C_w)}{\partial t} - \nabla \cdot (C_w \mathbf{U}_\mathrm{w} - D_{dis} \nabla C_w) - R_c \cdot a_{wn} = 0 \tag{4.27}$$

where Φ is the porosity, $\mathbf{U}_\mathrm{w}$ is the specific water flux, D_{dis} is the dispersion coefficient, and C_w is the macro-scale 2-NSA concentration. Water saturation (S_w) in the reactive transport model is obtained from the macro-scale two-phase flow model in Tatomir et al. (2018), where the extended Darcy's law for two phase flow was applied. This requires knowing of the petrophysical properties of the porous media, i.e. the capillary pressure-saturation relation functions and relative permeabilities of both phases for push-pull processes, which need to be determined with complicated processes. Whereas the macro-scale two-phase flow model is not required here for the numerical experiment at pore-scale. Since the saturation in the region drained or flooded behind the moving front remains almost unchanged spatially, the saturation distribution can be explicitly represented by step functions based on the pore-scale simulation results. With the constant front

advancing velocity in push and pull processes (u_f^D and u_f^I), assuming the one-dimension domain at $0 \leq x \leq X_{max}\ mm$ with the inlet at $x = 0$ and t_D for the total time of drainage process, the location of the front can be directly calculated with $u_f^D \cdot t$ for primary drainage and $u_f^D \cdot t_D - u_f^I \cdot (t - t_D)$ for main imbibition. The water saturation during the drainage (push stage) is defined as:

$$\begin{cases} S_w = S_w^D \quad for\ \ x \leq u_f^D \cdot t \\ S_w = 1 \quad for\ \ x > u_f^D \cdot t \end{cases} \tag{4.28}$$

and the water saturation during the imbibition (pull stage) is defined as:

$$\begin{cases} S_w = 1 \quad for\ \ x > u_f^D \cdot t_D \\ S_w = S_w^I \quad for\ \ u_f^D \cdot t_D - u_f^I \cdot (t - t_D) < x \leq u_f^D \cdot t_D \\ S_w = S_w^D \quad for\ \ x \leq u_f^D \cdot t_D - u_f^I \cdot (t - t_D) \end{cases} \tag{4.29}$$

The specific interfacial area is defined as:

$$\begin{cases} a_{wn} = 0 \quad for\ \ S_w = 1 \\ a_{wn} = a_{wn}^I \quad for\ \ S_w = S_w^I \\ a_{wn} = a_{wn}^D \quad for\ \ S_w = S_w^D \end{cases} \tag{4.30}$$

where u_f^D, u_f^I, S_w^D, S_w^I, a_{wn}^D, a_{wn}^I are constants, obtained from pore-scale simulation results. The accuracy of the explicit expression of the two-phase flow is given in section 4.6.1. The specific water flux during the drainage (push) phase is defined as:

$$\begin{cases} \mathbf{U}_\mathrm{w} = 0 \quad for\ \ x \leq u_f^D \cdot t \\ \mathbf{U}_\mathrm{w} = q_w^D\ m/s \quad for\ \ x > u_f^D \cdot t \end{cases} \tag{4.31}$$

The specific water flux during the imbibition (pull) phase is defined as:

$$\begin{cases} \mathbf{U}_\mathrm{w} = q_w^I\ m/s \quad for\ \ x > u_f^D \cdot t_D - u_f^I \cdot t \\ \mathbf{U}_\mathrm{w} = 0 \quad for\ \ x \leq u_f^D \cdot t_D - u_f^I \cdot t \end{cases} \tag{4.32}$$

The specific fluxes given are consistent with the boundary condition of the pore-scale simulation in section 4.3.1. With the assumed unit reaction rate in section 4.3.2, the tracer reaction rate for the simulation is calculated as: $R_c = R_c^{dif} \cdot b_{wn} = 4.16 \times 10^{-5}$ kg·s^{-1}m^{-2}.

4.4 Column experiment

The push-pull KIS tracer method is applied to column experiments. The materials and experimental setup are demonstrated in section 4.4.1, and the experimental procedure is explained in section 4.4.2.

4.4.1 Materials and setup

The setup of the column experiment is demonstrated in **Figure 4.2**(a). The stainless-steel column is positioned vertically, with a length of 30 cm and a diameter of 3 cm. Both ends of the column are sealed by two stainless-steel caps, embedded with a porous frit, which create a uniform distribution of fluids entering/leaving the column and retain the glass beads in the column. Both tubes on the two caps are connected to 3/2-way valves, and each tube leads to either a peristaltic pump connecting to a fluid tank, or an outlet with effluent collected with a measuring cylinder. The n-octane (dissolved with KIS tracer) tank is connected to the top of the column and the water tank is connected to the bottom of the column. The column is packed with glass beads, with the mean diameter of 248 μm. The glass beads have an average roundness of 0.983, and a neglectable surface roughness, as shown in **Figure 4.2**(b). The grain size distribution of the glass beads is shown in **Figure 4.2**(c). The unconsolidated porous medium has a porosity of 38% - 39%, and an intrinsic

permeability at 8×10^{-12} m^2 - 1×10^{-11} m^2 (measured by Tatomir et al., 2018). Furthermore, the deionized water is used as the wetting phase fluid and the n-octane is used as the non-wetting phase fluid. The main properties of the fluids have been given in section 4.3.1. The KIS tracer is dissolved in the n-octane at the concentration of 0.1 g/l, and the hydrolysis reaction rate of the tracer is determined as R_c=1.18×10^{-12} $kg \cdot m^{-2} \cdot s^{-1}$ (Tatomir et al. 2018).

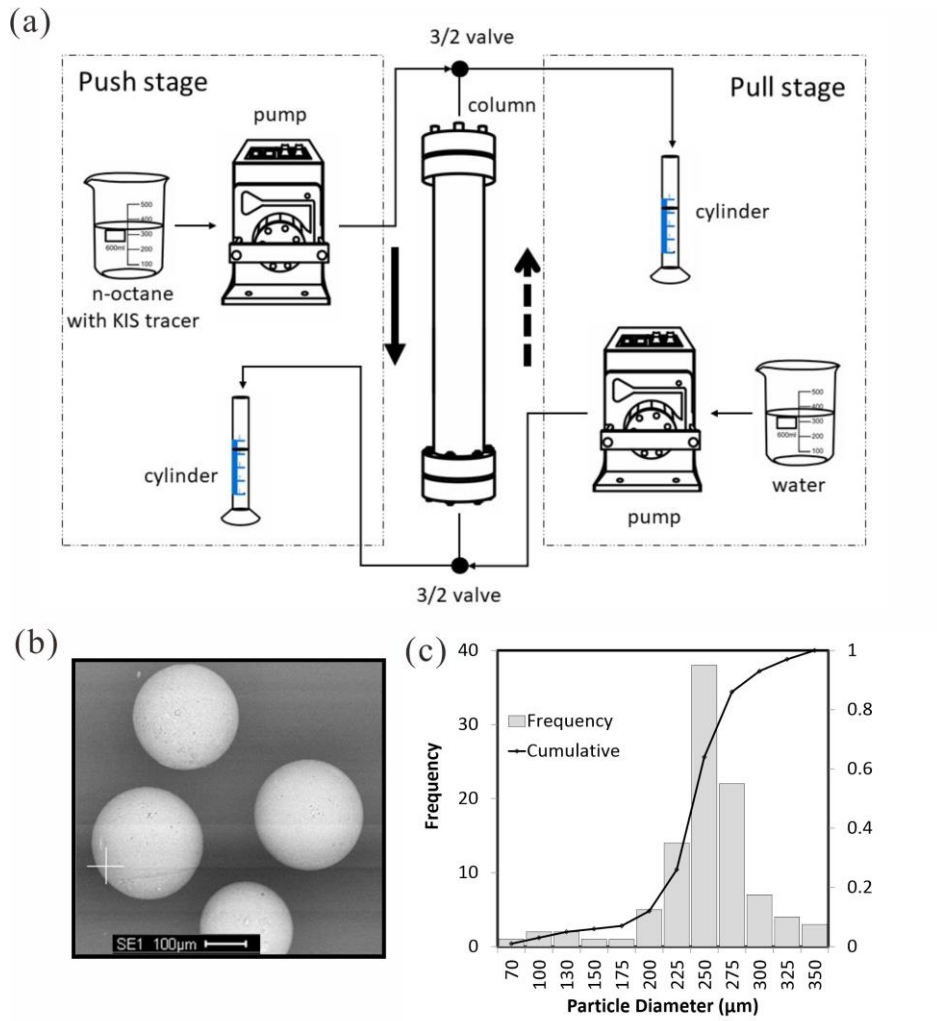

Figure 4.3 Sketch of (a) column experiment setup (with arrows showing the flow direction during push-pull process, (b) scanning electron microscopy image of the glass beads (Tatomir et al. 2018), and (c) grain size distribution of the glass beads.

4.4.2 Experimental procedure

Prior to the experiment, the column is first packed with the dry glass beads. The packing is done in small increments while vibrating the column to ensure a homogeneous medium. To prepare a water saturated column, the water is injected from bottom of the column to slowly displace the air inside the column, and the top of column is connected to the outlet. The total void space is determined from the injected water volume as 82 ml. After the column is saturated with water, water flushing

will continue for 24 hours to ensure that the sand is clean (no residual pollutants from previous experiments), and a constant background fluorescence signal can be determined in the effluent.

The experiment begins by injection of 30 ml n-octane (KIS tracer dissolved) at a flow rate of 0.5ml/min from top of the column, with the bottom of column connecting to the outlet. The n-octane injection (drainage process) last for 1 hour. The front of the n-octane is ensured not to arrive the bottom of the column, because about 55 ml n-octane is necessary for a breakthrough, determined from previous study by Tatomir et al. (2018). Then, by switching the valve, the water is injected at a flow rate of 1ml/min from bottom of the column, with the top of column as the outlet. At the beginning of the imbibition, there is only n-octane coming out from the column, the total effluent n-octane volume is about 18 ml. With observation of the first water bubble in cylinder at outlet, the water sample will be collected by 5ml measuring cylinders and transferred for concentration measurement in the fluorospectrometer. Each water sample volume is larger than 1ml to ensure an accurate fluorescent measurement. The time, the water sample volume and acid concentration are always recorded during the experiment to obtain the resulting tracer breakthrough curve. The measurement last until the decreasing of the acid concentration in water samples are very small (about 1.5 hour of imbibition), meaning the approaching of a steady state.

After each experiment the glass beads were washed and dried over 48 hours. The measured acid concentration is pretreated by deducting the background fluorescence signal, to obtain the final experiment data. In total three experiments are done in the same way (triplicate) to ensure the reproducibility.

4.5 Results and discussion

In section 4.5.1, we present the pore-scale concentration distribution patterns during the push-pull process and compare to the macro-scale reactive transport model. In section 4.5.2 the corresponding concentration BTCs are shown and their interpretation is being discussed. In section 4.5.3 the new push-pull KIS tracer method is applied in the column experiment.

4.5.1 Concentration distributions from the pore-scale simulation

The spatial concentration distribution at t=0.07 s, t=0.15 s, t=0.18 s, t=0.21 s, t=0.24 s, t=0.32 s during the push-pull process is illustrated in **Figure 4.4**(a), together with the corresponding average 2-NSA concentration over the REVs, in **Figure 4.4**(b).

During the primary drainage (push) phase (t=0.07 s, t=0.15 s in **Figure 4.4**a), the receding water is partially entrapped by the invading n-octane, forming the trapped water clusters. The local concentration of the reacted acid (2-NSA) in these trapped water clusters/pockets largely differ among each other, depending on the size of the associated interface and the volume of the water cluster. The water clusters with a smaller volume generally show much higher local 2-NSA concentrations. The reacted acid in the water clusters is not mixed with each other, because the water clusters are isolated from each other by the invading NAPL phase. During drainage, the effects of advective and dispersive transport of the reacted acid is minor, only noticeable at the moving front, where the reacted acid mass is low and negligible compared to that in trapped water clusters. The weak dispersion was also observed in the previous column drainage experiments reported by Tatomir et al. (2018). Average concentration monitored in the REVs for primary drainage is plotted in **Figure 4.4**b (t=0.07 s and t=0.15 s). It can be observed that during the push-stage average concentration in the domain linearly decreases in flow direction with its maximum

being near the inlet. This is because near the inlet the two fluids remain in contact with each other for longer, which means that tracer accumulates in the water clusters as a consequence of the reaction across the fluid-fluid interface.

The spatial 2-NSA concentration distribution during main imbibition (pull) phase is shown in **Figure 4.4**(a) at *t*=0.18 s, *t*=0.21 s. The invading water pushes the NAPL front back, with mobile NAPL flowing towards the outlet (left boundary) and the immobile NAPL being trapped in the domain (residual trapping). With the front being pushed back during main imbibition, the trapped water clusters are released and connected again with the flowing bulk water. In the meantime, the reacted acid present in these water clusters is released and mixed with the flowing water. The acid dissolved and mixed in the flowing water is subjected to advective-dispersive-diffusive transport during main imbibition, which leads to a non-linearly decreasing concentration gradient in longitudinal direction, as shown in **Figure 4.4**(b) at *t*=0.18 s, *t*=0.21 s. The main processes facilitating mixing of acid with fresh water in the flooded region are mechanical dispersion and molecular diffusion. When the wetting-phase front arrives at the inlet (left boundary) at *t*=0.21 s, the effluent changes from NAPL to water, and the tracer breakthrough commences.

As main imbibition (pull stage) proceeds, the 2-NSA concentration and phase distribution patterns approach steady state, shown in **Figure 4.4**(a) for *t*=0.24 s and *t*=0.32 s. The KIS tracer dissolved in the residual NAPL, i.e. trapped NAPL clusters in the domain, continues to react at the interface with the flowing water, and the generated acid mass is further transported towards the left boundary and the measurement (control/reference) line. When the system approaches steady state, a constant effluent acid concentration can be obtained, resulting from the reaction at the interfaces associated with the residual NAPL. The average 2-NSA concentration in the porous domain almost linearly decreases in longitudinal direction, as shown in **Figure 4.4**b (*t*=0.32 s).

Then, the macro-scale reactive transport model is compared it to pore-scale simulation results, as shown in **Figure 4.4**(b). The concentration distribution of the macro-scale reactive transport model (blue dashed lines) match very well with the pore-scale simulation results (red dots) in the push-pull process. The root-mean-square errors (RMSE) range from 0.0006 to 0.0024 kg/m^3. The dispersion coefficient applied for the simulation of main imbibition (D_{dis}^{I}=1×10^{-5} m^2/s) is two orders of magnitude larger than that for the primary drainage phase (D_{dis}^{D}=1×10^{-7} m^2/s). This observation of significant differences between the dispersion coefficients from primary drainage and main imbibition matches the results from the experimental study by Chen et al. (2021), applying X-RCT.

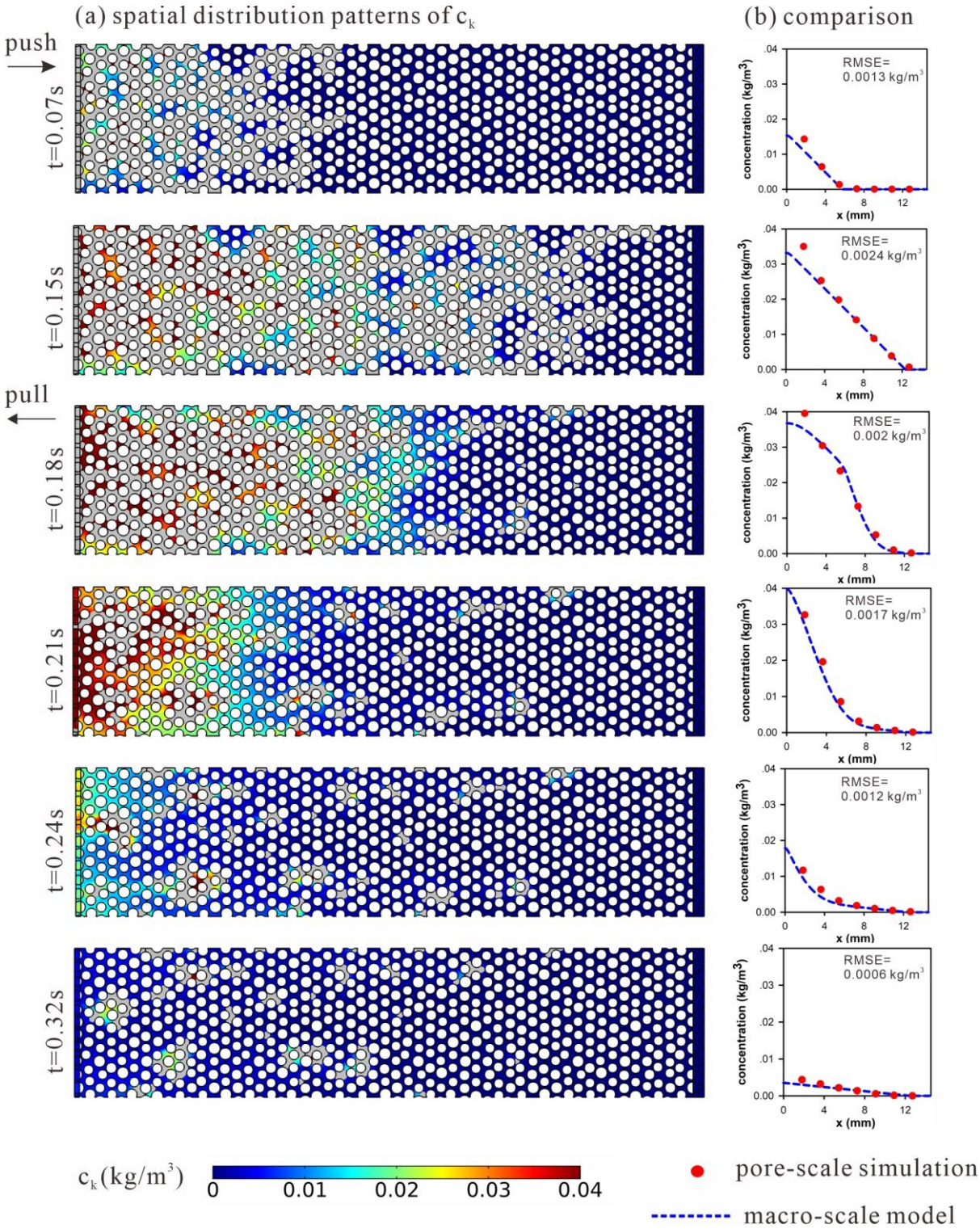
(a) spatial distribution patterns of c_k
(b) comparison
push
pull
t=0.07s
t=0.15s
t=0.18s
t=0.21s
t=0.24s
t=0.32s
RMSE= 0.0013 kg/m³
RMSE= 0.0024 kg/m³
RMSE= 0.002 kg/m³
RMSE= 0.0017 kg/m³
RMSE= 0.0012 kg/m³
RMSE= 0.0006 kg/m³
concentration (kg/m³)
x (mm)
c_k (kg/m³)
0
0.01
0.02
0.03
0.04
pore-scale simulation
macro-scale model

Figure 4.4 Plot of the 2-NSA concentration during the push-pull process at t=0.07 s, t=0.15 s, t=0.18 s, t=0.21 s, t=0.24 s and t=0.32 s: (a) spatial distribution of 2-NSA concentration from pore-scale simulation, with NAPL plotted in gray; (b) comparison between averaged 2-NSA concentration in the REVs from pore-scale simulation (red dots) and NSA concentration predicted by the macro-scale reactive transport model (in blue dashed lines).

Furthermore, the accuracy of explicit expression of two-phase flow is tested by comparing it to the average S_w and a_{wn} obtained from the REVs, at t=0.07 s, t=0.15 s for primary drainage and t=0.18 s, t=0.24 s for main imbibition, as shown in **Figure 4.5**. It is observed that, with S_w^D=0.376, S_w^I=0.906, a_{wn}^D=976 1/m, a_{wn}^I=340 1/m, the macro-scale explicit expression (dashed line in **Figure 4.5**) can generally approximate the pore-scale simulated two-phase flow. During primary drainage, S_w and a_{wn} in the drained region are more or less spatially invariable, and thus the explicit expression using the step functions matches the pore-scale simulation of saturation and interfacial area (with RMSE up to 0.047 for the saturation and 67 1/m for the specific interfacial area). However, during main imbibition, S_w in the flooded region shows slightly increasing trends toward the right, which causes a small deviation (with RMSE up to 0.085), shown in **Figure 4.5** at t=0.18 s and t=0.24 s. Thus, the predicted a_{wn} during main imbibition also has slightly larger deviations with RMSE up to 223 1/m. It is worth noting that the explicit expression assuming a sharp and stable front approximates the pore-scale simulation very well. Reason being that because the porous domain is small in extent macroscopically it can be considered as highly homogeneous.

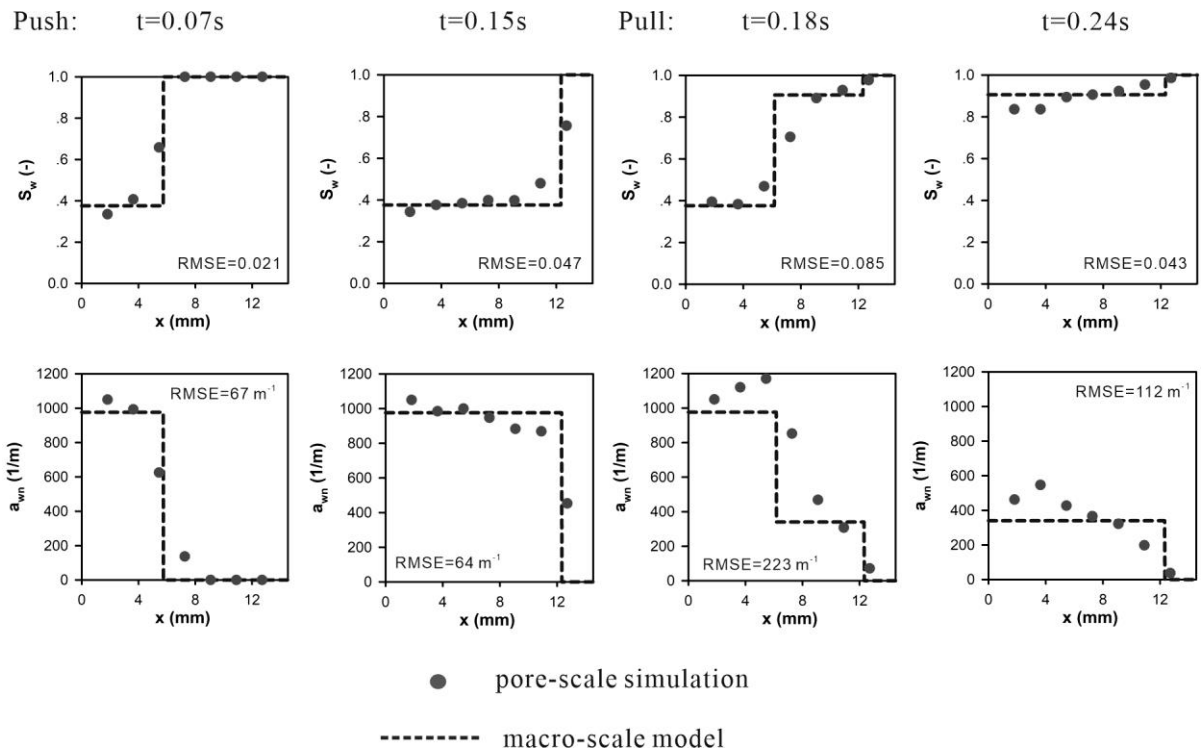

Figure 4.5 S_w and a_{wn} obtained from the REVs of pore-scale simulations (in dots), and S_w and a_{wn} given by explicit expression for the macro-scale reactive transport model (in dashed lines), during the push-pull process.

4.5.2 Interpretation of the breakthrough curve

After calibrating the two-phase flow (saturation distribution and specific interfacial area) to the pore-scale numerical experiment, the 2-NSA concentration breakthrough curves obtained from the pore-scale simulations (dotted line) and the macro-scale reactive transport model (continuous line) are shown in **Figure 4.6**(a). It can be seen that the macro-scale reactive transport model matches the concentration breakthrough curve of the pore-scale numerical experiment well, with RMSE=0.0012 kg/m^3. The effluent 2-NSA concentration decreases non-linearly with time, and the rate of decrease in concentration slows down with time. The tailing concentration is asymptotically reaching a plateau when the system approaches a steady state. In a push-pull KIS tracer experiment, the dispersion coefficient and the specific interfacial area need to be obtained by fitting the concentration BTCs of the experiment and the macro-scale reactive transport model. Thus, it is necessary to understand how these two parameters (a_{wn} and D_{dis}) affect the concentration BTCs by a sensitivity analysis.

The sensitivity analysis is performed by systematically changing one parameter at a time using the calibrated macro-scale model of section 4.5.1, while keeping all other parameters constant. The interfacial area for primary drainage (a_{wn}^{D}) is swapped and plotted in **Figure 4.6**(b). Peak concentration at early times of breakthrough significantly changes with respect to different a_{wn}^{D} values. This is because the concentration peak is mainly controlled by 2-NSA released from trapped water clusters, where the reaction rate is determined by the interfacial area created in the drained

region during primary drainage. The 2-NSA released from trapped water clusters accumulates in the retracting water during the "pull" stage, and this leads to the peak of concentration right after the breakthrough. Because all drained regions are flooded after breakthrough during main imbibition, a_{wn}^{D} no longer affects the concentration BTCs at steady state. The interfacial area in main imbibition (a_{wn}^{I}) is also systematically varied and plotted in **Figure 4.6**(c). It can be observed that the steady state tailing 2-NSA concentration varies with different a_{wn}^{I} values. At steady state, the cumulative volume of the NAPL clusters and the fluid-fluid interfaces do not change, resulting in a constant production rate of the reacted tracer in the whole porous domain. The 2-NSA production at steady state strongly depends on the magnitude of the interfacial area in contact with the residual NAPL phase formed during main imbibition. Furthermore, **Figure 4.6**(d) shows results of the sensitivity analysis with respect to the dispersion coefficient during main imbibition (D_{dis}^{I}). It can be observed that a change in dispersion coefficient changes the shape of the BTC, i.e. for higher dispersion coefficients, the decrease in concentration takes longer for steady-state concentration to be reached, and the peak concentration is lower. The time for the BTCs to reach steady-state concentration only depends on the dispersion coefficient, and it is not affected by the magnitude of the interfacial area.

The results imply that, by matching the macro-scale model breakthrough and the corresponding BTCs obtained from a push-pull KIS tracer experiment, the dispersion coefficient can directly be determined from the time it takes for the BTCs to approach tailing concentration plateau. Then the specific interfacial areas created during primary drainage and during main imbibition can be determined from the magnitudes of the peak concentration and tailing concentration from the BTCs, respectively.

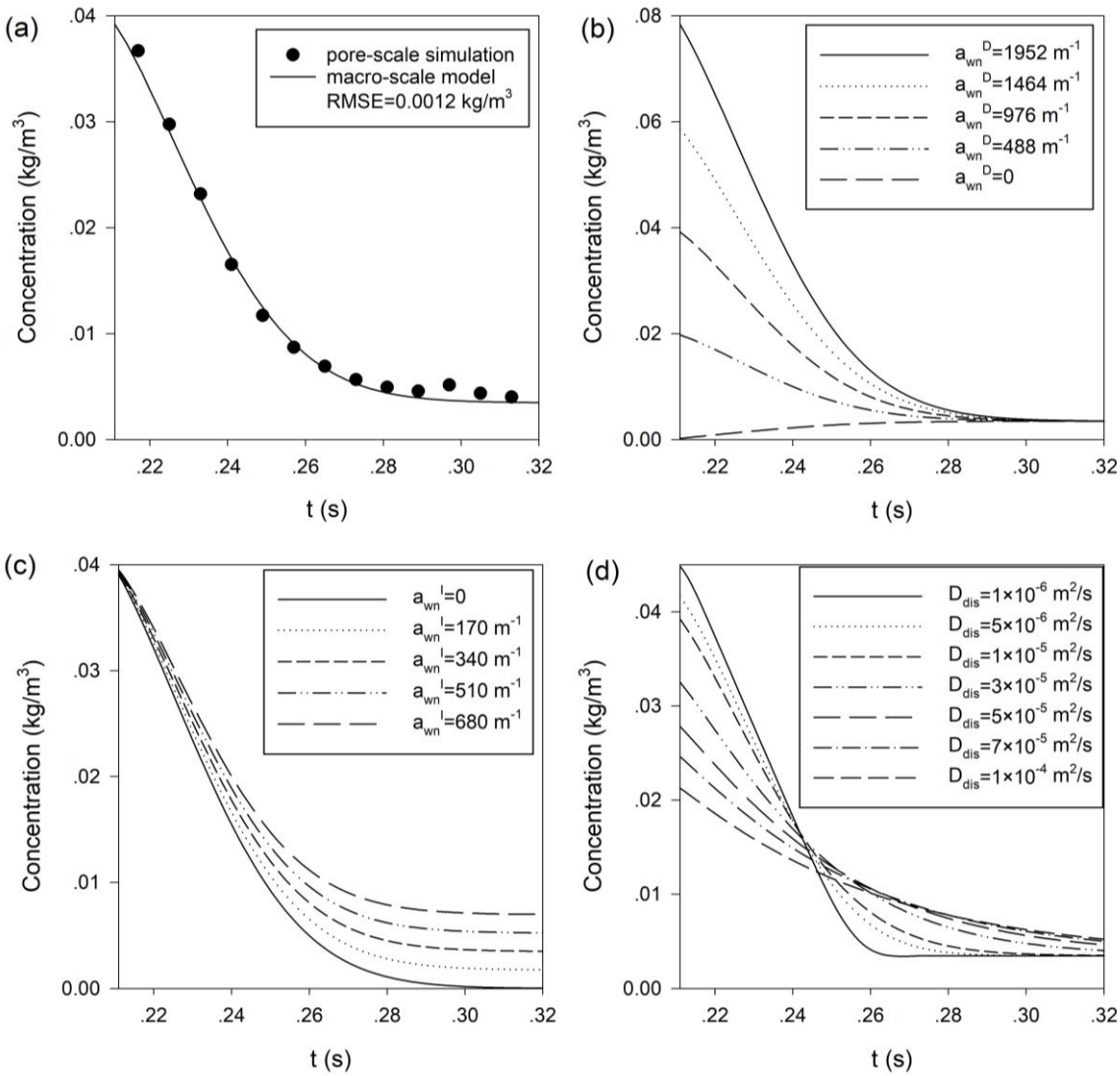

Figure 4.6 Plot of the 2-NSA concentration BTCs: (a) comparison of the concentration BTC monitored at the measurement line (control plane) of the pore-scale simulations (dots) and of the calibrated macro-scale model (line). Sensitivity analysis of (b) specific interfacial area during primary drainage (a_{wn}^{D}), (c) specific interfacial area during main imbibition (a_{wn}^{I}), and (d) dispersion coefficient for main imbibition (D_{dis}^{I}).

4.5.3 Application to column experiments

Finally, the concept of the push-pull KIS tracer method is proved through the column experiment. The concentration breakthrough curves from three (triplicate) experiments are obtained and plotted in **Figure 4.7**(a). The three (triplicate) experiments fit each other well, which proves the reproducibility of the experiment. Each experiment has about 17 usable data points (after breakthrough and before the steady state), and each water sample has volume of 2-5 ml depending on the time interval. This implies that the limitation of few usable water samples in the previous

drainage KIS tracer experiments is overcame by the push-pull setting. With the sufficient sample volume, the shapes of the BTCs can be more accurately determined.

To measure the FIFA, the data need to be interpreted by matching to the macro-scale reactive transport model (Eq.4.27), where two phase flow condition is first determined. The saturation distribution in the column experiment is again approximated with the step functions described in Section 4.3.4 and a sharp front is assumed. This is reasonable because it is observed from the top of column during the "pull" stage that the effluent turning from n-octane (100%) to water (100%) when the first water bubble is observed. This fast change may result from a sharp front. Another reason could be that the sphere glass beads used are well-sorted with quite uniform grain sizes around 250 μm. From the previous drainage experiment by Tatomir et al. (2018), it is known that about 55ml n-octane is used to drain the full column. As the total void space is 82 ml, the $S_w^D = 0.33$ is calculated. With injection of 30 ml n-octane in one hour, the maximum distance of the front travelled during drainage can be calculated as 16.4 cm, and front velocity u_f^D=4.545×10^{-5} m/s is calculated. As 18ml n-octane is recovered during main imbibition, $S_w^I = 0.73$ can be calculated for the flooded region. With the observation time for effluent turning from n-octane to water (*t*=4680s), the front velocity can be calculated u_f^D=1.515×10^{-4} m/s.

Then, it is found that with the dispersion coefficient D_{dis}^I=8×10^{-7} m^2/s, the specific interfacial area a_{wn}^D=240 1/m and a_{wn}^I=120 1/m, the BTC predicted from the macro-scale reactive transport model (Eq.4.27) can well fit the experimental data with RMSE up to 0.29 μg/l, as shown in in **Figure 4.7**(a). The obtained average specific interfacial areas for primary drainage and main imbibition are consistent with the results from Culligan et al. (2004) and slightly smaller than that from Porter et al. (2010), where the FIFA is measured with X-RCT, as shown in in **Figure 4.7**(b). The measured FIFA is also within the range predicted with the KIS tracer experiment in the previous work of Tatomir et al. (2020) for primary drainage. Additionally, the results imply that the push-pull KIS tracer is not sensitive to water films adsorbed on grain surfaces, since the FIFA measured is much smaller than that predicted from IPTT tracer methods (with film associated FIFA included), e.g. work by Brusseau et al. (2009), Brusseau et al. (2010) and McDonald et al. (2016). Because the water films have thicknesses of only few molecules, the small mass could make it deplete fast with the hydrolysis reaction to the tracer. Thus, the water films contribute very little in the experiment. It worth noting that, the capillary condensed water for the grains with rough surfaces is not relevant for this study, because the glass beads applied here have smooth surfaces.

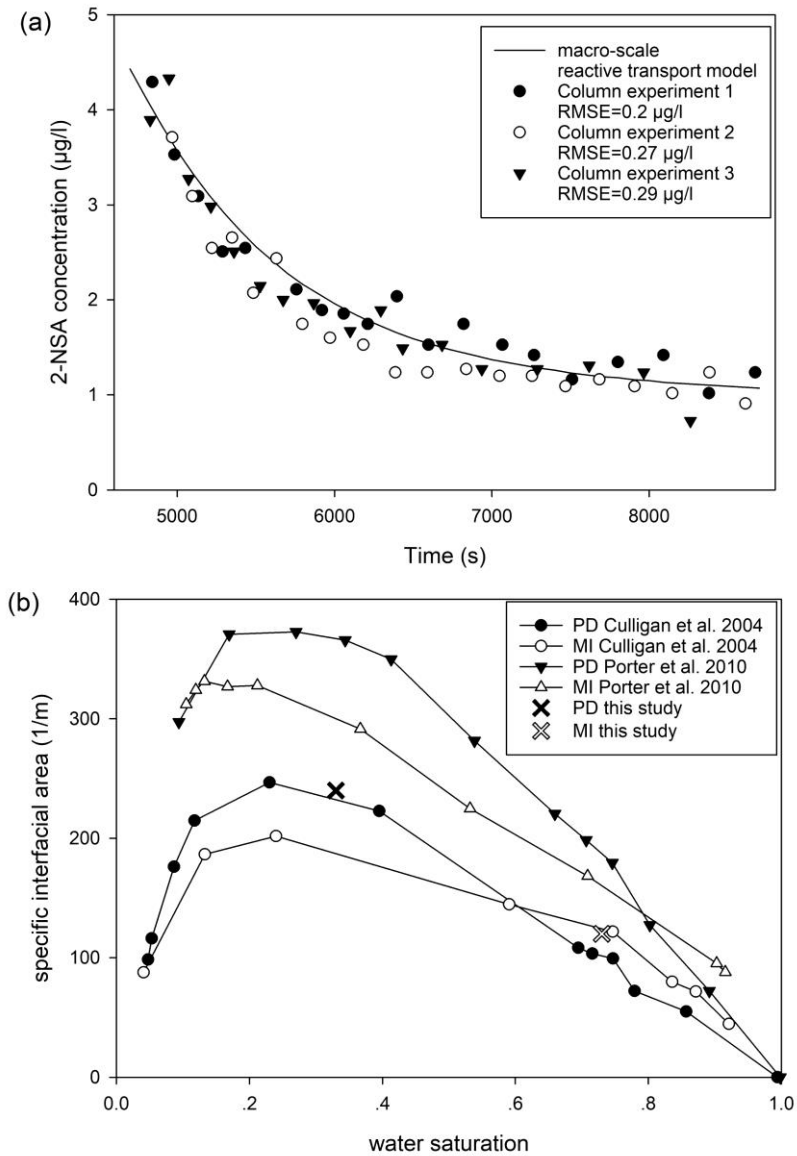

Figure 4.7 Results from the column experiment: (a) fitting of the BTCs from the macro-scale reactive transport model to the (triplicate) column experimental results; (b) comparing the measured specific FIFA from primary drainage (PD) and main imbibition (MI) to the results obtained from X-RCT by Culligan et al. (2004) and Porter et al. (2010).

4.6 Summary and Conclusions

KIS tracer reactive transport was studied by pore-scale simulations conducted employing the PFM-CST model for a 2D porous medium push-pull experiment in order to investigate whether the pore-scale processes can be simulated in a large-scale continuum modelling approach and in how far important parameter such as interfacial area a_{wn} and dispersion coefficient D_{dis} can independently be obtained from the experimental breakthrough signal. The ability of the new push-pull KIS tracer

method for determination of the FIFA was demonstrated in the column experiment. The major results and findings of the study are listed below:

- The advective and dispersive transport of the tracer is very weak during primary drainage but becomes more prominent during main imbibition. The dispersion coefficient for main imbibition can be two orders of magnitude larger than that for primary drainage.
- The tracer concentration BTCs show a non-linearly decreasing profile with time, i.e. the slope of the BTCs reduces with time, and the tailing concentration reaches a plateau.
- After calibrating the two-phase flow condition (distribution of S_w and $\mathbf{U}_w$), it is found that previously developed macro-scale KIS tracer reactive transport models by (Tatomir et al. 2015; Tatomir et al. 2018) can be used for simulation and interpretation of push-pull experiments.
- It is found that the magnitude of the peak at the beginning of BTCs is determined by the specific interfacial area created during primary drainage, and the constant tailing concentration is determined by the specific interfacial area associated with residual NAPL after main imbibition. The time to approach steady-state tailing concentration plateau depends largely on the dispersion coefficient.
- Through the column experiment with the push-pull KIS tracer method, the specific FIFA for the porous medium comprised of sphere glass beads with the mean diameter of 248μm is determined as a_{wn}^{D}=240 1/m at saturation of $S_w^D = 0.33$ during the primary drainage and a_{wn}^{I}=120 1/m at saturation of $S_w^I = 0.73$ during the main imbibition.

This study demonstrated a new "push-pull KIS tracer method", for measuring the (capillary-associated) FIFA during dynamic two-phase displacement processes. This method has the potential to be considered in field-sale applications. Future work is required to implement the column experiment with a variety of "push-pull" flow rates, to measure the FIFA at different saturations. Future work is also required to extend the application the "push-pull KIS tracer method" to measure the FIFA for porous media in a wider range of porous media comprised of glass beads and natural soils with different grain sizes and textures.

4.7 Acknowledgement

We acknowledge funding by the German Research Foundation (Deutsche Forschungsgemeinschaft, DFG) Project Number 428614366. HS and NKK acknowledge funding by the DFG within the Collaborative Research Center 1313 (Project Number 327154368 – SFB 1313). HS acknowledges funding by DFG under Germany's Excellence Strategy - EXC 2075 - 390740016.

All data used to support this work are reported in the manuscript and the supporting information in the respective tables and figures.

4.8 Reference

Alpak FO, Riviere B, Frank F (2016) A phase-field method for the direct simulation of two-phase flows in pore-scale media using a non-equilibrium wetting boundary condition. Comput Geosci 20:881–908. https://doi.org/10.1007/s10596-015-9551-2

Badalassi VE, Ceniceros HD, Banerjee S (2003) Computation of multiphase systems with phase field models. J Comput Phys 190:371–397. https://doi.org/10.1016/S0021-9991(03)00280-8

Basirat F, Yang Z, Niemi A (2017) Pore-scale modeling of wettability effects on CO2–brine displacement during geological storage. Adv Water Resour 109:181–195. https://doi.org/10.1016/j.advwatres.2017.09.004

Brusseau ML, Narter M, Janousek H (2010) Interfacial Partitioning Tracer Test Measurements of Organic-Liquid/Water Interfacial Areas: Application to Soils and the Influence of Surface Roughness. Environ Sci Technol 44:7596–7600. https://doi.org/10.1021/es101312n

Brusseau ML, Narter M, Schnaar G, Marble J (2009) Measurement and Estimation of Organic-Liquid/Water Interfacial Areas for Several Natural Porous Media. Environ Sci Technol 43:3619–3625. https://doi.org/10.1021/es8020827

Cahn JW, Hilliard JE (1959) Free Energy of a Nonuniform System. III. Nucleation in a Two-Component Incompressible Fluid. J Chem Phys 31:688–699. https://doi.org/10.1063/1.1730447

Chen Y, Steeb H, Erfani H, Karadimitriou NK, Walczak MS, Ruf M, Lee D, An S, Hasan S, Connolley T, Vo NT, Niasar V (2021) Nonuniqueness of hydrodynamic dispersion revealed using fast 4D synchrotron x-ray imaging. Sci Adv. https://doi.org/10.1126/sciadv.abj0960

Culligan KA, Wildenschild D, Christensen BSB, Gray WG, Rivers ML, Tompson AFB (2004) Interfacial area measurements for unsaturated flow through a porous medium. Water Resour Res 40:W12413. https://doi.org/10.1029/2004WR003278

Davis BM, Istok JD, Semprini L (2002) Push–pull partitioning tracer tests using radon-222 to quantify non-aqueous phase liquid contamination. J Contam Hydrol 58:129–146. https://doi.org/10.1016/S0169-7722(02)00010-4

Ferrari A, Lunati I (2013) Direct numerical simulations of interface dynamics to link capillary pressure and total surface energy. Adv Water Resour 57:19–31. https://doi.org/10.1016/j.advwatres.2013.03.005

Gao H, Tatomir AB, Karadimitriou NK, Steeb H, Sauter M (2021a) A Two-Phase, Pore-Scale Reactive Transport Model for the Kinetic Interface-Sensitive Tracer. Water Resour Res 57:e2020WR028572. https://doi.org/10.1029/2020WR028572

Gao H, Tatomir AB, Karadimitriou NK, Steeb H, Sauter M (2021b) Effects of surface roughness on the kinetic interface-sensitive tracer transport during drainage processes. Adv Water Resour 157:104044. https://doi.org/10.1016/j.advwatres.2021.104044

Godinez-Brizuela OE, Karadimitriou NK, Joekar-Niasar V, Shore CA, Oostrom M (2017) Role of corner interfacial area in uniqueness of capillary pressure-saturation- interfacial area relation under transient conditions. Adv Water Resour 107:10–21. https://doi.org/10.1016/j.advwatres.2017.06.007

Gómez K, Gonzalez-Gil G, Schroth MH, Zeyer J (2008) Transport of Methane and Noble Gases during Gas Push−Pull Tests in Variably Saturated Porous Media. Environ Sci Technol 42:2515–2521. https://doi.org/10.1021/es072036y

Hassanizadeh SM, Gray WG (1990) Mechanics and thermodynamics of multiphase flow in porous media including interphase boundaries. Adv Water Resour 13:169–186. https://doi.org/10.1016/0309-1708(90)90040-B

Istok J d., Field J a., Schroth M h., Sawyer T e., Humphrey M d. (1999) Laboratory and Field Investigation of Surfactant Sorption Using Single-Well, “Push-Pull” Tests. Groundwater 37:589–598. https://doi.org/10.1111/j.1745-6584.1999.tb01146.x

Istok JD, Field JA, Schroth MH, Davis BM, Dwarakanath V (2002) Single-Well “Push−Pull” Partitioning Tracer Test for NAPL Detection in the Subsurface. Environ Sci Technol 36:2708–2716. https://doi.org/10.1021/es015624z

Istok JD, Humphrey MD, Schroth MH, Hyman MR, O’Reilly KT (1997) Single-Well, “Push-Pull” Test for In Situ Determination of Microbial Activities. Groundwater 35:619–631. https://doi.org/10.1111/j.1745-6584.1997.tb00127.x

Jacqmin D (1999) Calculation of Two-Phase Navier–Stokes Flows Using Phase-Field Modeling. J Comput Phys 155:96–127. https://doi.org/10.1006/jcph.1999.6332

Karadimitriou NK, Hassanizadeh SM, Joekar-Niasar V, Kleingeld PJ (2014) Micromodel study of two-phase flow under transient conditions: Quantifying effects of specific interfacial area. Water Resour Res 50:8125–8140. https://doi.org/10.1002/2014WR015388

Liu H, Valocchi AJ, Werth C, Kang Q, Oostrom M (2014) Pore-scale simulation of liquid CO2 displacement of water using a two-phase lattice Boltzmann model. Adv Water Resour 73:144–158. https://doi.org/10.1016/j.advwatres.2014.07.010

Lowengrub J, Truskinovsky L (1998) Quasi–incompressible Cahn–Hilliard fluids and topological transitions. Proc R Soc Lond Ser Math Phys Eng Sci 454:2617–2654. https://doi.org/10.1098/rspa.1998.0273

McDonald K, Carroll KC, Brusseau ML (2016) Comparison of Fluid-Fluid Interfacial Areas Measured with X-ray Microtomography and Interfacial Partitioning Tracer Tests for the same Samples. Water Resour Res 52:5393–5399. https://doi.org/10.1002/2016WR018775

Meakin P, Tartakovsky AM (2009) Modeling and simulation of pore-scale multiphase fluid flow and reactive transport in fractured and porous media. Rev Geophys 47:RG3002. https://doi.org/10.1029/2008RG000263

Miller CT, Poirier-McNeil MM, Mayer AS (1990) Dissolution of Trapped Nonaqueous Phase Liquids: Mass Transfer Characteristics. Water Resour Res 26:2783–2796. https://doi.org/10.1029/WR026i011p02783

Montemagno CD, Gray WG (1995) Photoluminescent volumetric imaging: A technique for the exploration of multiphase flow and transport in porous media. Geophys Res Lett 22:425–428. https://doi.org/10.1029/94GL02697

Porter ML, Wildenschild D, Grant G, Gerhard JI (2010) Measurement and prediction of the relationship between capillary pressure, saturation, and interfacial area in a NAPL-water-glass bead system. Water Resour Res 46. https://doi.org/10.1029/2009WR007786

Schaffer M, Maier F, Licha T, Sauter M (2013) A new generation of tracers for the characterization of interfacial areas during supercritical carbon dioxide injections into deep saline aquifers: Kinetic interface-sensitive tracers (KIS tracer). Int J Greenh Gas Control 14:200–208. https://doi.org/10.1016/j.ijggc.2013.01.020

Schroth MH, Istok JD, Haggerty R (2000) In situ evaluation of solute retardation using single-well push–pull tests. Adv Water Resour 24:105–117. https://doi.org/10.1016/S0309-1708(00)00023-3

Tatomir A, Vriendt KD, Zhou D, Gao H, Duschl F, Sun F, Licha T, Sauter M (2018) Kinetic Interface Sensitive Tracers: Experimental Validation in a Two-Phase Flow Column Experiment. A Proof of Concept. Water Resour Res 54:10,223-10,241. https://doi.org/10.1029/2018WR022621

Tatomir A, Zhou D, Gao H, Dimache A-N, Iancu I, Sauter M (2019) Modelling of kinetic interface sensitive tracers reactive transport in 2D two-phase flow heterogeneous porous media. E3S Web Conf 85:07003. https://doi.org/10.1051/e3sconf/20198507003

Tatomir AB, Gao H, Pötzl C, Karadimitriou NK, Licha T, Class H, Helmig RH, Sauter M (2020) Estimation of NAPL-Water interfacial areas for unconsolidated porous media by kinetic interface sensitive (KIS) tracers. In: Earth Space Sci. Open Arch. http://www.essoar.org/doi/10.1002/essoar.10503948.1. Accessed 25 Apr 2021

Tatomir AB, Jyoti A, Sauter M (2016) Monitoring of CO2 Plume Migration in Deep Saline Formations with Kinetic Interface Sensitive Tracers (A Numerical Modelling Study for the Laboratory). In: Vishal V, Singh TN (eds) Geologic Carbon Sequestration: Understanding Reservoir Behavior. Springer International Publishing, Cham, pp 59–80

Tatomir AB, Schaffer M, Kissinger A, Hommel J, Nuske P, Licha T, Helmig R, Sauter M (2015) Novel approach for modeling kinetic interface-sensitive (KIS) tracers with respect to time-dependent interfacial area change for the optimization of supercritical carbon dioxide injection into deep saline aquifers. Int J Greenh Gas Control 33:145–153. https://doi.org/10.1016/j.ijggc.2014.11.020

Tomich JF, Dalton RL Jr, Deans HA, Shallenberger LK (1973) Single-Well Tracer Method To Measure Residual Oil Saturation. J Pet Technol 25:211–218. https://doi.org/10.2118/3792-PA

Urmann K, Gonzalez-Gil G, Schroth MH, Hofer M, Zeyer J (2005) New Field Method: Gas Push−Pull Test for the In-Situ Quantification of Microbial Activities in the Vadose Zone. Environ Sci Technol 39:304–310. https://doi.org/10.1021/es0495720

Yue P, Feng JJ, Liu C, Shen J (2004) A diffuse-interface method for simulating two-phase flows of complex fluids. J Fluid Mech 515:293–317. https://doi.org/10.1017/S0022112004000370

Zhou C, Yue P, Feng JJ, Ollivier-Gooch CF, Hu HH (2010) 3D phase-field simulations of interfacial dynamics in Newtonian and viscoelastic fluids. J Comput Phys 229:498–511. https://doi.org/10.1016/j.jcp.2009.09.039

5. Kinetic Interface Sensitive Tracers – Experimental Validation in a Two-Phase Flow Column Experiment. A Proof of Concept

A. Tatomir[1], K. De Vriendt[1], D. Zhou[1], H. Gao[1], F. Duschl[2], F. Sun[1], T. Licha[1], and M. Sauter[1]

Citation:

Tatomir A, Vriendt KD, Zhou D, Gao H, Duschl F, Sun F, Licha T, Sauter M (2018) Kinetic Interface Sensitive Tracers: Experimental Validation in a Two-Phase Flow Column Experiment. A Proof of Concept. Water Resour Res 54:10,223-10,241. https://doi.org/10.1029/2018WR022621

[1] Department of Applied Geology, Geoscience Centre of the University of Göttingen, Goldschmidtstr. 3, 37077, Göttingen, Germany

[2] Department of Structural Geology and Geodynamics, Geoscience Centre of the University of Göttingen, Goldschmidtstr. 3, 37077, Göttingen, Germany

Corresponding author: Alexandru Tatomir (alexandru.tatomir@geo.uni-goettingen.edu)

Abstract:

The quantification of the interfacial area (IFA) between different fluids in a multiphase system in porous media has been a subject of growing interest in disciplines where mass-transfer across fluid interfaces is of importance. In this study, a proof of concept for a novel kinetic interface sensitive (KIS) tracer is provided through employing a well-controlled dynamic column experiment in conjunction with a macroscale two phase flow reactive transport model. KIS-Tracers were designed to determine the effective IFA between a non-wetting and a wetting phase, e.g. CO_2 and brine, in order to assess for example chemical reaction rates and mass transfer at this specific boundary. This study shows for the first time the potential of KIS tracers in assessing the specific IFA for a known capillary pressure-saturation relationship under laboratory conditions, using a principle, low-cost experimental setup.

An academic two phase flow four component reactive transport numerical model using a standard vertex-centered finite volume method, and a commercial two phase flow two component transport model using the finite element method were developed to simulate the oil flooding of an initially water saturated column and KIS tracer breakthrough curves obtained from experimental data. These curves were subsequently used to approximate the specific IFA using a polynomial relationship. A highly controlled experimental setup and a well characterized porous media system were a key aspect in reducing the level of uncertainty within the experimental system, ultimately contributing towards the well matched numerical results to the n-octane and KIS tracer column tests results.

5.1 Introduction

Quantification of the fluid-fluid interfacial area (IFA) is essential for the understanding of multi-phase fluid flow and the mass- and energy-transfer processes in porous media systems (Miller et al. 1990; Hassanizadeh and Gray 1990; Reeves and Celia 1996; Niessner and Hassanizadeh 2009; Kibbey and Chen 2012). At the pore-scale level, the distribution of fluid phases in the porous matrix determines macro-scale quantities, such as (residual) saturations, the fluid-fluid interfacial areas (IFAs), the capillary pressures, and the relative permeability of each phase involved (Reeves and Celia 1996). The importance of tracking the fluid-fluid interface is of significance in many multidisciplinary fields and problems where (reactive) mass-transfer across an interface of relevance (e.g. dissolution, hydrolysis, volatilization and adsorption) (Helland and Skjæveland 2007; Joekar-Niasar and Hassanizadeh 2011).

During the past decade, extensive research and attention has been directed towards using deep geologic formations as a mean for CO_2 storage. Subsurface injection of CO_2 is not only believed to be one of the simplest routes to sequestration, but large storage capacities of such formations make this method of greenhouse gas control an area of particular interest (Lackner 2003; IPCC 2005; Cook 2017). For the successful deployment of this technique, a robust understanding of CO_2 migration with time is essential for optimizing injection strategies and enhancing CO_2 trapping mechanisms. Furthermore, robust monitoring techniques, such as tracer methods are required to investigate the actual flow path and reservoir volume and to demonstrate the technology to be safe and ready to be deployed. As a result, fields such as enhanced oil recovery, assessment of potential nuclear waste repositories, and the remediation of non-aqueous phase liquid contaminated sites may largely benefit from understanding and tracking fluid-fluid interfaces in porous media.

Macroscopic interphase mass transfer is implicitly understood to be a function of the mass transfer coefficient and the specific IFA between the two phases in question, a_{wn}, (Miller et al. 1990; Powers et al. 1992).

$$r^k_{\alpha\to\beta} = R^k_{\alpha\to\beta} a_{wn}\left(C^k_{\beta,s} - C\right). \tag{5.1}$$

Since little is known about the a_{wn}, a common approach has been to lump this quantity with the mass transfer rate coefficient in the Sherwood number (e.g., Zhang and Schwartz 2000).

$$R^k_{\alpha\to\beta} = Sh\frac{D_m}{d_{50}^2}, \tag{5.2}$$

$$Sh = \alpha Re^{\beta_1} S_n^{\beta_2}, \tag{5.3}$$

where the mass transfer coefficient or reaction rate coefficient ($R^k_{\alpha\to\beta}$) is a property of the Sherwood number (Sh), the aqueous phase molecular diffusion (D_m) and the mean grain diameter (d_{50}). The Sherwood number can be defined by the Reynolds parameter (Re), the saturation of the non-wetting phase (S_n) and three fitting empirical parameters (α, β_1, β_2). While this method provides a useful estimation of mass transfer across an interface, it does not allow for the independent determination of the a_{wn}. Therefore, for reactive transport modelling purposes, where the IFA is of importance, the mass transfer coefficient and the a_{wn} needs to be defined independently.

Thermodynamically consistent theoretical approaches for describing macroscale flow and transport in porous media including the conservation of mass, momentum and energy while accounting for the presence of the interfaces between fluid-phases were proposed during the last two decades (e.g., Gray and Hassanizadeh 1989; Hassanizadeh and Gray 1990, 1993; Gray and Miller 2005; Gray et al. 2013; Gray and Miller 2014). The per volume normalized fluid-fluid IFA constitutes the macroscale quantity of interest for the validation of these theories and models. Alternatively, theoretical approaches calculate IFAs from simplified geometric assumptions about the pore geometry, such as idealized identical spheres packing, (e.g., Gvirtzman and Roberts 1991; Likos and Jaafar 2013), capillary tube approaches (e.g., Cary 1994) and computed using pore-network models (e.g., Reeves and Celia 1996).

Hassanizadeh and Grey's (1993) proposed theory on the definition of macroscale capillary pressure in porous media based on a thermodynamic approach allows for the extension of the classical capillary pressure saturation relationship ($p_c - S_w$) to a relationship including the specific IFA $p_c - S_w - a_{wn}$. Using a pore-scale network model, this theory was first tested by Reeves and Celia (1996). Their study successfully demonstrated that specific IFA could be predicted based on known values of capillary pressure and saturation for a given study. They also showed that the $p_c - S_w - a_{wn}$ relationship yields a convex shaped surface, demonstrating a non-unique functional relationship between these variables. Their study was also the first to suggest the a_{wn} could be seen as a function of p_c and S_w as opposed to $p_c = f(S_w, a_{wn})$, originally proposed by Hassanizadeh and Gray (1993). This functional dependency of a_{wn} on S_w and p_c was also experimentally demonstrated by Cheng et al. (2004). Computational studies using pore-network models have also been used to investigate the $p_c - S_w - a_{wn}$ relationship (Held and Celia, 2001; Helland and Skjaeveland, 2007; Joekar-Niasar et al., 2008; Joekar-Niasar et al., 2010). In these studies, IFA was also demonstrated to be a crucial parameter in diminishing or removing the hysteresis commonly seen in $p_c - S_w$ and $k_r - S_w$ relationships (Joekar-Niasar et al. 2008).

While valuable information is gained from these theoretical models, the geometric simplifications and static nature of most experiments has left the reliability of these models to be questioned (Kim et al. 1999). Only once a reliable measurement technique for a_{wn} is available, the $p_c - S_w$ constitutive relationships can be expanded to include three fundamental variables. To further understand the $p_c - S_w - a_{wn}$ relationship, numerous researchers have demonstrated the use of tracers as a tool to measure the IFA between different phases (gas-fluid, fluid-fluid), as well as, the use of computed micro-tomography (CMT) measurements (Dalla et al. 2002; Culligan et al. 2004; Schnaar and Brusseau 2005; Culligan et al. 2006; Brusseau et al. 2007; Costanza-Robinson et al. 2008; Narter and Brusseau 2010; Wildenschild and Sheppard 2013; Peche et al. 2016; McDonald et al. 2016), and MRT (Johns and Gladden 1999). Standard interfacial (partitioning) tracers typically are classified into water-phase tracers (often surfactants) (Karkare and Fort 1996; Kim et al. 1997; Saripalli et al. 1997, 1998; Annable et al. 1998; Schaefer et al. 2000; Anwar et al. 2000; Jain et al. 2003; Chen and Kibbey 2006; Brusseau et al. 2007; Narter and Brusseau 2010; Brusseau et al. 2015; Li et al. 2016), and gas-phase tracers (Brusseau et al. 1997; Kim et al. 1999; Costanza-Robinson and Brusseau 2002; Brusseau et al. 2006; Simon and Brusseau 2007), which are introduced in unsaturated or saturated systems. Even though most of the research focuses on air-water systems, NAPL-water-porous media fluid systems have been investigated for the determination of IFA at both lab e.g., (Saripalli et al. 1997, 1998; Jain et al. 2003; Dobson et al. 2006; Porter et al. 2010; McDonald et al. 2016; Li et al. 2016), and field-scales e.g., (Nelson and Brusseau 1996; Annable et al. 1998; Simon and Brusseau 2007). The subsequent effluent tracer concentration and resulting breakthrough curve is then measured and the retardation of the partitioning tracer breakthrough with respect to the non-partitioning tracer breakthrough is a measure to the magnitude of the IFA. A valuable literature review and classification of the water tracer techniques for determining IFAs is given in (Kibbey and Chen 2012). According to their discussion, one drawback of the surfactant miscible displacement techniques is that it may induce surfactant flow leading to methodological violations on IFA estimates (Costanza-Robinson and Henry 2017). CMT measurements are capable of providing direct measurements of fluid-fluid and gas-fluid interfaces and they have also been used in conjunction with tracer measurements and numerical simulations as a means of validating results (Culligan et al. 2006; Brusseau et al. 2006, 2007; Porter et al. 2009; Narter and Brusseau 2010; Porter et al. 2010; McDonald et al. 2016). Most commonly reported in the literature CMT derived interfaces are smaller than those obtained with the IFA tracer techniques, caused by pore-scale features (e.g., microscopic surface roughness) which are sometimes under the resolution of the CMT scanner (Narter and Brusseau 2010), and sometimes the differences in the IFAs that they measure (e.g., Grant and Gerhard 2007; McDonald et al. 2016). IPTT measure the "total" IFA (including the area associated with thin wetting-fluid films) while CMT provide a good measurement for the capillary-associated IFA, even though with this technique it is challenging to differentiate between the two IFAs. Despite the suite of aqueous and gaseous tracers available, they were only applied in static or quasi-static conditions. Little has yet been done in the delineation of the fluid-fluid interfaces, for dynamic flow conditions (Tatomir et. al, 2016). A review of tracer techniques commonly used in monitoring carbon capture and storage projects can be found in (Myers et al. 2012, 2013; Tatomir et al. 2016; Niemi et al. 2017). Several studies using a combination of numerical models and experimental work have investigated the uniqueness of the $p_c - S_w - a_{wn}$ surface under equilibrium and non-equilibrium conditions. Static experiments imply the absence of the transient effects, thus the $p_c - S_w - a_{wn}$ is only a function of the intrinsic properties of the medium and fluid type (Joekar-Niasar and Hassanizadeh 2012). Using a micromodel, (Bottero 2009) (chapter 8), first posed the question as to whether the $p_c - S_w - a_{wn}$ functional relationship was independent of dynamic processes. It was found that within the estimated measurement error (10-15%), both static and dynamic data points could be

fitted to a single $p_c - S_w - a_{wn}$ surface. A numerical study performed by Joekar-Niasar and Hassanizadeh (2012) using a dynamic pore-network found that $p_c - S_w - a_{wn}$ curves depended on the capillary number. The difference between equilibrium and non-equilibrium $p_c - S_w - a_{wn}$ surfaces increase as viscous forces increase, specifically during imbibition. Despite this, they concluded that within the range of uncertainty, the $p_c - S_w - a_{wn}$ surface can provide an acceptable estimate under dynamic conditions. More recently (Karadimitriou et al. 2014) carried out an experimental study using a micromodel in order to investigate the impact of transient two-phase flow on the specific IFA. Their study was able to corroborate the observation by Joekar-Niasar and Hassanizdeh (2012) showing that the $p_c - S_w - a_{wn}$ surface was dependent on the capillary number. Zhong et al. (2016) investigated the use of a modified IPTT method originally presented by Jain et al. (2003) that employs two phase flow conditions, allowing for the investigation of IFAs at non-wetting saturations larger than residual saturation. Their study found that experiments done using the multiphase flow method was comparable to those found using standard IPTT methods.

In an effort to address some of the current limitations and provide a new method to understanding the specific IFA under dynamic conditions, we apply a new class of tracers, termed kinetically interface sensitive (KIS) tracer, developed by Schaffer et al. (2013). The reactive tracer has shown promise in its ability to characterize the IFA between the wetting phase formation fluid and the injected non-wetting phase fluid (n-octane). Moreover, the KIS tracer has the potential to answer questions regarding available storage capacities of a reservoir, the influence of pressure stimulation on mixing, significance of fingering at field scale, residual saturation of CO2 and the optimization of operational strategies. While previous works have discussed the KIS tracer with respect to CO_2 sequestration, we show the applicability of the KIS-TT method in all research domains that involve the displacement by non-wetting fluid.

This work follows previous research carried out by Tatomir et al. (2015, 2016), where a mathematical and numerical framework was established for the design and application of the KIS tracer in laboratory experiments and theoretical studies (Tatomir et al. 2015). In this paper, we provide a proof of concept for the use of KIS tracers by designing a relatively inexpensive, simple and highly controlled column experiment to study the dynamic fluid-fluid IFA and compare them with numerical results from both an academic code (DuMu^x) and a commercial code (COMSOL Multiphysics 5.2 finite element tool box). The study solely focuses on capillary associated fluid-fluid IFAs during the drainage process (i.e., non-wetting displacement of the wetting fluid).
We begin by presenting the experimental setup and numerical framework for the column test, followed by the experimental methods and results to determining key parameters and IFA. A validation of the numerical models as presented by Tatomir et al. (2015) and Tatomir et al. (2016) is concomitantly done by comparing it to experimentally determined breakthrough curves.

5.2 Theory

5.2.1 KIS tracers' principles

KIS tracers are a novel category of reactive tracers developed by Schaffer et al. (2013), capable of describing the spatial and temporal development of the non-wetting/wetting phase fluid interface. Originally intended to provide information about the injected supercritical CO_2 ($scCO_2$) plume and of the interface between $scCO_2$/brine, the developed stable KIS tracer is a non-polar hydrolysable phenolic ester (phenyl naphthalene-2-sulphonate, 2-NSAPh, CAS 62141-80-4). The non-polarity

of the KIS tracer allows it to be mixed directly with the $scCO_2$ and simultaneously injected into the porous medium. Additionally, the KIS tracer was designed in such a way that allows for the use of standard equipment to achieve high temporal resolution and high selectivity even for low detection limits (Schaffer et al., 2013). Naphthalenesulfonates are consequently very fluorescent and can be detected in the ranges of µg/l using fluorescence spectrometry. Upon contact with the formation fluid (brine), the KIS tracer undergoes an irreversible hydrolysis reaction at the brine-$scCO_2$ interface. The KIS tracer hydrolyses into two highly wetting-phase soluble products that negligibly back partition into the non-wetting phase. Because the reaction kinetics of the tracer is known, a time-concentration relationship along with the IFA can be determined as a function of the reservoir conditions. Accordingly, the higher the concentration of reaction products in the water phase, the larger the brine-CO_2 IFA. The hydrolysis reaction at the interface can be described as:

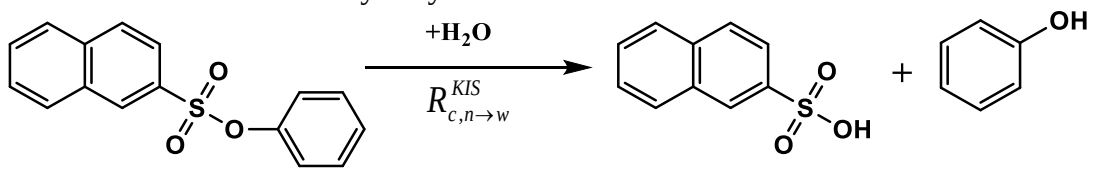

(5.4)

Phenyl Naphthalene-2-Sulfonate Naphthalene-2-Sulfonic Acid Phenol

where $R_{c_{n\to w}}^{KIS}$ is the reaction rate coefficient, dependent on the physical and chemical conditions of the system. Figure 1 illustrates the conceptual model behind the KIS tracer at the pore and molecular level with respect to IFAs. For a more in depth justification of assumptions surrounding the KIS tracer, please refer to Schaffer et al. (2013).

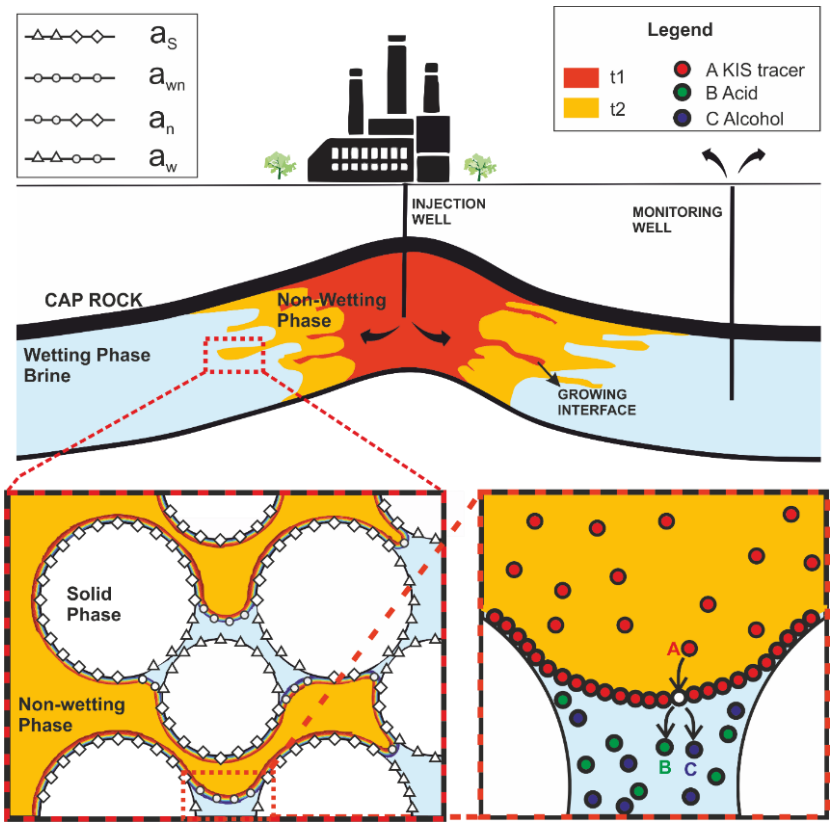

Figure 5.1. Conceptual Model of KIS tracers at different scales of considerations: (top) field-scale application of the KIS tracer at a CO_2 storage pilot site; (left) pore-scale illustration of the types of IFAs (a_{wn}, capillary associated IFA, a_n, area of the non-wetting phase, a_w area of the wetting phase, a_s area of the solid phase; (right) the molecular/IFA-scale depicting the hydrolysis reaction, eq. (5.4)

5.2.2 Immiscible wetting phase displacement by the non-wetting phase

The drainage process, defined as the non-wetting phase displacement of the wetting phase, can be mathematically represented by the governing macro-scale equations for immiscible two phase porous media flow:

$$\frac{\partial(S_\alpha \phi \rho_\alpha)}{\partial t} - \nabla \cdot (\rho_\alpha v_\alpha) - \rho_\alpha q_\alpha = 0 \text{ , with } \alpha = w, n \tag{5.5}$$

$$v_\alpha = -\mathrm{K}\frac{k_{r\alpha}}{\mu_\alpha}(\nabla p_\alpha - \rho_\alpha \mathbf{g}) \text{ .} \tag{5.6}$$

The system of partial differential equations (5.5) is closed with the following equations:

$$S_w + S_n = 1, \tag{5.7}$$

$$p_n - p_w = p_c, \tag{5.8}$$

where α denotes the phase (with *w*, as the wetting phase and *n* as the non-wetting phase), S_α is the phase saturation, ρ_α is the phase density, ϕ is the porosity of the matrix q_α is the phase source or sink term, K is the intrinsic permeability, $k_{r\alpha}$ is the relative permeability, μ_α is the phase dynamic viscosity, **g** is the gravity term, $p_\alpha$is the phase pressure, p_c denotes the capillary pressure and v_α is the apparent velocity of the fluid as given by the extended multiphase Darcy's law.

The functional correlation between saturation and capillary pressure has been derived by many researchers (e.g., Leverett 1941; Brooks and Corey 1964; Van Genuchten 1980). For this research the macroscopic capillary pressure-saturation relationship determined from laboratory experiments is expressed by the Brooks-Corey model:

$$p_c(S_w) = p_d S_e^{-\frac{1}{\lambda}}, \tag{5.9}$$

Where the effective saturation is defined as:

$$S_e = \frac{S_w - S_{wr}}{1 - S_{wr}}. \tag{5.10}$$

The relative permeability-saturation relationship is written according to the Burdine theorem (Burdine 1953; Helmig 1997):

$$k_{rw}(S_w) = S_e^{\frac{2+3\lambda}{\lambda}}, \tag{5.11}$$

$$k_{rn}(S_w) = (1 - S_e)^2 \left(1 - S_e^{\frac{2+\lambda}{\lambda}}\right) \tag{5.12}$$

Where S_{wr} denotes the residual saturation, p_d refers to the entry pressure and λ is the pore-size distribution parameter. The two-phase flow system discussed herein is concerned with isothermal, immiscible displacement of two incompressible fluids in a homogeneous, incompressible solid matrix.

5.2.3 KIS tracer transport in multiphase system

Multicomponent transport in a multiphase flow porous media system is commonly formulated as (Bear 1988; Helmig 1997):

$$\mathrm{MB}(\kappa) \coloneqq \sum_{\alpha} \frac{\partial(\phi S_\alpha \rho_\alpha x_\alpha^\kappa)}{\partial t} - \nabla \cdot \sum_{\alpha} \left\{ \rho_\alpha x_\alpha^\kappa \frac{k_{r,\alpha}\mathbf{K}}{\mu_\alpha} (\nabla p_\alpha - \rho_\alpha \mathbf{g}) \right\} - \nabla \cdot \sum_{\alpha} \left\{ \rho_\alpha D_{pm,\alpha}^\kappa \nabla x_\alpha^\kappa \right\} - q_\alpha^\kappa - r_{\alpha\to\beta}^\kappa = 0 \tag{5.13}$$

where x_α^k is the mole fraction of component κ in phase α., $D_{pm,\alpha}^\kappa$ is the hydrodynamic dispersion tensor, q_α^κ is the sources or sink term, and $r_{\alpha\to\beta}^\kappa$ denotes the reaction rate over the fluid-fluid interface of component κ in phase α to the phase β, and the mass balance operator symbol $\mathrm{MB}(\kappa)$. Equation (5.14) is added to the set of closing relations (5.7) and (5.8).

$$\sum_k x_\alpha^k = 1 \ . \tag{5.14}$$

The application and model development of KIS tracer in a $scCO_2$-brine fluid system, which is a miscible two phase flow five component transport, κ (i.e., H_2O, CO_2, ester, acid, alcohol) inside of the two fluid phases (brine and $scCO_2$) is discussed in Tatomir et al. (2015, 2016). In an immiscible two phase flow system such as n-octane and water in a glass beads packed column, the KIS tracer is present only in the non-wetting phase, while hydrolysis reaction products are present only in the wetting-phase. Therefore, eq. (5.13) can be rewritten in the form of the commonly used advection-dispersion-reactive transport equation (5.15), and solved decoupled from the two-phase flow equations, assuming there is no back-partitioning, secondary reactions, or any other mass transfer processes (e.g., n-octane dissolved in water phase, or water in n-octane phase).

$$\frac{\partial(\phi S_\alpha c_\alpha^\kappa)}{\partial t} - \nabla \cdot \left(c_\alpha^\kappa \boldsymbol{v}_\alpha - D_{pm,\alpha}^\kappa \nabla c_\alpha^\kappa \right) - q_\alpha^\kappa - r_{\alpha\to\beta}^\kappa = 0, \quad \alpha = w, n \tag{5.15}$$

Here, $c_\alpha^\kappa \equiv \rho_\alpha x_\alpha^\kappa$ is the concentration of component κ in phase α (2-NSAPh/ KIS tracer, n-octane, H_2O, 2-NSA/acid, phenol/alcohol). One transport equation is required for solving each component; however, not all components influence each other or are necessary to be computed. Subsequently, if we consider the stoichiometry from eq. (5.4) (i.e., one mole of 2-NSAPh tracer reacts with one mole of water to produce one mole of 2-NSA and one mole of phenol), it is sufficient to solve only two transport equations, i.e., for the KIS tracer transport in the non-wetting phase and for the acid in the water phase. While the n-octane and the H_2O mass balances are accounted for by the immiscible two phase flow model eq. (5.5), the phenol component is produced at the same molar rate as the acid (assuming it has a similar hydrodynamic dispersion coefficient) therefore there is no need to solve the respective transport equation.

Transport of each component is governed by the advective flux and the hydrodynamic dispersion, the latter of which is the sum of the molecular diffusion and the mechanical dispersion (Bear 1972):

$$D_{dis,\alpha,ii} = \alpha_L \frac{v_i^2}{|v|} + \alpha_T \frac{v_j^2}{|v|} \tag{5.16}$$

$$D_{dis,\alpha,ij} = D_{dis,\alpha,ji} = (\alpha_L - \alpha_T) \frac{v_i v_j}{|v|} \tag{5.17}$$

where α_L, α_T are the longitudinal and transversal dispersivities. (Bear 1972) indicates that the magnitude of α_L found in many column experiments is approximately equal to a pore or grain-size and the α_T values are 8 to 24 times smaller than α_L. The molecular diffusive tensor in multiphase multicomponent systems can be expressed using the Millington and Quirk (1961) expression:

$$D_m = \phi S_\alpha \tau_L D_L \tag{5.18}$$

$$\tau_L = \phi^{1/3} S_\alpha^{7/3} \tag{5.19}$$

Where D_L represents the molecular diffusion constant and τ_L denotes the tortuosity. The $D_L$of 2-NSAPh in n-octane, and of 2-NSA and phenol in water are small. In water, they have a range of $1{\cdot}10^{-9}$ to $1{\cdot}10^{-10}$ m^2/s. Combining the mechanical dispersion and molecular diffusion tensors we arrive at the following expression for $D_{pm,\alpha}^{\kappa}$:

$$D_{pm,\alpha}^{\kappa} = \delta_{ij}\alpha_L \boldsymbol{v} + (\alpha_L - \alpha_T)\frac{D_{pm,\alpha}^{\kappa} v_j}{v} + \delta_{ij}\phi^{3/4} S_\alpha^{10/3} D_L \tag{5.20}$$

where δ_{ij} is the Kronecker delta, and v_i is the *i*th component of the average velocity vector $\boldsymbol{v}$.

5.2.4 Mass transfer processes across the fluid-fluid interface

The mass transfer processes across the wetting and non-wetting phase interfaces can be considered as three independent processes: (1) adsorption of the KIS tracers onto the interface; (2) a hydrolysis reaction of the KIS tracer in contact with water and (3) water soluble reaction products that are distributed into water/brine away from the interface. According to Schaffer et al. (2013), the concentrations of KIS tracer reaction products depend on the interface size and time. The larger the interface, the larger the mass of the reacted product. The longer the time the two fluid phases are in contact, the larger the mass of reacted solute.

5.2.4.1 Hydrolysis reaction rate

Static batch experiments showing the hydrolysis of 2-NSAPh in n-octane/pure water fluid systems resulted in a linear relationship between concentration curves of 2-NSA over time, indicating a zero-order kinetic rate -- a key assumption towards the suitability of 2-NSAPh as a KIS tracer (Schaffer et al., 2013). The hydrolysis reaction rate is expressed as:

$$-\frac{dc_\alpha^\kappa}{dt} = r_{n\to w}^{\kappa} = R_{c_{n\to w}}^{\kappa} \cdot a_{wn}\ , \tag{5.21}$$

5.2.4.2 Sorption at the interface

Schaffer et al. (2013) suggested that the accumulation of the KIS tracer at the fluid interface maybe described by a type of non-permeable mono-layer adsorption isotherm that can describe the amount of the tracer at the interface over time. It is thus possible to apply a Langmuir isotherm described as:

$$\theta_k = \frac{c_{KIS}}{c_{KIS,max}} = \frac{\kappa_L c_a}{1+\kappa_L c_a}, \tag{5.22}$$

where $\theta_k$is the fractional occupancy of the adsorption sites, c_{KIS} is the KIS tracer concentration on the interface which is approximately equal to the maximum concentration of the saturated interface, $c_{KIS,max}$, and c_a is the KIS tracer concentration in the non-wetting phase. κ_L is the Langmuir sorption coefficient. Since our tracer is injected in excess, we assume, similar to Schaffer et al. (2013) that the interface is always fully saturated throughout the flooding process with respect to the KIS tracer (i.e. $\theta_k = 1$).

5.2.5 Fluid-fluid interfacial area considerations

The IFAs are typically classified into two types, i.e., the capillary-associated IFAs, a_{wn}, and the film-associated IFAs (Dalla et al. 2002; Porter et al. 2010; Kibbey and Chen 2012) (see Figure 5.1). Among the various IFA measurement techniques there are ambiguities regarding the effective IFA

being measured. For example, image analysis techniques are not capable to accurately distinguish between mobile-IFA's and film-IFA's. The KIS-TT method relies on measuring the concentration of the reaction products at the outflow; therefore, it is able to capture the mobile (capillary-associated) IFA.

Standard macro-scale mathematical models have typically only been used to consider the volumetric distribution of fluid phase (i.e. saturation and pressure). They usually do however not account for the fluid-fluid IFA, nor the phase distribution. Hassanizadeh and Gray (1990) derived a thermodynamically rational multiphase flow theory that is capable of accounting for interfacial forces. In doing so, they also propose a constitutive relationship between capillary pressure, saturation and fluid-fluid IFA $p_c - S_w - a_{wn}$. While their work tackles the shortcomings of the extended Darcy's law formulation of multiphase flow (lack of physical insight into dynamic effects of hysteresis associated with capillary pressure and relative permeability), the equations, even by the authors appreciation, are overly complex and contain numerous material parameters for which no information is available (Niessner and Hassanizadeh, 2008). As a result, a series of simplifying assumptions suggested by Niessner and Hassanizadeh (2008), are used for the numerical modelling in this paper, (i.e., porosity does not change with time, phases are incompressible, interfacial mass density is constant, mass exchange between phases and interfaces has negligible effect on mass balance of phases, cross-coupling terms in flow velocity among phases and interfaces are negligible, the porous media is perfectly wettable with respect to the wetting phase).

For the incorporation of the specific fluid-fluid IFA in the two-phase reactive transport equations, we assume the functional relationship $a_{wn} = a_{wn}(S_w, p_c)$. This allows for a single valued relationship during drainage and imbibition (Niessner and Hassanizadeh 2008). Joekar-Niasar et al. (2008) showed that a second-order polynomial expression was capable of capturing the functional dependency between saturation, pressure and IFA.

$$a_{wn}(S_w, p_c) = a_{00} + a_{10}S_w + a_{01}p_c + a_{11}S_w p_c + a_{20}S_w^2 + a_{02}p_c^2 \tag{5.23}$$

Tatomir et al. (2013) has also suggested a polynomial expression (eq. (5.24) that is capable of expressing the relationship which avoids non-physical capillary and saturation values.

$$a_{wn}(S_w, p_c) = a_0(S_w)^{a_1}(1 - S_w)^{a_2}(p_c^{max} - p_c)^{a_3} \tag{5.24}$$

5.2.6 Estimating specific interfacial areas

While considerable work has been done in order to derive multiphase flow formulations that explicitly account for IFAs, these formulations are still limited by the lack of information surrounding key parameters and the model associated complexity. As a result, we turn to available literature to estimate a_{wn}. The IFAs determined from the models will provide an estimate to which we can compare against the numerical model.

A thermodynamically driven IFA model derived by Grant and Gerhard (2007) was used in order to approximate the specific IFA. This model was chosen as it has shown particular success in matching experimentally derived specific IFAs from several studies. A summary of literature that showed success using this model is given in supporting information (SI) Table 5.S 1.
The model is built upon concepts presented by Leverett (1941) and assumes that the IFA is directly influenced by the work done on the system and thought to be directly proportional the area under

the pressure-saturation curve. According to Leverett (1941), the total IFA, could be calculated by the following expression:

$$a_n(S_w) = \phi \cdot \frac{[\Phi_{nw}(S_w)]}{\sigma_{nw}} \tag{5.25}$$

Where σ_{nw} represents the interfacial tension and $[\Phi_{nw}(S_w)]$ represents the area under the $p_c - S_w$ curve given by:

$$\Phi_{nw}(S_w) = -\int_X^{S_w} p_c(S_w) dS_w \tag{5.26}$$

where X is defined as the saturation when $p_c = 0$. Grant and Gerhard (2007) provides an extension to this model, which allows for the determination of the specific IFA. The equation for determining the area under the $p_c - S_w$ drainage curve is given by:

$$[\Phi_{nw}(S_w)]^D = -\int_{S_w}^{S_w^i} [p_c(S_w) dS_w]^D \quad S_r \leq S_w^i < S_w^M \tag{5.27}$$

where S_w denotes the saturation when the capillary pressure is equal to zero, for the drainage process, this is set to unity; S_w^i represents the current wetting phase saturation. In order to arrive at the specific IFA, data is used from pore network simulations observed by Dalla et al. (2002). Dalla et al. (2002) data is used in this instance because it allows calculating a_{wn} from the thermodynamic approximation of total a_{wn}, specifically in instances where this data is not available (Grant and Gerhard 2007). The following polynomial expression is used to fit the a_{wn}/a_n ratio with respect to saturation:

$$\psi(S_w) = \frac{a_{wn}}{a_n} = -4.8871 \cdot (S_w)^4 \cdot 13.18 \cdot (S_w)^3 - 11.901 \cdot (S_w)^2 + 4.6119 \cdot (S_w) - 0.0073 \tag{5.28}$$

An energy dissipation factor is also added into the formulation since not all the work done on the system is converted into surface energy, resulting in what was previously an overestimation of the IFA (Dalla et al. 2002). An energy dissipation factor determined by Grant and Gerhard (2007) of Ed = 0.21 was used in this model after calibrating their model with experimental data from Brusseau et al. (2006) in addition to good fitting of the model with data from Culligan et al. (2004). The final form of the explicit IFA submodel becomes:

$$a_{wn}(S_w^i) = \psi(S_w^i) \cdot E_d \cdot \phi \cdot \frac{[\Phi_{nw}(S_w)]^D}{\sigma_{nw}} \tag{5.29}$$

5.3 Material and Methods

5.3.1 Laboratory setup

Highly controlled systems are crucial in minimizing the number of processes occurring simultaneously in the system. This is of particular importance when proving the concept of novel (tracer) technologies such as the KIS-TT (e.g., Schaffer et al. 2013; Maier et al. 2015). Column experiments are economical, easily understood scientific tools for the validation of theories and assumptions in the field of flow and transport in porous media. Several factors were identified for designing and conducting a successful two-phase reactive transport experiment:

1. **Well-known, well-defined, adjustable system:** The designed experimental setup must provide a controlled two phase flow environment (Figure 5.2). A known geometry and well-

defined, adjustable boundary-condition must be guaranteed in order to prove the concept of the KIS tracers in immiscible two-phase porous media flow systems. The core of the experiment is a stainless-steel column with a length of 25 cm and a diameter of 3 cm. The column is sealed by two stainless steel porous frits which create a uniform distribution of fluids and retain the glass beads in the column. The column was positioned vertically for all experiments; however little influence of the column position was noticed (Figure 5.3b)

2. **Materials with stable physic-chemical properties:** It must be ensured that the results are not dominated by material effects. The chemical stability of the used materials (e.g., tubes, porous frits, valves, porous system) was tested (SI Text S1).
3. **Well-characterized porous media system:** Characterization of the two-phase flow media and wetting properties is vital. The porous media system is composed of artificial hydrophilic mono-sized spherical glass beads with the mean diameter of 238 μm. The ratio of the column diameter to the glass bead diameter ranges between 100 and 430. Thus, preferential flow along the column walls (also known as wall effect) is minimized and can be neglected (Coutelieris and Delgado 2012). Prior to the immiscible displacement, the column is fully water saturated. This is accomplished by uniformly packing the dry glass beads, followed by the slow imbibition of water into the column to avoid air entrapment. The packing is done in increments while vibrating the column to avoid any clumping and to ensure adequate packing. Furthermore, the known geometry of the mono-grain-size artificial porous media allows the calculation of physical properties of the porous medium (e.g., porosity, permeability) and the estimation of a geometry-surface relationship. A summary of porous media properties are provided in Table 5.1 and in SI Text S2.
4. **Well-defined wetting and capillary behavior:** In order to properly characterize two phase flow dynamics, the wettability of the sand and the capillary pressure-saturation behavior must be investigated. Contact angle (θ) analysis revealed a strongly water wet system with θ=10° ± 3°. The $p_c - S_w$ relationship was determined by use of mercury intrusion porosimetry (MIP), with the system being scaled to the appropriate fluid properties (SI Text S2.e)
5. **Well-understood tracer kinetics:** Work in this paper is built upon the in-depth study of the KIS tracer kinetics by Schaffer et al. (2013). Therefore, identical chemicals are used to ensure comparability with their results. The two-phase system consists of ultra-pure water and 97% pure n-octane. For the KIS tracer we use a synthesized product prepared by Schaffer et al. (2013) in addition to a product synthesized externally, i.e., 2-NSAPh.

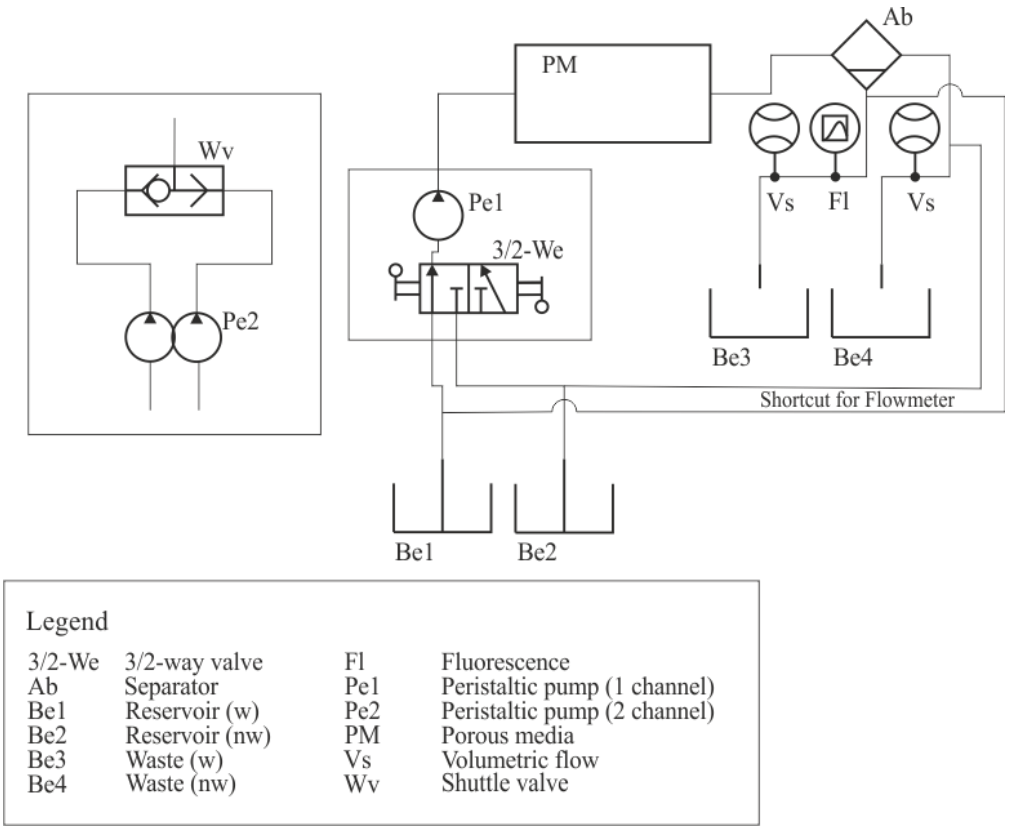

Figure 5.2. Experimental set up for the column experiment

Table 5.1. Summary of porous media and fluid properties

Parameter Name	Unit	Symbol	Value/ Range
Porosity	(-)	ϕ	0.47
Intrinsic Permeability	(m^2)	K	8.0e-12 - 1.0e-11
Bulk Density	(g/cm^3)	ρ_b	2.65
Pore Diameter	(μm)	d	75 - 120
Lambda (Brooks-Corey)	(-)	λ	3.65
Contact angle	(°)	θ	10 ± 3
Entry pressure	(Pa)	p_d	1606
Residual wetting phase saturation	(-)	S_{wr}	0.016
Longitudinal dispersivity	(m)	α_L	1e-3
Transversal dispersivity	(m)	α_T	1e-5
Diffusion coefficient	(m^2/s)	D_m	1e-9
Density water	(kg/m^3)	ρ_w	1000
Density n-octane	(kg/m^3)	ρ_n	703
Viscosity of water	$(Pa \cdot s)$	μ_w	1.00E-03
Viscosity of n-octane	$(Pa \cdot s)$	μ_n	5.42E-04
Injection rate into the column	(ml/min)	Q	0.64 - 0.93

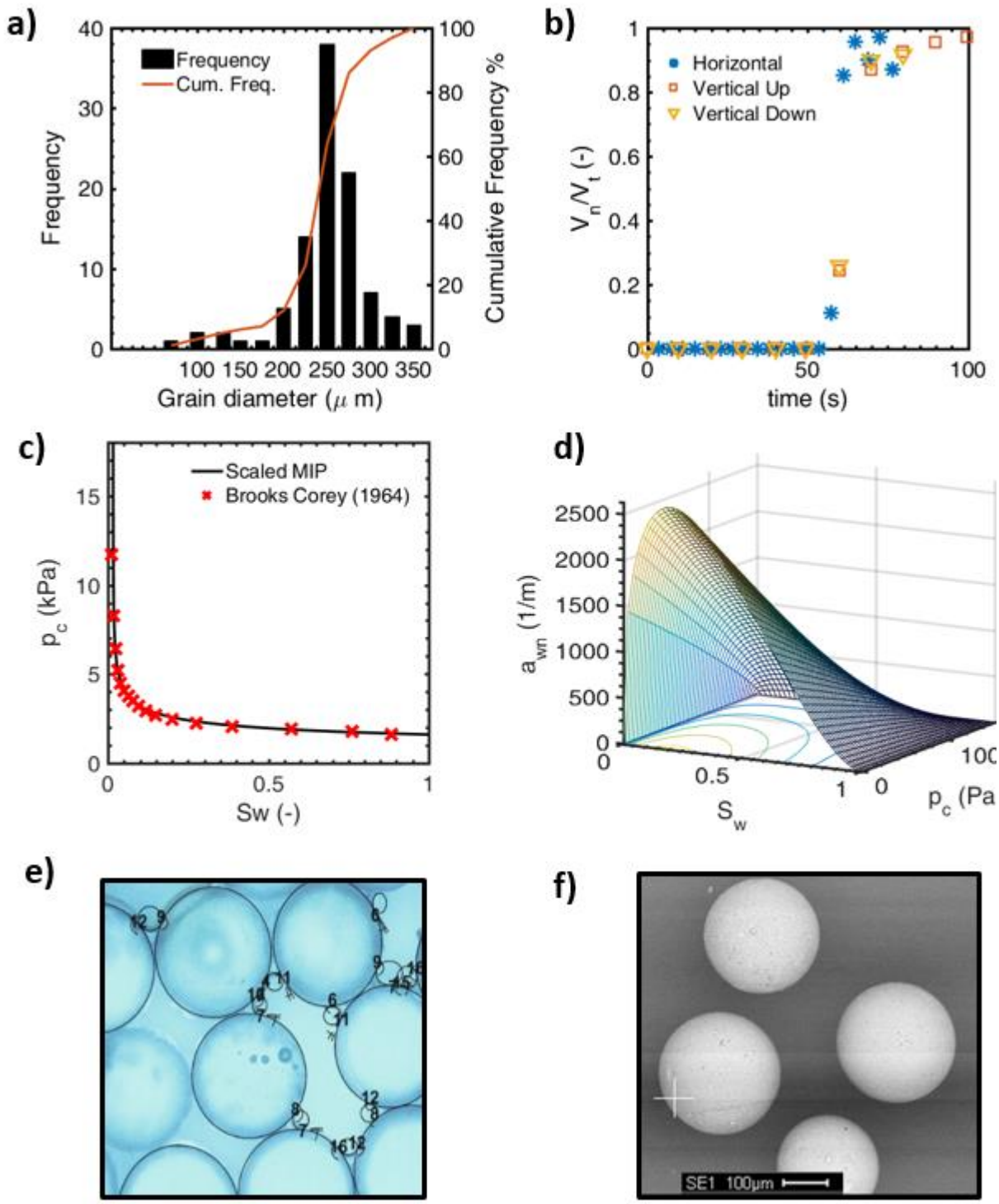
a)
Frequency
Cum. Freq.
Frequency
Cumulative Frequency %
Grain diameter (μ m)
b)
Horizontal
Vertical Up
Vertical Down
V_n/V_t (-)
time (s)
c)
Scaled MIP
Brooks Corey (1964)
p_c (kPa)
Sw (-)
d)
a_{wn} (1/m)
S_w
p_c (Pa
e)
f)
SE1 100μm

Figure 5.3. Key experimental base data: **a**) Grain size distribution and the cumulative distribution function (line); **b**) comparison of n-octane breakthrough curves in two phase flow experiments for different flow directions. Note, that the horizontal mode has a higher sampling rate to resolve the n-octane front in greater detail; **c**) scaled MIP data (mercury-air scaled to octane-water) fitted using eq. (5.9); **d)** calculated $p_c - S_w - a_{wn}$ surface with eq. (5.24) **e**) microscopic photograph of the used glass beads and the contact angle (25x magnification) in n-octane/water fluid-system. The glass is wetted with ultra-pure water and surrounded by n-octane; **f)** scanning electron microscopy image of the glass beads with no-measurable surface roughness.

5.3.2 Experimental procedure

5.3.2.1 Fluid properties

The use of n-octane by Schaffer et al (2013) was originally planned as a surrogate for $scCO_2$ to avoid having to use high pressure cells together with the associated difficulties that arise when sampling. Schaffer et al. (2013) showed that n-octane was a suitable surrogate for $scCO_2$ due to similar densities, solubility's and log K_{ow}, for the given system of study. Furthermore, the low cost, toxicity and vapor pressure of n-octane makes the use of n-octane particularly attractive. The use of n-octane in this study is particularly attractive as it allows for easier transferability into studies pertaining to NAPL contamination in groundwater. A summary of the fluid properties is shown in Table 5.1.

5.3.2.2 KIS tracer preparation and deployment

A series of KIS-TT were performed to determine the dynamic evolution of the n-octane/water IFA. The results are separated into experiments using the in-house synthesized (*old*) tracer and the commercially synthesized tracer (*new*).

A total of 4 non-wetting phase flooding experiments (two with the *old* - EXOT01, EXOT02, and two with *new*- EXNT01, EXNT02) were performed in the glass bead filled column under ambient conditions. The KIS tracer (2-NSAPh), was first dissolved in n-octane at a concentration of 0.5 g/l. 30 ml of this solution was then injected into the column followed by pure n-octane (chaser). The injection rate was set to a sufficiently slow flow rate to avoid any residual air in the system. Three experiments were conducted for reproducibility reasons, each using freshly packed glass beads. After each experiment the glass beads were washed and dried over 48 hours. To capture the two phase flow BTC, the outflow during the n-octane experiments was first collected in a 5 ml graduated measuring cylinder, where the volume of the wetting phase was measured in conjunction with the sample collection times. After that, the cylinder content was collected in 5 ml vials until the arrival of the n-octane (SI Figure 5.S 2). In order to get a better representation of the BTC, the sampling intervals were kept much shorter when the n-octane was first observed at the outlet. For extracting the water from the cylinder, a glass syringe was used and subsequently placed into a cuvette for analysis by a fluorospectrometer. A pre-calibrated curve allowed for the conversion of the 2-NSA intensity readings into concentration.

5.3.3 Hydrolysis at the interface

In the study of Schaffer et al. (2013) the reaction rate coefficient ($R_{n\rightarrow w}^{2NSA}$) value was determined by implementing a linear regression line over the concentration – time data after 3000 minutes when the concentration increase over time became constant (Figure 5.4b). The authors claim the early-time data could be the result of partitioning of impurities, the initial saturation of the interface or the establishment of constant diffusion gradients. At a pH of 6 and temperature of 40°C, they determined a $R_{n\rightarrow w}^{2NSA}$ of 5e-13 kg·m^{-2}s^{-1}. Static batch experiments using the same tracer were performed both in continuous flow-through and manual cuvette fluorescence measurements of the sample. Since a n-octane flooding experiment generally takes under 6000 seconds, our results remain in the non-linear portion of the kinetic reaction. To simplify the problem, we carry out a linear regression across each data point to determine a single-valued kinetic rate as would be expected by a pseudo zero-order reaction (see Table 5.2). Experiments have shown that the reaction rate is strongly dependent on the initial concentration (Figure 5.4a and 5.5b). In this study, all KIS-TTs are performed using an initial concentration of 0.5g/L (Figure 5.4c). Note that Schaffer's et al. (2013) determined reaction rate for late time (after 3000 minutes) is approximately one order of magnitude lower than that determined from early time experiments (Figure 5.4d).

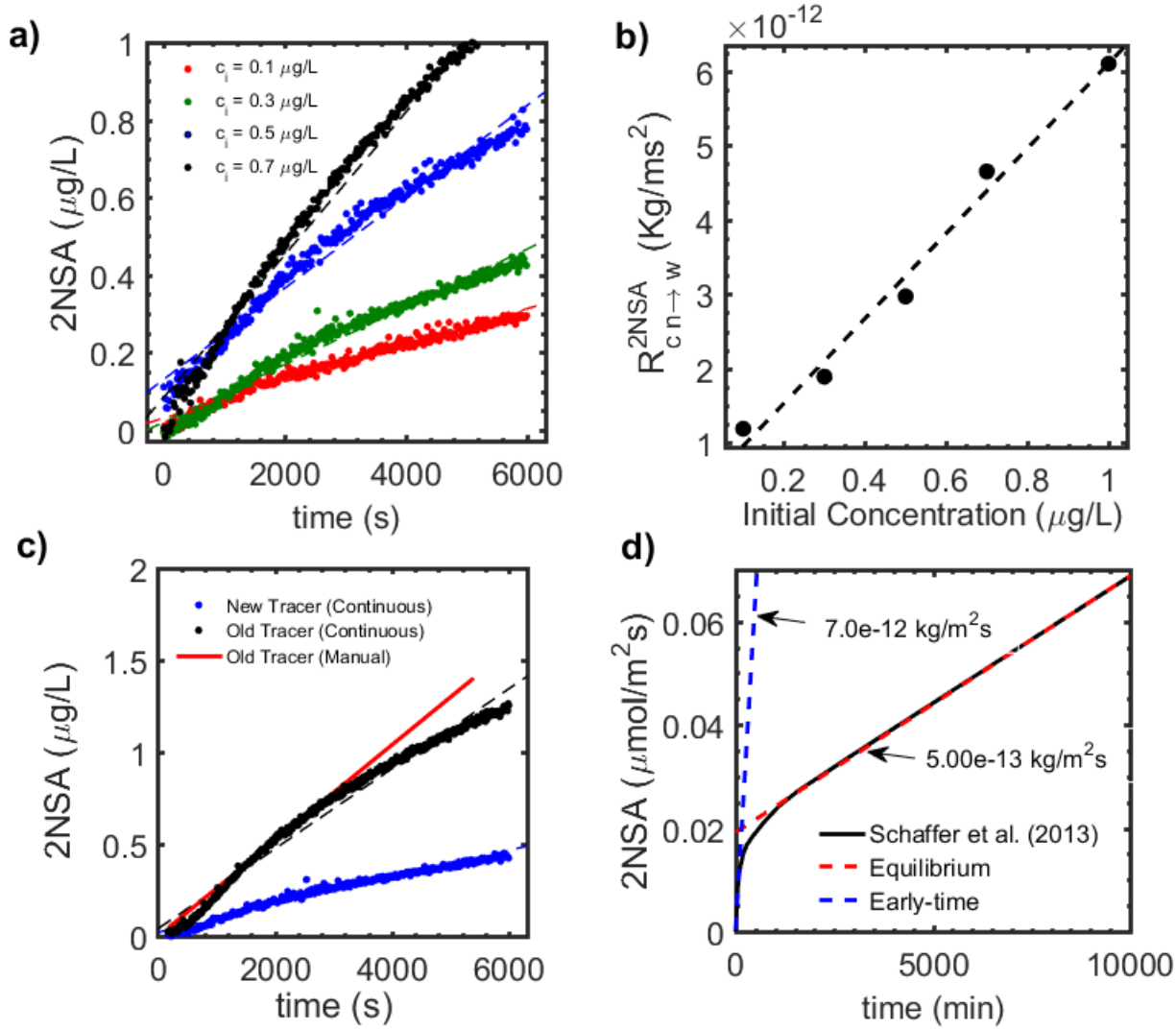

Figure 5.4. Determination of the hydrolysis kinetic rate using static batch test experiments: **a**) 2-NSA concentration evolution over time for different initial concentrations of the KIS tracer (i.e. 0.1, 0.3, 0.5, 0.7 μg/l); **b)** calculated hydrolysis reaction rate for different initial starting concentrations; **c**) 2-NSA concentration over time for an initial concentration of 0.5g/L using the *new* (commercially purchased) and *old* (self-synthesized) tracer; **d**) observed concentration of 2-NSA over time taken from Schaffer et al. (2013) using continuous measurements.

Table 5.2. Summary table of hydrolysis reaction rates as shown in Figure 5.4

Tracer	Method	Cuvette Volume (ml)	Cuvette Area (mm^2)	$R_{c_{n\rightarrow w}}^{2NSA}$ (kg/m^2s)[1]	R^2
Old	Continuous[2]	2.5	100.00	5.71e-12	0.983
Old	Continuous	2.5	100.00	5.44e-12	0.981
Old	Manual[3]	4	176.63	5.85e-12	0.869
New	Continuous	2.5	100.00	2.95e-12	0.976
Old from Schaffer et. al (2013) (early time)	Continuous	3	100	~7.00e-12	1
Old from Schaffer et. al (2013) (late time)	Continuous	3	100	5.00e-13	1

[1] Values determined by applying a linear regression through experimental data (**Figure 5.4c)**
[2] Continuous measurements are taken every 20s by maintaining constant fluid-fluid IFA in the cuvette while the tracer solution is recirculated (see Schaffer et al. 2013)
[3] The measurements are taken manually with glass pipettes at different times. The value represents the slope of the linear regression line calculated across the data points

5.3.4 Modeling multiphase flow and transport of KIS-tracer reaction product breakthrough

The numerical model describing the two-phase flow and reactive transport for the KIS tracer system (eq. (5.5)-(5.24)) is implemented under two numerical simulators — numerical toolbox DuMu^x (Flemisch et al. 2011), and the finite element simulation software COMSOL Multiphysics^{TM}5.2 for code comparison reasons.

The importance of code inter-comparison increases with the increasing complexity surrounding thermodynamic processes in porous media systems (e.g., multi-phase flow, reactive transport across fluid-fluid interface, etc.). The advantage of such code comparisons is that in addition to laboratory experiments, it provides a double implementation of the same mathematical model into two separate software that have different conceptual designs. DuMu^x is a free open-source, academic code, for flow and transport processes in porous media. Several notable publications involving the DuMu^x participating in benchmark studies involving CO_2 storage (Class et al. 2009; Nordbotten et al. 2012) and fractured media flow (Flemisch et al. 2017) have been shown. Its flexible programming framework allowed for the implementation of the mathematical model and the dimensioning of the field and laboratory experiments using a $scCO_2$-brine fluid system (Tatomir et al. 2015). The model is a two-phase four-component flow and transport model with an extended capillary pressure-saturation relationship to include a_{wn}. Here, the model has been modified accordingly so that the two fluid-phases — n-octane and water, are immiscible. The spatial discretization applied is a fully upwind - vertex centered finite volume method (FVM), also known as the "box" method (Helmig 1997). The time discretization is the implicit Euler scheme,

which is known for its numerical stability and the Newton-Raphson method is employed to linearize the system of partial differential equation.

Comsol Multiphysics, on the other hand, is a commercial software with an intuitive GUI that includes pre- and post-processing steps. With the ability to write the set of governing partial differential equations into one of its interfaces, Comsol achieves a flexibility similar to academic codes. A sensitivity analysis to determine the KIS tracer behavior with regard to changes in flow and transport parameters performed with the Comsol model is discussed in Tatomir et al. (2016). Comsol spatial discretization is finite element method (FEM), and the time discretization is backward Euler.

Due the symmetry of the column, the geometry can be simplified to a 2D rectangular domain. The boundary conditions (BCs) on the side walls of the column are set to no-flow boundaries. At the inflow, BCs for the non-wetting flux are set to Neumann type, as for the transport of KIS tracer equation, the BC is Dirichlet, both matching the values recorded in the experiments, i.e., specific non-wetting flux of n-octane (1 mg/l / A_{column}), $c_{in} = 0.5\ g/l$. The outflow BC is Dirichlet for all 4 primary variables ($p_w = 1.0e5\ Pa$, $S_n = 0.0$, $C_n^{2NSAPh} = 0.0\ (g/l)$, $C_w^{2NSA} = 0.0\ (g/l)$); the same as for initial conditions. The list of the parameters used in the numerical models is given in Table 5.1.

5.4 Results and discussion

5.4.1 Two phase flow sensitivity analysis

The two phase flow experimental data was matched by performing a parametric sweep on the two most uncertain parameters in the experiment — permeability and injection rate. In the case of parameter “permeability”, both, the porous media (glass beads) and the porous frits permeabilities were determined with a falling head permeameter. It was found that the low permeability of the porous frits impacts significantly the overall permeability of the system. Difficulties quantifying the exact effect of the porous frits resulted in permeability being approximated numerically. The variability in the injection rates due to the peristaltic pump was shown to be in the order of approximately +/- 0.05 ml/min. Since the numerical simulation is particularly sensitive to these parameters, a parameter sweep was performed to best fit the experimental data. The final fitting curves for two phase flow conditions are presented in Figure 5.5 integrated (SI Text S3). Only one curve is shown for both the Dumu^x and Comsol solutions since the numeric results overlapped almost perfectly. However, this is only accomplished for slightly differing permeability’s and injection rates. The curves consistently show best-fitting for permeabilities in the range between 2e-12 m^2 and 3e-12 m^2. A harmonic mean would suggest the permeability of the porous frits to be on the order of 3e-14 m^2 to 6e-14 m^2. Both models show an ability to effectively match the experimental data, however, they tend to underestimate the final outflow values. This difference likely originates from the difficulty associated with reading the remaining volume of the wetting fluid due to limited markings and increased effects of wetting to the glass that tended to occur near the end of the experiments, resulting in an overestimation of the V_n/V_t ratio.

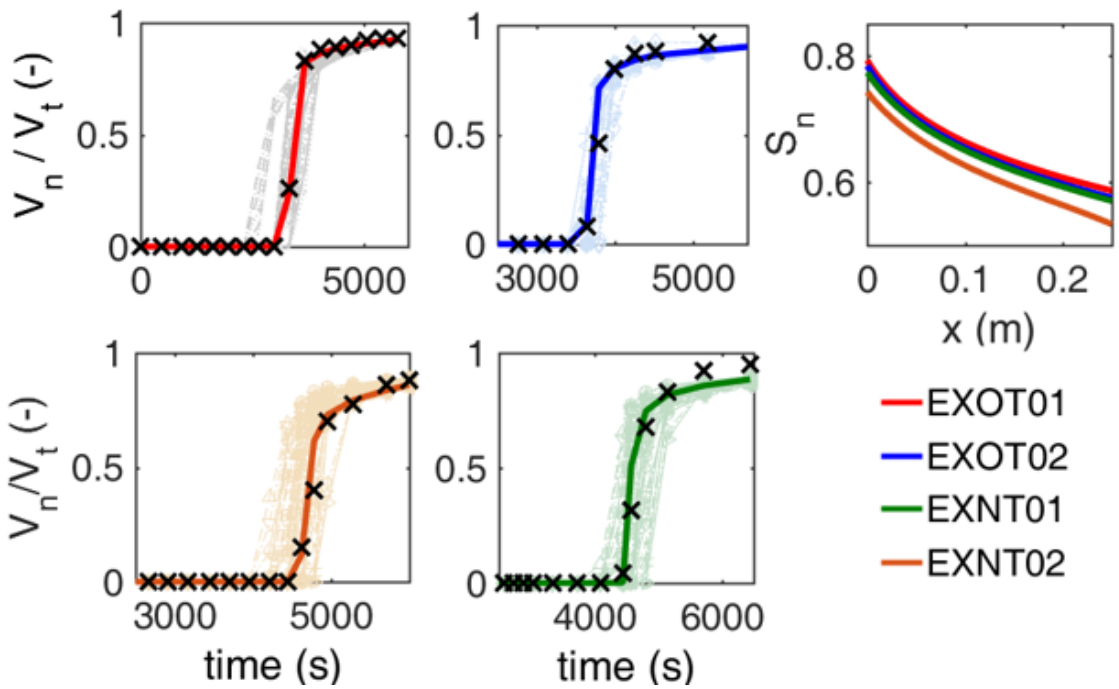

Figure 5.5. Best fitting predicted BTC and the predicted saturation over the column length for each experiment (EXNT01 stands for experiment with new tracer 01; EXOT01 stands for experiment with old tracer 01)

Table 5.3. Summary of best fitting injection rate and permeability for each experiment

COMSOL/ DuMu^x	Injection Rate (ml/min)	Permeability (m^2)	Date
EXNT01	0.670 / 0.660	2e-12 / 1e-12	17.08
EXNT02	0.640 / 0.630	3e-12 / 1e-12	22.08
EXOT01	0.930 / 0.900	2e-12 / 1e-12	15.02
EXOT02	0.835 / 0.810	2e-12 / 1e-12	21.04

5.4.2 Reactive Transport

A prerequisite for the correct matching of the experimental data is to know the capillary pressure saturation-specific IFA relationships. Multiple studies have shown the ability to match drainage and imbibition data onto bi-quadratic surfaces that show the relationship between $p_c - S_w - a_{wn}$. Projecting this surface onto a 2D plane for S_w-a_{wn}, we attain a curve that shows an increase in a_{wn} up until some wetting saturation $S_w(a_{wn}^{max})$, followed by a decrease in the specific IFA with a continued increase in wetting saturation. Studies by Culligan et al. (2004) and Porter et al. (2010), using spherical glass beads have shown that for main drainage, the range of $S_w(a_{wn}^{max})$ lies approximately between 0.20-0.35. For simplicity, we assume that S_w^{max} occurs at 0.25, which also corresponds to the a_{wn}^{max} obtained when using the explicit IFA model (SI Figure 5.S 7). For matching the experimental data, we make a numerical sweep on the parameter a_0, allowing us to scale the maximum specific IFA (a_{wn}^{max}), while retaining the general curve shape. In Figure 5.6 the predicted saturations along the column (Figure 5.6a), over time (Figure 5.6b) and along with the $S_w - a_{wn}$ relationship are shown for experiment EXNT01. For the given system and the

experimental times, we observe that the represented non-wetting saturations remain approximately between 0.45 and 0.78. When matching the 2-NSA concentrations to a a_{wn}, we classify the best-fitting curves according to their a_{wn}^{max}, as labelled in Figure 5.6c.

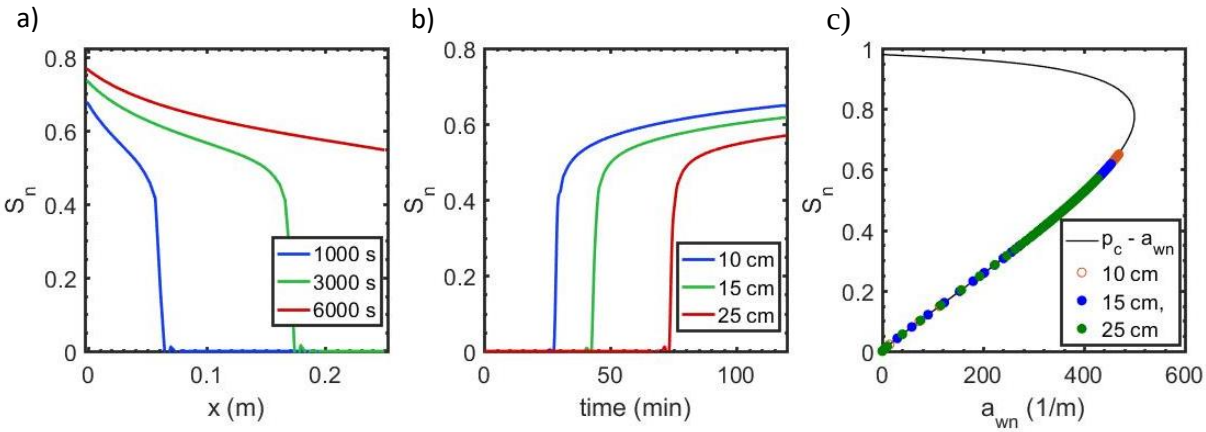

Figure 5.6. Predicted results for experiment EXNT01. **a**) Non-wetting saturation along the column length **b**) non-wetting saturation over time and **c**) the non-wetting saturation for predicted values of specific IFA

5.4.2.1 Pre-processing of data

The experimental 2-NSA results were initially pre-processed to remove any anomalous data that deviated significantly from the predicted trend. One significant issue that arose during the sampling and handling of the vial is the introduction of contamination for which the fluorospectrometer shows high sensitivity. Great caution was taken to avoid this. However, without the development of continuous sampling methods, some contamination resulting in erroneous measurements is inevitable. As a result, it is difficult to assign any value of uncertainty associated with the final result. All data collected ahead of the arrival of the tracer that showed any signal was assigned a value of zero.

5.4.2.2 Fitting the tracer breakthrough experimental results

The experimental results were fitted by running a parameter sweep on parameter a0 from the polynomial equation (5.24). This parameter controls the maximum specific IFA, a_{wn}^{max} while maintaining the general shape of the $S_w - a_{wn}$ curve. For capturing all experimental data points, we present the entire range of a_{wn}^{max} numerical solutions required to fit the most off-set data points (Figure 5.7). In order to illustrate the difficulties associated with the interpretation of the concentration measurements, imperfect and data limited experiments such as experiment EXOT01 are also presented.

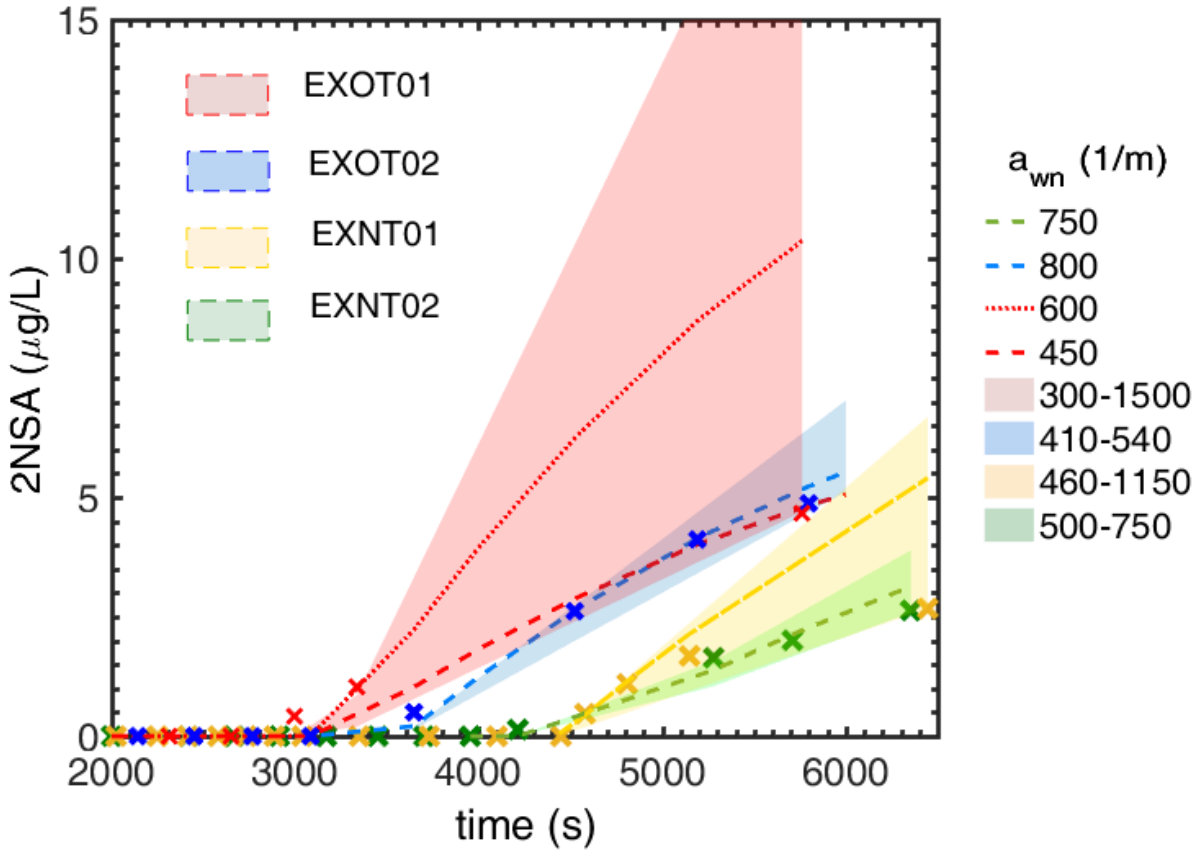

Figure 5.7. Numerical simulations for each KIS tracer experiment. The highlighted area denotes the entire spectrum of results required to fit the most off-set data points, the dashed lines show the best fitting solution for the non-linear description of the hydrolysis reaction rate over time.

As expected with low dispersion and zero-order kinetics, the numerical solution for 2-NSA shows a linear increase with time. The model performs well in predicting early time data, however, late-time 2-NSA concentrations are consistently lower than expected, deviating from the numerically predicted values. One may consider that since the concentration of 2-NSA over time when determining the $R_{n\rightarrow w}^{2NSA}$ behaves non-linearly at early times, assuming strictly zero order kinetics may not adequately capture the changes in kinetic rates throughout the experiment. This is taken into consideration in the experiments displayed in Figure 5.7 (SI Text S2.h). The deviations can also be explained by an increased measurement error at later times (as V_n/V_t approaches unity) due to smaller sample volumes.

5.4.3 Evaluation of the specific interfacial area

Assuming a single-valued $R_{n\rightarrow w}^{2NSA}$, the variation in specific IFA can be expected to range between 330 1/m (m^2/m^3) and 1500 1/m. For the non-linear characterization of $R_{n\rightarrow w}^{2NSA}$, the a_{wn}^{max} (excluding experiment EXOT01), was found to range between 800 1/m and 1150 1/m. The a_{wn}^{max} calculated for the best fitted experiments (EXNT01 and EXNT02) were found to be similar (800 1/m and 750 1/m respectively). This suggest that as long as the reaction rate is well-characterized, we can expect similar specific IFAs for the same sand, independent of the tracer employed. A summary of the results is provided in Table 5.4. Shifting the $S_w(a_{wn}^{max})$ above or below the assumed value of 0.25

would generate slightly different results for a_{wn}^{max}. However, for the range of saturations observed in model, this would not likely be of large significance.

Experimental and geometric models have shown that the magnitude of a_{wn}^{max} is inversely proportional to the grain size of the porous material – increasing linearly with decreasing grain diameters (Brusseau et al. 2009; Narter and Brusseau 2010; Likos and Jaafar 2013). Although direct comparability of specific IFAs between literature and those obtained here is difficult due to differing experimental techniques, porous material and fluid systems, the range of values of a_{wn}^{max} approximated using the KIS-TT method is in general, larger than that found by Culligan et al. (2013) and Porter et al. (2010).

Table 5.4. Summary of calculated specific IFAs

Experiment	a_{wn}^{max} upper limit (1/m)	a_{wn}^{max} lower limit $(1/m)$	Non/linear fitting
EXNT01	1150	460	1150
EXNT02	750	500	750
EXOT01	1500	300	450/600
EXOT02	540	410	800

Using the explicit IFA model developed by Grant and Gerhard (2007), an a_{wn}^{max} of approximately 1300 1/m was calculated – almost double the value predicted in our numerical model (Figure 5.S 7). In order to achieve a similar result, the $R_{n\to w}^{2NSA}$ would have to be almost twice as small. Despite the IFA model being successfully used in the literature (see SI Table 5.S 1), it has yet to be verified in experiments performed under transient conditions. Grant and Gerhard (2007) assume a dissipation factor of 0.2 for all experiments (Table 5.S 1) and a curve by Dalla et al. (2002) to determine the specific IFA from the total IFA. While this has proved rather successful, these values and relationships are likely system dependent (Agaoglu et al. 2015). Since our experiment was done under dynamic conditions, it may be that the energy dissipation factor should also be lower than 0.2 (i.e., conversion from mechanical energy to surface energy may be lower than expected). Another possible reason for the difference may be attributed to using MIP method to determine the $p_c - S_w$ relationship and subsequent conversion to other fluid system.

It is evident that generating a unique $p_c - S_w - a_{wn}$ relationship is of essential for obtaining unique solutions for a_{wn}. Joekar and Hassanizadeh (2008) and Karadimitriou et al. (2017) both found that a single $p_c - S_w - a_{wn}$ relationship may also not be adequate in describing flow for different values of the macroscale capillary number due to changing interfacial velocities. While the sensitivity of the macroscopic capillary number over the entire $p_c - S_w - a_{wn}$relationship is unknown, it is possible that the simplified model assuming a single $p_c - S_w - a_{wn}$is insufficient in accurately predicting the specific IFA in a dynamic system.

5.5 Summary and Conclusions

This research provides a proof of concept for the new category of tracers termed kinetic interface sensitive tracers. Four tracer column experiments were conducted at different pumping rates with two tracers. The KIS-TT method has shown potential to capture the dynamic development of the n-octane-water specific IFA using a simple and inexpensive experimental set-up. The study presents two macroscale immiscible two-phase flow models (using FEM and vertex centered finite volume methods) capable of matching both the experimentally determined n-octane and 2-NSA

concentration BTCs with reasonable comparability. To achieve best fitting numerical results with respect to the experimental data, parameters Q_{in}, and K were optimized to fit the n-octane BTC followed by the optimization of the a_{wn} to fit the 2-NSA concentration BTC. Our predictions of a_{wn} varied quite significantly, however this is largely attributed to measurement difficulties. In limited data experiments such as, EXOT01, a_{wn} ranged from 300 m^{-1} up to 1500 m^{-1}, while in better controlled experiments (EXOT02) the variation range is limited up to approximately 25% of the mean.

The KIS-TT methods have the potential supplementing traditional methods of determining IFAs (i.e., IPTT, CMT). In addition, the KIS-TT method allows us to draw a bridge between results gathered from CMT and that from IPTT methods since it is assumed that the inability for the CMT method to resolve surface roughness is a large contributor to consistently larger a_{wn} observed in IPTT experiments (Brusseau et al. 2006). The use of KIS tracers can provide insights into differentiating between mobile and immobile regions. Immobile regions being the volumes occupied by water in the flow network which are either rate-limited or totally inaccessible. Identification of such regions is difficult by image processing because the analyses should be performed by applying a global metric considering the variation of the local concentrations over time. Experiments play a key role in identifying these regions (Karadimitriou et al. 2016) – especially for tracer techniques used in field applications.

Our numerical models have shown the capacity to predict the experimental data. The concept behind the KIS-TT allows for further development and can provide additional degree of validation to other macroscale numerical models that consider specific IFA, such as those proposed by Niessner and Hassanizadeh (2008). Assuming a method could be developed that allows for much higher sampling resolution, it may also be a valuable technique in determining important parameters in thermodynamically consistent multiphase flow models.

5.6 Acknowledgements

This research has received funding by the European Community's 7th Framework Programme FP7 under grant number 309067, TRUST project, and the European Commission Horizon 2020 Research and Innovation Programme under grant agreement 636811, FracRisk project. We are grateful to Dr. Frieder Maier for his important help to design and construct the experimental setup. The authors would like to thank Mr. Christopher Pötzl and Prof. Dr. S. Siegesmund (University of Göttingen) for the MIP laboratory test. The authors are grateful to Dr. Kirsten Techmers for the SEM measurements. Last but not least, we are thankful to Prof. Rainer Helmig, Dr. Johannes Hommel for constructive discussions.

5.7 References

Agaoglu B, Copty NK, Scheytt T, Hinkelmann R (2015) Interphase mass transfer between fluids in subsurface formations: A review. Adv Water Resour 79:162–194 . doi: 10.1016/j.advwatres.2015.02.009

Annable MD, Rao PSC, Hatfield K, et al (1998) Partitioning Tracers for Measuring Residual NAPL: Field-Scale Test Results. J Environ Eng 124:498–503 . doi: 10.1061/(ASCE)0733-9372(1998)124:6(498)

Anwar AHMF, Bettahar M, Matsubayashi U (2000) A method for determining air–water interfacial area in variably saturated porous media. J Contam Hydrol 43:129–146 . doi: 10.1016/S0169-7722(99)00103-5

Bear J (1988) Dynamics of fluids in porous media. Dover, New York

Bear J (1972) Dynamics of fluids in porous media. American Elsevier, New York. London and Amsterdam

Bell WK, van Brakel J, Heertjes PM (1981) Mercury Penetraton and Retraction Hysteresis in Closely Packed Spheres. Powder Technol 29:75–88 . doi: 10.1016/0032-5910(81)85006-1

Bottero S (2009) Advances in the Theory of Capillarity in Porous Media. PhD Thesis, Utrecht University

Brooks RH, Corey AT (1964) Hydraulic properties of porous media. Hydrol Pap No 3 3:

Brusseau ML, Narter M, Schnaar G, Marble J (2009) Measurement and Estimation of Organic-Liquid/Water Interfacial Areas for Several Natural Porous Media. Environ Sci Technol 43:3619–3625 . doi: 10.1021/es8020827

Brusseau ML, Ouni AE, Araujo JB, Zhong H (2015) Novel methods for measuring air-water interfacial area in unsaturated porous media. Chemosphere 127:208–213 . doi: 10.1016/j.chemosphere.2015.01.029

Brusseau ML, Peng S, Schnaar G, Costanza-Robinson MS (2006) Relationships among air-water interfacial area, capillary pressure, and water saturation for a sandy porous medium. Water Resour Res 42:W03501 . doi: 10.1029/2005WR004058

Brusseau ML, Peng S, Schnaar G, Murao A (2007) Measuring Air−Water Interfacial Areas with X-ray Microtomography and Interfacial Partitioning Tracer Tests. Environ Sci Technol 41:1956–1961 . doi: 10.1021/es061474m

Brusseau ML, Popovičová J, Silva JAK (1997) Characterizing gas-water interfacial and bulk-water partitioning for gas-phase transport of organic contaminants in unsaturated porous media. Environ Sci Technol 31:1645–1649 . doi: 10.1021/es960475j

Burdine NT (1953) Relative Permeability Calculations From Pore Size Distribution Data. J Pet Technol 5: . doi: 10.2118/225-G

Cary JW (1994) Estimating the surface area of fluid phase interfaces in porous media. J Contam Hydrol 15:243–248 . doi: 10.1016/0169-7722(94)90029-9

Chen L, Kibbey TCG (2006) Measurement of air-water interfacial area for multiple hysteretic drainage curves in an unsaturated fine sand. Langmuir ACS J Surf Colloids 22:6874–6880 . doi: 10.1021/la053521e

Cheng J-T, Pyrak-Nolte LJ, Nolte DD, Giordano NJ (2004) Linking pressure and saturation through interfacial areas in porous media. Geophys Res Lett 31:L08502 . doi: 10.1029/2003GL019282

Class H, Ebigbo A, Helmig R, et al (2009) A benchmark study on problems related to CO2 storage in geologic formations : Summary and discussion of the results (Original paper). Comput Geosci 13:409–434

Cook PJ (2017) CCS Research Development and Deployment in a Clean Energy Future: Lessons from Australia over the Past Two Decades. Engineering 3:477–484 . doi: 10.1016/J.ENG.2017.04.014

Corapcioglu MY, Fedirchuk P (1999) Glass bead micromodel study of solute transport. J Contam Hydrol 36:209–230 . doi: 10.1016/S0169-7722(98)00145-4

Costanza-Robinson MS, Brusseau ML (2002) Air-water interfacial areas in unsaturated soils: Evaluation of interfacial domains. Water Resour Res 38:1195 . doi: 10.1029/2001WR000738

Costanza-Robinson MS, Harrold KH, Lieb-Lappen RM (2008) X-ray Microtomography Determination of Air−Water Interfacial Area−Water Saturation Relationships in Sandy Porous Media. Environ Sci Technol 42:2949–2956 . doi: 10.1021/es072080d

Costanza-Robinson MS, Henry EJ (2017) Surfactant-induced flow compromises determination of air-water interfacial areas by surfactant miscible-displacement. Chemosphere 171:275–283 . doi: 10.1016/j.chemosphere.2016.12.072

Coutelieris FA, Delgado JMPQ (2012) Transport Phenomena in Porous Structures. In: Transport Processes in Porous Media. Springer, Berlin, Heidelberg, pp 39–85

Culligan KA, Wildenschild D, Christensen BSB, et al (2006) Pore-scale characteristics of multiphase flow in porous media: A comparison of air–water and oil–water experiments. Adv Water Resour 29:227–238 . doi: 10.1016/j.advwatres.2005.03.021

Culligan KA, Wildenschild D, Christensen BSB, et al (2004) Interfacial area measurements for unsaturated flow through a porous medium. Water Resour Res 40:W12413 . doi: 10.1029/2004WR003278

Dalla E, Hilpert M, Miller CT (2002) Computation of the interfacial area for two-fluid porous medium systems. J Contam Hydrol 56:25–48

Dobson R, Schroth MH, Oostrom M, Zeyer J (2006) Determination of NAPL−Water Interfacial Areas in Well-Characterized Porous Media. Environ Sci Technol 40:815–822 . doi: 10.1021/es050037p

Flemisch B, Berre I, Boon W, et al (2017) Benchmarks for single-phase flow in fractured porous media (accepted). Adv Water Resour

Flemisch B, Darcis M, Erbertseder K, et al (2011) DuMux: DUNE for multi-{phase, component, scale, physics, …} flow and transport in porous media. Adv Water Resour 34:1102–1112 . doi: 10.1016/j.advwatres.2011.03.007

Frevel LK, Kressley LJ (1963) Modifications in Mercury Porosimetry. Anal Chem 35:1492–1502 . doi: 10.1021/ac60203a020

Fukunishi Y, Tateishi T, Suzuki M (1996) Octane/Water Interfacial Tension Calculation by Molecular Dynamics Simulation. J Colloid Interface Sci 180:188–192 . doi: 10.1006/jcis.1996.0288

Giesche H (2006) Mercury Porosimetry: A General (Practical) Overview. Part Part Syst Charact 23:9–19 . doi: 10.1002/ppsc.200601009

Grant GP, Gerhard JI (2007) Simulating the dissolution of a complex dense nonaqueous phase liquid source zone: 1. Model to predict interfacial area. Water Resour Res 43:W12410 . doi: 10.1029/2007WR006038

Gray WG, Hassanizadeh SM (1989) Averaging theorems and averaged equations for transport of interface properties in multiphase systems. Int J Multiph Flow 15:81–95 . doi: 10.1016/0301-9322(89)90087-6

Gray WG, Miller CT (2005) Thermodynamically constrained averaging theory approach for modeling flow and transport phenomena in porous medium systems: 1. Motivation and overview. Adv Water Resour 28:161–180 . doi: 10.1016/j.advwatres.2004.09.005

Gray WG, Miller CT (2014) Introduction to the Thermodynamically Constrained Averaging Theory for Porous Medium Systems

Gray WG, Miller CT, Schrefler BA (2013) Averaging theory for description of environmental problems: What have we learned? Adv Water Resour 51:123–138 . doi: 10.1016/j.advwatres.2011.12.005

Gvirtzman H, Roberts PV (1991) Pore scale spatial analysis of two immiscible fluids in porous media. Water Resour Res 27:1165–1176 . doi: 10.1029/91WR00303

Hassanizadeh SM, Gray WG (1993) Thermodynamic basis of capillary pressure in porous media. Water Resour Res 29:3389–3405 . doi: 10.1029/93WR01495

Hassanizadeh SM, Gray WG (1990) Mechanics and thermodynamics of multiphase flow in porous media including interphase boundaries. Adv Water Resour 13:169–186 . doi: 10.1016/0309-1708(90)90040-B

Helland JO, Skjæveland SM (2007) Relationship between capillary pressure, saturation, and interfacial area from a model of mixed-wet triangular tubes. Water Resour Res 43:W12S10 . doi: 10.1029/2006WR005698

Helmig R (1997) Multiphase Flow and Transport Processes in the Subsurface: A Contribution to the Modeling of Hydrosystems, 1st edn. Springer

IPCC (2005) IPCC special report on carbon dioxide capture and storage. Metz, B., Davidson, O., de Coninck, H.C., Loos, M., Meyer, L.A. (Editors): Prepared by Working Group III of the Intergovernmental Panel on Climate Change. Cambridge University Press

Jain V, Bryant S, Sharma M (2003) Influence of Wettability and Saturation on Liquid−Liquid Interfacial Area in Porous Media. Environ Sci Technol 37:584–591 . doi: 10.1021/es020550s

Joekar-Niasar V, Hassanizadeh S, Leijnse A (2008) Insights into the Relationships Among Capillary Pressure, Saturation, Interfacial Area and Relative Permeability Using Pore-Network Modeling. Transp Porous Media 74:201–219 . doi: 10.1007/s11242-007-9191-7

Joekar-Niasar V, Hassanizadeh SM (2011) Specific interfacial area: The missing state variable in two-phase flow equations? Water Resour Res 47:W05513 . doi: 10.1029/2010WR009291

Joekar-Niasar V, Hassanizadeh SM (2012) Uniqueness of Specific Interfacial Area–Capillary Pressure–Saturation Relationship Under Non-Equilibrium Conditions in Two-Phase Porous Media Flow. Transp Porous Media 94:465–486 . doi: 10.1007/s11242-012-9958-3

Johns null, Gladden null (1999) Magnetic Resonance Imaging Study of the Dissolution Kinetics of Octanol in Porous Media. J Colloid Interface Sci 210:261–270 . doi: 10.1006/jcis.1998.5950

Karadimitriou NK, Hassanizadeh SM, Joekar-Niasar V, Kleingeld PJ (2014) Micromodel study of two-phase flow under transient conditions: Quantifying effects of specific interfacial area. Water Resour Res 50:8125–8140 . doi: 10.1002/2014WR015388

Karadimitriou NK, Joekar-Niasar V, Babaei M, Shore CA (2016) Critical Role of the Immobile Zone in Non-Fickian Two-Phase Transport: A New Paradigm. Environ Sci Technol 50:4384–4392 . doi: 10.1021/acs.est.5b05947

Karadimitriou NK, Joekar-Niasar V, Brizuela OG (2017) Hydro-dynamic Solute Transport under Two-Phase Flow Conditions. Sci Rep 7:6624 . doi: 10.1038/s41598-017-06748-1

Karkare MV, Fort T (1996) Determination of the Air−Water Interfacial Area in Wet "Unsaturated" Porous Media. Langmuir 12:2041–2044 . doi: 10.1021/la950821v

Kibbey TCG, Chen L (2012) A pore network model study of the fluid-fluid interfacial areas measured by dynamic-interface tracer depletion and miscible displacement water phase advective tracer methods. Water Resour Res 48:W10519 . doi: 10.1029/2012WR011862

Kim H, Rao PSC, Annable MD (1999) Gaseous Tracer Technique for Estimating Air–Water Interfacial Areas and Interface Mobility. Soil Sci Soc Am J 63:1554–1560 . doi: 10.2136/sssaj1999.6361554x

Kim H, Rao PSC, Annable MD (1997) Determination of effective air-water interfacial area in partially saturated porous media using surfactant adsorption. Water Resour Res 33:2705 . doi: 10.1029/97WR02227

Lackner KS (2003) Climate change. A guide to CO2 sequestration. Science 300:1677–1678 . doi: 10.1126/science.1079033

Leverett MC (1941) Capillary Behavior in Porous Solids. Trans AIME 142:152–169 . doi: 10.2118/941152-G

Li M, Zhai Y, Wan L (2016) Measurement of NAPL–water interfacial areas and mass transfer rates in two-dimensional flow cell. Water Sci Technol 74:2145–2151 . doi: 10.2166/wst.2016.397

Likos WJ, Jaafar R (2013) Pore-Scale Model for Water Retention and Fluid Partitioning of Partially Saturated Granular Soil. J Geotech Geoenvironmental Eng 139:724–737 . doi: 10.1061/(ASCE)GT.1943-5606.0000811

Maier F, Schaffer M, Licha T (2015) Temperature determination using thermo-sensitive tracers: Experimental validation in an isothermal column heat exchanger. Geothermics 53:533–539 . doi: 10.1016/j.geothermics.2014.09.007

Mayer RP, Stowe RA (1965) Mercury porosimetry—breakthrough pressure for penetration between packed spheres. J Colloid Sci 20:893–911 . doi: 10.1016/0095-8522(65)90061-9

McDonald K, Carroll KC, Brusseau ML (2016) Comparison of fluid-fluid interfacial areas measured with X-ray microtomography and interfacial partitioning tracer tests for the same samples. Water Resour Res 52:5393–5399 . doi: 10.1002/2016WR018775

Miller CT, Poirier-McNeil MM, Mayer AS (1990) Dissolution of Trapped Nonaqueous Phase Liquids: Mass Transfer Characteristics. Water Resour Res 26:2783–2796 . doi: 10.1029/WR026i011p02783

Millington RJ, Quirk JP (1961) Permeability of porous solids. Trans Faraday Soc 57:1200–1207

Myers M, Stalker L, Pejcic B, Ross A (2013) Tracers – Past, present and future applications in CO2 geosequestration. Appl Geochem 30:125–135 . doi: 10.1016/j.apgeochem.2012.06.001

Myers M, Stalker L, Ross A, et al (2012) Method for the determination of residual carbon dioxide saturation using reactive ester tracers. Appl Geochem 27:2148–2156 . doi: 10.1016/j.apgeochem.2012.07.010

Narter M, Brusseau ML (2010) Comparison of Interfacial partitioning tracer test and high-resolution microtomography measurements of fluid-fluid interfacial areas for an ideal porous medium. Water Resour Res 46: . doi: 10.1029/2009WR008375

Nelson NT, Brusseau ML (1996) Field Study of the Partitioning Tracer Method for Detection of Dense Nonaqueous Phase Liquid in a Trichloroethene- Contaminated Aquifer. Environ Sci Technol 30:2859–2863 . doi: 10.1021/es960148b

Niemi A, Bensabat J, Bergmann P, et al (2017) Field Injection Operations and Monitoring of the Injected CO2. In: Geological Storage of CO2 in Deep Saline Formations. Springer Netherlands, pp 381–471

Niessner J, Hassanizadeh SM (2008) A model for two-phase flow in porous media including fluid-fluid interfacial area. Water Resour Res 44:10 PP. . doi: 200810.1029/2007WR006721

Niessner J, Hassanizadeh SM (2009) Non-equilibrium interphase heat and mass transfer during two-phase flow in porous media—Theoretical considerations and modeling. Adv Water Resour 32:1756–1766 . doi: 10.1016/j.advwatres.2009.09.007

Nordbotten JM, Flemisch B, Gasda SE, et al (2012) Uncertainties in practical simulation of CO2 storage. Int J Greenh Gas Control 9:234–242 . doi: 10.1016/j.ijggc.2012.03.007

Peche A, Halisch M, Tatomir A (2016) Development of a numerical workflow based on μ-CT-imaging for the determination of capillary pressure-saturation-specific interfacial area relationship in two-phase flow pore-scale porous media systems: A case study on Heletz sandstone. Solid Earth Discuss 1–29 . doi: 10.5194/se-2016-39

Porter ML, Schaap MG, Wildenschild D (2009) Lattice-Boltzmann simulations of the capillary pressure–saturation–interfacial area relationship for porous media. Adv Water Resour 32:1632–1640 . doi: 10.1016/j.advwatres.2009.08.009

Porter ML, Wildenschild D, Grant G, Gerhard JI (2010) Measurement and prediction of the relationship between capillary pressure, saturation, and interfacial area in a NAPL-water-glass bead system. Water Resour Res 46:W08512 . doi: 10.1029/2009WR007786

Powers SE, Abriola LM, Weber WJ (1992) An experimental investigation of nonaqueous phase liquid dissolution in saturated subsurface systems: Steady state mass transfer rates. Water Resour Res 28:2691–2705 . doi: 10.1029/92WR00984

Reeves PC, Celia MA (1996) A Functional Relationship Between Capillary Pressure, Saturation, and Interfacial Area as Revealed by a Pore-Scale Network Model. Water Resour Res 32:2345 . doi: 10.1029/96WR01105

Saripalli KP, Kim H, Rao PSC, Annable MD (1997) Measurement of Specific Fluid−Fluid Interfacial Areas of Immiscible Fluids in Porous Media. Environ Sci Technol 31:932–936 . doi: 10.1021/es960652g

Saripalli KP, Rao PS., Annable M. (1998) Determination of specific NAPL–water interfacial areas of residual NAPLs in porous media using the interfacial tracers technique. J Contam Hydrol 30:375–391 . doi: 10.1016/S0169-7722(97)00052-1

Sato T, Tanahashi H, Loáiciga HA (2003) Solute dispersion in a variably saturated sand. Water Resour Res 39:1155 . doi: 10.1029/2002WR001649

Schaefer CE, DiCarlo DA, Blunt MJ (2000) Experimental measurement of air-water interfacial area during gravity drainage and secondary imbibition in porous media. Water Resour Res 36:885–890 . doi: 10.1029/2000WR900007

Schaffer M, Maier F, Licha T, Sauter M (2013) A new generation of tracers for the characterization of interfacial areas during supercritical carbon dioxide injections into deep saline aquifers: Kinetic interface-sensitive tracers (KIS tracer). Int J Greenh Gas Control 14:200–208 . doi: 10.1016/j.ijggc.2013.01.020

Schnaar G, Brusseau ML (2005) Pore-Scale Characterization of Organic Immiscible-Liquid Morphology in Natural Porous Media Using Synchrotron X-ray Microtomography. Environ Sci Technol 39:8403–8410 . doi: 10.1021/es0508370

Simon MA, Brusseau ML (2007) Analysis of a gas-phase partitioning tracer test conducted in an unsaturated fractured-clay formation. J Contam Hydrol 90:146–158 . doi: 10.1016/j.jconhyd.2006.09.010

Sternberg SPK (2004) Dispersion Measurements in Highly Heterogeneous Laboratory Scale Porous Media. Transp Porous Media 54:107–124 . doi: 10.1023/A:1025708313812

Tatomir A, Maier F, Schaffer M, et al (2013) Modelling of Kinetic Interface Sensitive Tracers for Two-Phase Systems. In: Hou MZ, Xie H, Were P (eds) Clean Energy Systems in the Subsurface: Production, Storage and Conversion. Springer Berlin Heidelberg, pp 65–74

Tatomir AB, Jyoti A, Sauter M (2016) The Monitoring of CO2 plume migration in deep saline formations with kinetic interface sensitive tracers. In: Singh TN, Vikram V (eds) Geologic Carbon Sequestration: Understanding Reservoir Concepts. Springer, p 336

Tatomir AB, Schaffer M, Kissinger A, et al (2015) Novel approach for modeling kinetic interface-sensitive (KIS) tracers with respect to time-dependent interfacial area change for the optimization of supercritical carbon dioxide injection into deep saline aquifers. Int J Greenh Gas Control 33:145–153 . doi: 10.1016/j.ijggc.2014.11.020

Van Genuchten MT (1980) A Closed-Form Equation for Predicting the Hydraulic Conductivity of Unsaturated Soils. Soil Sci Soc Am 44:

Wildenschild D, Sheppard AP (2013) X-ray imaging and analysis techniques for quantifying pore-scale structure and processes in subsurface porous medium systems. Adv Water Resour 51:217–246 . doi: 10.1016/j.advwatres.2012.07.018

Zhang H, Schwartz FW (2000) Simulating the in situ oxidative treatment of chlorinated ethylenes by potassium permanganate. Water Resour Res 36:3031–3042 . doi: 10.1029/2000WR900173

Zhong H, El Ouni A, Lin D, et al (2016) The two-phase flow IPTT method for measurement of nonwetting-wetting liquid interfacial areas at higher nonwetting saturations in natural porous media. Water Resour Res 52:5506–5515 . doi: 10.1002/2016WR018783

6. Estimation of NAPL-Water interfacial areas for unconsolidated porous media by kinetic interface sensitive (KIS) tracers

Alexandru Tatomir[1,2], Huhao Gao[2], Christopher Pötzl[3], Nikolaos Karadimitriou[4], Tobias Licha[5], Holger Class[6], Rainer Helmig[6], and Martin Sauter[2]

Citation:

Tatomir AB, Gao H, Pötzl C, Karadimitriou NK, Licha T, Class H, Helmig RH, Sauter M (2020) Estimation of NAPL-Water interfacial areas for unconsolidated porous media by kinetic interface sensitive (KIS) tracers. In: Earth Space Sci. Open Arch. https://www.essoar.org/doi/abs/10.1002/essoar.10503948.1 Accessed 20 May 2022

[1]Department of Earth Sciences, Geocentrum, Uppsala University, Villavägen 16, 752 36 Uppsala, Sweden.

[2]Department of Applied Geology, Geoscience Centre of the University of Göttingen, Goldschmidtstr. 3, 37077 Göttingen, Germany

[3]Department of Structural Geology and Geodynamics, Geoscience Centre of the University of Göttingen, Goldschmidtstr. 3, 37077 Göttingen, Germany

[4]Department of Structural Engineering, University of Stuttgart, Pfaffenwaldring 7, 70569 Stuttgart, Germany

[5]Department of Applied Geology, Institute of Geology, Mineralogy and Geophysics, Ruhr University Bochum, Universitätsstr. 150, 44801 Bochum, Germany

[6]Department of Hydromechanics and Modelling of Hydrosystems, University of Stuttgart, Pfaffenwaldring 7, 70569 Stuttgart, Germany

Corresponding author: Alexandru Tatomir (alexandru.tatomir@geo.uu.se; alexandru.tatomir@geo.uni-goettingen.de)

Abstract:

Employing kinetic interface sensitive (KIS) tracers, we investigate three different types of glass-bead materials and two natural porous media systems to quantitatively characterize the influence of the porous-medium grain-, pore-size and texture on the "mobile" interfacial area between an organic liquid and water. By interpreting the breakthrough curves (BTCs) of the reaction product of the KIS tracer hydrolysis we obtain a relationship for the specific interfacial area (IFA) and wetting saturation. The immiscible displacement process coupled with the reactive tracer transport across the fluid-fluid interface is simulated with a Darcy-scale numerical model. The results show that the current reactive transport model is not always capable to reproduce the breakthrough curves of tracer experiments and that a new theoretical framework is required.

Total solid surface area of the grains, i.e., grain surface roughness, is shown to have an important influence on the capillary-associated IFA by comparing results obtained from experiments with spherical glass beads having very small or even no surface roughness and those obtained from experiments with the natural sand. Furthermore, a linear relationship between the mobile capillary associated IFA and the inverse mean grain diameter can be established. The results are compared with the data collected from literature measured with high resolution microtomography and partitioning tracer methods. The capillary associated IFA values are consistently smaller because KIS tracers measure the mobile part of the interface. Through this study the applicability range of the KIS tracers is considerably expanded and the confidence in the robustness of the method is improved.

6.1 Introduction

The interfacial area between fluid-phases plays a critical role in the coupled multiphase flow, solute transport and reaction processes in porous media (Miller et al. 1990; Hassanizadeh and Gray 1990; Reeves and Celia 1996). Some applications, where the fluid-fluid interfacial area (FIFA) plays a major role, are the geological storage of CO_2 (e.g., Niemi et al. 2016), oil and gas recovery, the remediation of contaminated sites, such as per- and poly-fluoroalkyl substances (PFAS) (e.g., Brusseau 2018; Brusseau 2019).

The fluid-fluid interfacial areas can be classified in capillary-associated interfacial areas (IFAs) (e.g., menisci), and film-associated interfacial areas, or surface-adsorbed (Costanza-Robinson and Brusseau 2002; Brusseau et al. 2006; Porter et al. 2010). The sum of the two represents the total interfacial area. The capillary-associated IFA, a_{wn}, can be further subdivided into immobile (or stagnant), $a_{wn}^{immobile}$, or mobile, a_{wn}^{mobile} (Figure 6.1) (Joekar-Niasar and Hassanizadeh 2012a)

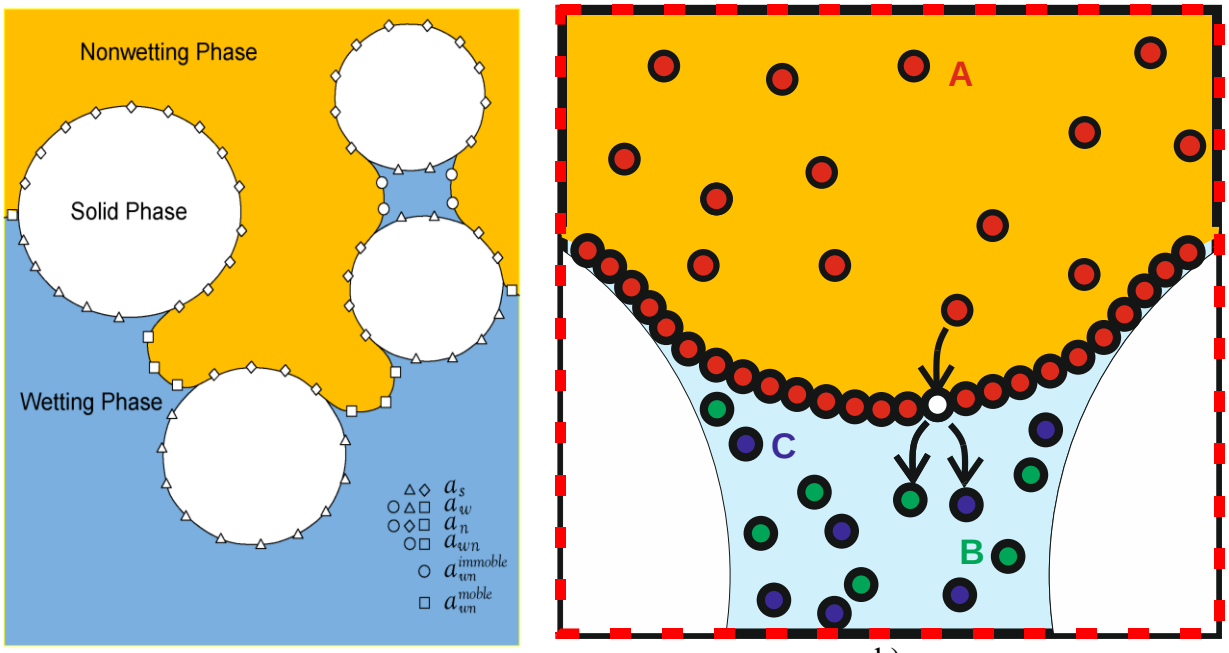

a) b)

Figure 6.1: a) Illustration of the different types of interfacial areas b) KIS tracer (A) adsorption on the fluid-fluid interface, followed by hydrolysis to form two by-products (B+C) dissolved in water, an acid and alcohol.

6.1.1 Models for calculating the FIFA

Due to difficulties in directly measuring the FIFA, initial studies focused on developing theoretical and modelling approaches employing normalized interfacial area per unit of representative elementary volume (REV) (Leverett 1941; Gvirtzman and Roberts 1991; Hassanizadeh and Gray 1993; Cary 1994; Reeves and Celia 1996; Bradford and Leij 1997; Held and Celia 2001; Oostrom et al. 2001; Dalla et al. 2002; Dobson et al. 2006) The models can be roughly classified into the following categories: pore-geometry models, where the porous media is represented using an idealized spherical packing (e.g., Gvirtzman and Roberts 1991; Likos and Jaafar 2013), or a bundle of capillary tubes (Cary 1994; Oostrom et al. 2001), and thermodynamic-based models (Leverett 1941; Bradford and Leij 1997; Grant and Gerhard 2007) measuring the net amount of reversible work. With the development of computational capabilities other categories were added: pore-network models that use a simplified representation of the porous media as a network of pore-bodies and pore-throats (Reeves and Celia 1996); pore-morphology models (e.g., (Dalla et al. 2002); and direct pore-scale numerical simulations using particle-based methods such as the Lattice Boltzmann (Porter et al. 2010), and smooth particle hydrodynamics, and grid-based computational fluid dynamics methods such as the level-set-, volume-of-fluid-, and phase field-methods (Gao et al. 2020). The pore-scale models calculate explicitly the magnitude of FIFA and allow the calculation of upscaled per-volume normalized quantities, i.e., capillary pressure, saturation and specific interfacial areas, required by the continuum-based, Darcy-scale multiphase flow simulators. The expression of the FIFA as volume averaged quantity allows its straightforward implementation into the Darcy-scale type flow simulators since no additional parameters other than the initial ones are required.

6.1.2 Measurement techniques for fluid-fluid interfacial area

Several experimental methods were proposed to measure the fluid-fluid interfacial areas (FIFAs): interface partitioning tracer test (IPTT), where the tracer is dissolved in aqueous (Kim et al. 1997; Saripalli et al. 1997; Anwar et al. 2000; Brusseau et al. 2007) or in gaseous phase (Kim et al. 1999; Costanza-Robinson and Brusseau 2002), high-resolution industrial X-ray microtomography (XMT), and synchrotron XMT (Culligan et al. 2006; Brusseau et al. 2008; Narter and Brusseau 2010; Porter et al. 2010; Peche et al. 2016; McDonald et al. 2016; Lyu Ying et al. 2017; Patmonoaji et al. 2018; Araujo and Brusseau 2020), the gas adsorption chemical reaction (GACR) (Lyu Ying et al. 2017), thin micro-models (Karadimitriou et al. 2016), and the kinetic interface sensitive tracer method (Tatomir et al. 2018). The experimental methods for measuring the FIFA are usually applied in controlled laboratory conditions, i.e. tracer methods, XMT, micro models, (e.g., Dobson et al. 2006; Porter et al. 2010; Karadimitriou et al. 2016; McDonald et al. 2016; Tatomir et al. 2018), but also in the field, i.e. tracer methods (Nelson and Brusseau 1996; Annable et al. 1998; Simon and Brusseau 2007). Some methods are inherently designed for laboratory conditions only, e.g. micro-models, and XMT.

Usually, standard tracer techniques measure the FIFA in steady state conditions, when a residual saturation is formed. For instance, the gas-phase IPTT implies that a residual water saturation is created in the column, while the gas phase together with two tracers, a conservative and a reactive one, being circulated. The tracer partitioning on the fluid-fluid interface is interpreted from breakthrough curves (BTCs) and the FIFA is calculated.

Most of the literature related to measurement of FIFA address to air-water fluid systems. However, there is a consistent body of literatures which addresses to NAPL-water or organic fluid-water fluid systems (Dobson et al. 2006; Schnaar and Brusseau 2006; Brusseau et al. 2008; Brusseau et al. 2009; Narter and Brusseau 2010; Brusseau et al. 2010; Zhong et al. 2016; Tatomir et al. 2018).

The kinetic interface sensitive (KIS) tracer method was proposed by Tatomir et al. (2018) for quantifying the FIFA in a dynamic immiscible displacement process. A proof of concept was provided using controlled column experiments with a well-characterized glass-bead porous medium. The experimental results were interpreted by specifically developed numerical models for multiphase flow coupled with reactive transport showing a general agreement of the FIFA size with the theory. KIS tracers are first dissolved in the non-wetting phase and then injected. When they come in contact with water, they hydrolyze to form two highly soluble components in water, i.e., an acid and an alcohol. A KIS tracer stable component, with a zero-order reaction rate was synthesized by Schaffer et al. (2013). The interpretation of the breakthrough curves of the "byproduct acid" provides information about the size of the FIFA. Since the measurements are performed for the tracer arriving at the outlet together with the mobilized water, KIS tracers are considered to measure the mobile component of the capillary associated interface, a_{wn}^{mobile}.

6.1.3 Studies comparing the experimental methods for FIFA measurement

The magnitude of the FIFA reported in the literature depends on the measurement technique employed. This is because it is not always clear which part of the FIFA a particular technique measures, either the total interfacial area, the capillary-associated IFA, or some combination of both the capillary-associated IFA and some part of the film associated area.

Thus, compared to aqueous-phase IPTT the gas-phase IPTT generally yields larger IFA (Costanza-Robinson and Brusseau 2002). It is hypothesized that the gas-phase IPTT measures both capillary and film-adsorbed FIFA while the aqueous-phase IPTT measure primarily FIFA formed by water held by capillarity, e.g. pendular rings. At low water saturations the FIFA measured with gas-phase IPTT showed exponential increase (Kim et al. 1999; Costanza-Robinson and Brusseau 2002; Peng and Brusseau 2005). Similarly, using gas-phase IPTT, Peng and Brusseau (2005) showed that at low water saturations, the maximum air-water IFA approached those of the normalized solid surface areas, a_s. This indicates that indeed the gas phase IPTT measure the total FIFA, as this was orders of magnitude larger than the calculated, GSSA, but in good agreement with the SSSA measured with N_2/BET method.

Several studies reported that IPTT measured FIFAs were larger than those measured with XMT, which can only scan with a certain resolution (Brusseau et al. 2006; Brusseau et al. 2007; Brusseau et al. 2010; Brusseau et al. 2015; McDonald et al. 2016). Narter and Brusseau (2010) compared the aqueous-phase IPTT with high-resolution micro-tomography for an organic liquid-water -glass bead porous medium system, in an attempt to address the hypothesis that the surface roughness has an influence on the FIFA. Their findings suggest that IPTT and micro-tomography provide robust FIFA values that are comparable when the porous medium has no surface roughness. In that sense, the maximum specific FIFA, was similar to the SSSA measured with N_2/BET and using the smooth-sphere assumption. (Narter and Brusseau 2010; Zhong et al. 2016; Lyu Ying et al. 2017). An explanation for this is that the computed micro-tomography measured IFAs do not include areas associated with microscopic surface heterogeneities, i.e. roughness-associated surface area (Brusseau et al. 2009; Brusseau et al. 2010). A review of the tracer-based methods for measuring air-water IFAs is provided in (Costanza-Robinson and Brusseau 2002), while the various sources of error of the IPTT are discussed in (Brusseau et al. 2008).

Note that relationships between the capillary associated IFA and the size of the total interfacial area can be established. Grant and Gerhard (2007) used the previous pore-network data of Dalla et al. (2002) to obtain the ratio of capillary-associated IFA to total IFA as a function of the saturation. Thus, the total IFA obtained from their thermodynamic model is able to be related to capillary-associated IFA for a given fluid saturation.

6.1.4 Porous media characteristics influence on FIFA

The size of FIFA is mediated by the pore-scale fluid configuration effects which are hard to quantify. At the macro-scale, the FIFA is usually expressed as a function of fluid saturation. Also, the capillary-associated IFA was observed to increase monotonically with increasing capillary pressure and then to plateau at values that correspond to areas associated with residual water saturation (Brusseau et al. 2006)

Literature studies have shown that porous medium texture influences the FIFAs, namely, porous media with larger solid surface areas generate larger fluid-fluid interfacial areas. Several studies demonstrate that fluid-fluid interfacial area is a function of soil properties such as **grain size**, **grain size distribution**, and **surface roughness** (Cary 1994; Anwar et al. 2000; Peng and Brusseau 2005; Cho and Annable 2005; Dobson et al. 2006; Brusseau et al. 2008; Brusseau et al. 2009; Brusseau et al. 2010; Jiang et al. 2020)**.** In the following, the available studies of major relevance on the influence of these parameters are described.

6.1.5 Grain-size influence on fluid-fluid interfacial area

Both the IFA models and experiments show that the maximum total specific FIFA is a function of inverse median grain diameter (e.g., Anwar et al. 2000; Brusseau et al. 2009).Costanza and Brusseau (2000) used the theoretical model-based data reported by (Cary 1994) to evaluate the influence of porous-medium grain size on FIFA. One observation of these studies was that porous media with smaller grain sizes have larger specific FIFAs. Using four high purity sands (Dobson et al. 2006) conducted aqueous-phase interface-partitioning tracer tests in NAPL-water fluid systems and compared the results with the theoretical models (Bradford and Leij 1997; Oostrom et al. 2001) and a modified version of (Bradford and Leij 1997). Even though the measured specific IFA were increasing with decreasing median grain diameter, not all the reported experimental results (only three out of four) were following the theoretically expected trend.

Brusseau et al. (2009) use ten porous media to study the influence of grain-size and texture on FIFA. The results show that the specific FIFA and maximum specific FIFA correlate very well with the inverse grain diameter. Also, the IFA correlates with SSSA and with the inverse median grain diameter (IMGD). This, however, is obtained with tracer techniques which are indirect measurement of IFA (Brusseau et al. 2009).

6.1.6 Porous-medium-texture influence on the fluid-fluid interfacial area

Besides the mean grain diameter, surface roughness is one of key parameters influencing not only the fluid-fluid interface, but also the degree of wettability, the permeability of the medium, or the capillary pressure- and relative permeability-saturation relationships.

Peng and Brusseau (2005) used the gas phase IPTT to measure the air-water FIFA for eight soils and natural sands. The values were compared to the normalized surface areas of the porous media. It was observed that FIFAs were generally larger for materials with larger SSSA measured with N_2/BET method, incorporating the surface roughness.

Analyzing ten different types of porous media, comprising different grain-size distributions and geochemical properties, Brusseau et al. (2009) report that grain-size distributions have minimal impact on the FIFA. Brusseau et al. (2010) conducted aqueous phase IPTT on two soils (Vinton and Eustis) and found that the maximum NAPL -water IFAs are much larger than those obtained by geometric calculation with the smooth-sphere assumption (GSSA). Their observations suggest that surface roughness has a significant impact on interfacial area and that the glass beads' total specific IFA is similar to the SSSA predicted using the smooth-sphere assumption. A linear relationship between the total solid area measured with N_2/BET and the IPTT-measured IFA is established. However, this is based on a total of seven measurements, one very large N_2/BET value being dominant. Because the film-associated areas are a significant component of the FIFAs measured with IPTT, they conclude that the IPTT methods measure some fraction of the interfacial area associated with surface roughness.

Zhong et al. (2016) used a modified version of aqueous-phase IPTT to measure FIFA for several porous media made of glass beads, sand and Vinton soil during a series of drainage and imbibition. The modified IPTT allows measuring the IFA at higher saturations than residual. The maximum total FIFAs were compared to the SSSA measured with N_2/BET and to those estimated based on GSSA.

Recently, Jiang et al. (2020) investigated the role of microscale surface roughness on the FIFA assuming a triangular bundle-of-cylindrical capillaries, their model belonging to the pore-geometry model category. The exponential increase of the total FIFA observed with the gas-phase IPTT method when wetting saturation approaches zero can be explained by the impact of surface roughness on the film-associated IFA.

6.1.7 Objective

To date, the KIS tracer method has been tested only for an ideal glass-bead well-sorted uniform medium. An important step in the development of the KIS tracer method is the implementation of the method for different soil types followed by the interpretation and comparison of the results. Two categories of porous media are to be used, glass-beads and natural sands, having different textures, grain- and pore-size distributions. By extending the applicability range of the KIS tracers to several porous media, the generated set of tracer breakthrough curves is used, subsequently, to verify the current modelling approaches.

For understanding the influence of **mean grain size**, **grain and pore-size distributions**, and **surface roughness,** on the IFA, an extensive characterization of the glass beads and of the natural sand is initially performed with digital image analysis and mercury intrusion porosimetry. Our objective is to compare the IFA, obtained by KIS-tracer experiments in terms of the maximum capillary associated specific interfacial area with published experimental data using various measurement techniques and models.

6.2 Materials and methods

6.2.1 Materials

6.2.1.1 Laboratory setup

The testing procedure and experimental apparatus are those of our previous study (Tatomir et al. 2018). The experimental apparatus (Figure 6.2) consists of a stainless-steel column, 250 mm long and 30 mm in diameter. Two metal frits with extremely fine meshes are placed either end of the column holding the sand inside the column. A peristaltic pump with adjustable flow rate is first used for saturating the column with water and later for providing a constant flow to the bottom of the vertically oriented column of n-octane with dissolved KIS tracer. The peristaltic pump can set the ratio of working power, but the actual flow rate depends on the permeability of the system.
The chemical stability of the materials (e.g., tubings, column) was tested in the presence of ultra-pure water and n-octane. We observed that many carbon-based materials (i.e., tubings) interact with the n-octane inducing either swelling or brittleness. Therefore, only materials which did not react with n-octane were selected when constructing the experimental setup **Figure 6.2**. Naphthalenesulfonates are highly fluorescent and can be detected at low concentration levels in the range of μg/l using fluorescence spectrometry. The 2-NSA concentration in water was measured using a Cary Eclipse fluorescence spectrophotometer from Varian Inc. The excitation wavelength is 225 nm and the emission wavelength 338 nm.

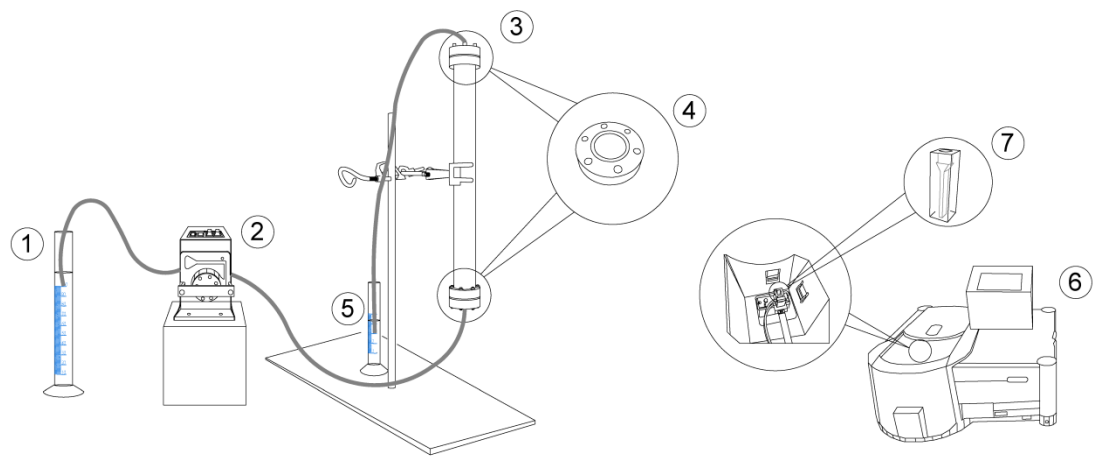

Figure 6.2: Experimental setup of two-phase flow system. 1) Reservoir of n-octane with KIS tracer. 2) Peristaltic pump. 3) Sand column. 4) Cap embedded with frit. 5) 5ml measuring cylinder. 6) Fluorescence spectrophotometer. 7) High precision fluorescence cuvette.

6.2.1.2 Porous media

Five porous media – three glass-beads media and two natural sands - are used to investigate the influence of grain-size and texture on n-octane-water interfacial area. The relevant properties of the porous media are described in **Table 6.1**. Examples of microscopic images of the grains and the grain-size distributions obtained by digital image analysis performed on these images are shown in **Figure 6.3**. The images were processed using ImageJ software to determine the grain-diameters, roundness, Feret diameter, aspect ratio and circularity (Tatomir et al. 2016a). The three glass-bead porous media are a very fine sand (10-80 µm, $d_{50} = 55\ \mu m$), a fine sand GB170 (120-230 µm, $d_{50} = 170\ \mu m$) and fine-to-medium sand GB240 (160-320 µm, $d_{50} = 240\ \mu m$). GB240 from GRACE (Glass beads 80/60 mesh) is very well sorted with the most uniformly distributed spectrum. The natural-sand porous media can be described as fine sand NS210, (120-320 µm, $d_{50} = 210\ \mu m$) and medium sand NS250 (180-380 µm, $d_{50} = 250\ \mu m$).

The capillary pressure – saturation relationships were determined by mercury-intrusion porosimetry (MIP). To scale the relationships to the n-octane-water system, we used the contact angles, $\theta_{o,w}$, which were determined using digital image analysis (DIA) on microscopic images using the n-octane-water fluid system together with the grains of each porous media (**Table 6.1**). The conversion of an air-mercury system to an octane-water system is accomplished by rearranging Washburn relationship as given in eq. (6.1).

$$p_{c_{o,w}} = p_{c_{Hg,a}} \cdot \frac{\sigma_{o,w} \cdot cos\theta_{o,w}}{\sigma_{Hg,a} \cdot cos\theta_{Hg,a}} \tag{6.1}$$

where $p_{c_{w,o}}$, $p_{c_{Hg,a}}$, are the capillary pressure for the water-octane fluid system, mercury-air respectively. The mercury – air contact angle $\theta_{Hg,a}$ is 140° and $\sigma_{Hg,a}$ is 480 mN·m^{-1}. $\sigma_{o,w}$, the interfacial tension of water-n-octane is 50.8 mN·m^{-1} at room temperature (Fukunishi et al. 1996). The curves were fitted to those of the Brooks and Corey (1964) model by minimizing the root mean square error when determining the pore-size index λ, entry pressure p_e, and residual water saturation, S_{wr} in eq. (6.2):

$$p_c(S_w) = p_d \cdot \left(\frac{S_w - S_{wr}}{1 - S_{wr}}\right)^{-1/\lambda} \tag{6.2}$$

A high value of the pore index λ corresponds to a flat curve from the entry pressure, S_w=1, until reaching the residual saturation values, indicating the medium is well-sorted and implicitly the pore-throats are of similar size.

Analogously to the uniformity coefficient for grain size distributions, we propose a uniformity coefficient for the pores, defined as the ratio of $C_{pu} = p_{60}/p_{10}$, where p_{60} and p_{10} are the pore diameters corresponding to 60% and 10% finer on the cumulative pore-size distribution curve. A low C_{pu} signifies that the medium is composed of similar pore sizes, equivalent to being well-sorted. **Figure 6.4**a investigates the relationship between the mean pore diameter, p_{50}, the C_{pu} and the d_{50}. **Figure 6.4**b shows that the SSSA decreases almost linearly with the mean pore diameter. The distributions of the pores in each of the five materials are determined with mercury intrusion porosimetry, by applying the Washburn equation. The frequencies and cumulative distributions of the pore-size distributions are plotted in **Figure 6.5**. The glass beads are spherical and of uniform diameter and therefore, the theoretical specific solid surface area can be calculated using the smooth-sphere assumption expressed in (cm^{-1}) using eq. (6.3) or in (m^2/g), using eq. (6.4), (Costanza-Robinson and Brusseau 2002; Peng and Brusseau 2005):

$$GSSA(cm^{-1}) = \frac{6(1-\phi)}{d_{50}} \tag{6.3}$$

$$GSSA\ (m^2/g) = \frac{6}{d_{50} \cdot \rho_p} \tag{6.4}$$

where d_{50}, is the mean particle diameter (cm), ρ_p is the particle density which is 2.65 g cm^{-3}.
The theoretical total interfacial areas can be estimated based on geometrical calculations for smooth spheres and compared to the specific solid surface areas measured with the MIP method, SSSA-MIP.

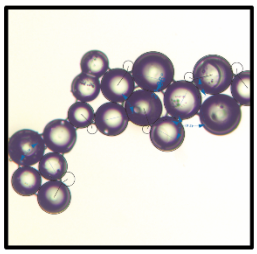

GB55

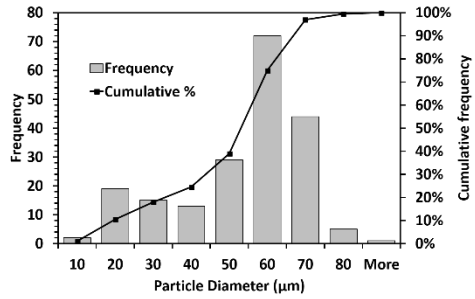

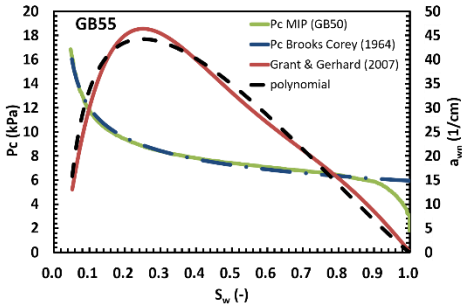

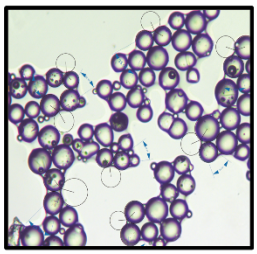

GB170

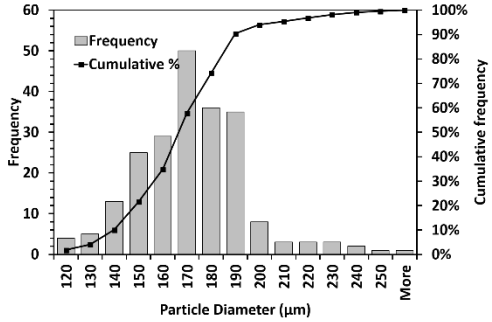

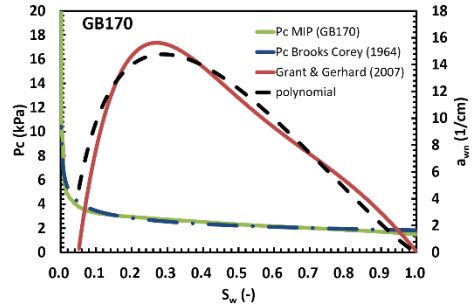

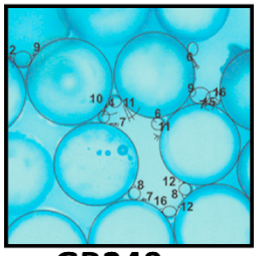

GB240

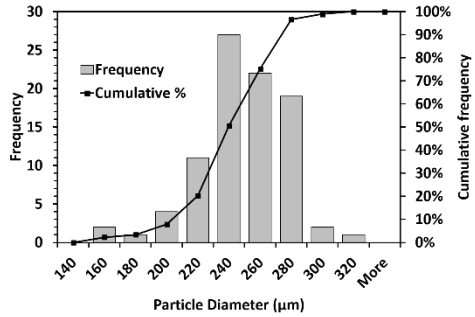

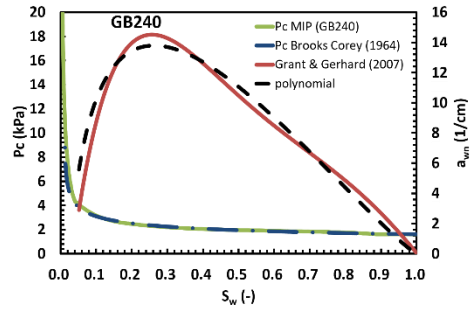

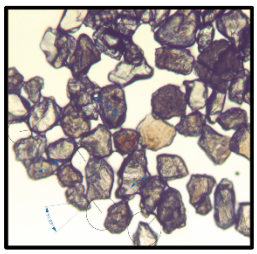

NS210

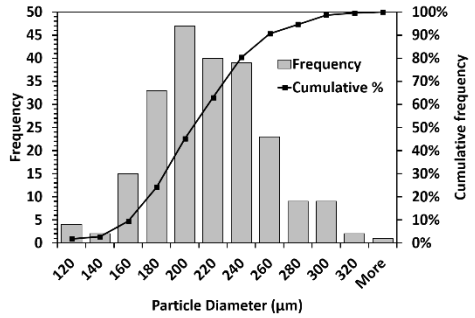

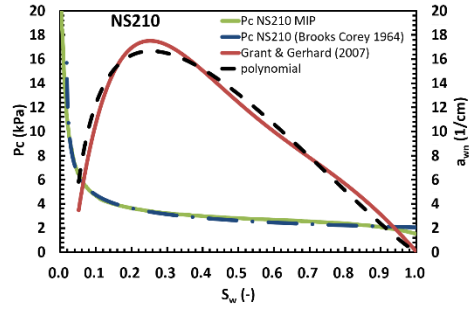

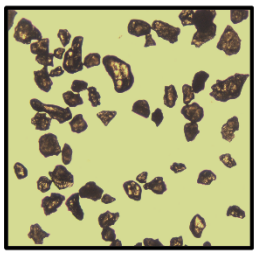

NS250

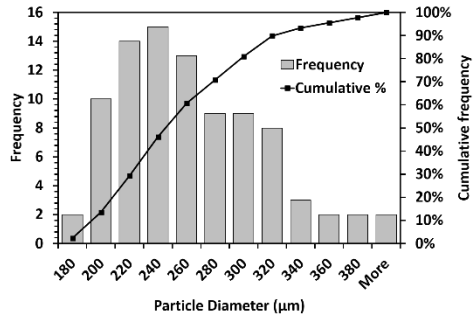

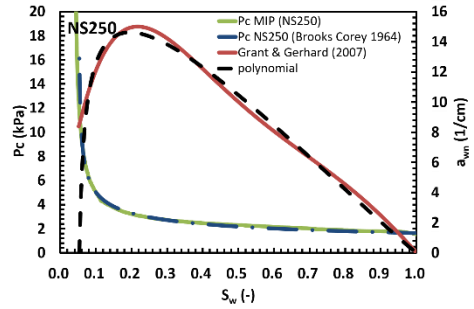

Figure 6.3: Characterization of the five porous media used in the KIS tracer experiments: three glass beads (GB55, GB170 and GB240) and two natural sands (NS210 and NS250). Digital illustration of the media (left column), grain-size (distribution) with the cumulative frequency curve (middle), capillary pressure-saturation, $p_c - S_w$ relationship determined with MIP, and the calculated $a_{wn} - S_w$relationship with the explicit interfacial area model of (Grant and Gerhard 2007)

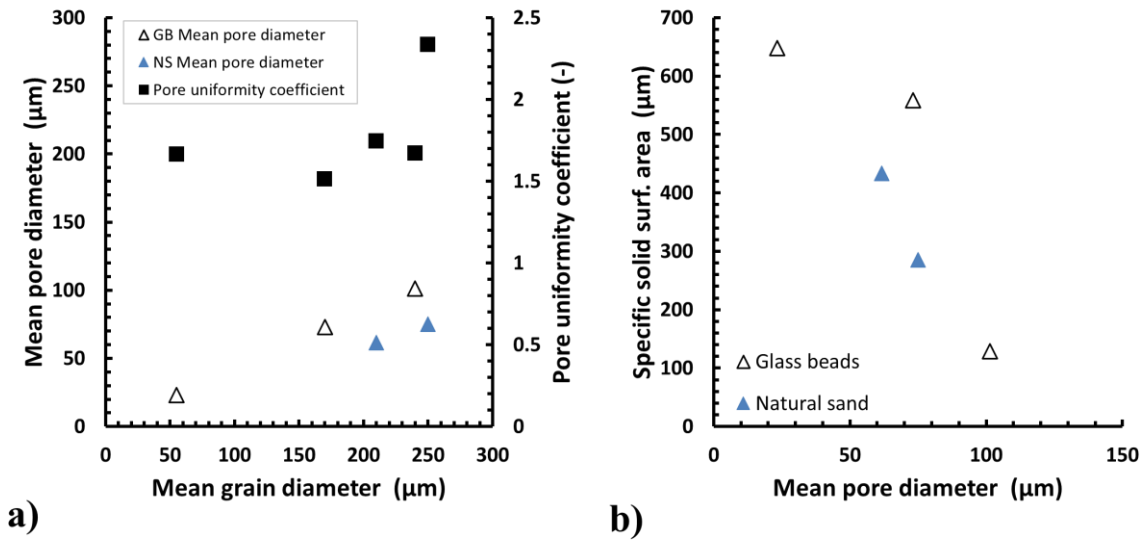

Figure 6.4: a) Relationship between mean pore-throat diameter (measured with MIP), p_{50}, pore uniformity coefficient ($C_{pu} = p_{60}/p_{10}$) and the mean grain diameter (measured with DIA), d_{50}; **b)**The upper p_{50} values at GB55 and NS250 are corrected to remove the micro-porosity determined with MIP.

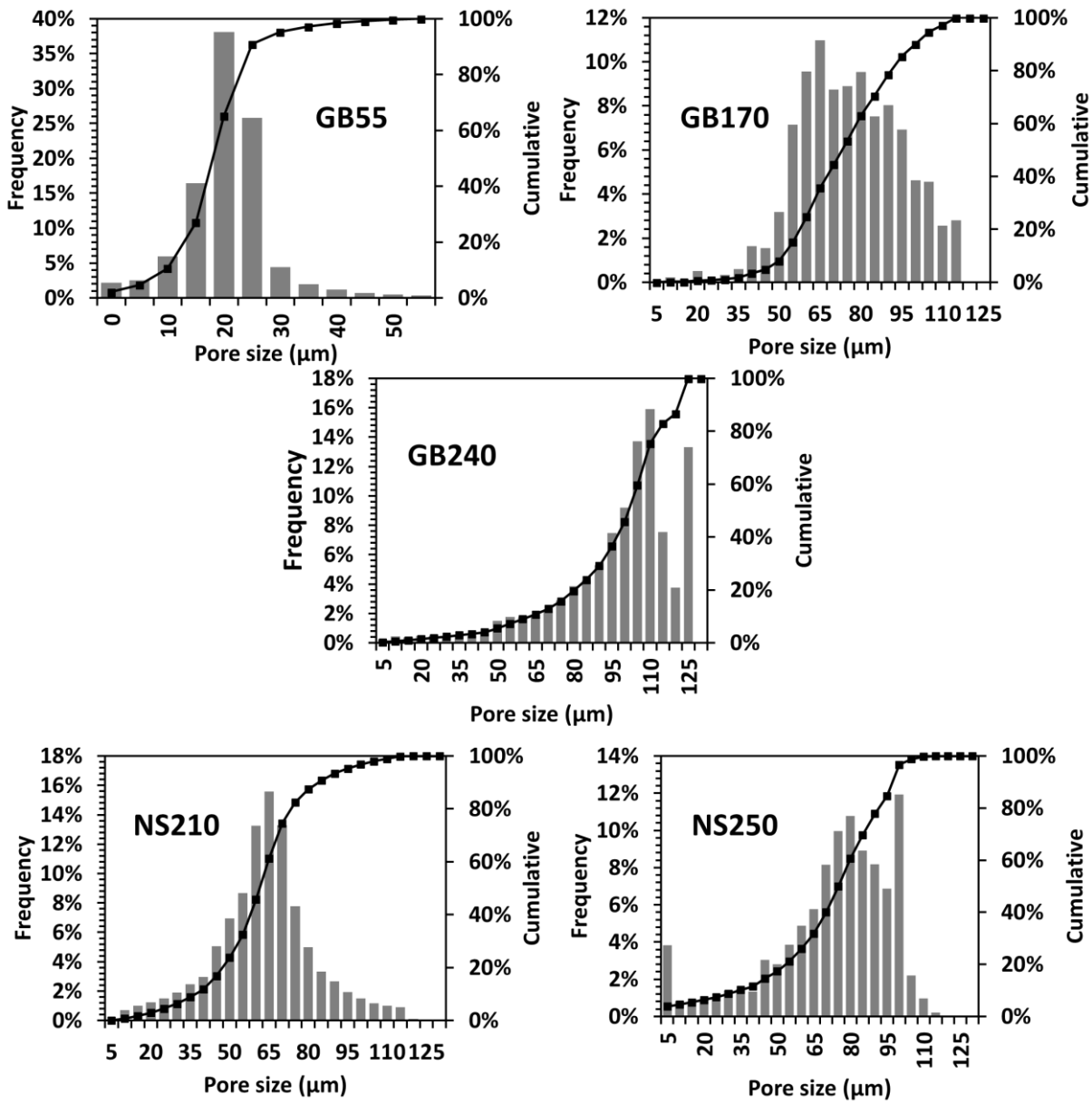

Figure 6.5: Pore-diameter distribution determined with mercury-intrusion porosimetry, based on Washburn model (Washburn 1921)

Table 6.1. Summary of relevant properties of the porous media used in the KIS tracer two-phase flow experiments

Parameter Name	Unit	Symbol	GB55	GB170	GB240	NS210	NS250
Porosity	$(-)$	ϕ	0.411	0.455	0.464	0.432	0.445
Intrinsic permeability	(m^2)	K	8e-13 – 2e-12	4e-12 – 1.1e-11	8e-12 - 1e-11	6e-13 – 8e-13	3e-12-9e-12
d_{50} mean grain diameter	(μm)	d_{50}	55	167	240	206	248

d_{10}	(μm)	d_{10}	20	140	205	161	198
d_{60}	(μm)	d_{60}	57	172	244	214	258
Uniformity coefficient $C_u = d_{60} / d_{10}$	$(-)$	C_u	2.85	1.23	1.19	1.33	1.30
Mean pore diameter[a]	(μm)	p_{50}	23.28	73.15	101.35	61.69	75.01
Pore uniformity coefficient[a] $P_u = p_{60} / p_{10}$	$(-)$	P_u	1.67	1.51	1.67	1.75	2.34
SSSA- MIP (Rootare and Prenzlow 1967)	(cm^{-1})	a_s	615	558	128	419	274
GSSA=$6(1-\phi)/d_{50}$	(cm^{-1})	a_s	643	196	134	165	134
Bulk density of the glass beads	(g/cm^3)	ρ_b	1.65	1.65	1.6	1.65	1.67
Lambda (Brooks-Corey)	$(-)$	λ	3.614	3.606	3.650	2.925	2.663
Contact angle n-octane - water	$(°)$	θ	32± 6	34± 9	10 ± 3	32± 10	32± 10
Entry pressure	(Pa)	p_d	5937	1819	1606	2050	1642
Residual wetting phase saturation	$(-)$	S_{wr}	0.024	0.00	0.016	0.015	0.051
Longitudinal dispersivity	(m)	α_L	1e-3	1e-3	1e-3	1e-3	1e-3
Transversal dispersivity	(m)	α_T	1e-5	1e-5	1e-5	1e-5	1e-5
Feret diameter(mm)	(mm)		0.054	0.173	0.24	0.245	0.273
Circularity	$(-)$		0.857	0.855	0.898	0.676	0.593
Aspect ratio	$(-)$		1.062	1.065	1.018	1.457	1.59
Roundness	$(-)$		0.95	0.955	0.983	0.713	0.701

[a] Based on mercury intrusion porosimetry measurements

Table 6.2: Fluid and soil-fluid properties

Parameter Name	Unit	Symbol	Value/ Range
Diffusion coefficient	(m^2/s)	D_m	1e-9
Density water	(kg/m^3)	ρ_w	1000
Density n-octane	(kg/m^3)	ρ_n	703
Viscosity of water	$(Pa \cdot s)$	μ_w	1.00e-03
Viscosity of n-octane	$(Pa \cdot s)$	μ_n	5.42e-04
Surface tension n-octane - water [a]	(N/m)	$\sigma_{o,w}$	0.0508
Longitudinal dispersivity [b]	(m)	α_L	1e-3
Transversal dispersivity	(m)	α_T	1e-5

[a] Measurements of surface tension determined by capillary rise method showed no differences between pure n-octane and n-octane with 2g/l dissolved KIS tracer

[b] Measured by single-phase tracer experiments in the column

6.2.2 Methods

In this study the KIS tracer method is used to quantify the FIFA in several unconsolidated porous materials. The KIS tracer experimental procedure was developed and described in Tatomir et al. (2018). The technique consists of transient drainage experiments of an initially fully water saturated porous media filled column. The drainage/invading fluid is n-octane with KIS tracer dissolved in it. The laboratory experimental outcomes are volumetric outflow BTCs and KIS tracer reaction product in water phase, i.e., 2-NSA concentration BTCs.

6.2.2.1 KIS tracers

KIS tracers, developed by Schaffer et al. (2013), are a category of non-polar, hydrolysable phenolic esters. In contact with water they undergo an irreversible reaction at the fluid-fluid interface to form two highly soluble products, i.e., an acid and an alcohol, Eq. (6.5). Their non-polarity allows KIS tracers to be dissolved in non-polar liquids, e.g., n-octane. Due to the pronounced fluorescent properties of their reaction products, the detection is performed by a fluorescence spectrophotometer.

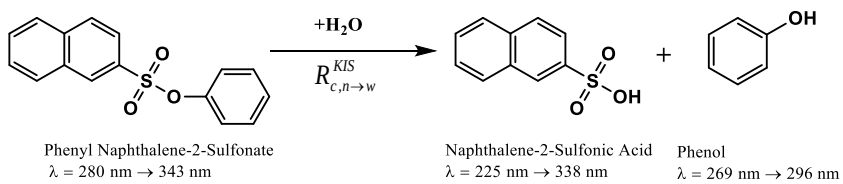

(6.5)

where $R^{KIS}_{c,n\rightarrow w}$, is the reaction rate constant, determined in static batch experiments.
The KIS tracer method was developed for tracking the FIFA in dynamic conditions (Tatomir et al. 2018). Explicitly, the method is developed for the primary drainage process, i.e., non-wetting phase displacing the wetting phase in a proof of concept study using well-characterized glass beads in well-controlled laboratory conditions. By interpreting the volumetric ratios at outflow and the reacted KIS tracer product acid breakthrough curves, we can derive the specific IFA relationship of the fluid-fluid-porous media system.

Note that the 2-NSA mass reacted in pendular rings of wetting fluid, around the contact points of the porous media, cannot leave the column and is not being measured. Only the fraction of the fluid-fluid interface belonging to the terminal menisci in contact with the continuous wetting fluid body or mobile part is quantified by the KIS tracer technique.

6.2.2.2 Kinetics of the tracer, new insights

The KIS tracer hydrolysis reaction at the fluid-fluid interface was shown in static batch experiments to lead to a linear increase of concentration after about 2000 – 3000 minutes (Schaffer et al. 2013), independent on the initial KIS tracer concentration in the non-wetting phase, i.e. n-octane. However, at the early stage (up to 100-200 minutes) was observed that the reaction rate is increasing linearly depending on the initial concentration of the KIS tracer in the non-wetting phase (**Figure 6.6**). With the pumping rates ranging between 0.3 and 1.5 ml/min one column experiment usually takes around 6000 seconds. Therefore, the kinetic rates of the experiment are the ones represented in **Figure 6.6**b). Generally, a higher reaction rate is preferable to obtain higher 2NSA concentrations in water, because they can be better detected and measured with the fluorescence spectrophotometer. Using an initial concentration of 2g/l KIS tracer, we extend our previous range of testing which was 1g/l (Tatomir et al. 2018). It can be observed that the resulting kinetic rate coefficient $R^{2NSA}_{n\rightarrow w}$ =1.25 10^{-11} kg·m^{-2}·s follows very well the linear behavior.

In this study, the experiments are conducted with an initial concentration of 0.5 g/l (all experiments with GB55 and NS210, and two of the experiments with GB170) and 2g/l (all experiments with GB240 and NS250 and one experiment with GB170) (**Figure 6.8**). Note that the previous study (Tatomir et al. 2018) was conducted with the GB240 glass-bead medium with an initial KIS tracer concentration of 0.5g/l.

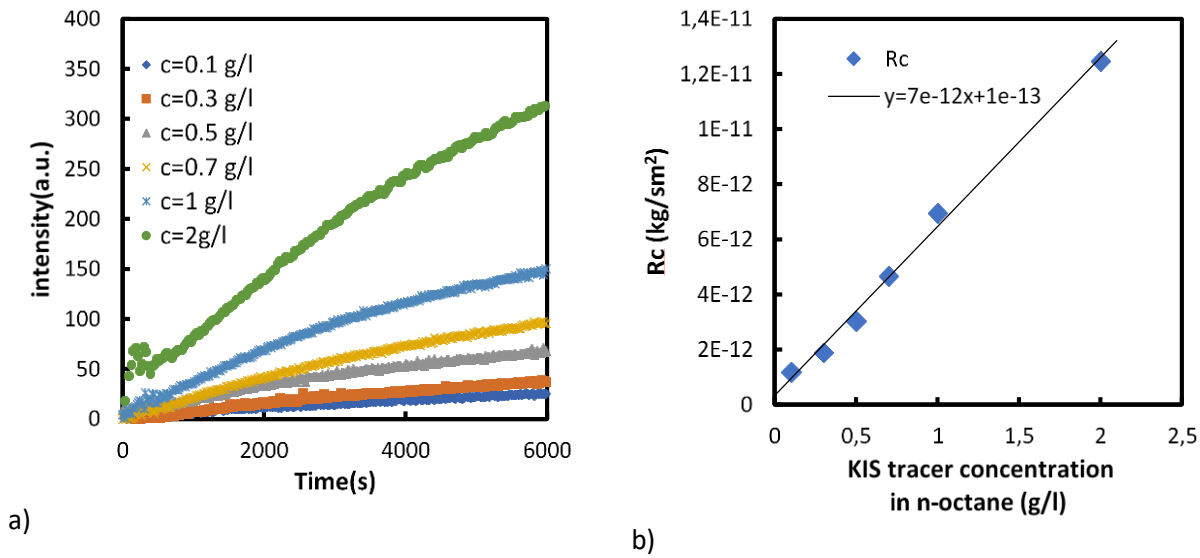

Figure 6.6: Measured kinetic rates in static batch experiments. a) 2-NSA concentration reaction rates over time expressed in intensity units as a function of initial 2-NSAPh concentration in n-octane. b) calculated hydrolysis reaction rates as a function of initial 2-NSAPh concentration using the experiments in subfigure a). Here the unit of intensity $a.u = 86.293 \cdot c_{2NSA} + 62.6$

The hydrolysis reaction is expressed as:

$$-\frac{dc_\alpha^\kappa}{dt} = r_{n\rightarrow w}^\kappa = R_{c_{n\rightarrow w}^\kappa} \cdot a_{wn} \,, \tag{6.6}$$

where c_α^κ is the concentration of component κ in phase α, $R_{c_{n\rightarrow w}^\kappa}$ is the reaction rate constant. For component 2-NSA in water phase, $R_{c_{n\rightarrow w}^{2NSA}}$ was determined in static batch experiments (Figure 6.6). The a_{wn} is the capillary associated IFA. According to Joekar-Niasar and Hassanizadeh (2012) a_{wn} can be expressed using the polynomial expression in Eq. (6.7):

$$a_{wn}(S_w, p_c) = a_0(S_w)^{a_1}(1 - S_w)^{a_2}(p_c^{max} - p_c)^{a_3} \tag{6.7}$$

where a_{wn} is the capillary associated IFA, S_w is the wetting saturation, p_c is the capillary pressure, $a_0, a_1, a_2, a_3, p_c^{max}$ are empirically fitted parameters.
The transport of hydrolyzed KIS tracer in water, i.e. 2-NSA, is controlled by advection and diffusion processes.

6.2.3 NAPL-Water Experiments

The steel-column was packed with dry granular material (i.e. sand, or glass beads) using slight vibrations while packing to ensure uniform bulk properties. After packing the column is slowly filled with water from the bottom to avoid air entrapment. The columns are saturated for more than 24 hours by pumping deaired ultra-pure deionized water. The porous medium properties are reported in **Table 6.1**.

The 2-NSAPh (non-polar hydrolysable phenolic ester, phenyl naphthalene-2-sulphonate) in concentrations of 0.5 g/l and 2g/l in the n-octane, is used as the KIS tracer. Approximately 30 ml

of the solution is then injected into the column at a rate between 0.4 and 0.8 ml/min. At the outlet the two-phase flow breakthrough curve (BTC) was captured by collecting the fluid volumes in 5 ml graded measuring cylinder. Using a glass syringe, the water containing reacted KIS tracer is taken and placed in a 500 µl cuvette to be analyzed in the spectrophotometer. A predefined calibration curve allows the conversion of intensity readings into 2-NSA concentration (**Figure 6.6**). After the analysis, the water is collected in 5-ml vials. Initially, at the outlet, only water is being drained from the system. Just before the arrival of the first n-octane at the outlet, the sampling intervals are taken more often for a higher temporal resolution of the BTC. The sampling frequency is dictated by the minimum volume of water required to fill the cuvette that is placed in the spectrophotometer.

After every experiment the glass beads and the natural sands are washed and dried for more than 48 h. The porous steel frits of the columns are washed and dried before each experiment and the packing process repeated. However, each packing will lead to a different grain geometric configuration, which may lead to differences in petrophysical parameters, i.e. permeability, tortuosity with little influence on porosity.

6.2.4 Data analysis: Mathematical modelling and interpretation of the results

The interpretation of the experimental results is done using numerical modeling. The mathematical and numerical model to handle the column-scale, i.e. Darcy (REV) scale, is an immiscible two-phase flow model with reactive transport and it accounts for the specific IFA (Tatomir et al. 2018). The mathematical model is implemented in COMSOL Multiphysics v5.5. Several models capable of addressing the KIS tracers in multiphase flow in porous-media systems were developed in the past (Tatomir et al. 2013; Tatomir et al. 2015; Tatomir et al. 2016b; Tatomir et al. 2018). Besides the immiscible two-phase flow models, a compositional model investigating the KIS tracer application in supercritical CO_2 – brine fluid systems was developed in the $DuMu^X$ simulator (Flemisch et al. 2011; Tatomir et al. 2015). Comparing the two models applied with experimental data, Tatomir et al. (2018) showed only minor differences. In this study, the results were interpreted with the COMSOL implemented model only.

A two-step approach is employed to interpret the results. The first step is the calibration of the two-phase flow model to the experiment by performing a sensitivity analysis with respect to flow rate, Q, and intrinsic permeability, K. It is estimated that both have the highest measurement uncertainty, due to the expected small oscillations in the pumping rate (±0.05 ml/min) and the unknown influence of repacking the columns, and of the column frits. The peristaltic pump is set to operate at a fixed number of rotations per minute. As pressure in the column and the n-octane reservoir at the inlet changes during the experiment, flow rate fluctuations can be expected. The permeabilities of the sand are determined by falling head permeameter, which may provide a wide range of permeability values. Adding to the uncertainty of the permeability measurement is the effect of the porous frits and of repacking before each experiment.

Once the outflow volume ratio curves are matched, we proceed with the calibration of the concentration breakthrough curves of the KIS tracer reaction product, i.e. 2-NSA. In this sense, a sensitivity analysis using the specific interfacial-area relationship, $a_{wn} - S_w$, as the unknown parameter is conducted. The reaction rate expressed in Eq. (6.6) depends on the reaction rate coefficient, known from experiments and on a_{wn}. Initially, the Grant and Gerhard (2007) thermodynamically derived model is used to approximate the specific IFA a_{wn} curves from the

MIP measured $p_c - S_w$ relationships. Afterwards, the polynomial expression in Eq. (6.7) is used to fit the modelled a_{wn}, by finding best fitting parameters, a_0, a_1, a_2, p_c^{max}. This provides the theoretical $a_{wn} - S_w$ of the fluid-fluid porous medium system.

The second step comprises the calibration of the KIS reaction product breakthrough curves. This is performed running a parameter sweep on parameter a_0 in Eq. (6.7). This parameter controls the maximum specific IFA, a_{wn}^{max} while maintaining the general shape of the $S_w - a_{wn}$ curve.
The solute dispersivities were determined using fluorescent tracer experiments to be 10^{-3} m (Tatomir et al. 2018). Note that dispersivities measured in single-phase flow conditions is not necessarily valid when another fluid-phase is present (Karadimitriou et al. 2016). Applying the root mean square error (RMSE) as a criterion the best fitting curves were found.

In order to compare with the experimental and modelling BTC curves, the modelling results are post-processed. The volumetric ratios of the non-wetting phase to total fluid measured at the outlet are integrated over the sampling intervals, to obtain the values at the times when the samples were taken. For further details of the mathematical models, see Tatomir et al. (2018) proof of concept study.

6.3 Results

The experimental and modelling results for the three sets of tests performed on each of the five porous media, three glass beads, GB55, GB170, GB240, and two natural sands, NS210, NS250, are presented in section 6.3 and discussed in section 6.4.

6.3.1 Two-phase flow calibration

All fifteen experimental breakthrough curves (BTCs) of the volume fraction of the non-wetting phase to total fluid volume together with the model calibration BTCs are illustrated in **Figure 6.7**. The modelling parameters determined from the petrophysical characterization of the natural sands and glass beads samples are reported in **Table 6.1** and of the fluid system in **Table 6.2**.

First, we calibrate the immiscible two-phase flow model by performing the parameter sweep with a combination of flow rates and permeabilities. The fitting of the modelling results to the experimental data is shown in **Figure 6.7**. It can be observed that the two-phase flow model can well match the experimental breakthrough curve, with the root mean square errors ranging up to 0.057 for the best fitting model curves, as showed in **Table SI 6.1**. Deviations are found mainly in two experiments performed with GB170, where the change in the non-wetting to total volumetric ratio at breakthrough is gentler in the experimental data compared to that of the modelled breakthrough. In contrast, for NS210, the non-wetting phase breakthrough is fast and only little water volume is being displaced out of the column, leading to a smaller number of data points. This becomes apparent in the increase of non-wetting to total volume ratio at breakthrough occurring more rapidly in the experimental BTC than the modelled ones.

Even though the frits are washed and dried before each experiment and the packing processing follows the exact same procedure (vibrating and adding small increments) for each experiment,

differences are hard to avoid. The reproducibility of the experiments is mainly affected by repacking and by the frits condition, which are reflected by the overall permeability of the system. Therefore, the calculated flow rates and permeabilities in **Table SI 1** for the three experiments belonging to each sand category are slightly different.

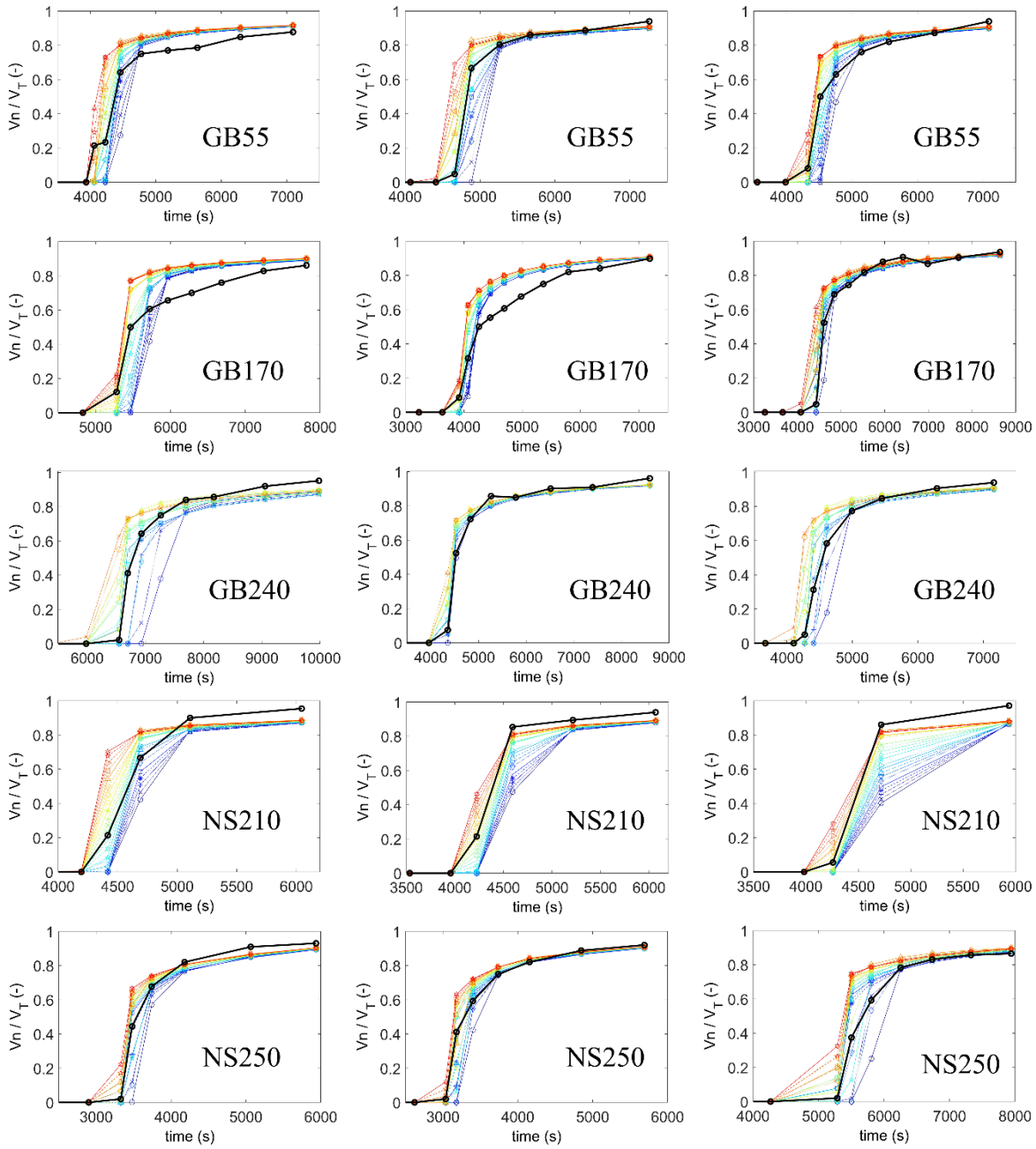

Figure 6.7: Breakthrough of the volumetric fraction of non-wetting phase to total fluid volume at the column outlet, experimental data (black) and simulated breakthrough curves with sensitivity analysis (color). The variation ranges are provided in **Table SI 6.1**

6.3.2 Interpretation of the hydrolyzed KIS tracer reaction product breakthrough curves

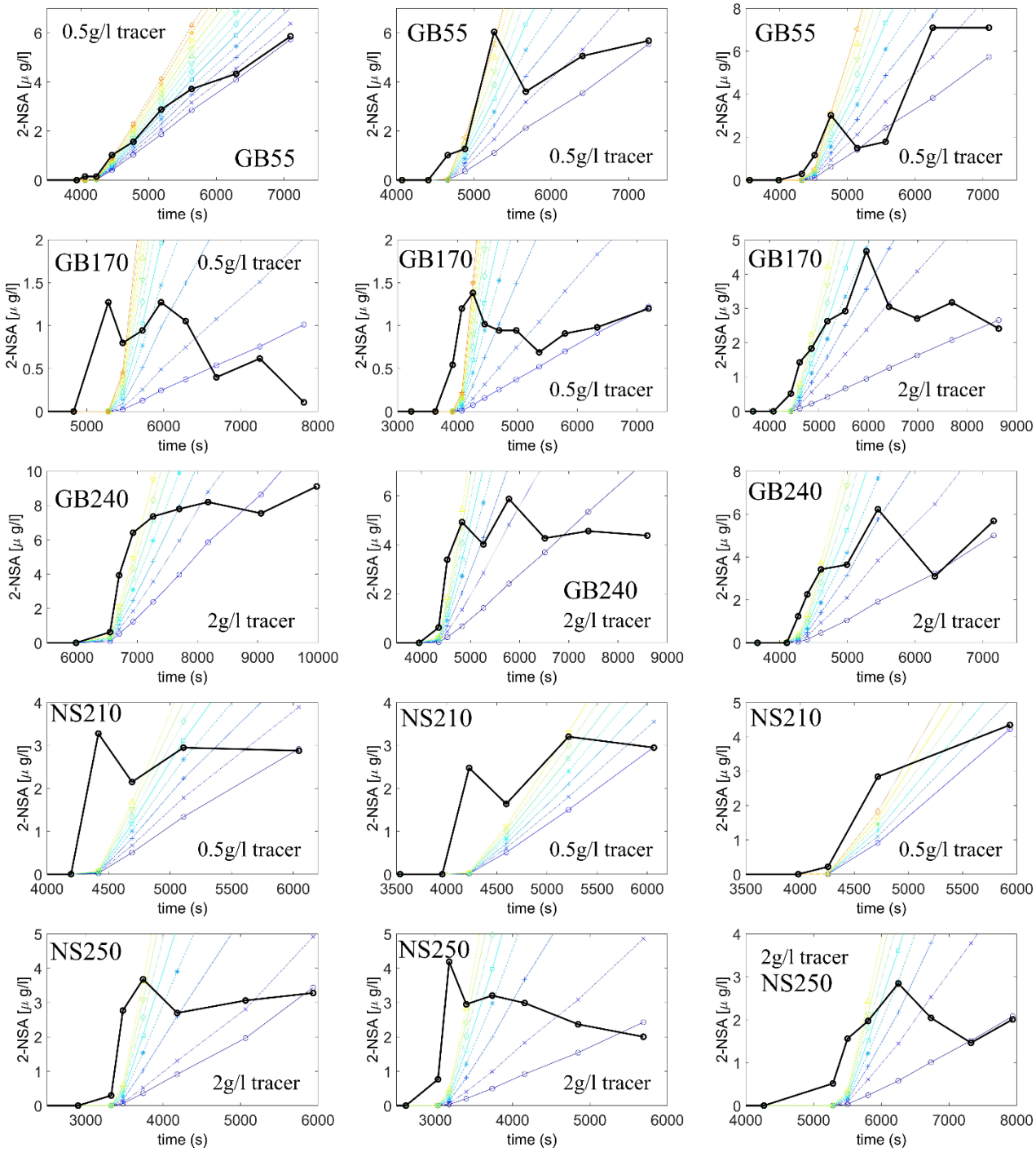

Figure 6.8: Breakthrough curve of 2-NSA concentration (hydrolyzed KIS tracer) at column outlet. The black curve shows the experimental-data, while the colored plots correspond to a range of fitting coefficient a_0, varied between $a_{0,min}$ and $a_{0,max}$ (yellow) given in **Table 6.3**. The initial KIS tracer concentration in n-octane is specified in each subfigure

Table 6.3: Parameters ranges, $a_{0,min}$ to $a_{0,max}$ used to identify the best fitting for the capillary-associated IFA, a_{wn} in Eq. (6.7). Here $a_{0,GG}$ and $a_{0,BF}$ are the a_0 parameter best fit to the Grant and Gerhard (2007) model, and to the experimental data

Soil category	$a_{0,min}$	$a_{0,max}$	$a_{0,GG}$	$a_{0,BF}$	a_1	a_2	a_3	p_c^{max} (Pa)
GB55	9.67×10^{-6}	4×10^{-5}	5.22×10^{-5}	1.33×10^{-5}	0	1.11	1.94	23287
GB170	4×10^{-6}	7.33×10^{-5}	5.23×10^{-5}	6.67×10^{-6}	0	1.21	2.18	5749
GB240	1×10^{-5}	8×10^{-5}	5.31×10^{-5}	$1.33e\times10^{-5}$	0	1.15	2.14	5804
NS210	3.5×10^{-6}	8.5×10^{-5}	5.95×10^{-5}	4.33×10^{-5}	0	1.15	2	9466
NS250	5.33×10^{-6}	6×10^{-5}	6.06×10^{-5}	6.33×10^{-6}	0	1.05	1.83	15491

The breakthrough curves of the reacted 2-NSA concentration are plotted in **Figure 6.8**. Measured 2-NSA concentrations in water range between 0 and 8 µg/l. With a constant kinetic rate dependent on the initial tracer concentration in n-octane (**Figure 6.1**), the mass transfer across the fluid-fluid interface is a function of only fluid-fluid interfacial area. In order to obtain the range of the specific interfacial area when fitting to the experimental data, the parameter a_0 in the polynomial equation (7) is swapped to change the magnitude of the $a_{wn} - S_w$ curve while maintaining the shape of the curve (Tatomir et al. 2018). The calculated root mean square error ranges between 0.3 and 2.3 for the best fitting parameter a_0, as shown in **Table SI 6.1**. Compared to the non-wetting phase fluid to total volume ratio BTCs calibration, the modelled 2-NSA BTCs have a larger deviation from the experimental data. Generally, the trend of the BTCs is ascending. However, a clear linearly increasing trend, as it is predicted by the numerical models, is not always seen in the experimental data. This indicates that either we deal with a systematic experimental error, or the theoretical framework underlying the current coupled two-phase flow and reactive-transport model needs to be reconsidered. This is further addressed in the discussion.

6.3.3 Capillary-associated specific interfacial area calculation

The range of the $a_{wn} - S_w$ curves and the best fitting curves found for the five porous materials are illustrated in **Figure 6.9** with gray shading. The gray shading corresponds to the range of a_0 values (**Table 6.3**) that scale the $a_{wn} - S_w$ curves so that all experimental data points of the 2-NSA BTCs in **Figure 6.8** are captured. The maximum $a_{0,max}$ values correspond to the peak matching the first points on the BTC, the curve with steepest slope, while the minimum, $a_{0,min}$, corresponds to the curves matching the points on the tailing of the BTC. Once a_0 is determined, the a_{wn}^{max} value can be obtained from the $a_{wn}(S_w)$ curve, which usually exists at water saturation ranging between

0.2 and 0.35. The best fitting $a_0$values, $a_{0,BF}$, obtained on grounds of RMSE are given in **Table SI 6.1** together with the a_{wn}^{max} and the RMSE values and are plotted in **Figure 6.10**.

The a_{wn} predicted by the explicit IFA model of Grant and Gerhard (2007), using the MIP $p_c - S_w$ curves is within the areas resulting from the interpretation of the 2-NSA tracer breakthrough curves, for all grains, except for the natural sand NS250. In this case, the Grant and Gerhard (GG) model overestimates the a_{wn}. Generally, the GG model provides larger FIFA than those providing the best fit resulting from the tracer interpretation. For NS210 the best fit of the third experiment matches almost exactly the GG model. On average the GG model predicts a_{wn}values that can be even five times larger than those obtained for the model best fits.

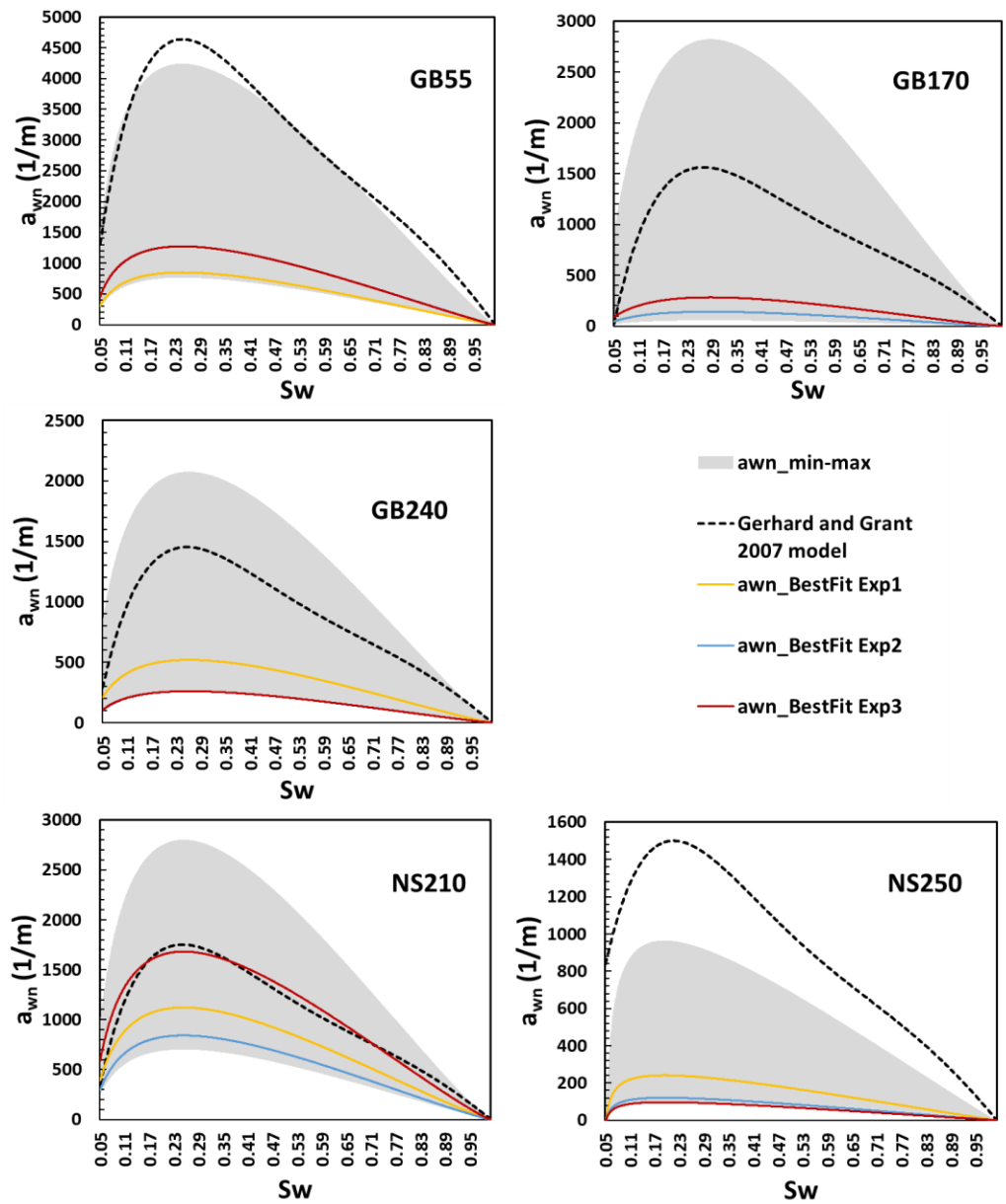

Figure 6.9: Ranges for the specific capillary associated IFA, $a_{wn} - S_w$ relationships, for the five porous media. The best fitting curves in each experiment (Exp.1 - yellow, Exp.2 - blue, Exp.3 - red), and the Gerhard and Grant model applied to MIP derived $p_c - S_w$ curves

6.4 Discussion

Assuming two fluid phases inside the porous medium as being stagnant. Since there is no force applied, the IFA between the fluids remains constant and the KIS tracer hydrolysis over the fluid-fluid interface produces a steady increase of the 2-NSA concentration in water. As time passes, the 2-NSA concentration diffuses away from the fluid-fluid interface with the only driving force of the process being the concentration gradient, i.e., molecular Brownian motion. When the non-wetting phase starts to displace the wetting phase, a transition zone is formed, where saturation changes with time. During this process, only the tracer concentration in water in direct proximity to the outflow is measured. In other words, only the interfaces belonging to the front can contribute to the measured concentration at the outlet. The longer the two fluids remain in contact the higher the outlet concentration should be. In reality, the pore distribution inside the column forms complex geometrical patterns. The macro-scale displacement front is in fact formed of fingers following various tortuous pathways.

Therefore, an early arrival of the concentration peak corresponds to a larger number of fingers arriving at the outlet, which are followed by other fingers that are halted due to the presence of a confinement in the pore space, and the competitive domination of fingers occupying smaller pores than the first ones that, combined, result in a lower outlet concentration. Some of the fingers may also mobilize water in the capillaries which may eventually be pushed to regions that are stagnant. In these regions the advective transport flux is almost zero. The water in these regions never reaches the outlet and, implicitly, the corresponding concentration is never measured. Visualization of the mobile and immobile zones can be done for instance in thin transparent (quasi-) two-dimensional micromodels (Karadimitriou et al. 2016). In a few words, the effects taking place on the pore scale can and will affect the corresponding outflow concentration and, given the experimental setup, it is physically impossible to identify the pore-scale filling sequence mechanism.

The immiscible displacement can be studied as a function of the capillary number, $Ca = v\mu_i/\sigma$ and the viscosity ratio $M = \mu_i/\mu_d$ (Lenormand et al. 1988), where v is the velocity of the invading fluid, μ_i and μ_d are the dynamic viscosities of the invading and displaced fluids, and σ is the interfacial tension between the two fluids. A stable front means that the transition zone (width) is constant in time. If the displacing or the invading fluid is less viscous than the displaced fluid the front tends to become unstable. In our case $M = 0.5$ and the Ca of the fifteen experiments is between 0.4 and 3.5 (Appendix SI Table 1). When M gets smaller, preferential flow starts to occur, increasing the lengths and widths of the transition zone (e.g., Heiß et al. 2011). For the KIS tracer experiments, a stable front having a narrow transition zone will lead to fewer measurement points

than compared to those induced by an unstable flow with a large transition zone. The NS210 experiments have the highest Ca numbers, 2.58, 2.7 and 3.6 while the NS250 the lowest, i.e., 0.34, 0.59 and 0.62 (**Table SI 2**). For NS210 the BTCs have maximum 4 measurements, while in for NS250 the minimum number of points is 6.

6.4.1 Hydrolyzed KIS tracer breakthrough curves

Examining the 2-NSA breakthrough curves in **Figure 6.8**, the two main differences between modelled and experimental results are: First, after phase breakthrough for most of experiments (11 out of 15), the BTCs exhibit an early concentration peak immediately after the first arrival, usually within the first three sampling times. The second difference is the deviation of the experimental BTC from a straight line. They have a non-linear behavior characterized by a slower increase in concentration, or even by a decrease at late times (i.e., first experiment GB170, second experiment NS250). The concentration peak and the concentration decrease are not present in the BTC predicted by the models but the breakthrough curves appear as straight lines. In fact, such effects cannot be reproduced by our current model. Closest to the predicted linear trend of the reactive transport model are the BTCs for the GB55. The curves consist of more than 6 measurement points. With the lowest grain-uniformity coefficient, C_u, value of 1.19, GB240 is the most uniform medium, closest to an ideal mono-size medium. RMSE values for of the GB240 obtained when matching the volumetric ratios BTCs during the two-phase flow model calibration are the lowest of the five materials. The three GB240 experiments are conducted with an initial KIS tracer concentration of 2g/l. The same glass beads were used in our previous study (Tatomir et al. 2018), where we ran four experiments with an initial KIS tracer concentration of 0.5 g/l. In comparison to our previous study where the BTCs had maximum four measurement points, the BTCs have now eight measurement points. Two of the four results in (Tatomir et al. 2018) provided a narrow a_{wn}^{max} range, i.e., 4.1 -5.4 cm^{-1} , 5.0 -7.5 cm^{-1}, and the other two large a_{wn}^{max} ranges, i.e. 3.0-15 and 4.6 – 11.5 cm^{-1}. The best fitted results in **Table SI 1** give a_{wn}^{max} ranges between 2.6 – 5.19 cm^{-1} which can be considered in good agreement with our previous set of experiments.

Generally speaking, the confidence in measurements increases when a larger number of measurement points is available. Even though the first GB170 experiment has eight measurement points the BTC presents a clear descending trend, while the other two experiments tend to flatten out.

From **Figure 6.9** the largest a_{wn}^{max}error range, i.e. $a_{wn}^{max}(a_{0,\max}) - a_{wn}^{max}(a_{0,\min})$ is encountered for the GB55, 8.2 - 42.4 cm^{-1}. Excluding the GB55, the natural sands with a larger surface roughness do not have a larger range of a_{wn}^{max} than the glass beads. The calculated IFAs range for natural sands is 13.99 cm^{-1} for NS210, 13.19 cm^{-1} for NS250 is smaller than that of the glass beads, 34.2 cm^{-1} for GB55, 19.55 cm^{-1} for GB170 and 18.2 cm^{-1} for GB240.

6.4.2 Potential explanations of discrepancies in tracer BTC

The discrepancies between the modelled and experimental results are believed to highlight the complexity of the coupled multiphase flow and reactive transport processes. The shape of 2-NSA concentration BTCs highly depend on the front behavior when it reaches the outlet. Once being at the outlet the non-wetting phase is continuous, while in the domain entrapped regions of wetting fluid were formed. Let us consider the porous medium being as a bundle of capillaries. Those with the largest apertures/radii are the capillaries first invaded by the non-wetting phase in the displacement process. Should these capillaries represent the largest part, it becomes clear why a concentration peak arrives at the beginning of BTC, just ahead of the fluid-fluid interface reaching the outlet. For a continuum-scale model, assuming the medium as homogeneous, such type of preferential flow will be averaged.

An early breakthrough peak and other discrepancies could also be explained by artefacts resulting from injection and sampling procedures. Concentration ranges are small, below 10 µg/l, i.e., experimental errors could also be expected. Care was taken when conducting the experiments and several procedures were tried and repeated, and therefore, we do not consider experimental errors and artefacts as a likely reason for the discrepancies.

The parametric study on a_0 values used to scale the $a_{wn} - S_w$ curves covers all experimental data points of the 2-NSA BTCs in **Figure 6.9**. Therefore, it is reasonable to assume that one of the $a_{wn} - S_w$ represents the "true" solution. One can see that the theoretical model of Grant and Gerhard (2007) is in four cases within the parameter range, even providing an exact match for the third experiment with NS210. This indicates the specific IFAs measured with KIS tracer method are within a reasonable range.

6.4.3 Grain-diameter-size influence on IFA

Previous literature studies, reviewed in the introduction, revealed that the total specific IFA, a_n, and its related, a_{wn}, are inversely proportional to the mean grain size (Brusseau et al. 2009; Brusseau et al. 2010). They observe very strong correlation between total specific interfacial area and IMGD. Furthermore, a_n, was observed to have a linear dependency on water saturation. It decreases linearly with S_w , $a_n = a_n^{max}(1 - S_w)$, where the a_n^{max} is the maximum total specific interfacial area. The a_n^{max} was shown to be approximately equal with the solid surface area (a_s) (Porter et al. 2010; Brusseau et al. 2010). The value of a_n is shown to be smaller for smooth glass beads and larger for natural sands, or soils, (e.g., Brusseau et al. 2009). The curve is reported to have virtually no hysteresis, somewhat unexpected as since the $a_{nw} - S_w$ curves present hysteresis. We found that GB55 has a much larger specific interfacial area compared to GB170 and GB240. The largest specific IFA is recorded for NS210. This implies that materials with smaller grain diameters will have larger specific interfacial area.

6.4.4 Determination of maximum specific capillary-associated interfacial area with the KIS tracer method

In **Figure 6.10** the maximum values for specific capillary associated IFA, a_{nw}^{max}, obtained with KIS tracer method are plotted. We plot the three sets of a_{nw}^{max} obtained for each soil category, the average value and the error range corresponding to the minimum and maximum a_0 values. Implementing a linear regression line over the $a_{nw}^{max} - IMGD$ data we obtain the following relation for the glass-beads material:

$$a_{wn}^{max} = 0.0636/d_{50} - 0.4393 \tag{6.8}$$

Similar to values reported in the literature for total maximum total FIFA, a_n^{max} , the a_{wn}^{max} follows a linearly increasing trend with an increase in IMGD. There is a clear distinction between the slopes of the linear regression lines of natural sand materials and glass beads. Having a larger surface roughness than the glass beads, the natural sand a_{wn}^{max} has a much larger increase in slope with IMGD.

The capillary-associated IFAs of the five materials determined with the thermodynamically based explicit IFA model (Grant and Gerhard 2007), follow a linear relationship $a_{wn.\,GG}^{max}$ when plotted against the IMGD. In this case no discrepancy between the natural sands and glass beads is observed.

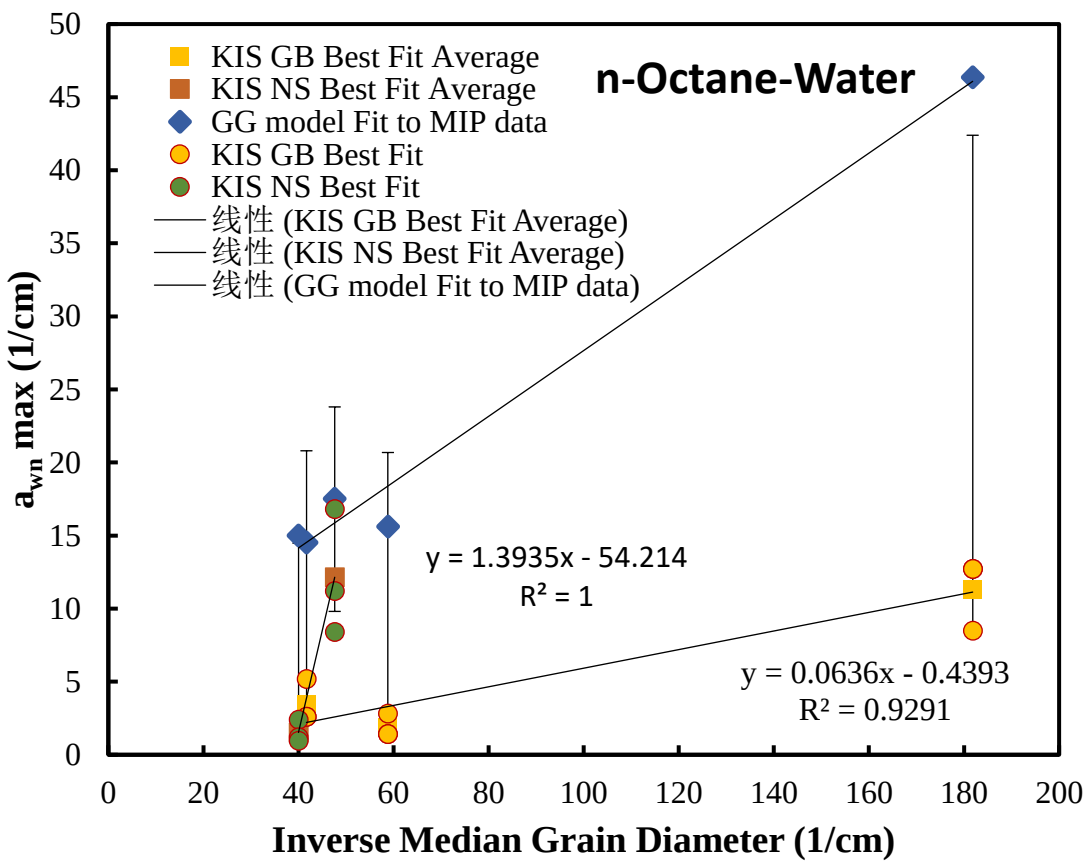

Figure 6.10: Relationship between n-octane/water maximum specific capillary associated interfacial area, a_{wn}^{max} and inverse median grain diameter. Values determined using the KIS tracers on the five porous media, GB55, GB170, GB240, NS210, NS250. The values for a_{nw}^{max} are reported in **Table SI 1**.

6.4.5 Comparison of maximum capillary associated-specific interfacial area with literature

The comparison of FIFA with the literature data needs to account first for the type of IFA being compared, i.e. total or capillary associated IFA, and for the different porous media-fluid system types. Most commonly, the fluid-systems used in the reported experiments are air-water and, less often, NAPL-water. To the authors' knowledge there are only four studies that report the measured specific capillary associated IFA (Culligan et al. 2006; Brusseau et al. 2006; Porter et al. 2010; Araujo and Brusseau 2020). XMT was used in each of these studies.

Figure 6.11 plots the a_{wn}^{max} values obtained with the KIS tracer method and with XMT experiments using NAPL-water fluid system from (Culligan et al. 2006; Porter et al. 2010), and air-water fluid system from (Brusseau et al. 2006; Araujo and Brusseau 2020). Likos and Jaafar (2013) developed a pore-geometry model that calculates the specific IFA based on the measured grain-size distributions. They apply their model to four porous media (small glass beads, F75 Ottawa sand, large glass beads, river sand) and plot the capillary-associated IFA, a_{nw}. Note that the capillary-associated IFA determined by Culligan et al. (2006) for air-water and oil-water fluid systems in the same porous medium found the that the capillary-associated IFA for oil-water is larger than that of air-water during main drainage. The surface tension of air-water is higher and the XMT revealed that air phase is located in larger continuous fluid configurations while the oil forms smaller, less well-connected configurations at similar saturations, leading to larger interfacial areas. Here, we do not apply any scaling to a_{wn} values.

It is observed that the literature values plotted against the IMGD, follow a linear trend which is larger than the prediction line of a_{wn}^{max}- IMGD obtained from the KIS tracer experiments. The theoretically determined a_{wn}^{max} values using the (Grant and Gerhard 2007) model (illustrated in **Figure 6.9**, dashed black curves) are in good agreement with the regression line applied through the literature values. For the n-octane-water fluid system the capillary-associated IFA, a_{wn}^{max} determined by KIS tracers ranges between 3.00 (d_{50}=55 μm) and 4.64 (d_{50}=250 μm) times smaller than the capillary associated IFA reported in the literature. The explanation for this behavior is that the KIS tracer method only measures the mobile fraction of the fluid-fluid interface, which correspond to the mobile terminal menisci displacing the water in the system(Figure 6.1).

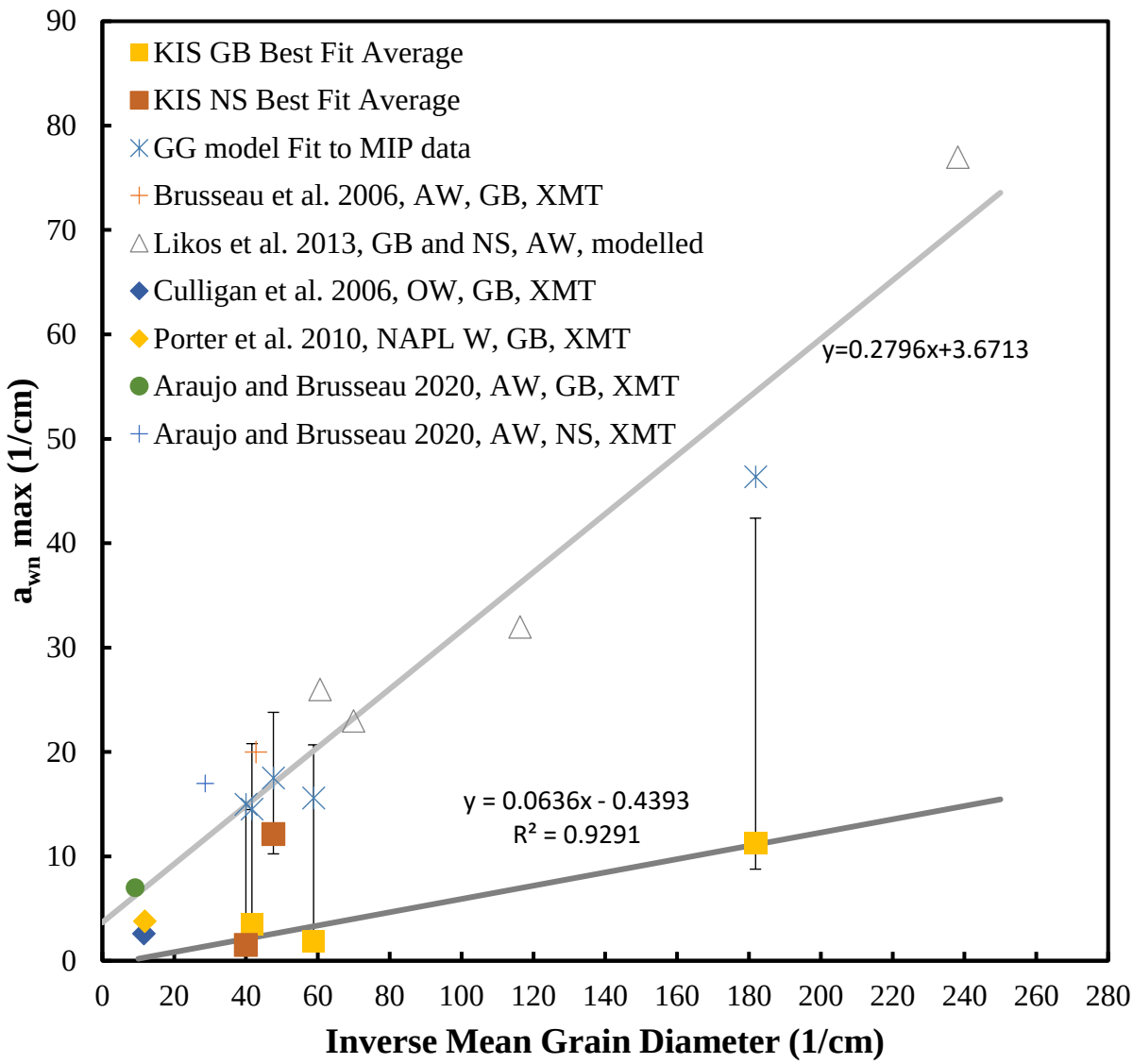

Figure 6.11: Mobile a_{wn}^{max} determined by KIS tracer experiment in an n-octane-water fluid system and comparison with literature data for capillary associated interfacial area.

6.4.6 Comparison of total specific interfacial area with literature data

Direct evaluation of the influence of grain diameters, their surface area and their fluid-fluid interfaces is difficult to perform for the entire set of published data because of the different types of surface area information reported, and because reported experiments are conducted with different types of fluid-porous media systems, e.g. air-water, NAPL-water, organic-liquid -water, etc. With very few exceptions, the literature compiled data contain IFA measured under residual-saturation conditions, i.e. imbibition conditions. Note, the interfacial area obtained for imbibition conditions is smaller.

Specific fluid-fluid interfaces reported in Brusseau et al. (2009; 2010) for organic-liquid-water fluid systems and at further data from (Kim et al. 1997; Zhong et al. 2016; Araujo and Brusseau

2020) are plotted against the inverse mean grain diameter on a log-log scale (**Figure 6.12**). It is apparent that the general trend for all interfacial areas, a_{wn}^{max}, the a_{wn}^{max} measured by the KIS tracers, a_n^{max}, and a_n^{max} calculated with the geometric-based smooth sphere approach (GSSA) can be expressed as linear functions increasing with IMGD. The calculated total specific solid surface areas with the (Rootare and Prenzlow 1967) model applied to the MIP data match closely the linear trend reported values from the literature. For the two natural sands the a_n^{max} values (NS SSSA-MIP) are higher than the corresponding GSSA.

It can be observed that the total maximum IFA, a_n^{max} predicted by the (Grant and Gerhard 2007) model corresponding to the best fitted $a_{wn} - S_w$ curves for the five porous media are smaller than the linear trend of a_n^{max} of porous media with surface roughness from literature (Brusseau et al. 2010), and also smaller than the porous media with no surface roughness, or calculated with the GSSA (Brusseau et al. 2010). On the log-log scale, the linear functions are approximately parallel to each other. A much steeper increase of the a_n^{max} with IMGD is observed for the category of natural soils.

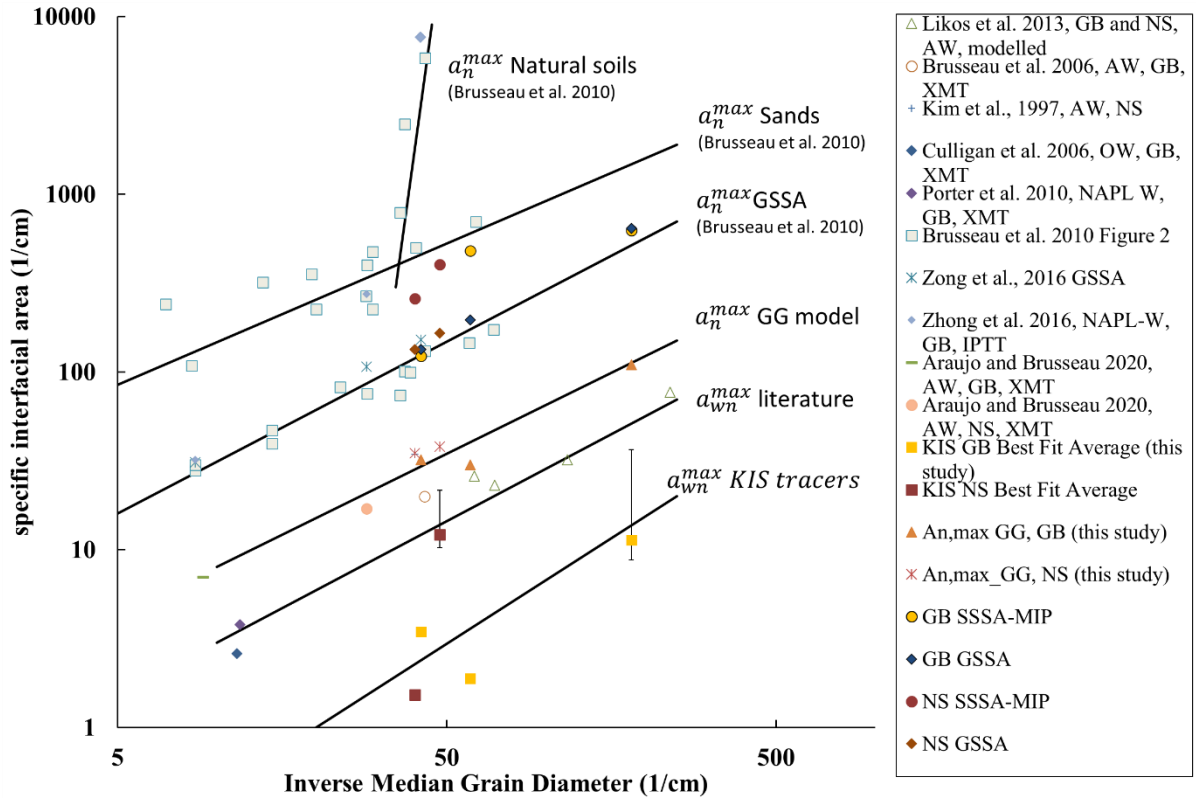

Figure 6.12: Compiled total specific IFA, a_n, and capillary-associated IFA, a_{wn}^{max} from the literature and this study. The total IFA for the five materials calculated as SSSA-MIP and GSSA, and the mobile capillary-associated IFAs determined with KIS tracer method

6.4.7 Texture influence on IFA

Here, we investigate the influence on a_{wn}^{max} of texture parameters: mean pore size, pore-uniformity coefficient, specific solid surface area, SSA geometrically calculated (GSSA), and grain roundness (**Figure 6.13**). A higher solid surface area, which incorporates a higher solid surface roughness, is correlated to a higher specific FIFA. For the five porous media, mean pore-sizes (measured with

MIP) correlate well with the mean grain size (measured with DIA) (**Figure 6.4**). Therefore, when plotting a_{wn}^{max} with the mean pore size (**Figure 6.13**a) we see that the larger the mean pore-size the smaller the capillary-associated IFA.

The pore-size distribution is reflected in the pore-uniformity coefficient. **Figure 6.13**b) shows the influence on C_{pu} on a_{wn}^{max} . The specific solid-grain surface areas of the five materials were derived from the MIP measurements by applying the (Rootare and Prenzlow 1967) model, i.e., SSSA-MIP, and were also calculated geometrically using the smooth sphere assumption, i.e. GSSA. Their influence on the a_{wn}^{max} is plotted in **Figure 6.13**c) and d). In most literature studies the specific solid surface is measured with N_2/BET technique which commonly measures larger values than the SSSA-MIP and GSSA, e.g.(Narter and Brusseau 2010).

Generally, it can be concluded that the larger the SSSA the larger the a_{wn}^{max}. The very fine glass beads medium GB55 and the NS210 have the highest SSSA and the highest a_{wn}^{max} (**Table 6.1**). GB55 has the highest SSSA close to the GSSA value, 643 µm. GB55 resulting a_{wn}^{max}, is slightly smaller than the NS210 which has a large SSSA, measured by MIP. This is a further demonstration that the KIS tracer method can provide a robust characterization technique of fluid-fluid IFA, determine correctly the mobile capillary-associated IFA, since the same trend as in the literature is found. Similar to the findings of (Brusseau et al. 2009) for total FIFA, other texture parameters such as the grain- and pore-size distributions, roundness, Feret diameter, have minimal impact on the mobile capillary-associated IFA.

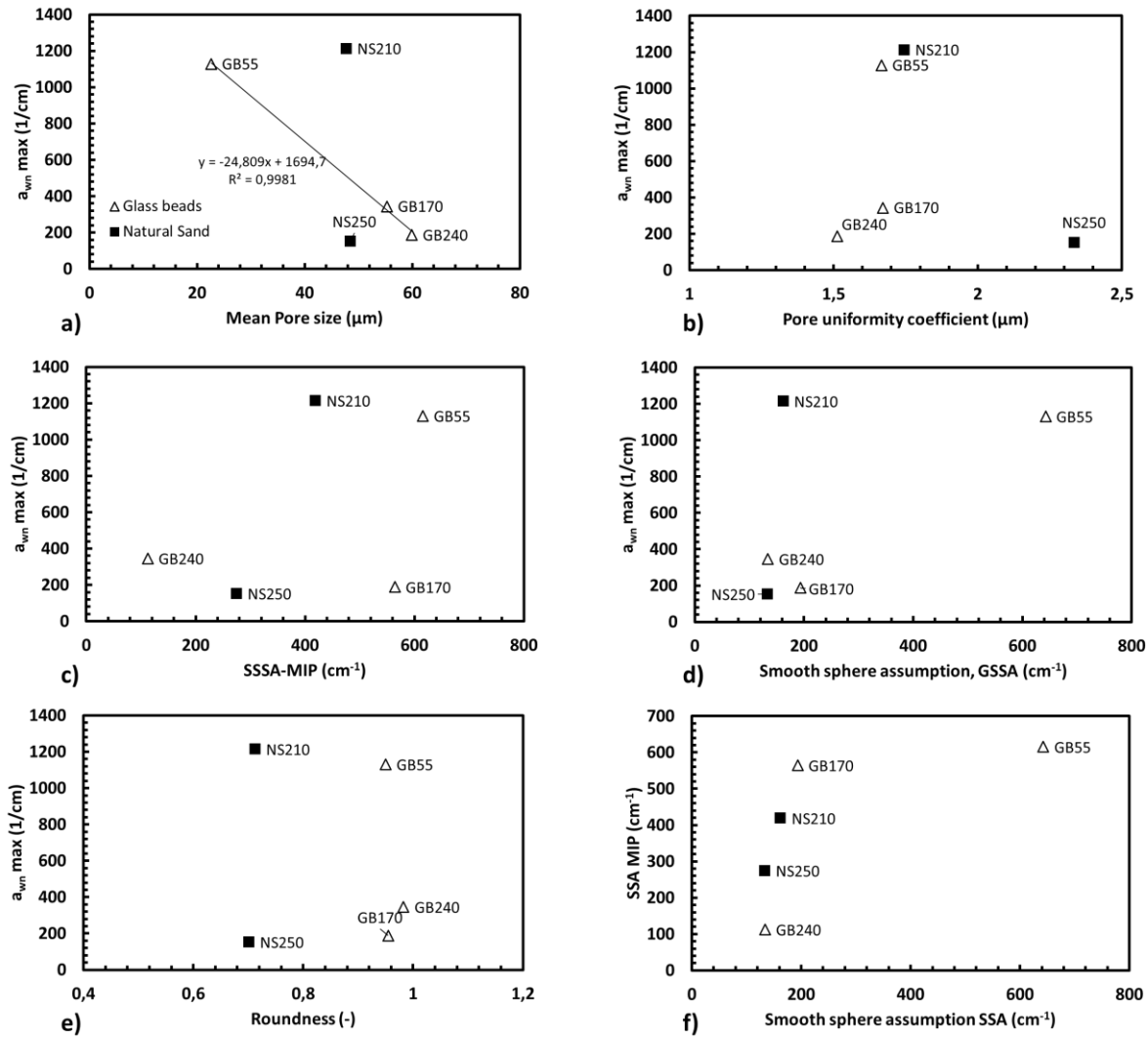

Figure 6.13: Specific capillary-associated IFA variation depending on the texture related parameters.

6.5 Conclusions

- We demonstrated that the KIS tracers allow studying the moving fluid-fluid interfaces in complex three-dimensional systems. On the basis of 15 sets of measurements performed on five different porous media, we were able to test and successfully extend the range of applicability of the KIS tracers, previously applied only to one type of glass-beads material. We were able to determine the specific capillary associated IFA and its linear relationship with the IMGD. We also observed new phenomena in the tracer BTC, not predicted by Darcy-scale coupled multiphase flow and reactive-transport models.
- The KIS tracer method can serve as a technique to improve our predictive capability of existing numerical schemes in constraining inverse models. The experimental results constitute an important data-set regarding the fate of an interface-depending reactive contaminant. The discrepancy between the experimental results and the numerical approaches underlines the limitation of existing approaches to fully resolve the processes taking place in the pore space. By

using the quantitative results obtained by the experiments, a future perspective is to attempt to match those by means of tuning average properties, like tortuosity, coordination number, while keeping in mind the processes affected by the pore geometry itself, e.g., non-Fickian transport.

- KIS tracer measured maximum specific FIFA magnitude increases linearly with inverse mean grain diameter, following a similar trend like the one reported in the literature (Costanza-Robinson and Brusseau 2002; Brusseau et al. 2009; Brusseau et al. 2010) obtained with other methods, e.g., IPTT and XMT. However, the values measured with the KIS tracer method range between 3.00 and 4.64 times smaller than the maximum capillary-associated IFA including both mobile and immobile parts, and, as expected, smaller than the total FIFA, a_n^{max}. The explanation for this observation is that the concentration of the reacted KIS tracer at the outflow is composed only of the solute transported with the mobile part of the water. Some fraction of the reacted solute becomes trapped in stagnant flow regions and it is never measured (to these add up the terminal menisci, pendular ring/ wedge menisci).
- We provide a compilation of the literature reported data for the specific fluid-fluid interfaces. Comparison of the measured and interpreted data herein with literature data provides further insights into the characterization of the fluid-fluid /NAPL-water interfaces. Similar to the observations made for the total specific interfacial area, natural sands, with higher roughness lead to larger capillary-associated IFA than the smooth glass beads. Other than the solid surface area we cannot make any conclusive statement about the influence on capillary-associated IFA of the other texture related parameters, e.g. grain- and pore-size distribution, uniformity coefficients, roundness, etc.
- The current continuum-scale (Darcy-scale) numerical models for reactive transport in two-phase flow in porous media need to be reconsidered. Many of the experimental breakthrough curves exhibit an early concentration peak and are flattening or decreasing towards the end of the drainage process. Current multiphase-flow models with reactive transport are unable to reproduce these effects. Therefore, to improve the predictive modelling capacities a new theoretical modeling framework is required.
- The micro-scale mechanisms need to be investigated separately with pore-scale and pore-network modelling of the reactive-transport and multiphase-flow-coupled processes. A promising approach to interpret the KIS tracer BTCs uses a pore-scale reactive transport model developed by Gao et al. (2020).
- For the future, the measurement accuracy of the KIS tracer method should be improved by adding pressure sensors to acquire information regarding the pressure change during the experiment, precise control of the flow rates attainable with high-precision pumps, development of a continuous sampling method to remove the errors during sampling.
- In addition, further research is needed to extend the applicability of the method to a wider range of flow conditions and fluid-fluid-porous media systems, e.g., natural soils, soils with wider variety of diameters and textures.

Until now the KIS tracer method has not been compared against another measurement technique. KIS tracers have the potential to be applied as a complementary technique for measuring FIFA. In this way, the mobile and the immobile parts of the capillary-associated IFA can be identified, or one can differentiate between mobile and immobile flow regions. This study represents an important step towards establishing KIS tracers as a robust characterization technique capable of measuring fluid-fluid interfacial area in multiphase flow in porous media systems.

6.6 Acknowledgments

This project was funded by the German Research Foundation, DFG, under project number 428614366, the European Community's 7th Framework Programme FP7 under grant number 309067 (trust-co2.org), and Horizon 2020 Research and Innovation Programme, FracRisk project (https://ec.europa.eu/inea/en/horizon-2020/projects/H2020-Energy/Shale-gas/FracRisk) under grant number 636811. We are grateful for the support of SFB1313 Collaborative Research Center (Project Number 327154368). We are also grateful to Florian Duschl and Dejian Zhou for the support with the laboratory work. All data used to support this work are reported in the manuscript and the Appendix in the respective tables and figures.

6.7 References

Annable MD, Rao PSC, Hatfield K, Graham WD, Wood AL, Enfield CG (1998) Partitioning Tracers for Measuring Residual NAPL: Field-Scale Test Results. J Environ Eng 124:498–503 . https://doi.org/10.1061/(ASCE)0733-9372(1998)124:6(498)

Anwar AHMF, Bettahar M, Matsubayashi U (2000) A method for determining air–water interfacial area in variably saturated porous media. J Contam Hydrol 43:129–146 . https://doi.org/10.1016/S0169-7722(99)00103-5

Araujo JB, Brusseau ML (2020) Assessing XMT-Measurement Variability of Air-Water Interfacial Areas in Natural Porous Media. Water Resour Res 56:e2019WR025470 . https://doi.org/10.1029/2019WR025470

Bradford SA, Leij FJ (1997) Estimating interfacial areas for multi-fluid soil systems. J Contam Hydrol 27:83–105 . https://doi.org/10.1016/S0169-7722(96)00048-4

Brooks RH, Corey AT (1964) Hydraulic properties of porous media. Hydrol Pap No 3 3:

Brusseau ML (2018) Assessing the potential contributions of additional retention processes to PFAS retardation in the subsurface. Sci Total Environ 613–614:176–185 . https://doi.org/10.1016/j.scitotenv.2017.09.065

Brusseau ML (2019) The influence of molecular structure on the adsorption of PFAS to fluid-fluid interfaces: Using QSPR to predict interfacial adsorption coefficients. Water Res 152:148–158 . https://doi.org/10.1016/j.watres.2018.12.057

Brusseau ML, Janousek H, Murao A, Schnaar G (2008) Synchrotron X-ray microtomography and interfacial partitioning tracer test measurements of NAPL-water interfacial areas. Water Resour Res 44:W01411 . https://doi.org/10.1029/2006WR005517

Brusseau ML, Narter M, Janousek H (2010) Interfacial partitioning tracer test measurements of organic-liquid/water interfacial areas: application to soils and the influence of surface roughness. Environ Sci Technol 44:7596–7600 . https://doi.org/10.1021/es101312n

Brusseau ML, Narter M, Schnaar G, Marble J (2009) Measurement and Estimation of Organic-Liquid/Water Interfacial Areas for Several Natural Porous Media. Environ Sci Technol 43:3619–3625 . https://doi.org/10.1021/es8020827

Brusseau ML, Ouni AE, Araujo JB, Zhong H (2015) Novel methods for measuring air–water interfacial area in unsaturated porous media. Chemosphere 127:208–213 . https://doi.org/10.1016/j.chemosphere.2015.01.029

Brusseau ML, Peng S, Schnaar G, Costanza-Robinson MS (2006) Relationships among air-water interfacial area, capillary pressure, and water saturation for a sandy porous medium. Water Resour Res 42:W03501 . https://doi.org/10.1029/2005WR004058

Brusseau ML, Peng S, Schnaar G, Murao A (2007) Measuring Air−Water Interfacial Areas with X-ray Microtomography and Interfacial Partitioning Tracer Tests. Environ Sci Technol 41:1956–1961 . https://doi.org/10.1021/es061474m

Cary JW (1994) Estimating the surface area of fluid phase interfaces in porous media. J Contam Hydrol 15:243–248 . https://doi.org/10.1016/0169-7722(94)90029-9

Cho J, Annable MD (2005) Characterization of pore scale NAPL morphology in homogeneous sands as a function of grain size and NAPL dissolution. Chemosphere 61:899–908 . https://doi.org/10.1016/j.chemosphere.2005.04.042

Costanza MS, Brusseau ML (2000) Contaminant Vapor Adsorption at the Gas−Water Interface in Soils. Environ Sci Technol 34:1–11 . https://doi.org/10.1021/es9904585

Costanza-Robinson MS, Brusseau ML (2002) Air-water interfacial areas in unsaturated soils: Evaluation of interfacial domains. Water Resour Res 38:1195 . https://doi.org/10.1029/2001WR000738

Culligan KA, Wildenschild D, Christensen BSB, Gray WG, Rivers ML (2006) Pore-scale characteristics of multiphase flow in porous media: A comparison of air–water and oil–water experiments. Adv Water Resour 29:227–238 . https://doi.org/10.1016/j.advwatres.2005.03.021

Dalla E, Hilpert M, Miller CT (2002) Computation of the interfacial area for two-fluid porous medium systems. J Contam Hydrol 56:25–48

Dobson R, Schroth MH, Oostrom M, Zeyer J (2006) Determination of NAPL−Water Interfacial Areas in Well-Characterized Porous Media. Environ Sci Technol 40:815–822 . https://doi.org/10.1021/es050037p

Flemisch B, Darcis M, Erbertseder K, Faigle B, Lauser A, Mosthaf K, Müthing S, Nuske P, Tatomir A, Wolff M, Helmig R (2011) DuMux: DUNE for multi-{phase, component, scale, physics, …} flow and transport in porous media. Adv Water Resour 34:1102–1112 . https://doi.org/10.1016/j.advwatres.2011.03.007

Fukunishi Y, Tateishi T, Suzuki M (1996) Octane/Water Interfacial Tension Calculation by Molecular Dynamics Simulation. J Colloid Interface Sci 180:188–192 . https://doi.org/10.1006/jcis.1996.0288

Gao H, Tatomir AB, Karadimitriou NK, Steeb H, Sauter M (2020) A two-phase, pore-scale reactive transport model for the kinetic interface- sensitive tracer (to be submitted). Water Resour Res

Grant GP, Gerhard JI (2007) Simulating the dissolution of a complex dense nonaqueous phase liquid source zone: 1. Model to predict interfacial area. Water Resour Res 43:W12410 . https://doi.org/10.1029/2007WR006038

Gvirtzman H, Roberts PV (1991) Pore scale spatial analysis of two immiscible fluids in porous media. Water Resour Res 27:1165–1176 . https://doi.org/10.1029/91WR00303

Hassanizadeh SM, Gray WG (1993) Thermodynamic basis of capillary pressure in porous media. Water Resour Res 29:3389–3405 . https://doi.org/10.1029/93WR01495

Hassanizadeh SM, Gray WG (1990) Mechanics and thermodynamics of multiphase flow in porous media including interphase boundaries. Adv Water Resour 13:169–186 . https://doi.org/10.1016/0309-1708(90)90040-B

Heiß VI, Neuweiler I, Ochs S, Färber A (2011) Experimental investigation on front morphology for two-phase flow in heterogeneous porous media. Water Resour Res 47:W10528 . https://doi.org/10.1029/2011WR010612

Held RJ, Celia MA (2001) Pore-scale modeling extension of constitutive relationships in the range of residual saturations. Water Resour Res 37:165–170 . https://doi.org/10.1029/2000WR900234

Hilfer R, Øren PE (1996) Dimensional analysis of pore scale and field scale immiscible displacement. Transp Porous Media 22:53–72 . https://doi.org/10.1007/BF00974311

Jiang H, Guo B, Brusseau ML (2020) Pore-Scale Modeling of Fluid-Fluid Interfacial Area in Variably Saturated Porous Media Containing Microscale Surface Roughness. Water Resour Res 56:e2019WR025876 . https://doi.org/10.1029/2019WR025876

Joekar-Niasar V, Hassanizadeh SM (2012a) Analysis of Fundamentals of Two-Phase Flow in Porous Media Using Dynamic Pore-Network Models: A Review. Crit Rev Environ Sci Technol 42:1895–1976 . https://doi.org/10.1080/10643389.2011.574101

Joekar-Niasar V, Hassanizadeh SM (2012b) Uniqueness of Specific Interfacial Area–Capillary Pressure–Saturation Relationship Under Non-Equilibrium Conditions in Two-Phase Porous Media Flow. Transp Porous Media 94:465–486 . https://doi.org/10.1007/s11242-012-9958-3

Karadimitriou NK, Joekar-Niasar V, Babaei M, Shore CA (2016) Critical Role of the Immobile Zone in Non-Fickian Two-Phase Transport: A New Paradigm. Environ Sci Technol 50:4384–4392 . https://doi.org/10.1021/acs.est.5b05947

Kim H, Rao PSC, Annable MD (1997) Determination of effective air-water interfacial area in partially saturated porous media using surfactant adsorption. Water Resour Res 33:2705 . https://doi.org/10.1029/97WR02227

Kim H, Rao PSC, Annable MD (1999) Gaseous Tracer Technique for Estimating Air–Water Interfacial Areas and Interface Mobility. Soil Sci Soc Am J 63:1554–1560 . https://doi.org/10.2136/sssaj1999.6361554x

Lenormand R, Touboul E, Zarcone C (1988) Numerical models and experiments on immiscible displacements in porous media. J Fluid Mech 189:165–187 . https://doi.org/10.1017/S0022112088000953

Leverett MC (1941) Capillary Behavior in Porous Solids. Trans AIME 142:152–169 . https://doi.org/10.2118/941152-G

Likos WJ, Jaafar R (2013) Pore-Scale Model for Water Retention and Fluid Partitioning of Partially Saturated Granular Soil. J Geotech Geoenvironmental Eng 139:724–737 . https://doi.org/10.1061/(ASCE)GT.1943-5606.0000811

Lyu Ying, Brusseau Mark L., El Ouni Asma, Araujo Juliana B., Su Xiaosi (2017) The Gas-Absorption/Chemical-Reaction Method for Measuring Air-Water Interfacial Area in Natural Porous Media. Water Resour Res 53:9519–9527 . https://doi.org/10.1002/2017WR021717

McDonald K, Carroll KC, Brusseau ML (2016) Comparison of fluid-fluid interfacial areas measured with X-ray microtomography and interfacial partitioning tracer tests for the same samples. Water Resour Res 52:5393–5399 . https://doi.org/10.1002/2016WR018775

Miller CT, Poirier-McNeil MM, Mayer AS (1990) Dissolution of Trapped Nonaqueous Phase Liquids: Mass Transfer Characteristics. Water Resour Res 26:2783–2796 . https://doi.org/10.1029/WR026i011p02783

Narter M, Brusseau ML (2010) Comparison of Interfacial partitioning tracer test and high-resolution microtomography measurements of fluid-fluid interfacial areas for an ideal porous medium. Water Resour Res 46: . https://doi.org/10.1029/2009WR008375

Nelson NT, Brusseau ML (1996) Field Study of the Partitioning Tracer Method for Detection of Dense Nonaqueous Phase Liquid in a Trichloroethene- Contaminated Aquifer. Environ Sci Technol 30:2859–2863 . https://doi.org/10.1021/es960148b

Niemi A, Bensabat J, Shtivelman V, Edlman K, Gouze P, Luguot L, Hingl F, Benson SM, Pezard P, Rasmusson K, Tian L, Fagerlund F, Tatomir AB, Lange, Torsten, Sauter M, Freifeld B (2016) Overview of the Heletz site, its characterization and data analysis for CO2 injection and geological storage (submitted). Int J Greenh Gas Control xx:

Oostrom M, White MD, Brusseau ML (2001) Theoretical estimation of free and entrapped nonwetting–wetting fluid interfacial areas in porous media. Adv Water Resour 24:887–898 . https://doi.org/10.1016/S0309-1708(01)00017-3

Patmonoaji A, Tsuji K, Muharrik M, Suekane T (2018) Micro-tomographic analyses of specific interfacial area inside unconsolidated porous media with differing particle characteristics from microscopic to macroscopic scale. J Colloid Interface Sci 532:614–621 . https://doi.org/10.1016/j.jcis.2018.08.023

Peche A, Halisch M, Bogdan Tatomir A, Sauter M (2016) Development of a numerical workflow based on μ-CT imaging for the determination of capillary pressure–saturation-specific interfacial area relationship in 2-phase flow pore-scale porous-media systems: a case study on Heletz sandstone. Solid Earth 7:727–739 . https://doi.org/10.5194/se-7-727-2016

Peng S, Brusseau ML (2005) Impact of soil texture on air-water interfacial areas in unsaturated sandy porous media. Water Resour Res 41: . https://doi.org/10.1029/2004WR003233

Porter ML, Wildenschild D, Grant G, Gerhard JI (2010) Measurement and prediction of the relationship between capillary pressure, saturation, and interfacial area in a NAPL-water-glass bead system. Water Resour Res 46:W08512 . https://doi.org/10.1029/2009WR007786

Reeves PC, Celia MA (1996) A Functional Relationship Between Capillary Pressure, Saturation, and Interfacial Area as Revealed by a Pore-Scale Network Model. Water Resour Res 32:2345 . https://doi.org/10.1029/96WR01105

Rootare HM, Prenzlow CF (1967) Surface areas from mercury porosimeter measurements. J Phys Chem 71:2733–2736 . https://doi.org/10.1021/j100867a057

Saripalli KP, Kim H, Rao PSC, Annable MD (1997) Measurement of Specific Fluid−Fluid Interfacial Areas of Immiscible Fluids in Porous Media. Environ Sci Technol 31:932–936 . https://doi.org/10.1021/es960652g

Schaefer CE, DiCarlo DA, Blunt MJ (2000) Determination of Water-Oil Interfacial Area during 3-Phase Gravity Drainage in Porous Media. J Colloid Interface Sci 221:308–312 . https://doi.org/10.1006/jcis.1999.6604

Schaffer M, Maier F, Licha T, Sauter M (2013) A new generation of tracers for the characterization of interfacial areas during supercritical carbon dioxide injections into deep saline aquifers: Kinetic interface-sensitive tracers (KIS tracer). Int J Greenh Gas Control 14:200–208 . https://doi.org/10.1016/j.ijggc.2013.01.020

Schnaar G, Brusseau ML (2006) Characterizing Pore-Scale Configuration of Organic Immiscible Liquid in Multiphase Systems With Synchrotron X-Ray Microtomography. Vadose Zone J 5:641–648 . https://doi.org/10.2136/vzj2005.0063

Simon MA, Brusseau ML (2007) Analysis of a gas-phase partitioning tracer test conducted in an unsaturated fractured-clay formation. J Contam Hydrol 90:146–158 . https://doi.org/10.1016/j.jconhyd.2006.09.010

Tatomir A, Maier F, Schaffer M, Licha T, Sauter M (2013) Modelling of Kinetic Interface Sensitive Tracers for Two-Phase Systems. In: Hou MZ, Xie H, Were P (eds) Clean Energy Systems in the Subsurface: Production, Storage and Conversion. Springer Berlin Heidelberg, pp 65–74

Tatomir A, Vriendt KD, Zhou D, Gao H, Duschl F, Sun F, Licha T, Sauter M (2018) Kinetic Interface Sensitive Tracers: Experimental Validation in a Two-Phase Flow Column Experiment. A Proof of Concept. Water Resour Res 54:10,223-10,241 . https://doi.org/10.1029/2018WR022621

Tatomir AB, Halisch M, Duschl F, Peche A, Wiegand B, Schaffer M, Licha T, Niemi A, Bensabat J, Sauter M (2016a) An integrated core-based analysis for the characterization of flow, transport and mineralogical parameters of the Heletz pilot CO2 storage site reservoir. Int J Greenh Gas Control 48, Part 1:24–43 . https://doi.org/10.1016/j.ijggc.2016.01.030

Tatomir AB, Jyoti A, Sauter M (2016b) The Monitoring of CO2 plume migration in deep saline formations with kinetic interface sensitive tracers. In: Singh TN, Vikram V (eds) Geologic Carbon Sequestration: Understanding Reservoir Concepts. Springer, p 336

Tatomir AB, Schaffer M, Kissinger A, Hommel J, Nuske P, Licha T, Helmig R, Sauter M (2015) Novel approach for modeling kinetic interface-sensitive (KIS) tracers with respect to time-dependent interfacial area change for the optimization of supercritical carbon dioxide injection into deep saline aquifers. Int J Greenh Gas Control 33:145–153 . https://doi.org/10.1016/j.ijggc.2014.11.020

Washburn EW (1921) Note on a Method of Determining the Distribution of Pore Sizes in a Porous Material. Proc Natl Acad Sci U S A 7:115–116

Zhong H, El Ouni A, Lin D, Wang B, Brusseau ML (2016) The two-phase flow IPTT method for measurement of nonwetting-wetting liquid interfacial areas at higher nonwetting saturations in natural porous media. Water Resour Res 52:5506–5515 . https://doi.org/10.1002/2016WR018783

6.8 Appendix

Table SI 6.1. Best fitting parameters for the modelling of the KIS tracer experiments: 1) calibration of the volume ratio of the n-octane and water; 2) calibration of the 2-NSA concentration BTC.

Experiment index	**Volume ratio V_n/V_T BTC**							**2-NSA Concentration BTC**			**S_w at end of experiment**	
	Q_{min} (ml/min)	Q_{max} (ml/min)	Q_{BF} (ml/min)	K_{min} (m^2)	K_{max} (m^2)	K_{BF} (m^2)	RMSE	a_0	a_{wn}^{max} (m^{-1})	RMSE	Experiment	Model
GB55_1	0.6	0.64	0.61	2×10^{-13}	6×10^{-13}	6×10^{-13}	0.045241	1×10^{-5}	848	0.3162	0.18	0.36
GB55_3	0.54	0.58	0.55	1×10^{-13}	5×10^{-13}	5×10^{-13}	0.009795	1.5×10^{-5}	1270	1.2831	0.16	0.37
GB55_4	0.56	0.60	0.57	4×10^{-13}	8×10^{-13}	8×10^{-13}	0.026996	1.5×10^{-5}	1270	0.8899	0.2	0.37
GB170_2	0.53	0.57	0.55	8×10^{-13}	12×10^{-13}	1.1×10^{-12}	0.05649	5×10^{-6}	141	0.5561	0.26	0.35
GB170_3	0.67	0.71	0.68	5.8×10^{-12}	6.2×10^{-12}	6×10^{-12}	0.052176	5×10^{-6}	141	0.5145	0.27	0.36
GB170_6	0.62	0.66	0.62	3.0×10^{-12}	7.0×10^{-12}	5×10^{-12}	0.0129	1×10^{-5}	282	1.5397	0.28	0.35
GB240_1	0.42	0.46	0.44	1.0×10^{-12}	5.0×10^{-12}	2×10^{-12}	0.018418	2×10^{-5}	519	2.3039	0.27	0.36
GB240_2	0.65	0.68	0.65	4.0×10^{-12}	6.0×10^{-12}	4×10^{-12}	0.018708	1×10^{-5}	260	1.839	0.35	0.35
GB240_3	0.66	0.70	0.66	1.0×10^{-12}	5.0×10^{-12}	4×10^{-12}	0.023005	1×10^{-5}	260	1.5397	0.31	0.36
NS210_3	0.60	0.64	0.62	5.0×10^{-13}	9.0×10^{-13}	8×10^{-13}	0.0289	4×10^{-5}	1120	1.0787	0.35	0.38
NS210_4	0.62	0.66	0.65	7.0×10^{-13}	11×10^{-13}	8×10^{-13}	0.01687	3×10^{-5}	841	0.8517	0.38	0.37
NS210_5	0.61	0.65	0.64	4.0×10^{-13}	8.0×10^{-13}	6×10^{-13}	0.023323	6×10^{-5}	1680	0.5484	0.32	0.37
NS250_1	0.70	0.74	0.73	5.0×10^{-12}	9.0×10^{-12}	5×10^{-12}	0.0133	1×10^{-5}	241	1.3005	0.44	0.39
NS250_2	0.76	0.80	0.76	5.0×10^{-12}	9.0×10^{-12}	9×10^{-12}	0.015451	5×10^{-5}	121	1.6447	0.43	0.43
NS250_3	0.46	0.50	0.46	1.0×10^{-12}	5.0×10^{-12}	3×10^{-12}	0.017759	4×10^{-5}	96.5	0.9524	0.48	0.43

To calculate the capillary number for the Darcy-scale column experiments we apply the following transformation (Hilfer and Øren 1996):

$$Ca = \frac{\mu_i v_D L}{p_d K}$$

where μ_i is the dynamic viscosity of the invading fluid, v_D is the mean Darcy velocity of the invading fluid, p_d is the entry pressure of the nonwetting fluid into the porous material, and K is the intrinsic permeability.

Table SI 6.2. Calculated capillary number, Ca

Experiment	K $(\boldsymbol{m^2})$	φ (-)	$\boldsymbol{p_d}$ $(\boldsymbol{Pa})$	$\boldsymbol{v_D}$ $(\boldsymbol{m/s})$	Ca
GB55_1	6E-13	0.411	5937	3.5E-05	**1.228**
GB55_3	5.00E-13	0.411	5937	3.16E-05	**1.329**
GB55_4	8.00E-13	0.411	5937	3.27E-05	**0.861**
GB170_2	1.10E-12	0.455	1819	2.85E-05	**1.781**
GB170_3	6.00E-12	0.455	1819	3.52E-05	**0.404**
GB170_6	5.00E-12	0.455	1819	3.21E-05	**0.442**
GB240_1	2.00E-12	0.464	1606	2.24E-05	**0.870**
GB240_2	4.00E-12	0.464	1606	3.3E-05	**0.643**
GB240_3	4.00E-12	0.464	1606	3.35E-05	**0.653**
NS210_3	8.00E-13	0.432	2050	3.38E-05	**2.579**
NS210_4	8.00E-13	0.432	2050	3.55E-05	**2.704**
NS210_5	6.00E-13	0.432	2050	3.49E-05	**3.55**
NS250_1	5.00E-12	0.445	1642	3.87E-05	**0.589**
NS250_2	9.00E-12	0.445	1642	4.03E-05	**0.341**
NS250_3	3.00E-12	0.445	1642	2.44E-05	**0.618**

Table SI 6.3. Data sets used for the total specific interfacial areas (after Brusseau et al. 2010)

Porous medium	S_n	No. measurements	Data Source
Vinton Soil	0.15	4	(Brusseau et al. 2010)
Eustis soil	0.17	4	(Brusseau et al. 2010)
Mixed sand	0.26	2	(Brusseau et al. 2008)
45-50 mesh sand	0.17	8	(Brusseau et al. 2008)
12-20 mesh sand	0.29	6	(Dobson et al. 2006)
20-30 mesh sand	0.28	5	(Dobson et al. 2006)
30-40 mesh sand	0.27	6	(Dobson et al. 2006)
40-50 mesh sand	0.28	5	(Dobson et al. 2006)
10-12 mesh sand	0.12	1	(Cho and Annable 2005)
20-30 mesh sand	0.14	1	(Cho and Annable 2005)
30-40 mesh sand	0.12	1	(Cho and Annable 2005)
40-60 mesh sand	0.15	1	(Cho and Annable 2005)
80-100 mesh sand	0.16	1	(Cho and Annable 2005)
40-100 mesh sand	0.19	3	(Saripalli et al. 1997)
40-50 mesh sand	Variable	5	(Schaefer et al. 2000)

S_n- saturation of organic liquid

7. Numerical investigations of front morphology and role of heterogeneity in two-phase flow in porous media using kinetic interface sensitive tracers

A. Tatomir[1], H. Gao[1], H. Abdullah[1], and M. Sauter[1]

Citation:

Tatomir AB, Gao H, Abdullah H, Sauter M (2022) Numerical investigations of front morphology and role of heterogeneity in two-phase flow in porous media using kinetic interface sensitive tracers. Submitted to Hydrogeology Journal (under review).

[1]Department of Applied Geology, Geoscience Centre of the University of Göttingen, Goldschmidtstr. 3, 37077, Göttingen, Germany

Corresponding author: Alexandru Tatomir (alexandru.tatomir@geo.uni-goettingen.de)

Abstract:

Previous studies provided a sound concept and a strategy for laboratory experimental investigations of a novel reactive smart tracer, termed "kinetic interface sensitive (KIS)" tracer, and used for the determination of the specific capillary-associated fluid-fluid interfacial area in dynamic two-phase flow displacement processes in porous media. However, in order to further develop the tracer method towards its application in natural geological formations it is necessary to consider the influence of the heterogeneity of the properties of aquifer materials. It is not yet properly understood in how far the porous media heterogeneity affects the kinetic interface sensitive tracer experiment and the corresponding breakthrough curves. This study employs a Darcy-scale two-phase flow reactive transport model to investigate numerically the KIS tracers transport in heterogeneous porous media. The simulations are carried out for the primary drainage process in a domain formed of fine ($d_m = 55\mu m$) and coarse ($d_m = 240\ \mu m$) glass beads. In total 14 heterogeneity patterns are studied having different geometrical distributions, and numbers of inclusions/lenses. The results show that when the heterogeneity factor is low and displacement front roughness is small, the concentration breakthrough curves increase linearly. Furthermore, the slopes of the breakthrough curves linearly depend on the fraction of the bulk volume occupied by the low permeable sand inclusions. We found that the volume averaged specific interfacial area in the domain can be determined from the slopes of the breakthrough curves. Next, when the displacement front is intensively folded, i.e., has a large front roughness, the linear shape of the concentration breakthrough curve exhibits the following features: an earlier first arrival (breakthrough) time, a peak of concentration shortly after breakthrough, and a smaller slope in the following stage. Thus, the shape of the breakthrough curve can be used as indicator for the existence of preferential flow pathways inside the porous media.

7.1 Introduction

Understanding front displacement mechanisms and quantifying the fluid-fluid interfacial area in two-phase flow in porous media is important for many geoscientific disciplines, e.g., hydrogeology, environmental sciences, petroleum engineering, water resources, soil mechanics, etc.. For example, in the context of CO_2 storage in geological formations, the CO_2 residual and solubility trapping mechanisms are highly influenced by the magnitude of the interface separating the two fluid phases (i.e., brine and supercritical CO_2). Therefore, knowledge of the effective interfacial area, its magnitude, and the shape of the injected CO_2 plume is important to provide information on trapping effectiveness within the formation (Schaffer et al. 2013; Tatomir et al. 2016, 2018).

7.1.1 Front instability during displacement

Extensive theoretical and experimental work was dedicated to study the immiscible displacement process at the pore-scale (Lenormand et al. 1988). However, the pore-scale properties and flow regimes cannot be transferred directly to the continuum (Darcy-) scale. A stable front is compact and has a front roughness that becomes constant with time (**Figure 7.1**). In the cases where the invading fluid is less viscous than the defending fluid, the displacement front starts to become unstable and results in the formation of so-called fingers. Even though this has been the subject of research over the past decades the prediction of the unstable front growth with time is still not fully understood (Méheust et al. 2002; Heiß et al. 2011). The process of forming highly-mobile phase channelling through a less mobile phase has been termed as viscous fingering (Bakharev et al. 2020). The viscous fingering effect is characterized by viscous fingers that have a tree-like shape

that does not form loops and grows towards the exit (Lenormand et al. 1988). According to (Bakharev et al. 2020) the term viscous fingering was coined by (Engelberts and Klinkenberg 1951). Front instabilities can be triggered in several ways, by gravity and viscosity differences and by random variation in the permeability field. Channelling is the displacement front influence by the rock structure, i.e., variation in permeability and pore geometry accompanied by variations in capillary pressure and relative permeability and should not need to be confused with viscous fingering.

7.1.2 Experimental study on heterogeneity and front morphology

Understanding the fundamental fluid-fluid interfacial process and the quantification of the fluid-fluid interfacial area can be gained from microscopic scale experiments using methods such as high resolution X-ray microtomography (XMT) (Porter et al. 2010) or thin micromodels (Karadimitriou et al. 2016). At macro-scale the pore scale heterogeneities are averaged, but the pore-scale process effects cannot always be transferred to the macro-scale because the exact geometries of the pores is generally unknown, including the micro-structures at the grain surface level, e.g., grain-surface roughness. The heterogeneity of the medium is inherently different at the pore-scale, where a fluid can or cannot invade a space, in contrast to the Darcy (macro-) scale, where all the pore space can be invaded (Heiß et al. 2011). In addition, the limitation of computational resources becomes evident when solving a reservoir-scale or even a column-scale problem using a pore-scale model. The geologic heterogeneity in combination with unstable front behaviour results in complex entrapment architectures containing residual, ganglia and pools (Page et al. 2007).

Darcy-scale displacement experiments in intermediate-scale flow-cells, e.g. sandboxes, were conducted with the purpose of understanding the key processes (Brusseau et al. 2002; Fagerlund et al. 2007; Tatomir 2007; Heiß et al. 2011; Rasmusson et al. 2017). The drainage of a wetting fluid by a non-wetting non-aqueous phase liquid (NAPL) has been studied in different soils and structures (such as homogeneous, layered, or highly heterogeneous soils) using various varieties of sand (Schwille and Pankow 1988; Kueper et al. 1989; Dawe et al. 1992; Illangasekare et al. 1995; Oostrom et al. 1999; Grant et al. 2007; Fagerlund et al. 2007). A translucent sandbox experiment has the advantage of real-time tracking of the two fluid phases while allowing the quantification of the fluid saturations. Page et al. (2007) used an intermediate-scale 2-D tank to examine the dissolution behaviour of DNAPL entrapped in heterogeneous soil systems and to investigate the effects of DNAPL mass and morphology on mass flux data.

7.1.3 Darcy-scale modelling of front morphology

Darcy-scale models have the ability to capture the morphology of the transition zone at the displacement front. When immiscible displacement processes are modelled on large spatial scales, the Darcy-scale model is upscaled by averaging the effects of the sub-grid Darcy-scale heterogeneity. The growth rate of the transition zone between high and low saturation of a displacing fluid is an important feature that should be reproduced by an upscaled model. The transition zone is directly related to the morphology of the displacement front. The displacement front on the Darcy-scale should be considered as an outermost isoline of saturation of the displacing fluid, instead of a real interface on the pore scale. In the past, upscaling of immiscible displacement on the Darcy-scale has been studied. Results can be classified according to the stability of the front. Noetinger and Zargar (2004) employed a first-order perturbation approach

for a stabilizing displacement. He found that the transition zone becomes constant in time and can be quantified by the fluid properties as well as by the correlation length and the variance of the permeability field. The growth of the transition zone has been associated with a dispersive term (Langlo and Espedal 1994; Neuweiler et al. 2003; Bolster et al. 2009) for a neutrally stable displacement. For the unstable case without gravity or capillary forces, the transition zone is expected to grow linearly with time (Blunt et al., 1994).

7.1.4 The kinetic interface sensitive (KIS) tracer

KIS tracers constitute a novel category of reactive tracers developed by (Schaffer et al. 2013), aiming at the quantification of the non-wetting/wetting phase fluid interface during the application of geological storage of the supercritical CO_2. The developed stable KIS tracer is a non-polar hydrolysable phenolic ester (phenyl naphthalene-2-sulphonate, 2-NSAPh, CAS 62141-80-4), dissolved in the non-aqueous phase (e.g., NAPL, supercritical CO_2) and then injected into the aquifer. Upon contact with the formation fluid (brine), the KIS tracer undergoes an irreversible hydrolysis reaction at the interface. The KIS tracer hydrolyses into two products (an acid and a phenol) that are highly water soluble and the back partitioning into the non-wetting phase can be considered negligible. Because the reaction kinetics of the tracer is well studied in laboratory batch experiments (Schaffer et al. 2013; Tatomir et al. 2018, 2020), the measured reaction product concentration can be used to back-calculate the fluid-fluid interfacial area. The hydrolysis reaction at the interface can be described as:

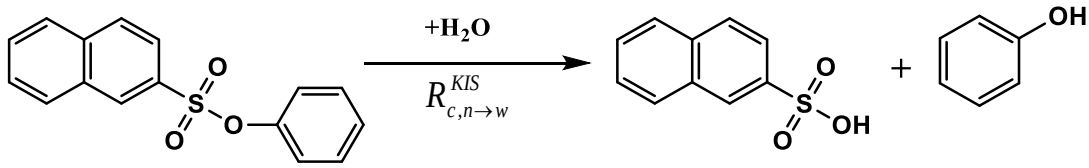

(7.1)

Phenyl Naphthalene-2-Sulfonate Naphthalene-2-Sulfonic Acid Phenol

where $R_{c_{n\to w}}^{KIS}$ is the reaction rate coefficient. Static batch experiments showing the hydrolysis of 2-NSAPh in n-octane/pure water fluid systems resulted in a linear relationship between concentration curves of 2-NSA over time, indicating a zero-order kinetic rate. This represents a key assumption towards the suitability of 2-NSAPh as KIS tracer (Schaffer et al., 2013).

Tatomir et al. (2015, 2016) established a mathematical and numerical framework for the design and application of the KIS tracer in laboratory experiments and theoretical studies (Tatomir et al. 2015). The KIS tracer is designed to measure the fluid-fluid interfacial area in a transient immiscible drainage process. The concept of tracer application was first validated by Tatomir et al. (2018) in controlled column experiments with a well-characterized porous medium composed of glass beads. The n-octane as the NAPL (with KIS tracer dissolved) was injected to drain an initially water saturated column packed with the glass beads. Water samples were collected and measured at defined time intervals at the column outlet to provide the breakthrough curves (BTCs) of fluid volumes, and the 2-NSA concentration in the aqueous phase. The experimental data were interpretated by employing the Darcy-scale, two-phase flow, reactive transport model for the KIS tracer developed by (Tatomir et al. 2015, 2016, 2019). The resulting maximum specific capillary associated interfacial area was measured at between 500-540m^{-1} for glass beads with a mean diameter of 240μm (Tatomir et al. 2018). Furthermore, to understand how the hydrodynamically stagnant zones can affect the KIS tracer transport, Gao et al. (2021a) developed a pore-scale, two-phase, reactive transport model for the KIS tracer. By analysing the size of the fluid-fluid

interfacial area and the reacted solute mass in the flowing and stagnant zones, (Gao et al. 2021a) proposed that the KIS tracer test determines the mobile capillary-associated interfacial area locating at the moving front. Gao et al. (2021b) further consider the condition of variable surface roughness of the mineral grains. They found that a mobile mass retention term needs only to be considered when the "root mean square roughness" is larger than 3 μm, concluding that the KIS tracer method is also feasible for determination of capillary associated interfacial area when the grain surface is rough (e.g. natural soils).

Despite the previous experimental and numerical studies that improved the soundness of the KIS tracer method, the answer to how the Darcy-scale porous media heterogeneity affects the KIS tracer test and the corresponding BTCs is not yet known. Commonly, all natural aquifers exhibit a certain degree of heterogeneity. Therefore, for further development of the KIS tracer technique towards field-scale applications it is necessary to consider the factor of porous media heterogeneity. The presence of heterogeneities can change the shape of a moving front as illustrated in **Figure 7.1**. Initially, the profile of the displacement front is considered for "smoothed conditions", i.e., having a small front roughness, but due to the porous medium heterogeneities and the fluid-matrix interaction several fingering scenarios can develop, having different front roughnesses.. Applying a KIS tracer to such a front would allow the studying of its temporal and spatial evolution by interpreting tracer BTCs. The concept implies that a larger interfacial area leads to an increase in the reacted mass of tracer in the wetting phase.

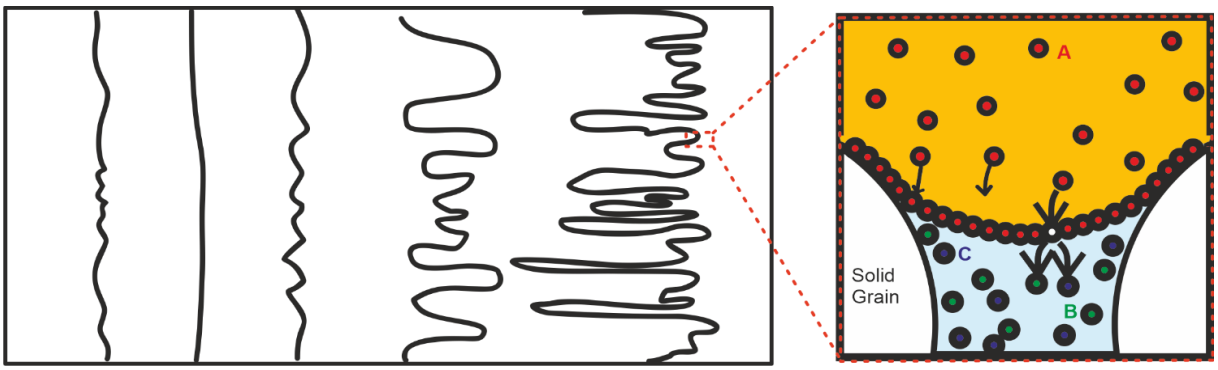

Figure 7.1 Development of a fingering front starting at initial conditions (left); smoothed, conserved, increased, branched front shapes (classification after Bakharev et al. 2020). On the right, the zoom-in pore-scale region showing a fluid-fluid interface where the hydrolysis reaction of the kinetic interface sensitive tracer happens (from Eq.7.1, KIS tracer is A: phenyl naphthalene-2-sulphonate, B: Naphthalene-2-sulphonate acid, and C: Phenol) .

7.1.5 Objective

In this study, a Darcy-scale two-phase reactive transport model is applied to simulate the KIS tracer transport during the primary drainage process in a heterogeneous porous media domain. The domain consists of lenses occupied by two kinds of grains (e.g., fine- and coarse-glass beads), forming in total 14 different heterogeneity patterns. The heterogeneities form regular patterns and are selected arbitrarily in order to produce different fingering and channelling distributions. The

study focuses on the understanding of how the front morphology, i.e., deformation of the front as a result of heterogeneity, affects the concentration of BTCs obtained from the KIS tracer test. Furthermore, we study the correlation between the concentration BTCs and the specific capillary associated interfacial area.

The paper is organized as follows: section 7.2 explains the mathematical model; section 7.3 demonstrates the numerical details; the results and discussions are given in section 7.4; and section 7.5 lists the main conclusions.

7.2 Mathematical model

7.2.1 Two-phase flow in porous media model

The drainage process, defined as the wetting phase being displaced by the non-wetting phase, can be mathematically represented by the governing macro-scale conservation equations for immiscible two-phase flow in porous media:

$$\frac{\partial(S_\alpha \phi \rho_\alpha)}{\partial t} - \nabla \cdot (\rho_\alpha \boldsymbol{v}_\alpha) - \rho_\alpha q_\alpha = 0 \text{ , with } \alpha = w, n \tag{7.2}$$

$$\boldsymbol{v}_\alpha = -\overline{\overline{\mathbf{K}}} \frac{k_{r\alpha}}{\mu_\alpha} (\nabla p_\alpha - \rho \mathbf{g}) \text{ .} \tag{7.3}$$

where α denotes the phase (with *w*, as the wetting phase and *n* as the non-wetting phase), S_α is the phase saturation, ρ_α is the phase density, ϕ is the porosity, $\overline{\overline{\mathbf{K}}}$ is the intrinsic permeability tensor, $k_{r\alpha}$ is the relative permeability of the phase, μ_α is the phase viscosity, p_α is the phase pressure, $q_\alpha$is the volumetric source or sink term, $\boldsymbol{v}_\alpha$ is the apparent velocity of the fluid as given by the extended multiphase Darcy's law, and **g** is the gravity term. The system of partial differential equations is closed with the following equations:

$$S_w + S_n = 1, \tag{7.4}$$

$$p_n - p_w = p_c, \tag{7.5}$$

where p_c is the capillary pressure.

The functional correlation between saturation and capillary pressure has been derived by many researchers (Leverett 1941; van Genuchten 1980; Brooks and Corey 1964). For this research the macroscopic capillary pressure-saturation relationship determined from laboratory experiments is expressed by the Brooks-Corey model:

$$p_c(S_w) = p_d S_e^{-\frac{1}{\lambda}}, \tag{7.6}$$

where p_d is the entry pressure, λ is the pore-size distribution parameter, and $S_e$the effective saturation is defined as:

$$S_e = \frac{S_w - S_{wr}}{1 - S_{wr}}, \tag{7.7}$$

where the $S_{wr}$is the residual wetting phase saturation.
The relative permeability-saturation relationship is written according to the Burdine theorem (Burdine 1953; Helmig 1993):

$$k_{rw}(S_w) = S_e^{\frac{2+3\lambda}{\lambda}}, \tag{7.8}$$

$$k_{rn}(S_w) = (1 - S_e)^2 \left(1 - S_e^{\frac{2+\lambda}{\lambda}}\right) \tag{7.9}$$

Further assumptions considered for the two-phase flow in porous media system discussed herein are: 1) the two fluids are immiscible, incompressible and move under isothermal conditions, 2) the solid matrix is incompressible and non-deformable.

7.2.2 KIS tracer reactive transport model

In an immiscible two-phase flow system such as n-octane and water in a column packed with glass beads, the KIS tracer is present only in the non-wetting phase, while the hydrolysis reaction by-products are present only in the wetting-phase, i.e., no back-partitioning is allowed/assumed. Therefore, theoretically, one transport equation is required for solving each component (see Eq.7.1, ester/KIS tracer, acid, and alcohol). Experimentally, only the acid concentration is measured in the water collected in the effluent (e.g., Tatomir et al. 2018). Furthermore, the components do not influence each other, nor undergo further secondary reactions, and no additional mass transfer process is active (e.g., n-octane dissolved in water phase, or water in n-octane phase). Subsequently, due to the zero-order reaction kinetics and the abundant KIS tracer initially present in the non-wetting phase, the depletion and transport of the tracer molecules are not necessary to be considered. Thus, for the formulation of the KIS tracer reactive transport model in immiscible two-phase flow in porous media, one transport equation is sufficient to solve the transport of the acid hydrolysis by-product.

The reactive transport model of the KIS tracer transport in the immiscible drainage process was demonstrated in (Tatomir et al. 2018). The transport of the acid is described by an advection-dispersion-reaction equation (Eq. 7.10), and it is solved decoupled from the two-phase flow equation system (Eq. (7.2)-(7.5)).

$$\frac{\partial(\phi S_w c_w^\kappa)}{\partial t} - \nabla \cdot \left(c_w^\kappa \boldsymbol{v_w} - D_{pm,w}^\kappa \nabla c_w^\kappa\right) - r_{n\to w}^\kappa = 0 \tag{7.10}$$

Here, c_w^κ is the concentration of the component acid (κ) in the aqueous phase (w), $D_{pm,w}^\kappa$ is the solute dispersivity, and $r_{w\to nw}^\kappa$ is the reaction source term. The longitudinal dispersivity of the acid was determined using fluorescent tracer experiments to be $D_{pm,w}^\kappa$=10^{-3} m for water-saturated flow in a glass beads packed column (Tatomir et al. 2018). Note that dispersivity measured in single-phase flow conditions is not necessarily valid when another fluid-phase is present (Karadimitriou et al. 2016). The hydrolysis reaction rate of the KIS tracer across the fluid-fluid interface is expressed as:

$$r_{n\to w}^\kappa = R_{c_{n\to w}}^{KIS} \cdot a_{wn}\ , \tag{7.11}$$

where a_{wn} is the specific fluid-fluid interfacial area.

According to Schaffer et al. (2013), with the constant reaction rate, the concentrations of KIS tracer reaction products depend on the fluid-fluid interfacial area and the duration the two fluids are in contact with each other. The larger the interfacial area, the larger the mass of the reacted product,

and similarly, the longer the time the two fluid phases are in contact, the larger the mass of reacted solute.

7.2.3 Explicit interfacial area model

The specific fluid-fluid interfacial area is incorporated into the two-phase reactive transport model by assuming a functional relationship $a_{wn} = a_{wn}(S_w, p_c)$, which can be reduced to a single valued relationship for drainage and imbibition processes (Niessner and Hassanizadeh 2009). Tatomir et al. (2013) have used a polynomial expression capable of avoiding non-physical capillary and saturation values:

$$a_{wn}(S_w, p_c) = a_0(S_w)^{a_1}(1 - S_w)^{a_2}(p_c^{max} - p_c)^{a_3}, \tag{7.12}$$

where a_0, a_1, a_2, a_3 and p_c^{max} are the parameters determined by fitting the above polynomial to experimental data or to models, e.g. the implicit model from Grant and Gerhard (2007). Note that the magnitude of a_{wn} is determined by the parameter a_0, while the overall shape of the $a_{wn}(S_w, p_c)$ curve is maintained (Tatomir et al. 2018).

7.2.4 Numerical implementation

The governing system of equations describing the two-phase flow and the reactive transport of the KIS tracer by-product acid in porous media is implemented in the commercial finite element simulation software Comsol Multiphysics™. The set of partial differential equations are written into one of its specialized interfaces, which is a feature that makes Comsol achieve a flexibility similar to academic codes. Tatomir et al. (2016) implemented the Comsol model and conducted a sensitivity analysis to determine the KIS tracer behaviour with regard to changes in flow and transport parameters. Tatomir et al. (2018) provided a validation of the Comsol implemented model by comparing it to the results obtained from a drainage experiment in a column packed with glass beads. The Comsol model was further validated by the same group with a code inter-comparison to DuMu^X (Flemisch et al. 2011), an open-source academic code for simulation of flow and transport processes in porous media (Tatomir et al. 2018). The spatial discretization is the finite element method (FEM), and the time discretization is backward Euler. All computations were performed on a single CPU with 8 cores, operating at 4.3 GHz, and 128 GB RAM.

7.3 Numerical model setup and data processing

7.3.1 Model application to immiscible displacement in a flow cell

A two-dimensional flow cell, measuring 0.22 m × 0.2 m, is designed as the domain of simulation. The domain is initially fully saturated with water, and the n-octane with dissolved KIS tracer is injected from the top boundary at the beginning of the simulations. The top boundary is the inlet where a Neumann boundary is defined with a constant specific flux of the non-wetting fluid at $q=9.26\times10^{-6}$ m/s, and the bottom boundary is the outlet, with Dirichlet boundary conditions (at constant wetting phase pressure of $p_w=1\times10^5$ pa and non-wetting phase saturation of $S_n=0$). The left and right sides of the domain are no-flow boundaries, as shown in **Figure** 7.2(a). Initially there is no solute present in the domain $c=0$. The solute is produced in the regions where wetting and non-wetting fluids are both present. The entire domain consists of three parts: a rectangular region next to the inlet (y>0.18 m), a rectangular region as the main study domain in the centre of the domain (0.04 m<y<0.18 m), and a rectangular region next to the outlet (y<0.04 m). The two rectangular regions next to the inlet and outlet boundaries are set to avoid any boundary effects on

the resulting breakthrough curves. The study domain is designed with two different types of porous media structures (a coarse glass-bead sand and a fine glass-bead sand) previously used in the column experiments conducted by (Tatomir et al. 2018) and (Tatomir et al. 2020). The properties of the fluids and of the two porous materials are given in Table 7.1. The study domain is divided into 77 square lenses (11 horizontal and 7 vertical) some filled with fine sand, while the others with coarse sand. The square lenses have side lengths of 0.02 m. By combining fine- and coarse-sand lenses different types of heterogeneous porous media are created. In total, 14 different inclusion patterns are considered, having different numbers and geometrical distributions, as shown in **Figure** 7.2(b). Due to their simplicity, Pattern 1 (homogeneous, all inclusions are occupied by coarse sand) and Pattern 2 (all lenses occupied by fine sand) are not shown.

A heterogeneity factor (γ) is introduced to quantify the degree of heterogeneity for each lens pattern. The heterogeneity factor (γ) is defined as the ratio of the effective permeability, K_{ef}, to the geometric mean permeability K_{ge} of the porous media (Eq. 7.13):

$$\gamma = K_{ef}/K_{ge} \tag{7.13}$$

If γ>1 then the porous medium is heterogeneous.

When the porous medium is highly heterogeneous (e.g., forming strong preferential flow pathways), the effective permeability becomes larger, and the corresponding ratio to the geometric mean permeability becomes larger.
The effective permeability can be obtained from simulating the steady-state single-phase flow, considering the monitored pressure change between inlet and outlet:

$$K_{ef} = \frac{\mu_w L \cdot q}{p_{w,in} - p_{w,out}}, \tag{7.14}$$

where L is the longitudinal distance between inlet and outlet, q is the specific flux, $p_{w,in}$ and $p_{w,out}$ is the averaged wetting phase pressure at inlet and outlet, respectively.

The geometric mean permeability of a pattern is dependent on the intrinsic permeability of both sands and the number of lenses comprised of both sands and can be calculated as:

$$K_{ge} = \sqrt[n_t]{(k_f)^{n_f} \cdot (k_c)^{n_c}} \tag{7.15}$$

where k_f and k_c are the permeabilities of fine sand and coarse sand, n_f and n_c are the numbers of lens occupied by the fine sand and the coarse sand, and n_t is the total number of the lens.
The breakthrough curves of the tracer product concentration are monitored at the measurement line y=0.05 m, as the fictitious outlet (see Figure 7.2a). The kinetic rate coefficient, $R_{c_{n\to w}}^{KIS}$, of the tracer is assumed at 1.5×10^{-11} kg·m^{-3}·s^{-1}.

Two scenarios are investigated: Case 1 - the so-called standard case with the parameters defined in **Table** 7.1, Case 2 - with the permeability of the heterogeneous inclusions modified such as to enhance the front deformation. In Case 2, the permeability of GB55 is reduced to 1×10^{-13} m^2, while all the other parameters are identical to those of Case 1. In total 28 simulations (14 heterogeneous geometrical patterns for each case) are performed for understanding how the concentration BTCs resulting from KIS tracer tests are affected by the porous media macro-scale heterogeneity. Additionally, the objective is also to find out what type of information a KIS tracer experiment can deliver about the front morphology and the heterogeneity of the porous medium.

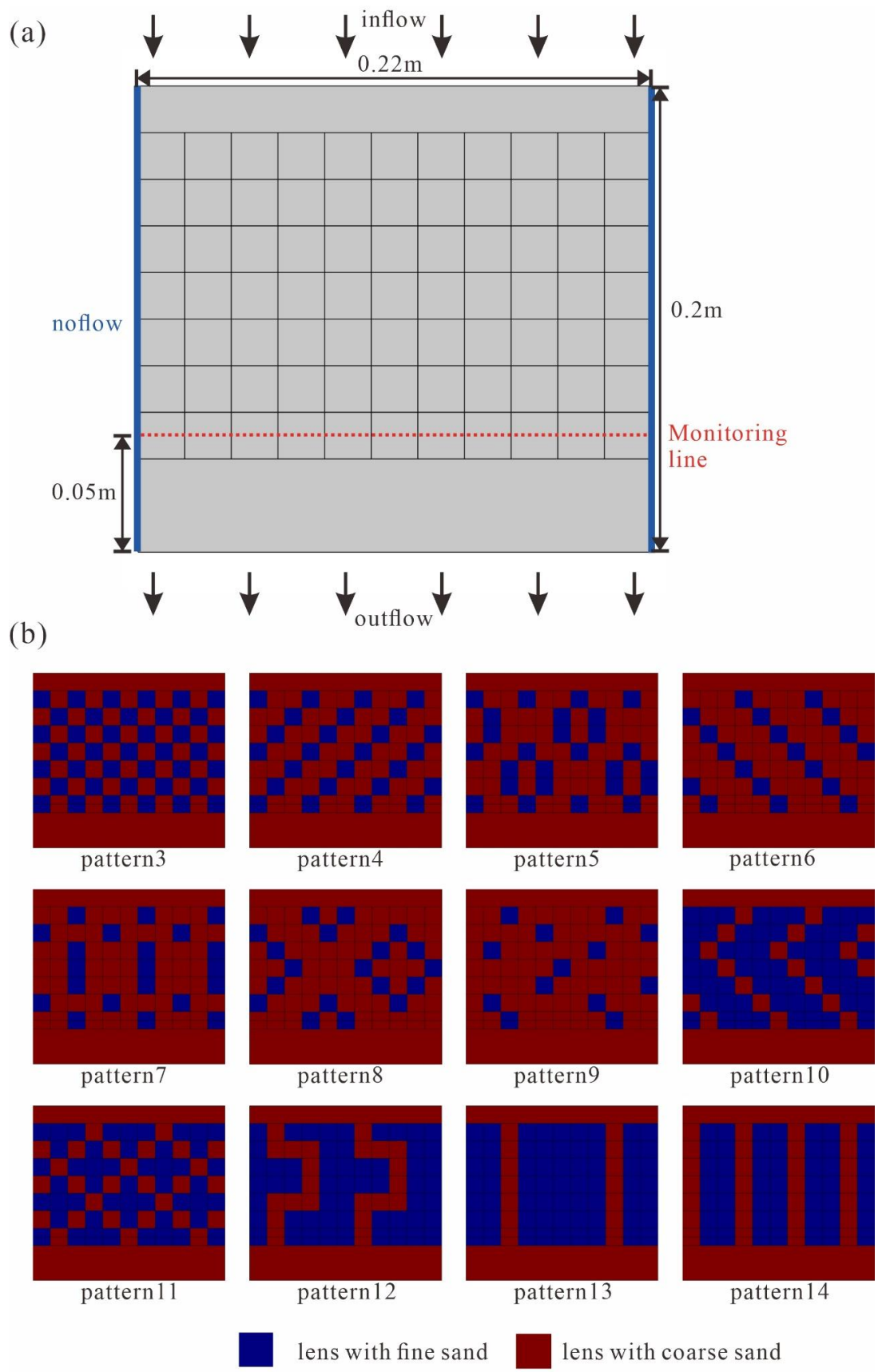
(a)
inflow
0.22m
noflow
0.2m
Monitoring line
0.05m
outflow
(b)
pattern3
pattern4
pattern5
pattern6
pattern7
pattern8
pattern9
pattern10
pattern11
pattern12
pattern13
pattern14
lens with fine sand
lens with coarse sand

Figure 7.2. a) Simulation domain, the boundary conditions and the monitoring line located at y=0.05 m; b) the fourteen heterogeneity patterns investigated (Pattern 1 and Pattern 2 are the ones where the domain is filled by coarse sand and fine sand and are not illustrated).

Table 7.1. Parameters of the porous medium (fine- and coarse-glass beads) and of the fluids used in the simulations

Symbol	Parameter name	Unit	GB55	GB240
d_m	Grain mean diameter	μm	55	240
k	Intrinsic permeability	m^2	8×10^{-13}	1×10^{-11}
ϕ	Porosity	-	0.411	0.464
P_d	Entry pressure	Pa	5937	1606
λ	Pore index coefficient (Brooks-Corey)	-	3.61	3.65
S_{wr}	Residual wetting saturation	-	0	0
$a0$		$Pa^{-1}m^{-1}$	5.22×10^{-5}	1.7×10^{-5}
$a1$		-	0	
$a2$		-	1.11	
$a3$		-	1.94	
p_c^{max}	Maximum capillary pressure	Pa	23287	
D_l	Longitudinal dispersivity	m	1×10^{-3}	
D_t	Transversal dispersivity	m	1×10^{-5}	
Fluids		octane	water	
Wetting behaviour		Non-wetting	wetting	
ρ	Density	kg/m^3	703	1000
μ	Dynamic viscosity	Pa·s	5×10^{-4}	1×10^{-3}

7.3.2 Data processing

The procedures used to interpret the data and to obtain the concentration BTCs and the averaged specific interfacial areas are further discussed. The concentration BTC is obtained by calculating the average solute concentration of acid in the water passing through a measurement line:

$$c_{BTC} = \frac{\mathbf{M}_{BTC}}{\mathbf{V}_{BTC}^{w}} \tag{7.16}$$

where $\mathbf{M}_{BTC}$ and $\mathbf{V}_{BTC}^{w}$ are the solute mass flux and the water volume flux passing through the measurement line. These two fluxes can be obtained by integration:

$$\mathbf{M}_{BTC} = \int_L \frac{\overline{\overline{\mathbf{K}}} \cdot k_{rw}}{\mu_w} \cdot \frac{dp}{dy} \cdot c \, dL \tag{7.17}$$

and

$$\mathbf{V}_{BTC}^{w} = \int_{L} \frac{\overline{\overline{\mathbf{K}}} \cdot k_{rw}}{\mu_w} \cdot \frac{dp}{dy} dL \tag{7.18}$$

where L indicates the length of the measurement line. Additionally, the averaged specific interfacial area in the domain can be calculated by:

$$a_{wn}^{avg} = \frac{\int_{V_b} a_{wn}\, dV}{V_b} \tag{7.19}$$

where V_b is the bulk volume of the porous media in the study domain.

7.4 Results and discussion

The resulting concentration BTCs corresponding to the different heterogeneous patterns are analysed, and their relations to the fraction of bulk volume occupied by each sand are discussed in section 7.4.1. Next, in section 7.4.2, the effect of the front morphology, i.e., the (strong) deformation of the front on the concentration BTCs, are further analysed and discussed.

7.4.1 Comparison of concentration BTCs with porous media heterogeneity

The heterogeneity factors for all patterns are plotted in **Figure** 7.3(a), and the acid concentration breakthrough curves resulting from all simulations of Case 1 are plotted in **Figure** 7.3(b). First, it is observed that the concentration BTCs from Pattern 1 and Pattern 2 both linearly increase. The concentration BTCs of Pattern 1 (domain only filled with coarse sand) has the lowest slope and that of Pattern 2 (only fine sand) has the steepest slope. The porous medium with fine sand generates a larger interfacial area during the drainage process, and thus the production rate of acid is higher, as can be expected. The simulated linearly increasing trend of the BTC is consistent with the observations of our previous experimental study in the homogeneous medium of (Tatomir et al. 2018). Furthermore, it is observed that the heterogeneous Patterns 3 to 11 (with the heterogeneity factor γ<1.36) also have linearly increasing concentration BTCs. Even though the hydraulic parameters of the fine sand inclusions/lenses are much different compared to those filled with coarse sand, the shapes of the fronts are not much affected. One example of the non-wetting phase saturation distribution at breakthrough for Pattern 11 is illustrated in **Figure** 7.4(a) (top). However, the shapes of the concentration BTCs are affected in Patterns 12 to 14 (with the heterogeneity factor γ >1.36). Similarly, one example of the non-wetting phase saturation distribution at breakthrough for pattern 14 is shown in **Figure** 7.4(a) (bottom). The Patterns 12 to 14 are characterized by larger numbers of fine sand lenses, while the distributions of the coarse sand lenses tend to create several shortcuts (i.e., highly conductive channels) for fluid flow (as shown in Figure 7.2). The preferential flow of the non-wetting fluid during drainage through such shortcuts/channels is illustrated in detail in **Figure** 7.4. The highly conductive channels formed in Patterns 12 to 14 induce a larger change in front morphology, which, furthermore, leads to a more accentuated deformation of the concentration BTCs. It is observed that the tracer first arrival (breakthrough) time occurs earlier for Patterns 12 to 14 compared to the Patterns 1 to 11, where breakthrough times are similar. Moreover, for Patterns 12 to 14, tracer breakthrough occurs earlier than the arrival of the non-wetting phase at the measurement line (one example for Pattern 14 is shown in **Figure** 7.4b). This is different from homogenous conditions when the tracer breakthrough always happens almost at the same time as the arrival of the non-wetting phase at the outlet (Tatomir et al. 2018). This effect is caused by the strong advection of the acid reaction product in the formed shortcut. The non-linear behavior of the concentration BTCs for Patterns 12

to 14 is only observed at the early stage of breakthrough (before 5000s). After the early stage (in this case after 5000s) the linearly increasing trend is followed again.

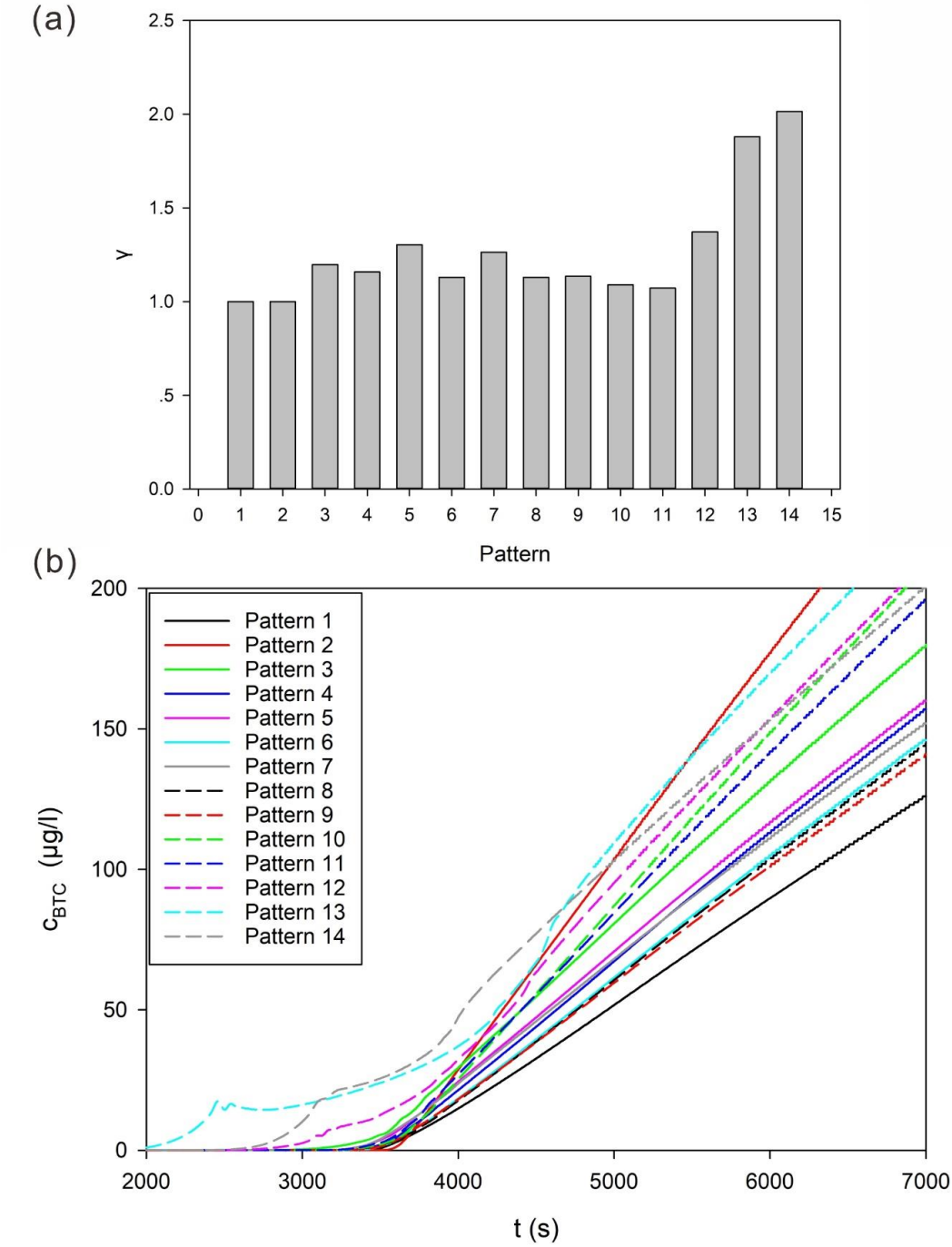

Figure 7.3. Plot of (a) the heterogeneity factor (γ) for the 14 patterns for Case 1 and (b) concentration breakthrough curves at the monitoring line for all simulated heterogeneity patterns.

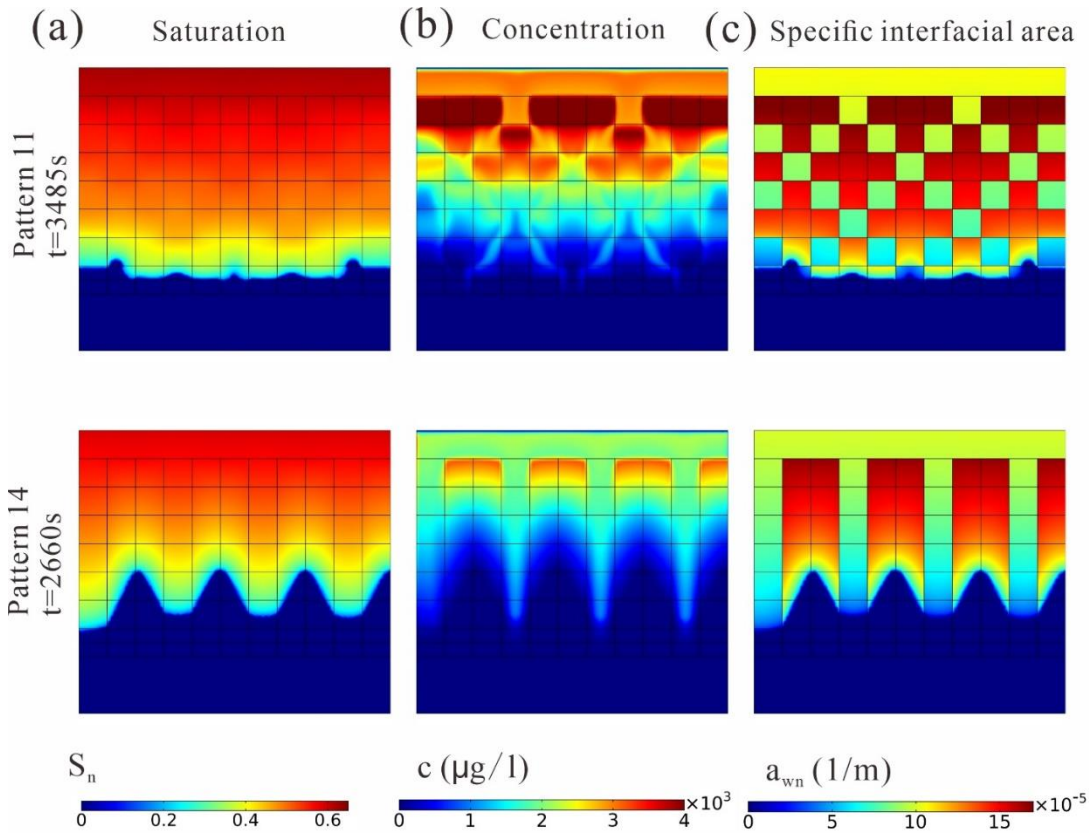

Figure 7.4. Plot of the distribution of (a) the non-wetting phase saturation, (b) acid concentration in water, and (c) specific interfacial area at the time of concentration breakthrough, for simulation of Pattern 11 and Pattern 14.

The slopes of the concentration BTCs obtained from all fourteen simulated heterogeneity patterns are plotted versus the fraction of bulk volume occupied by the fine sand (calculated from the numbers of the lenses of both sands), as shown in **Figure 7.5** (a). It can be observed that the slope of the concentration BTC linearly increases with the fraction of the bulk volume occupied by the fine sand inclusions. This is due to the fact that after drainage the overall interfacial area is larger for larger volumes of finer sand imbedded in the system, since the finer sand creates larger interfacial areas according to the $a_{wn} - S_w$ curves. This can also be observed from the specific interfacial area spatial distributions in **Figure** 7.4(c). This means that when the porous medium is composed of two material types of known hydraulic properties, by creating different specific interfacial areas during drainage and measuring the changes in the slope of the corresponding tracer concentration BTCs, one can determine the fraction of the total bulk volume occupied by the two porous materials. Furthermore, **Figure** 7.5(b) presents the correlation between the slopes of the concentration BTCs and the averaged specific interfacial area over the whole domain after drainage. The results imply that when the slopes of concentration BTCs for the homogeneous porous media formed by both sands are available, the averaged specific interfacial area in the domain formed by heterogeneous distribution of both sands can be directly determined from the corresponding measured concentration BTCs. These findings are limited to the condition where

the deformations of the displacement front and the deformations of the concentration BTCs are small, and for which a constant slope of the concentration BTC is available.

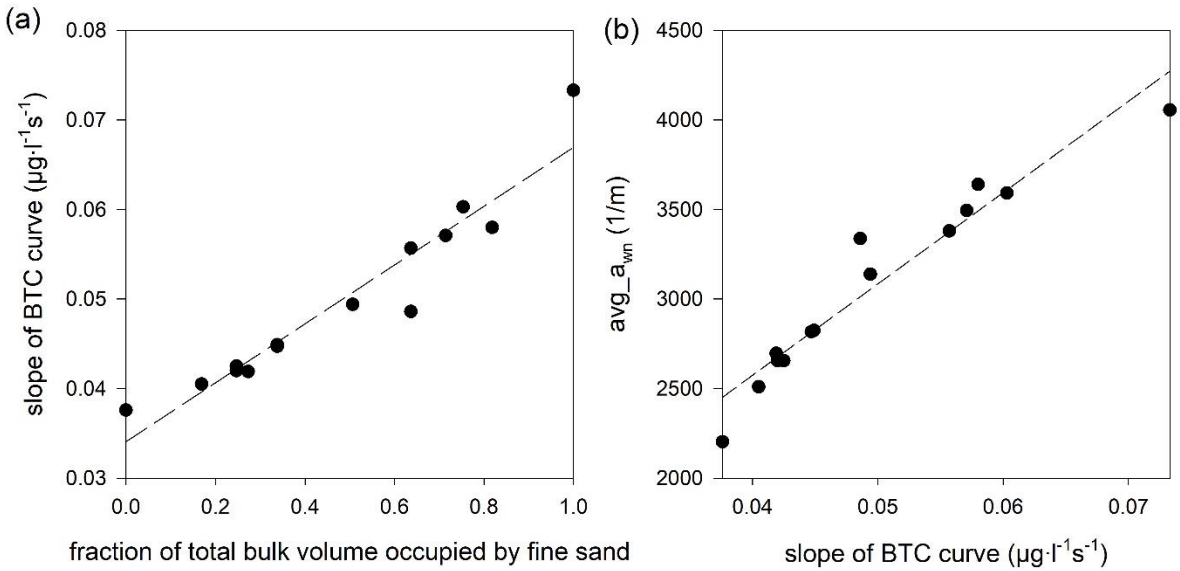

Figure 7.5. Plot of (a) the slope of the concentration BTCs versus the fraction of total bulk volume occupied by the fine sand; (b) the averaged specific interfacial area at the end of the drainage process versus the slopes of the concentration BTCs, resulted from all simulations of Case 1.

7.4.2 Concentration BTCs with strong deformation of the front

The deformation of the front is enhanced with increasing permeability contrast between the background coarse sand and that of the inclusions (fine sand). In this sense the permeability of the finer sand is set to 1×10^{-13} m^2, which is 100 times smaller than that of the coarser sand. All other hydraulic and fluid parameters are kept the same, as discussed in section 7.3. The heterogeneity factors for all patterns are plotted in **Figure** 7.6(a), and the concentration BTCs from all heterogeneity patterns after changing the permeability (Case 2) are plotted in **Figure** 7.6(b). The heterogeneity factors in the Case 2 for patterns 3 to 14 are all larger than 1.59. Comparing **Figure** 7.6 and **Figure** 7.3, we can observe that the concentration BTCs for patterns 4 to 9 still show a linear increasing profile, and the slopes of the BTCs mostly remain the same. However, the first arrivals are obviously earlier. While for patterns 3, 10 and 11, the original linearly increasing profiles of the BTCs modify their shape, and peaks are observed shortly after breakthrough. Also, the breakthrough times occur earlier. For patterns 12 to 14, where the concentration BTCs show peaks in both cases, it is observed that the late-stage slope of the curve becomes lower. In short, when large changes in the front morphology are involved, the tracer concentration BTCs will show some features other than linearly increasing curves, including an earlier breakthrough time, a first peak in concentration shortly after breakthrough, and a lower/flatter slope at later times. The non-linear features of the concentration BTC for heterogeneous porous media match to a certain extent the experimental results conducted in sand filled columns reported in Tatomir et al. (2020). This implies that one possible explanation for the non-linear BTCs from (Tatomir et al. 2020) is the

packing process which can produce a certain degree of heterogeneity inside the column despite the uniform grain size.

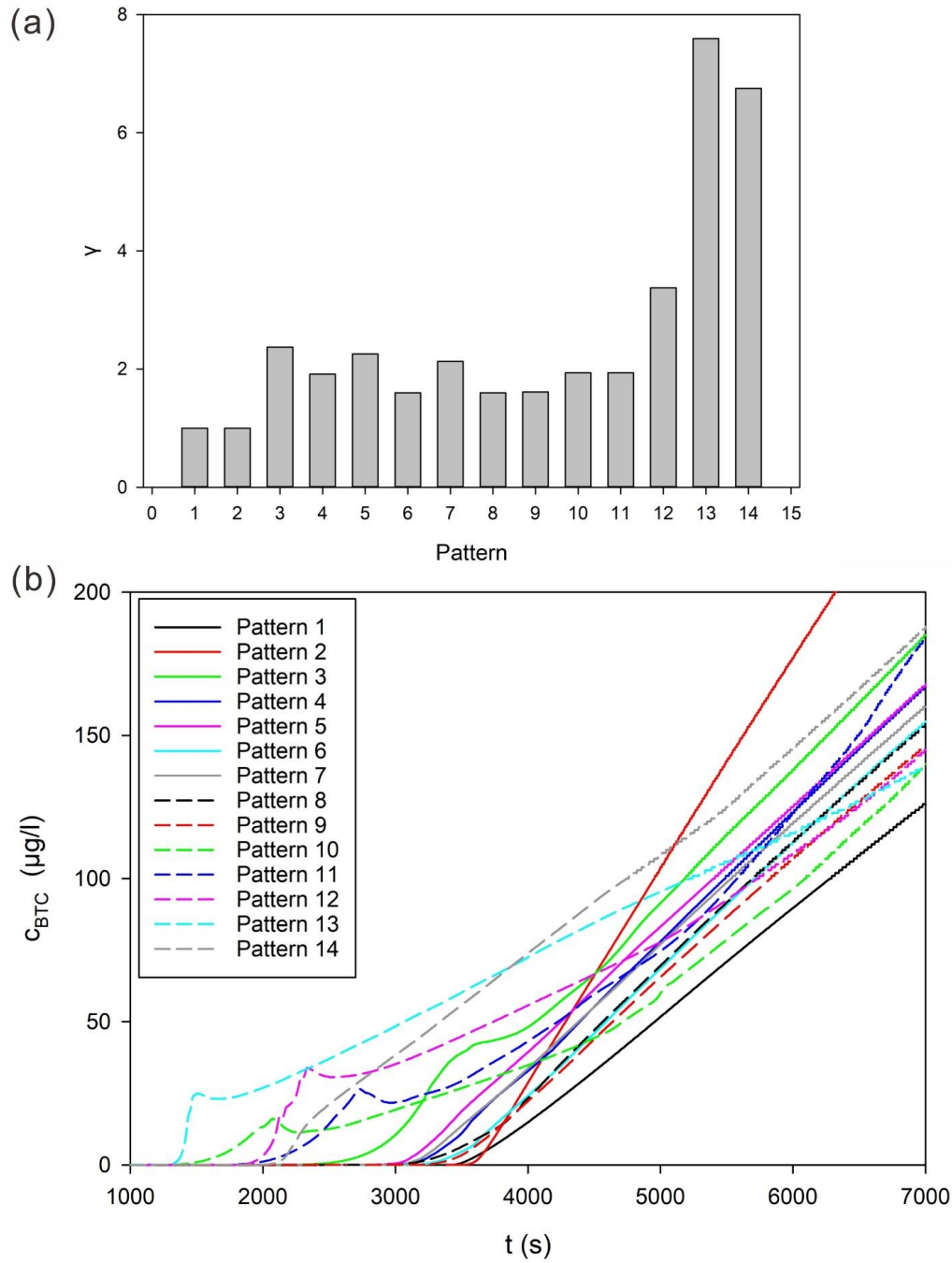

Figure 7.6. Plot of (a) the heterogeneity factor (γ) for the 14 patterns for Case 2 and (b)the concentration breakthrough curves at the measurement line for all simulated heterogeneity patterns with the inclusion lens permeability of 10^{-13} m^2, when the deformation of the front is enhanced.

One example to show the changing morphology of the invading front for Pattern 11 is given in **Figure 7.7** (a). Comparing the spatial distributions of Case 2 and Case 1 for Patter 11 (γ increased from 1.07 to 1.94) plotted in **Figure** 7.7(a) and **Figure** 7.4(a), the front shows a more intense folding/deformation when the permeability of the fine sand is reduced. Due to the lower permeability, the fine sand is not drained as soon as the front passes by, and thus some water becomes entrapped, and "holes" appear at the front. It can be observed in **Figure** 7.7(a) (with a zoom-in, **Figure** 7.7b) that the preferential flow in the coarse sand inclusions increases the acid advective transport in and towards these pathways, leading to a much higher acid concentration in the coarse sand lenses. The change of the concentration BTC for Pattern 11 is plotted in **Figure** 7.7(c), as an example. It is found that the entire deformed concentration BTC can be separated into three stages. The Stage 1 is a non-linear increase in concentration due to the advection of tracer by-product in the preferential flow pathways. From **Figure** 7.7 it can be seen that the concentration breakthrough happens at t=1900s, when the front has not yet arrived at the monitoring/control line. At t=2700s, the concentration BTC reaches a peak, which happens at approximately the same time with the arrival of the tip of the front (fingers), and marks the beginning of Stage 2. During Stage 2, the acid concentration continues to increase but at a smaller rate. This is because the interfacial areas responsible for the acid production, i.e., where the displacement front is present, are mainly the areas located in the preferential flow pathways. During Stage 2, most of the cross-sectional area at outlet (i.e., monitoring / control line) is not drained and contributes insignificantly to tracer BTC. As more areas become drained the slope of the tracer BTCs increases until reaching Stage 3. The Stage 3 is the period for which the largest proportion of the displacement front has passed through the measurement line (at t≈5100s), and the slope of concentration BTC reaches a stable value that is close to the conditions when the front does not exhibit large deformations. During Stage 3 all the cross-sectional area at the monitoring line contributes to the BTC which indicates that the interfacial area contributing to the tracer production remains constant. The tracer concentration is averaged over the monitoring line and represents the overall specific interfacial area in the domain.

The results imply that when a strong deviation from a linear behaviour of the front is involved, an accurate determination of the slope of the concentration BTC can only be accomplished based on the slope measured for Stage 3. Furthermore, when the degree of heterogeneity is large, i.e., represented by the occurrence of preferential flow pathways, Stage 3 is reached at much later times. For example, for Patterns 13 and 14, until t=7000s the concentration BTCs are still at Stage 2 (**Figure** 7.6).

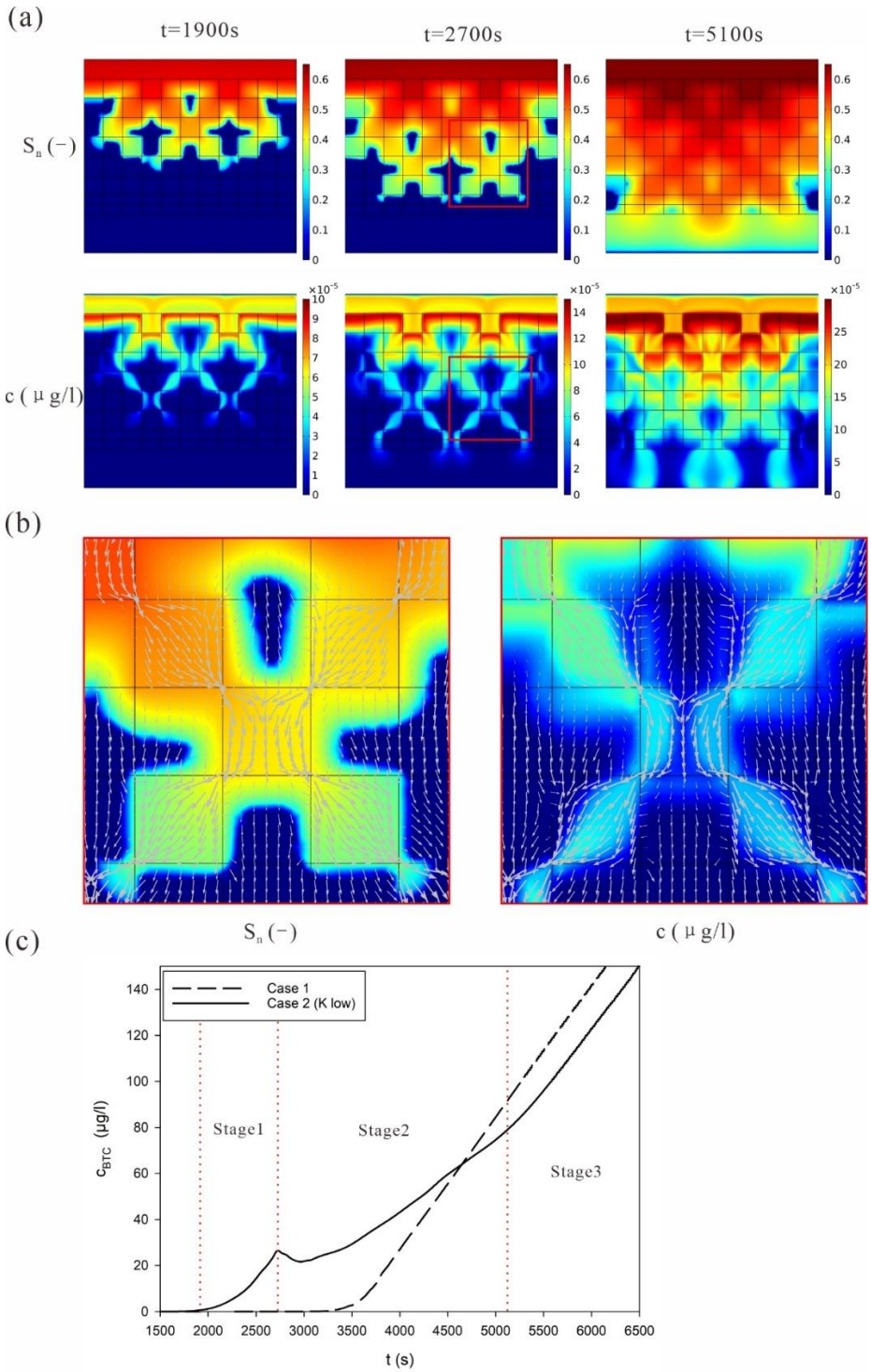
(a)
t=1900s
t=2700s
t=5100s
S_n (−)
c (μ g/l)
(b)
S_n (−)
c (μ g/l)
(c)
Case 1
Case 2 (K low)
Stage1
Stage2
Stage3
c_{BTC} (μg/l)
t (s)

Figure 7.7. Plot of (a) the nonwetting phase saturation and concentration distribution at three different time steps at t=1900s, 2700s and 5100s, from simulations of Pattern 11 when the front deformation is enhanced; (b) zoom-in of the marked domain selection at t=2700 s showing the advective transport towards and into the conductive lenses (the grey arrows are the streamlines computed for the wetting-phase velocity); (c) comparison of concentration breakthrough at the monitoring line for simulation of Pattern 11 before and after the front deformation enhancement.

7.5 Summary and Conclusions

In this numerical study we investigated how the porous media heterogeneity and the front morphology can affect the KIS tracer breakthrough and spatial-temporal concentration distribution. A total of fourteen heterogeneity patterns were created using two types of sands, assigned with the hydraulic parameters of two glass-bead materials used in our previous experimental studies (Tatomir et al. 2018, 2020). The degree of heterogeneity is described by a new heterogeneity factor (γ), defined as the ratio of effective permeability to the geometric mean permeability. The simulations were carried out for the primary drainage process (i.e., NAPL with dissolved KIS tracer being injected to displace water initially present in the porous material). The concentration BTCs were obtained by calculating the mass flux and the water volume flux across a monitoring line. Two cases were studied: Case1 with the standard parameters of two glass beads, and Case 2 where the permeability of fine sand is decreased to enhance the deformation of the front. The major findings of the study are listed below:

- In heterogeneous porous media, when the front morphology is not much affected by the inclusions/lenses (with the heterogeneity factor γ<1.36), the concentration BTCs appear as linearly increasing curves, and their early arrival times are similar. The slope of the concentration BTCs linearly depends on the relative fraction of bulk volume occupied by each type of sand. The slope of the concentration BTCs is linearly related to the spatially averaged specific interfacial area in the domain.
- The folding of the front is significantly enhanced when the permeability of the fine sand is decreased, or the permeability contrast between the two sands is increased. Besides, the folding of the front is also enhanced when the inclusions/lenses form preferential flow pathways, while the front is only slightly affected when the inclusions/lenses are more evenly distributed. .
- When the displacement front exhibits intense blending and deformation, the concentration BTCs, which otherwise display a linearly increasing concentration trend, become deformed. The deformed concentration BTCs show three main features: an earlier first arrival time, a peak of concentration shortly after first arrival, and a lower slope during the following stage stabilizing eventually at a constant slope. Based on the slopes of the concentration BTCs, the KIS tracer test in heterogeneous porous media can mainly be divided into three stages: Stage 1: non-linear increase of tracer concentration until the arrival of the first fingers of the non-wetting front, which coincides with a concentration peak; Stage 2: (after the peak) gradual increase in concentration reaching eventually a stable value for the slope which represents the beginning of Stage 3; Stage 3: the slope of the BTC continues to increase linearly at a constant slope close to the conditions when the front roughness is small (i.e., it is not folded).

The results imply that the KIS tracer test is capable of measuring the averaged specific interfacial area in heterogenous porous media. The measurement time needed is much longer for the concentration BTC to reach the stabilized slope when short-cuts and preferential flow pathways are involved. It is shown that the KIS tracer test can provide information not only on the averaged specific capillary associated interfacial area, but also on the volume fraction in the bulk volume that is occupied by the inclusions/lenses. Besides, the results also imply that based on the shape of the obtained concentration BTCs one can predict the extent of front deformation, as well as the extent of heterogeneity present in the studied porous media.

By considering porous media heterogeneity this work represents a milestone for further development of the KIS tracer technique towards being deployed in field-scale applications, e.g., the tracer could be applied in single-well push-pull tests or in well doublet configurations. Further research is required to develop the experimental procedure of applying the KIS tracer test in intermediate-scale flow-cells. The flow-cells allow the real-time tracking of the fluid phases, the quantification of the fluid saturations and the measurement of concentrations. This is important for improving the understanding of reactive transport in two-phase flow in porous media processes, and for providing a further validation of the numerical model in complex flow fields induced by the heterogeneous porous media.

7.6 Statements and declarations

We acknowledge the funding by the German Research Foundation (Deutsche Forschungsgemeinschaft, DFG) Project Number 428614366.

The authors declare they have no relevant financial or non-financial interests to disclose.

All authors contributed to the study conception and design. AT and HT have written the first draft of the manuscript and all authors commented and contributed to writing. All authors read and approved the final manuscript.

The datasets generated during the current study are published in the manuscript.

7.7 References

Bakharev F, Campoli L, Enin A, et al (2020) Numerical Investigation of Viscous Fingering Phenomenon for Raw Field Data. Transp Porous Media 132:443–464. https://doi.org/10.1007/s11242-020-01400-5

Bolster D, Barahona M, Dentz M, et al (2009) Probabilistic risk analysis of groundwater remediation strategies. Water Resour Res 45:. https://doi.org/10.1029/2008WR007551

Brooks RH, Corey AT HYDRAULIC PROPERTIES OF POROUS MEDIA. 37

Brusseau ML, Zhang Z, Nelson NT, et al (2002) Dissolution of Nonuniformly Distributed Immiscible Liquid: Intermediate-Scale Experiments and Mathematical Modeling. Environ Sci Technol 36:1033–1041. https://doi.org/10.1021/es010609f

Burdine NT (1953) Relative Permeability Calculations From Pore Size Distribution Data. J Pet Technol 5:71–78. https://doi.org/10.2118/225-G

Dawe RA, Wheat MR, Bidner MS (1992) Experimental investigation of capillary pressure effects on immiscible displacement in lensed and layered porous media. Transp Porous Media 7:83–101. https://doi.org/10.1007/BF00617318

Engelberts WF, Klinkenberg LJ (1951) Laboratory Experiments on the Displacement of Oil by Water from Packs of Granular Material. OnePetro

Fagerlund F, Illangasekare TH, Niemi A (2007) Nonaqueous-Phase Liquid Infiltration and Immobilization in Heterogeneous Media: 1. Experimental Methods and Two-Layered Reference Case All rights reserved. No part of this periodical may be reproduced or transmitted in any form or by any means, electronic or mechanical, including photocopying, recording, or any information storage and retrieval system, without permission in writing from the publisher. Vadose Zone J 6:471–482. https://doi.org/10.2136/vzj2006.0171

Flemisch B, Darcis M, Erbertseder K, et al (2011) DuMux: DUNE for multi-{phase, component, scale, physics, …} flow and transport in porous media. Adv Water Resour 34:1102–1112. https://doi.org/10.1016/j.advwatres.2011.03.007

Gao H, Tatomir AB, Karadimitriou NK, et al (2021a) A Two-Phase, Pore-Scale Reactive Transport Model for the Kinetic Interface-Sensitive Tracer. Water Resour Res 57:e2020WR028572. https://doi.org/10.1029/2020WR028572

Gao H, Tatomir AB, Karadimitriou NK, et al (2021b) Effects of surface roughness on the kinetic interface-sensitive tracer transport during drainage processes. Adv Water Resour 104044. https://doi.org/10.1016/j.advwatres.2021.104044

Grant GP, Gerhard JI (2007) Simulating the dissolution of a complex dense nonaqueous phase liquid source zone: 1. Model to predict interfacial area. Water Resour Res 43:. https://doi.org/10.1029/2007WR006038

Grant GP, Gerhard JI, Kueper BH (2007) Multidimensional validation of a numerical model for simulating a DNAPL release in heterogeneous porous media. J Contam Hydrol 92:109–128. https://doi.org/10.1016/j.jconhyd.2007.01.003

Heiß VI, Neuweiler I, Ochs S, Färber A (2011) Experimental investigation on front morphology for two-phase flow in heterogeneous porous media: FRONT MORPHOLOGY. Water Resour Res 47:. https://doi.org/10.1029/2011WR010612

Helmig R (1993) Theorie und Numerik der Mehrphasenströmungen in geklüftet-porösen Medien. Inst. für Strömungsmechanik und Elektronisches Rechnen im Bauwesen

Illangasekare TH, Ramsey JL, Jensen KH, Butts MB (1995) Experimental study of movement and distribution of dense organic contaminants in heterogeneous aquifers. J Contam Hydrol 20:1–25. https://doi.org/10.1016/0169-7722(95)00045-W

Karadimitriou NK, Joekar-Niasar V, Babaei M, Shore CA (2016) Critical Role of the Immobile Zone in Non-Fickian Two-Phase Transport: A New Paradigm. Environ Sci Technol 50:4384–4392. https://doi.org/10.1021/acs.est.5b05947

Kueper BH, Abbott W, Farquhar G (1989) Experimental observations of multiphase flow in heterogeneous porous media. J Contam Hydrol 5:83–95. https://doi.org/10.1016/0169-7722(89)90007-7

Langlo P, Espedal MS (1994) Macrodispersion for two-phase, immiscible flow in porous media. Adv Water Resour 17:297–316. https://doi.org/10.1016/0309-1708(94)90033-7

Lenormand R, Touboul E, Zarcone C (1988) Numerical models and experiments on immiscible displacements in porous media. J Fluid Mech 189:165–187. https://doi.org/10.1017/S0022112088000953

Leverett MC (1941) Capillary Behavior in Porous Solids. Trans AIME 142:152–169. https://doi.org/10.2118/941152-G

Méheust Y, Løvoll G, Måløy KJ, Schmittbuhl J (2002) Interface scaling in a two-dimensional porous medium under combined viscous, gravity, and capillary effects. Phys Rev E 66:. https://doi.org/10.1103/PhysRevE.66.051603

Neuweiler I, Attinger S, Kinzelbach W, King P (2003) Large Scale Mixing for Immiscible Displacement in Heterogeneous Porous Media. Transp Porous Media 51:287–314. https://doi.org/10.1023/A:1022370927468

Niessner J, Hassanizadeh SM (2009) Non-equilibrium interphase heat and mass transfer during two-phase flow in porous media—Theoretical considerations and modeling. Adv Water Resour 32:1756–1766. https://doi.org/10.1016/j.advwatres.2009.09.007

Noetinger B, Zargar G (2004) Multiscale Description and Upscaling of Fluid Flow in Subsurface Reservoirs. Oil Gas Sci Technol 59:119–139. https://doi.org/10.2516/ogst:2004010

Oostrom M, Hofstee C, Walker RC, Dane JH (1999) Movement and remediation of trichloroethylene in a saturated heterogeneous porous medium: 1. Spill behavior and initial dissolution. J Contam Hydrol 37:159–178. https://doi.org/10.1016/S0169-7722(98)00153-3

Page JWE, Soga K, Illangasekare T (2007) The significance of heterogeneity on mass flux from DNAPL source zones: An experimental investigation. J Contam Hydrol 94:215–234. https://doi.org/10.1016/j.jconhyd.2007.06.004

Porter ML, Wildenschild D, Grant G, Gerhard JI (2010) Measurement and prediction of the relationship between capillary pressure, saturation, and interfacial area in a NAPL-water-glass bead system. Water Resour Res 46:W08512. https://doi.org/10.1029/2009WR007786

Rasmusson M, Fagerlund F, Rasmusson K, et al (2017) Refractive-Light-Transmission Technique Applied to Density-Driven Convective Mixing in Porous Media With Implications for Geological CO_2 Storage: Experimental study of convective mixing. Water Resour Res 53:8760–8780. https://doi.org/10.1002/2017WR020730

Schaffer M, Maier F, Licha T, Sauter M (2013) A new generation of tracers for the characterization of interfacial areas during supercritical carbon dioxide injections into deep saline aquifers: Kinetic interface-sensitive tracers (KIS tracer). Int J Greenh Gas Control 14:200–208. https://doi.org/10.1016/j.ijggc.2013.01.020

Schwille F, Pankow JF (1988) Dense chlorinated solvents in porous and fractured media - Model experiments

Tatomir A (2007) Saturation Determination for Multiphase Systems in Porous Medium Using Light Transmission Method. Independent Study, University of Stuttgart

Tatomir A, Maier F, Schaffer M, et al (2013) Modelling of Kinetic Interface Sensitive Tracers for Two-Phase Systems. In: Hou MZ, Xie H, Were P (eds) Clean Energy Systems in the Subsurface: Production, Storage and Conversion. Springer, Berlin, Heidelberg, pp 65–74

Tatomir A, Vriendt KD, Zhou D, et al (2018) Kinetic Interface Sensitive Tracers: Experimental Validation in a Two-Phase Flow Column Experiment. A Proof of Concept. Water Resour Res 54:10,223-10,241. https://doi.org/10.1029/2018WR022621

Tatomir A, Zhou D, Gao H, et al (2019) Modelling of kinetic interface sensitive tracers reactive transport in 2D two-phase flow heterogeneous porous media. E3S Web Conf 85:07003. https://doi.org/10.1051/e3sconf/20198507003

Tatomir AB, Gao H, Pötzl C, et al (2020) Estimation of NAPL-Water interfacial areas for unconsolidated porous media by kinetic interface sensitive (KIS) tracers. In: Earth Space Sci. Open Arch. http://www.essoar.org/doi/10.1002/essoar.10503948.1. Accessed 12 Nov 2021

Tatomir AB, Jyoti A, Sauter M (2016) Monitoring of CO2 Plume Migration in Deep Saline Formations with Kinetic Interface Sensitive Tracers (A Numerical Modelling Study for the Laboratory). In: Vishal V, Singh TN (eds) Geologic Carbon Sequestration: Understanding Reservoir Behavior. Springer International Publishing, Cham, pp 59–80

Tatomir AB, Schaffer M, Kissinger A, et al (2015) Novel approach for modeling kinetic interface-sensitive (KIS) tracers with respect to time-dependent interfacial area change for the optimization of supercritical carbon dioxide injection into deep saline aquifers. Int J Greenh Gas Control 33:145–153. https://doi.org/10.1016/j.ijggc.2014.11.020

van Genuchten MTh (1980) A Closed-form Equation for Predicting the Hydraulic Conductivity of Unsaturated Soils. Soil Sci Soc Am J 44:892–898. https://doi.org/10.2136/sssaj1980.03615995004400050002x

8. Summary and perspectives

8.1 Summary and conclusions

In this thesis, we demonstrated a series of studies at both the pore- and core-scale for development of the KIS tracer method for determination of the FIFA in two-phase flow in porous media. The results provided insight into the transport of the KIS tracer and its reaction product during the two-phase flow. With both the understanding gained from pore-scale numerical studies and the validation from the core-scale experiments, we proved the concept of the KIS and its application in NAPL injection with both a dipole configuration and a push-pull setup. Besides, the results also answered how the tracer signal could change when the KIS tracer is applied to various types of porous media, e.g. grains surfaces at different roughness, grains at different sizes and shapes, aquifers at the different extent of heterogeneities, etc. Outcomes from each step of the research are summarized below.

First, we proposed a novel pore-scale model for simulating the KIS tracer reactive transport process for two-phase flow conditions in porous media. A new continuous species transport formula consistent with the PFM was derived. The fluid-fluid interface hydrolysis reaction of the KIS tracer, approximated by a zero-order reaction, was directly implemented as a bulk reaction at the diffusive interface with the PFM. We then provided adequate verifications, validations, and tests for the newly developed PFM-CST model. The simulation of the two-phase flow with the PFM was first verified with three processes: a co-current two-phase flow process at different viscosity ratios, a bubble relation process, and a film deposit process for two-phase displacement in a capillary tube. Then, the PFM-CST model was verified by comparing it to the analytical solution of a transient interphase mass transfer process, a reaction-diffusion process, and an advective-diffusion process. We found that when the applied partitioning coefficient is lower than 0.01, the model adequately describes the selective distribution of 2-NSA into water. Additionally, no artificial interface mass transfer in an advection-diffusion process was observed during the displacement at a high Péclet number, which showed the good performance of the model for the dynamic processes. Next, the model was tested by simulating the solute transport during drainage in a 2D silt at different Péclet numbers. The transition of the concentration profile from a diffusion-dominated regime to an advection-dominated regime when the Péclet number is increased from Pe=1 to Pe=100 was observed.

To understand how the stagnant zones affect the detectable solute mass in the experiment, we applied PFM-CST model to simulate the KIS tracer experiment in a realistic 2D sandstone porous medium at different Péclet numbers. The interfacial area and the reacted 2-NSA mass were separately quantified in the mobile and immobile zones, using a threshold local Péclet number. The threshold local Péclet number was obtained from its probability distribution during drainage. It was found that the mobile FIFA is much lower than the total FIFA and it varies little during the drainage process. An interpolation relationship between the 2-NSA mass in the mobile zones and the mobile interfacial area was proposed. The relationship is formulated by adding a mobile mass retention term (ξ), describing the part of 2-NSA produced by mobile interface that becomes residual in the immobile zones. The results implied that the KIS tracer experiment during drainage is possible to selectively measure the mobile FIFA.

Employing the PFM-CST model, we further studied the surface roughness of the KIS tracer experiment during primary drainage. The study was implemented in the 2D slits, with fractal surfaces at the root-mean-square roughness ranging from 0 to 15.8 μm. The mobile FIFA for a rough surface is found larger than the one for a smooth surface, due to "Haines jumps" happening for the moving meniscus. However, the rougher surfaces with higher R_{rms} lead to the narrowing of the flow channel, showing a decrease in the mobile FIFA. It was observed that when R_{rms}>3 μm the surface roughness has no effect on the film-associated interfacial area. The average film thickness increases linearly with R_{rms}. Furthermore, the retention of a part of the solute mass produced by the mobile FIFA in the water films at the troughs and grooves on the surface was observed. This retention is described by a film-associated mobile mass retention term (ξ_f). Finally, ξ_f was found to be linearly dependent on R_{rms}, when R_{rms}>3 μm. It was proved that the KIS tracer test is feasible for the measurement of the mobile FIFA during drainage in porous media with rough solid surfaces.

Next, we provided a proof of concept for the KIS tracer at the core-scale, using the simple and well-controlled column drainage experiments. The column was packed with glass beads, and four experiments were conducted at different pumping rates. The previously developed macro-scale model for the KIS tracer was used to simulate the experiment process. The parameters (i.e. flow rates and permeabilities) were optimized to fit the n-octane BTCs, followed by the determination of the specific FIFA through fitting the 2-NSA concentration BTCs. The predictions of the specific FIFA varied significantly due to measurement difficulties. The variation range of the determined specific FIFA was large (from 300 m^{-1} up to 1500 m^{-1}) in experiments with limited data points. In better-controlled experiments, the resulting specific FIFA ranged between 500-750m^{-1} for glass beads with a mean diameter of 240μm.

In an attempt to expand the application spectrum for more porous materials, we further demonstrated the employment of KIS tracer in 15 sets of column drainage experiments, performed on five different porous media. It was found that KIS tracer measured specific FIFA increases linearly with inverse mean grain diameter, and natural sands have larger specific FIFA than the smooth glass beads. A compilation of the literature reported data was provided for the specific FIFA measured from different methods. The FIFA measured with the KIS tracer method is about 3 to 5 times smaller than the literature data. The results implied that some fraction of the reacted solute becomes trapped in stagnant flow regions and it is never measured, and the KIS tracer experiment during drainage only measures the mobile FIFA, consistent with the pore-scale findings. Besides, many of the experimental BTCs showed an early concentration peak and were flattening at the end of the drainage. These effects were not possible to be reproduced by the current macro-scale two-flow reactive transport models.

Then, we investigated numerically how the porous media heterogeneity and the front morphology can affect the KIS tracer breakthrough at the core scale. The simulations were done on fourteen 2D heterogeneity patterns, created using two types of porous materials. It was observed the concentration BTCs appear as linearly increasing curves with similar arrival times when the deformation of the front morphology is slight. The slope of the concentration BTCs was linearly dependent on the volume of the inclusions and the spatially averaged specific FIFA in the domain. However, the concentration BTCs were deformed when the front exhibits intense blending and deformation, and the permeability contrast between the two sands increased. The deformed

concentration BTCs showed an earlier first arrival time, a peak of concentration shortly after first arrival, and a stabilized slope of the BTC at the end. The measurement of FIFA was mainly relied on the stabilized slope at the late stage of the breakthrough. The results implied that the shapes of the concentration BTCs from the KIS tracer experiment are relevant to the extent of front deformation and aquifer heterogeneity.

Finally, in contrast to a dipole configuration, a new push-pull KIS tracer method for measurement of total (mobile and immobile) capillary-associated FIFA was proposed. The pore-scale numerical experiments were conducted employing the PFM-CST model for a 2D porous medium. It was observed that the advective and dispersive transport of the tracer is very weak during primary drainage in the push stage but becomes more prominent during the main imbibition in the pull stage. The tracer concentration BTCs show a non-linearly decreasing profile with time, i.e. the slope of the BTCs reduces with time, and the tailing concentration reaches a plateau. It is found that the dispersion coefficient can be determined from the time to approach steady-state tailing concentration plateau, and the specific FIFA during push and pull processes can be determined separately from the magnitudes of the peak at the beginning of BTCs and the tailing concentration plateau. The push-pull KIS tracer method for the determination of the FIFA was also proved through the column experiment. We proved that previously developed macro-scale KIS tracer reactive transport models can be used for simulation and interpretation of push-pull experiments.

In conclusion, we studied the KIS tracer experiment in both a dipole configuration and a push-pull setup. The former focuses on the measurement of the mobile capillary-associated FIFA, and the latter focuses on the measurement of the total capillary-associated FIFA. For the experiments with the dipole configuration, it was often observed in the column experiments that the BTCs exhibited an early concentration peak and were flattening or decreasing towards the end of the drainage process (as shown in Chapter 6), and this cannot be predicted from our macro-scale model. There are several possible reasons for that. First, the packing process of the porous media may induce a certain extent of heterogeneities, which leads to the deformation of the BTCs. The shapes of the anomalous BTCs are consistent with those simulated BTCs from the drainage experiments in heterogeneous porous materials in Chapter 7. Second, the obtained BTCs are affected by manual measurement errors, resulting from the small volume of usable water samples being obtained from the column experiments. The very limited volume of usable water samples was reported from the column drainage experiments in both Chapter 5 and Chapter 6. Third, the advective-dispersive transport of the reacted tracer (2-NSA) is too weak during drainage. This weak transport of 2-NSA causes a departure of its concentration simulated at the outlet (inside the porous material) by the model and in the effluent (outside the porous material) from the experiments. The effluent water sample is an accumulation of released trapped water shortly after the first arrival of NAPL at the column outlet. These trapped water clusters may have different concentrations and they are not well-mixed due to the weak advective-dispersive transport, which was demonstrated in Chapter 4. Additionally, the pore-scale studies from Chapter 2 and Chapter 3 imply that the determination of the mobile FIFA with the dipole configuration requires knowledge of the 2-NSA mass retention term, resulting from the capillary trapping water in porous materials with both smooth and rough surfaces. Additional measurements on the porous materials (e.g. surface roughness) and the total 2-NSA mass in the effluent are required to estimate this retention term. Despite these difficulties, KIS tracer experiments with the dipole configuration can provide valuable information about the mobile FIFA and the dynamics of the interface during two-phase flow, which is not accessible for

most existing techniques for quantification of the FIFA. On the other hand, the push-pull setup of the KIS tracer experiment can avoid some of the above limitations from the dipole configuration, i.e. small volume of the usable water sample, weak transport of reacted tracer (2-NSA), and requirement of the retention term. The push-pull KIS tracer method can be a fast and practical way to measure the total capillary-associated FIFA in field-scale applications. Last but not least, it is shown in Chapter 4 that during both primary drainage and main imbibition, the macro-scale KIS tracer reactive transport models developed by Tatomir et al. (2015, 2016, 2018) can well predict the spatial 2-NSA concentration distributions inside the porous medium. This indicates that the reactive transport of the KIS tracer and its product 2-NSA has been well described by the macro-scale models, and the predictive capacities of the theoretical modeling framework are proved.

8.2 Further perspectives

Despite the promising progress in the development of the KIS tracer methods, further research is necessary to expand the spectrum of porous materials and fluids systems where the tracer can be applied and to bring the KIS tracer method closer to field application with the forward modeling considering different effects from natural aquifers, e.g. aquifer temperature, mineral composition, type of NAPL, heterogeneities, aquifer geometry, fractures, etc.

For the KIS tracer experiments with dipole configurations to determine the mobile FIFA, further work is required to study if the mobile mass retention term varies when applied to different pore geometries, or when using different fluid and porous media systems, e.g. changes in fluid viscosity ratio, different medium wettability, etc. In addition, one possibility to further improve the current macro-scale model for simulation of the effluent 2-NSA concentration is to differentiate the reacted tracer (2-NSA) in the flowing water and the stagnant water by two independent governing equations, and the effluent 2-NSA concentration is expected to be consistent with that in the flowing water. Furthermore, considering the intrinsic connection between the mobile FIFA and the displacement front, the KIS tracer method with dipole configurations may potentially be used to monitor the macroscopic interface, i.e. the isolines of saturation, between the two fluids and the front evolution during the displacement. Thus, further work is required to develop the experimental procedure of applying the KIS tracer test in intermediate-scale flow cells. The flow cells allow the real-time tracking of the fluid phases, the quantification of the fluid saturations, and the measurement of the tracer (2-NSA) concentrations, which is important for the dynamic two-phase flow in porous media.

For the KIS tracer experiments with push-pull setups to determine the total capillary-associated FIFA, future work is required to implement the column experiment with a variety of “push-pull” flow rates, so that the FIFA is measured at different saturations. Further experimental work is also required to extend the application spectrum of the “push-pull KIS tracer method”, by the column experiments using a wider range of porous media comprised of glass beads and natural soils with different grain sizes and textures. Besides, the present studies did not consider gravity, which may play an important role in CO_2 injection into the reservoirs in field applications. The aquifer geometry and heterogeneity along with the buoyancy forces of the NAPL could affect the tracer signal to a certain extent, compared to the condition of one-dimensional column experiments with homogeneous media. The performance of the tracer in field applications needs to be proved through forwarding numerical modeling studies. Furthermore, in the current studies, the KIS tracer is mainly injected along with NAPL during the primary drainage, i.e. NAPL (dissolved with the

tracer) is injected into water-saturated reservoirs. In many situations of the applications, such as geological CO_2 storage and NAPL contaminated-site remediation, the NAPL phase may initially exist in the reservoir/aquifer at a certain saturation. Thus, the KIS tracer method may be applied to aquifers/reservoirs with residual NAPL, which requires further studies. Additionally, to avoid chemical interference in field applications, more chemicals with (pseudo) zero-order reactions at the fluid-fluid interface, can serve as the KIS tracers, which need to be tested with laboratory experiments. Also, different NAPLs other than n-octane can be used in the KIS tracer experiments.